Universität Rostock Traditio et Innovatio

A comprehensive characterization of aerosols formed by photooxidation of emissions from combustion engines complying to latest regulation standards

Kumulative Dissertation

zur Erlangung des akademischen Grades

doctor rerum naturalium (Dr. rer. nat.)

der Mathematisch-Naturwissenschaftlichen Fakultät

der Universität Rostock

vorgelegt von

Andreas Paul

geb. Am 22.08.1994 in Dänemark

aus Hørning 8362, Dänemark

Rostock, November.2024

https://doi.org/10.18453/rosdok_id00005660

Reviewers:

Prof. Dr. George Biskos, Delft University of Technology, Department Geosciene and Remote Sensing, Atmospheric science

Prof. Dr. Udo Kragl, Universität Rostock, Mathematisch-Naturwissenschaftliche Fakultät, Abteilung Technische Chemie

Prof. Dr. Ralf Zimmermann, University of Rostock, Institute of Chemistry, Division of Analytical and Technical Chemistry

Thesis Handin Year: 2024

Thesis defence year: 2025

4. Erklärung gemäß § 4 Absatz 1 Buchstaben g und h der Promotionsordnung

Doktorandinnen/Doktoranden-Erklärung gemäß § 4 Absatz 1 Buchstaben g und h der Promotionsordnung der Mathematisch-Naturwissenschaftlichen Fakultät der Universität Rostock

Name Paul, Andreas

(Name, Vorname)

Anschrift Rådhuspladsen, 8362, Hørning

(Straße, PLZ, Wohnort)

Ich habe eine Dissertation zum Thema

A comprehensive characterization of aerosols formed by photooxidation of emissions

from combustion engines complying to latest regulation standards

an der Mathematisch-Naturwissenschaftlichen Fakultät der Universität Rostock angefertigt. Dabei wurde ich von Frau/Herrn

Prof. Dr. Ralf Zimmermann betreut.

Ich gebe folgende Erklärung ab:

1. Die Gelegenheit zum vorliegenden Promotionsvorhaben ist mir nicht kommerziell vermittelt worden. Insbesondere habe ich keine Organisation eingeschaltet, die gegen Entgelt Betreuerinnen/Betreuer für die Anfertigung von Dissertationen sucht oder die mir obliegenden Pflichten hinsichtlich der Prüfungsleistungen für mich ganz oder teilweise erledigt.

2. Ich versichere hiermit an Eides statt, dass ich die vorliegende Arbeit selbstständig angefertigt und ohne fremde Hilfe verfasst habe. Dazu habe ich keine außer den von mir angegebenen Hilfsmitteln und Quellen verwendet und die den benutzten Werken inhaltlich und wörtlich entnommenen Stellen habe ich als solche kenntlich gemacht.

Rostock, den 13.11.2024 .....

(Unterschrift)

Scientific CV

2010-2013 Highschool – Technical gymnasium Viby J

- A levels : Math, Danish, Biology, Chemistry and Analytical methods

2013-2016 Bachelor in Chemistry at Aarhus university

Bachelor project on X-ray crystallography

2017-2019 Masters in Chemistry at Aarhus University

Courses focused on aerosols and environmental chemistry

Master thesis on hygroscopicity of aerosols supervised by Merete Bilde

Published work from my Master:
Rosati et al. ***Environ. Sci.: Processes Impacts***, 2020,**22**, 1759-1767

2019-2025 PhD student at Rostock university located at Jülich Research Center (FZJ)

Supervision by Ralf Zimmermann, and local supervision at FZJ by Thorsten Hohaus

Publications during the PhD can be found under “List of original publications”

List of original publications

First-authorships

The following manuscripts were created by Andreas Paul as the first author and under review and published in peer-reviewed journals. The specific contributions of Andreas Paul are given below for each publication.

Publication #1

Title: Formation of Secondary aerosol from emissions of a Euro 6d-compliant gasoline vehicle with a particle filter.

Authors: Paul, Andreas; Fang, Zheng; Martens, Patrick; Mukherjee, Arya; Jakobi, Gert; Ihalainen, Mika; Kortelainen, Miika; Somero, Markus; Yli-Pirilä, Pasi; Hohaus, Thorsten; Czech, Hendryk; Kalberer, Markus; Sippula, Olli; Rudich, Yinon; Zimmermann, Ralf; Kiendler-Scharr, Astrid.

Journal: Environmental Science Atmosphere 4(7)

Year: 2024

DOI: 10.1039/D3EA00165B

Contribution: Andreas Paul carried out the data acquisition with the HR-ToF AMS during the experimental phase. Further, data analysis of the AMS data and comparison of data between all instruments was performed by Andreas Paul. The manuscript was primarily written by Andreas Paul with assistance of the coauthors for data interpretation and revisions.

Publication # 2

Title: The impact of photochemical aging on secondary aerosol formation from a marine engine

Authors: Paul, Andreas; Kokkola, Tuukka; Fang, Zheng; Ihalainen, Mika; Czech, Hendryk; Etzien, Uwe; Hohaus, Thorsten; Sippula, Olli; Rudich, Yinon; Buchholz, Bert; Zimmerman, Ralf.

Journal: NPJ *Climate and Atmospheric Science (in review)*

Year:2024

DOI: 10.21203/rs.3.rs-4983538/v1

Contribution: Andreas Paul carried out the data acquisition with the HR-ToF AMS during the experimental phase. Further, data analysis of the AMS and SMPS data was performed by Andreas Paul. The manuscript was primarily written by Andreas Paul with the assistance of the coauthors for data interpretation.

Co-authorships

Publication # 3

Title: On the Complementarity and Informative Value of Different Electron Ionization Mass Spectrometric Techniques for the Chemical Analysis of Secondary Organic Aerosols

Authors: Hartner, Elena; Paul, Andreas; Käfer, Uwe; Czech, Hendryk; Hohaus, Thorsten; Gröger, Thomas; Sklorz, Martin; Jakobi, Gert; Orasche, Jürgen; Jeong, Seongho; Brejcha, Ramona; Ziehm, Till; Zhang, Zhi-Hui; Schnelle-Kreis, Jürgen; Adam, Thomas; Rudich, Yinon; Kiendler-Scharr, Astrid, Zimmermann, Ralf.

Journal: ACS Earth and Space Chemistry 6(2)

Year: 2022

DOI: 10.1021/acsearthspacechem.2c00039

Contribution: Andreas Paul acquired and analyzed the data of the HR-TOF AMS. Further, the segment on HR-ToF AMS in the manuscript was written by Andreas Paul.

Publication # 4

Title: Effect of Atmospheric Aging on Soot Particle Toxicity in Lung Cell Models at the Air-Liquid Interface: Differential Toxicological Impacts of Biogenic and Anthropogenic Secondary Organic Aerosols (SOAs)

Authors: Offer, Svenja; Hartner, Elena; Di Bucchianico, Sebastiano; Bisig, Christoph; Bauer, Stefanie; Pantzke, Jana; J. Zimmermann, Elias; Cao,Xin; Binder, Stefanie; Kuhn, Evelyn; Huber, Anja; Jeong, Seongho; Käfer, Uwe; Martens, Patrick; Mesceriakovas, Arunas; Bendl, Jan; Brejcha, Ramona; Buchholz, Angela; Gat, Daniella; Hohaus, Thorsten; Rastak, Narges; Jakobi, Gert; Kalberer, Markus; Kanashova, Tamara; Hu, Yue; Ogris, Christoph; Marsico, Annalisa; Theis, Fabian; Pardo, Michal; Gröger, Thomas; Öder, Sebastian; Orasche, Jürgen; Paul, Andreas; Ziehm, Till; Zhang, Zhi-Hui; Adam, Thomas; Sippula, Olli; Sklorz, Martin; Schnelle-Kreis, Jürgen; Czech, Hendryk; Kiendler-Scharr, Astrid, Rudich, Yinon; Zimmermann, Ralf.

Journal: Environmental Health Perspectives 130(2):27003

Year: 2022

DOI: 10.1289/EHP9413

Contribution: Andreas Paul acquired and analyzed the data of the HR-TOF AMS. Further, revised the aerosol characterization segment of the manuscript.

Publication # 5

Title: Are reactive oxygen species (ROS) a suitable metric to predict toxicity of carbonaceous aerosol particles?

Authors: Zhi-Hui, Zhang; Hartner, Elena; Utinger, Battist; Gfeller, Benjamin; Paul, Andreas; Sklorz, Martin; Czech, Hendryk; Yang, Bin Xia; Su, Xin Yi; Jakobi, Gert; Orasche, Jürgen; Schnelle-Kreis, Jürgen; Jeong, Seongho; Gröger, Thomas; Pardo, Michal; Hohaus, Thorsten; Adam, Thomas; Kiendler-Scharr, Astrid, Rudich, Yinon; Zimmermann, Ralf; Kalberer, Markus.

Journal: Atmospheric Chemistry and Physics 22(3)

Year: 2022

DOI: 10.5194/acp-22-1793-2022

Contribution: Andreas Paul acquired and analyzed the data of the HR-TOF AMS. Further contributed to the data interpretation and revised in the manuscript.

Publication # 6

Title: Exposure to naphthalene and β-pinene-derived secondary organic aerosol induced divergent changes in transcript levels of BEAS-2B cells

Authors: Pardo, Michal; Offer, Svenja; Hartner, Elena; Di Bucchianico, Sebastiano; Bisig, Christoph; Bauer, Stafanie; Pantzke, Jana; J. Zimmermann, Elias; Cao, Xin; Binder, Stephanie; Kuhn, Evelyn; Huber, Anja; Jeong, Seongho; Käfer, Uwe; Schneider, Eric; Mesceriakovas, Arunas; Bendl, Jan; Brejcha, Ramona; Buchholz, Angela; Gat, Daniela; Hohaus, Thorsten; Rastak, Narges; Karg, Erwin; Jakobi, Gert; Kalberer, Markus; Kanashova, Tamara; Hu, Yue; Orgis, Christoph; Marsico, Annalisa; Theis, Fabian; Shalit, Tali; Gröger, Thomas; P. Rüger, Christopher; Öder, Sebastian; Orasche, Jürgen; Paul, Andreas; Zhang, Zhi-Hui; Adam, Thomas; Sippula, Olli; Sklorz, Martin; Schnelle-Kreis, Jürgen; Czech, Hendryk; Kiendler-Scharr, Astrid; Zimmermann, Ralf; Rudich, Yinon.

Journal: Environment International

Year: 2022

DOI: 10.1016/j.envint.2022.107366

Contribution: Andreas Paul acquired and analyzed the data of the HR-TOF AMS and approved of the manuscript.

Publication # 7

Title: Atmospheric aging increases the cytotoxicity of bare soot particles in BEAS-2B lung cells

Authors: Pardo, Michal; Czech, Hendryk; Offer, Svenja; Sklorz, Martin; Di Bucchianico, Sebastiano; Hartner, Elena; Pantzke, Jana; Kuhn, Evelyn; Paul, Andreas; Ziehm, Till; Zhang, Zhi-Hui; Jakobi, Gert; Bauer, Stafanie; Huber, Anja; J. Zimmermann, Elias; Rastak, Narges; Binder, Stephanie; Brejcha, Ramona; Schneider, Eric; Orasche, Jürgen; P Rüger, Christopher; Öder, Sebastian; Schnelle-Kreis, Jürgen; Hohaus, Thorsten; Kalberer, Markus; Sippula, Olli; Kiendler-Scharr, Astrid; Zimmermann, Ralf; Rudich, Yinon.

Journal: Aerosol Science and Technology

Year: 2023

DOI: 10.1080/02786826.2023.2178878

Contribution: Andreas Paul acquired and analyzed the data of the HR-TOF AMS and approved of the manuscript.

Publication # 8

Title: The effect of aging conditions at equal OH exposure in an oxidation flow reactor on the composition of toluene-derived secondary organic aerosols

Authors: Czech, Hendryk; Yli-Pirilä, Pasi; Tiitta, Petri; Ihalainen, Mika; Hartikainen, Anni; Schneider, Eric; Martens, Patrick; Paul, Andreas; Hohaus, Thorsten; P Rüger, Christopher; Jokiniemi, Jorma; Zimmermann, Ralf; Sippula, Olli.

Journal: Environmental Science: Atmospheres 4(7)

Year: 2024

DOI: 10.1039/d4ea00027g

Contribution: Andreas Paul operated the model simulations of the oxidation flow reactor in KinSim, and approved of the manuscript.

Publication # 9

Title: Emission dynamics of reactive oxygen species and oxidative potential in particles from a gasoline car and wood stove

Authors: Battist Utinger, Alexandre Barth, Andreas Paul, Arya Mukherjee, Steven John Campbell, Christa-Maria Müller, Mika Ihalainen, Pasi Yli-Pirilä, Miika Kortelainen, Zheng Fang, Patrick Mertens, Markus Somero, Juho Louhisalmi, Thorsten Hohaus, Hendryk Czech, Olli Sippula, Yinon Rudich, Ralf Zimmermann, and Markus Kalberer

Journal: Aerosol Research

Year: 2024

DOI: 10.5194/ar-2024-27

Contribution: Andreas Paul acquired and analyzed the data of the HR-TOF AMS. Further, Andreas Paul contributed to the data interpretation and approved the manuscript.

Signature of applicant: _____

Signature of Supervisor: _____

Acknowledgements

I would like to thank my supervisors Ralf Zimmermann and Thorsten Hohaus for their work with me and their guidance through this PhD. Further I would like to thank all my co-authors of my papers without whom I would not have been able to add my own contribution to the scientific field of aerosols. Additionally, I would like to extent a special thanks to Hendryk Czech who has been a great help throughout my PhD. Finally I would like to thank the late Astrid Kiendler-Scharr for her support during the start of my PhD journey.

Abstract

The presented dissertation addresses the chemical characterization and comprehensive analysis of aerosols formed from combustion engine emissions and exposed to photooxidation in an oxidation flow reactor. The aerosols composition was determined by applying a high-resolution time of flight aerosol mass spectrometer (HR-ToF AMS) allowing for a quantitative chemical characterization.

Aerosols are widely recognized as a significant threat to public health, with thousands of premature deaths attributable to aerosol pollution. Further, aerosols are considered a major factor influencing climate change. The chemical composition of the aerosol is crucial for its impact on climate and human health. It is not only dependent on the source of the aerosol or aerosol precursors but also the atmospheric photochemical aging that leads to secondary aerosol formation. Overall, this leads to large uncertainties in climate models and a lack of understanding on how aerosols impact public health.

For this work, the kinSim model was used to determine the RO_2 fate and the changes in photooxidation conditions present in the oxidation flow reactor. NO emissions were found to be a significant factor in terms of secondary aerosol formation from combustion engine exhaust gases, as NO quenched OH radical formation resulting in lower simulated atmospheric age and a significant change in RO_2 fate.

To test the impacts of a modern euro 6d compliant car, a Skoda Scala was run on an in lab rototest setup at 4 different speeds, 0 km/h (idling), 50 km/h, 80 km/h and 100 km/h. The euro 6d compliant car emitted no primary particles regardless of driving speed, however after atmospheric oxidation significant secondary aerosol formation was observed at all vehicle speeds. The primary gas phase emissions were characterized to determine the processes leading to aerosol formation after atmospheric oxidation. Comparing SOA with CO revealed that the majority of SOA at speeds under 80 km/h is formed from unburned fuel evaporation, which was linked to a few dominating aromatic VOCs: Toluene, Xylene and Trimethylbenzene. At over 80 km/h however the aerosol becomes less organic dominated in terms of mass and the primary source shifts from unburned fuel to incomplete combustion.

Furthermore, an auxiliary ship engine was run on two different fuels, low sulfur heavy fuel oil (LS-HFO) and marine gas oil (MGO). The resulting emissions were exposed to varying levels of ·OH radicals in an oxidation flow reactor to assess the impact of atmospheric aging on ship traffic emissions, and the impacts of fuel sulfur content regulations on aerosol formation. It was found that whilst LS-HFO has significantly higher primary aerosol emissions and form more secondary aerosols as a result of higher sulfate aerosol formation, the amount of SOA formed per kg fuel consumed for MGO was equivalent to that of the LS-HFO. Furthermore, the oxidation pathway of the SOA formation was found to be similar between the two fuel sources.

Zusammenfassung

Die vorliegende Dissertation befasst sich mit der chemischen Charakterisierung und umfassenden Analyse von Aerosolen, die sich aus Emissionen von Verbrennungsmotoren bilden und in einem Oxidationsströmungsreaktor einer Photooxidation ausgesetzt werden. Die Zusammensetzung der Aerosole wurde mit einem hochauflösenden Flugzeit-Aerosol-Massenspektrometer (HR-ToF AMS) bestimmt, das eine quantitative chemische Charakterisierung ermöglicht.

Aerosole sind weithin als erhebliche Bedrohung für die öffentliche Gesundheit anerkannt, da Tausende von vorzeitigen Todesfällen auf die Aerosolverschmutzung zurückzuführen sind. Darüber hinaus gelten Aerosole als ein wichtiger Faktor, der den Klimawandel beeinflusst. Die chemische Zusammensetzung des Aerosols ist entscheidend für seine Auswirkungen auf das Klima und die menschliche Gesundheit. Sie hängt nicht nur von der Quelle des Aerosols oder den Aerosolvorläufern ab, sondern auch von der photochemischen Alterung der Atmosphäre, die zur Bildung von Sekundäraerosolen führt. Insgesamt führt dies zu großen Unsicherheiten in den Klimamodellen und zu einem mangelnden Verständnis darüber, wie sich Aerosole auf die öffentliche Gesundheit auswirken.

Für diese Arbeit wurde das Modell kinSim verwendet, um den Verbleib von RO_2 und die Veränderungen der Photooxidationsbedingungen im Oxidationsflussreaktor zu bestimmen. Es wurde festgestellt, dass NO-Emissionen ein bedeutender Faktor für die Bildung sekundärer Aerosole aus Abgasen von Verbrennungsmotoren sind, da NO die Bildung von OH-Radikalen unterdrückt, was zu einem niedrigeren simulierten atmosphärischen Alter und einer signifikanten Veränderung des RO_2-Verhaltens führt.

Um die Auswirkungen eines modernen, die Euro 6d-Norm erfüllenden Fahrzeugs zu testen, wurde ein Skoda Scala in einem Labor-Rototestaufbau bei vier verschiedenen Geschwindigkeiten gefahren: 0 km/h (Leerlauf), 50 km/h, 80 km/h und 100 km/h. Das Euro 6d-konforme Auto emittierte unabhängig von der Fahrgeschwindigkeit keine Primärpartikel, jedoch wurde nach der atmosphärischen Oxidation bei allen Fahrzeuggeschwindigkeiten eine signifikante sekundäre Aerosolbildung beobachtet. Die primären Gasphasenemissionen wurden charakterisiert, um die Prozesse zu bestimmen, die zur Aerosolbildung nach der atmosphärischen Oxidation führen. Der Vergleich von SOA mit CO ergab, dass der größte Teil der SOA bei Geschwindigkeiten unter 80 km/h aus der Verdampfung von unverbranntem Kraftstoff gebildet wird, was mit einigen dominierenden aromatischen VOC in Verbindung gebracht wurde: Toluol, Xylol und Trimethylbenzol. Bei Geschwindigkeiten über 80 km/h wird das Aerosol jedoch weniger organisch dominiert, und die Hauptquelle verlagert sich von unverbranntem Kraftstoff zu unvollständiger Verbrennung.

Außerdem wurde ein Schiffshilfsmotor mit zwei verschiedenen Kraftstoffen betrieben, schwefelarmem Schweröl (LS-HFO) und Marinegasöl (MGO). Die daraus resultierenden Emissionen wurden in einem Oxidationsflussreaktor unterschiedlichen Mengen an ·OH-Radikalen ausgesetzt, um die Auswirkungen der atmosphärischen Alterung auf die Emissionen des Schiffsverkehrs und die Auswirkungen der Vorschriften für den Schwefelgehalt im Kraftstoff auf die Aerosolbildung zu bewerten. Es wurde festgestellt, dass LS-HFO zwar deutlich höhere primäre Aerosolemissionen aufweist und infolge der höheren Sulfataerosolbildung mehr sekundäre Aerosole bildet, die Menge an SOA, die pro verbrauchtem Kilogramm Treibstoff gebildet wird, bei MGO jedoch derjenigen von LS-HFO entspricht. Außerdem wurde festgestellt, dass der Oxidationsweg der SOA-Bildung bei den beiden Brennstoffquellen ähnlich ist.

Table of Contents

List of abbreviations

Abriviation	Meaning
APM	Aerosol particle mass analyser
CPC	condensation particle counter
DIP	Direct inlet prope
DMA	differential mobility analyser
FSC	Fuel sulphur content
FTIR-MS	Fourier transformed infared mass spectrometer
GC	gas chromatography
GDI	Gasoline direct injection
GPF	Gasoline particle filter
HC	Hydrocarbon
HFO	heavy fuel oil
HRToF-AMS	High resolution time of flight aerosol mass spectrometer
IMO	International maritime organization
IPCC	Intergovernmental panel on climate change
LDV	light duty vehicle
LS	low sulfur
MGO	marine gas oil
NMVOCs	non methane volatile organic compounds
OFR	Oxidation flow reactor
OM	Organic mass
PA	Primary aerosol
PAM	Potential aerosol mass
PEAR	Photochemical Emission Aging flow tube Reactor
PFI	port fuel injection
PM	particle mass
PN	particle number
POA	Primary organic aerosol
PTOF	particle time of flgiht
PTRMS	Proton transfer reaction mass spectrometer
Rempi-MS	Resonace enhanced multiphoton ionization
SA	Secondary aerosol
SECA	Sulphur emission controlled areas
SMPS	Scanning mobilti particle sizer
SOA	Secondary organic aerosol
TWC	Three way catalyst
UV	ultraviolet
VOCs	Volatile organic compounds

List of Figures

List of Tables

1. Motivation

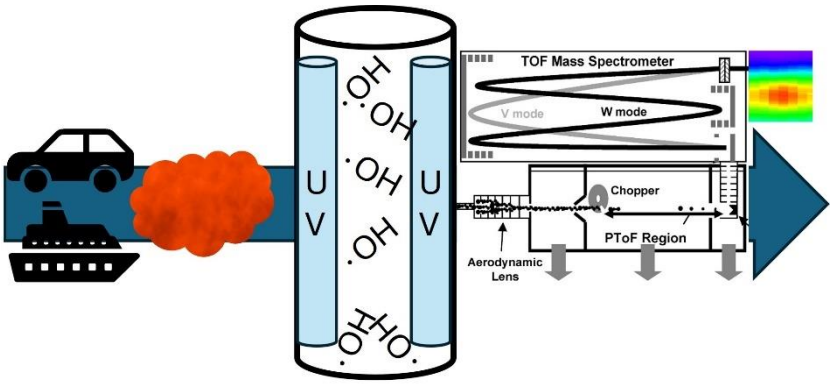

Figure 23 simplified graphical illustration of the experiments performed for this thesis

Combustion engines are widely used in modern society from energy production to air, sea and land transportation. These processes emit a multitude of inorganic and organic gases as well as particulate matter (PM) into the atmosphere. PM is considered a significant factor influencing climate change but is additionally known to have adverse health effects on public health.[1-3] The organic gases emitted can further react in the atmosphere leading to additional PM in the form of secondary organic aerosols (SOA). The majority of aerosols lead to a cooling effect due to reflections, backscattering and an increase in albedo due to increased cloud formation.[4-6] However, especially the impact of black carbon aerosols, often in the form of soot, increases global temperatures through absorption and reduction of artic albedo.[7]

Many studies have shown that inhalation of PM impacts the respiratory system with prolonged exposure resulting in development of cancer, cardiovascular disease and chronic respiratory diseases which all can lead to premature death. This has placed atmospheric aerosols in the top 5 of public health issues in terms of disability adjusted life years (DALYs) along with smoking and malnutrition.[3] Additionally, due to the high density of vehicles in urban areas PM from transport related combustion engines is especially important in areas with large concentrations of people. Different transport sectors are thus restricted in their emissions by either global or regional regulations. Regulations on emissions, engines or required exhaust aftertreatment can significantly impact the composition of the emissions. As recently as 2020 there were significant changes to regulations on shipping as the total permitted fuel sulfur content (FSC) was reduced from 2.5% to 0.5% on a global scale.[8, 9] Prior to these regulations the shipping industry accounted for 4% of global anthropogenic non-methane hydrocarbon (NMHC) emissions, and an estimated 400 thousand premature deaths per year globally due to aerosol emissions[10-15]. Therefore, understanding the impacts of such a change is paramount. Further, light duty vehicles such as personal cars have been regulated since 1992 within the EU.[16] As of 2015, the car fleet has been imposed to the EURO-6 regulations which for the first time required gasoline cars to be equipped with a gasoline particle filter (GPF) after 2020.

Chemical characterization of combustion engine aerosols is however difficult, as aerosols are not only directly emitted into the atmosphere but also form from gas phase emissions that oxidize during atmospheric transport. The aerosols are thus dependent on the emissions and therefore on fuel, engine, running conditions, and the atmospheric oxidation process.[17-27] This PhD work focused on the characterization of these aerosols from modern vehicles following the most up to date regulations. Utilizing the aerosol mass spectrometer (AMS), it was possible to observe the difference in aerosol composition dependent on driving speed for cars and fuel for ships and how current regulations impact

the chemical composition of the aerosol. Through such research, it is possible to get insight into how future regulations can be adjusted in order to further improve air quality and thus public health.

2. Introduction

2.1. Atmospheric oxidation

The primary oxidants in the atmosphere during the day are OH radicals, accounting for $90 \pm 25\%$ of the atmospheric oxidation capacity and NO_3 radicals during the night, accounting for $72 \pm 9\%$.[28] Whilst NO3 is formed in the atmosphere through reaction between ozone and NO_2, it is rapidly removed during the day though photodissociation to NO_2. Thus, the impact of NO_3 during the day is low assuming the presence of sunlight. In special cases such as thick plumes with low light penetration, NO_3 oxidation can additionally be observed during the day.[29] NO_3 oxidation runs with NO_3 donating an oxygen atom to a given organic compound returning to NO_2. Additionally, NO_3 can react further to form N_2O_5, another impactful atmospheric compound.[30] However, nighttime NO_3 oxidation whilst important for atmospheric aging is beyond the scope of this work.

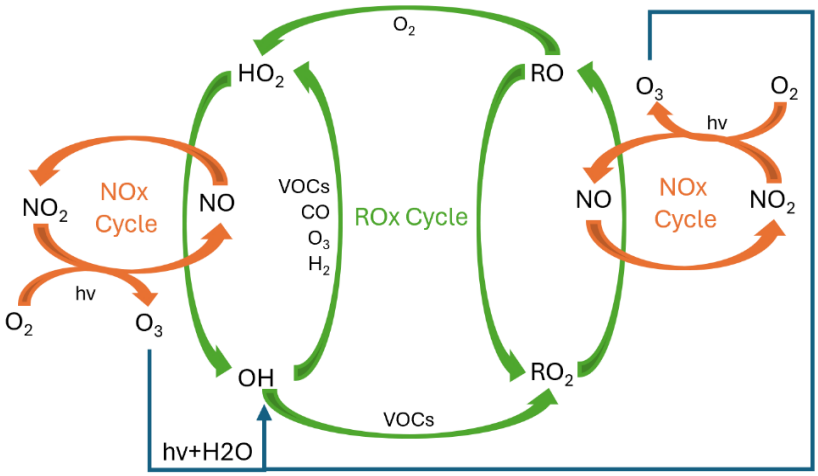

Figure 24. A simplified illustration of the daytime chemistry leading to the primary oxidants with the interaction between the ROx and NOx cycle.

Daytime OH radicals are formed primarily through photolysis of ozone at wavelengths below 300nm, forming the excited oxygen $O(^1D)$ radical (eq. 1) or the ground state oxygen $O(^3P)$ (eq.2). The $O(^1D)$ radical can then react with water and form the OH radical (eq.3). Alternatively, $O(^1D)$ can transfer its energy to a molecule M and return to the $O(^3P)$ ground state (eq. 4). $O(^3P)$ can also recombine with O_2 to form ozone (eq. 5) or react with ozone to form 2 O_2 (eq.6). [31, 32]The formation of OH radical for atmospheric oxidation is a complex equilibrium shown in a simplified way in figure 2. The tropospheric ozone required to start this reaction path primarily formed through photolysis of NO_2 by UV (<397nm) and subsequent reaction of the 3P oxygen with O_2 forming ozone and NO. The NO can then react with either organic peroxy radicals (RO_2, where "R" is an organic moiety) or hydroperoxyl radicals (HO_2) forming either RO or OH radicals and NO_2 completing the NOx cycle. The pathway of NO with HO_2 accounts for $68 \pm 4\%$ of all ozone production during the day. The RO_2 and HO_2 required for the NOx cycle forms through the ROx cycle. The ROx cycle is the cycle where OH radicals react with volatile organic compounds (VOCs) forming the radicals RO_2 or HO_2, the RO_2 is then degraded to RO through equilibrium with the reactions described in the NOx cycle. The RO further reacts with O_2 resulting in HO_2 formation, which then again through the NOx cycle can return to HO completing the ROx cycle. Further, oxidations of VOCs can occur without reaction with OH radicals through ozonolysis, the direct reaction between ozone and VOCs. Ozone reacts predominantly directly with C-C double bond containing VOCs to form ozonides that further react to form aldehyde, carboxyl and peroxide functional

groups. Average daytime concentrations of the OH radical are dependent on the location but range between 1.3-1.6 $\cdot 10^6$ molecules cm^{-3}. The average daily exposure to ·OH used in this dissertation is $1.5 \cdot 10^6$ molecules cm^{-3}. [33, 34]

$$\lambda(254nm) + O_3 \rightarrow O(\,^1D) + O_2 \quad \text{Eq. (1)}$$

$$\lambda(254nm) + O_3 \rightarrow O(\,^3P) + O_2 \quad \text{Eq. (2)}$$

$$O(\,^1D) + H_2O \rightarrow 2 \cdot OH \quad \text{Eq. (3)}$$

$$O\left(\,^1D\right) + M \rightarrow O\left(\,^3P\right) + M^* \quad \text{Eq. (4)}$$

$$O(\,^3P) + O_2 \rightarrow O_3 \quad \text{Eq. (5)}$$

$$O(\,^3P) + O_3 \rightarrow 2O_2 \quad \text{Eq. (6)}$$

2.2. Atmospheric aerosols

Aerosols are defined as a solid or liquid suspended in the gas phase, ranging in size from a few nanometers to hundreds of micrometers.[35] Within the definition of aerosols there are two main distinctions, primary and secondary aerosols. Aerosols emitted directly into the atmosphere are known as primary aerosols (PA). Whereas secondary aerosols (SA) are formed in the atmosphere from gas phase precursors that are oxidized in the atmosphere and undergo gas to particle reactions. Gas to particle conversion occur as a result of functionalization of the precursor gases, lowering volatility until the gas phase component can nucleate into new particles or partition by dissolving, adsorbing or condensing to existing particles. Both condensation and nucleation lead to an increase of particle mass (PM), but only nucleation leads to an increase in particle number (PN). Condensation is thermodynamically favored compared to nucleation. Thus, if a surface, such as preexisting particles, is available, it is more energetically favorable to condense onto the available surface than to nucleate new particles due to the lower chemical potential of the bulk liquid. This means that in general particle growth is favored over new particle formation.[36]

2.3. Atmospheric aerosol sources

Aerosols are ubiquitous in the atmosphere. Aerosol size and chemical composition is directly linked to their source and the environment in which they form. In addition to the PA and SA classifications, aerosols are divided depending on their source into biogenic, naturally occurring aerosols, and anthropogenic aerosols.

2.3.1 Primary aerosol sources

Biogenic PA sources include ocean sea spray and sandstorms emitted as a result of wind, but also volcanic activity, ash, soot, char and smoke from combustion processes such as wildfires.[37] The largest natural emissions of aerosols in terms of aerosol mass is related to sea spray which contains primarily inorganics, similar to the emissions associated with mineral dusts often founds in dry landscapes like deserts.[38] Furthermore, the biosphere releases pollen, plant debris and microorganisms into the atmosphere that all are considered biogenic PA, more specifically primary organic aerosols (POA).[39] Combustion related aerosols are largely a mix of POA and inorganic PA, as a result of the complexity of

incomplete combustion of organic materials. Anthropogenic PA are largely a result of combustion from either fossil fuel burning such as in the energy sector and the transport sector, or from wood burning in residential heating. Furthermore, more uncommon fuels such as waste burning as part of waste management results in combustion related aerosols as well.[40 41]

2.3.2 Secondary aerosol sources

Biogenic SA form from aerosol precursors emitted in large quantities by combustion, volcanic activity and the biosphere. These precursors can be either inorganic gases or volatile organic compounds (VOCs) leading to either inorganic SA or SOA, respectively.[42] The most common inorganic precursors are SOx, leading to sulphate containing aerosols, NOx, leading to nitrate containing aerosols, and NH_3, leading to ammonium containing aerosols. Anthropogenic SA are linked primarily to combustion, similarly to the anthropogenic PA. However, agricultural emissions such as NH_3 associated with large scale animal domestication and farming have a significant impact on SA formation.[41, 43-45]

2.3.3 Aerosol sources globally and regionally

Whilst biogenic aerosols globally account for the largest fraction of aerosols, anthropogenic aerosols can regionally be the main source of aerosol. Anthropogenic aerosols arise largely from combustion, such as from the energy sector, industry and traffic both on land, sea, and in the air (figure 3). Especially urban areas thus observe anthropogenic aerosols from these sources, which are linked to air pollution, reduced visibility, and smog, whereas rural aeras with heavy agriculture can be dominated by agricultural related aerosols. Developing regions typically have large amounts of biomass burning, residential and commercial aerosol emitting sources (figure 3), primarily due to the usage of wood burning for heat and cooking.[46]

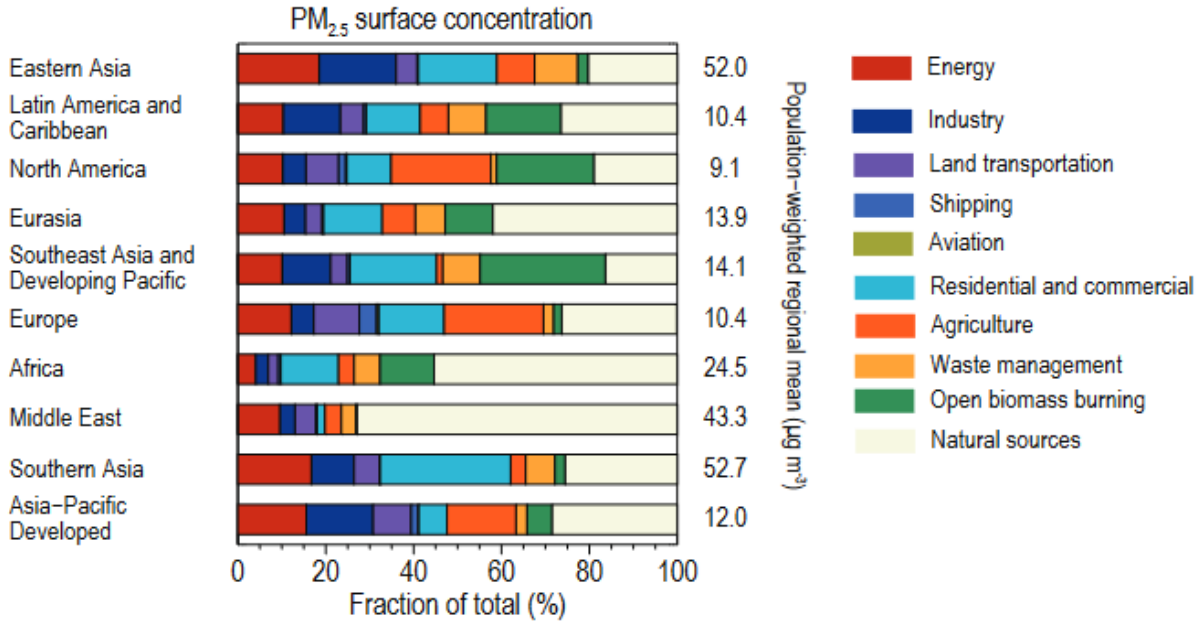

Figure 25. Illustration of the PM2.5 emission sources, attributed to the major regions in the world (2014. With the fractional contribution color coded from anthropogenic sources, with natural sources all combined into one source). Adapted from Figure 6.17 in IPCC, 2021: Chapter 6. In: Climate Change 2021: The Physical Science Basis. Contribution of Working Group I to the Sixth Assessment Report of the Intergovernmental Panel on Climate Change 2.3.4 Aerosol lifetime

All aerosols are relatively short lived as they are removed from the atmosphere both through wet and dry deposition. Wet deposition refers to the aerosol raining out either due to water uptake or

scavenging, whereas dry depositions refers to the aerosol impacting and sticking to the surface of a solid object. These two removal pathways result in aerosols' lifetime to range between seconds to a few weeks, largely dependent on the aerosol size, with larger particles staying suspended in air for shorter time than smaller particles.[37, 47, 48] The lifetime and thus the aerosol size is hugely important for the transport of aerosols. With longer lived aerosols impacting a larger area, and shorter-lived aerosols impacting only the regional or local aera of emission.[49] Freshly emitted aerosols are often larger and precipitate quickly out resulting in a only short range transportation, Sea spray aerosols as an example whilst the largest aerosol source in mass are often only suspended in air for seconds to hours and are thus only observable in coastal areas or on the sea. Comparably precursors that require oxidation to form SA, have an estimated lifetime of 13.1-15.7 days,[50] allowing them to undergo long range transport and thus impact regions further from the source.[49]

2.3.5. Atmospheric RO2 fate

RO_2 radicals in the atmosphere are important intermediate compounds, that due to their relatively high stability can accumulate to high concentrations. RO_2 radicals in the atmosphere terminate through various bimolecular pathways and unimolecular transformation. Figure 3 shows the common $RO_2\cdot$ termination pathways. Bimolecular termination partners include NO, NO_2, $RO_2\cdot$, $HO_2\cdot$ and ·OH, the $RO_2\cdot$ fate distribution dependent on the availability of the partner molecule.[51]

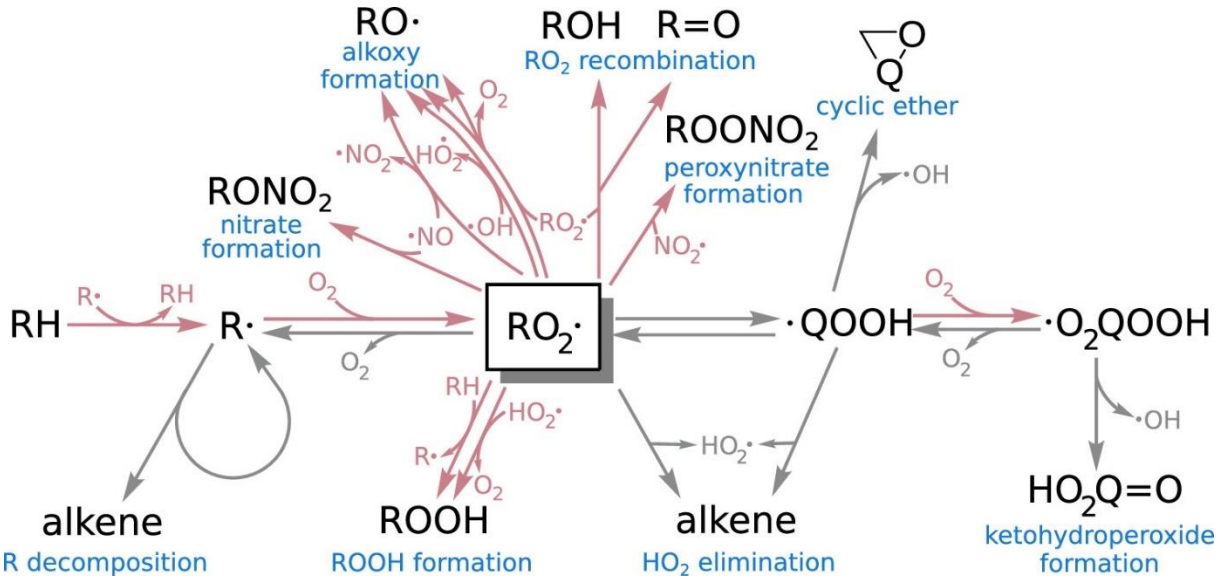

Figure 26. overview of atmospheric RO2 radical chemistry. Common unimolecular transitions (grey) and bimolecular (red) reactions of RO2. Adapted from Goldman et al. 2021

The resulting stable organic compound formed is highly dependent on the chemical pathway of its formation. The highly oxygenated organics resulting from the RO_2 termination can further condense into the particle phase. Thus, understanding the conditions of oxidation is crucial in order to predict both gas phase VOCs, but also the chemical composition of SOA. Further unimolecular $RO_2\cdot$ can terminate through HO_2 elimination to form alkenes, or after intermolecular hydrogen abstraction by the peroxy radical to form a hydroperoxyalkyl radical which through further reactions leads to either ·OH or $HO_2\cdot$ elimination and a stable organic compound. All the possible termination pathways are

attainable to some degree in the atmosphere dependent on concentration of RO_2 and potential reaction partners. Where pristine environments with no pollutants are dominated by RO_2-RO_2 and unimolecular transformation of RO_2· as primary RO_2· termination pathways. A heavily NOx polluted environment, e.g. typical high density urban areas[52], mostly results in RO_2·-NO as the primary RO_2 fate. Thus, the same VOCs would form significantly different SOA, dependent on the concentrations of NO, HO_2· and ·OH during oxidation.

2.3.6. Laboratory aerosol aging

Atmospheric oxidation is extremely complex with various interacting compounds emitted from different sources, all interfering through convoluted reaction pathways forming both gas, liquid, and solid particles products. Further, environmental effects such as humidity, temperature and UV intensity greatly impact the SA formation. Additionally, there are meteorological effects such as wind and convection transporting gases and aerosols around the globe. Performing controlled experiments in such a complex scenario is unrealistic. The alternative therefore is to reduce the complexity by removing all inputs and starting with a pristine environment. There are two common approaches to this in the laboratory, the batch reactor also referred to as atmospheric aerosol chamber and the oxidation flow reactor (OFR). Both aerosol chambers and OFRs are filled with synthetic air or other gases to achieve pristine conditions with background concentrations of particles < 10 cm^{-3}, VOCs (C5-C10) < 1 ppb, and O_3 < 1 ppb.[53] Further, this decouples these types of experiments from atmospheric trace gases and reduces the complexity of the atmospheric processes.

Aerosol chambers are typically operated as batch reactors, thus compounds of interest are added continuously stirred, typically with a small fan to ensure that all gases are well mixed. Depending on the oxidation process that should be studied, the chamber is then either illuminated with UV lights simulating daytime oxidation or kept dark allowing for nighttime oxidations to be simulated. This leads to oxidative products forming at similar rates as it would in the atmosphere. This approach allows for studies to determine SOA yields and reaction rates accurately as well as to study the processes occurring in the atmosphere with concentrations near atmospheric concentrations. As reactions occur at similar rates as in the atmosphere, aerosol chamber experiments can last multiple hours or even days in order to reach higher ages. However, an upper limit to the time that can be simulated in an aerosol chamber is dependent primarily on wall losses and when all input compounds have reacted. In general though, aerosol chambers aim to reduce the impact of the chamber walls, as the goal is to simulate free atmosphere gas and suspended particles. Low wall interactions are achieved by using a non-reactive wall such as polytetrafluoroethylene, glass or steel, and by decreasing the surface to volume ratio. Aerosol chambers are therefore widely used for simulating gas phase reactions and can range in size and shape dramatically from a few m^3 to large chambers of hundreds of m^3.[53]

OFRs are typically smaller than aerosol chambers, but are operated as a continuous flow reactor, where the compounds of interest are continuously added often at concentrations above those typically observed in the atmosphere and exposed to high concentrations of ·OH, depending on the target age of the aerosols. As concentrations increase the SOA yield typically increase, meaning the amount of SOA formed from a certain compound. The oxidation in an OFR consequently results in an aerosol output which has been exposed to ·OH concentrations equivalent to X days of ·OH oxidation processes in the atmosphere, thus called equivalent age (eqv. age), and a potentially elevated SOA yield. The degree of oxidation is primarily dependent on the achieved ·OH concentration and the residence time

in the OFR. The residence time in OFRs varies between seconds to minutes, depending on size and flow rate. In total this results in the ability for the OFRs to reach oxidization states equivalent to days or weeks in the atmosphere within the time of a few seconds or minutes continuously. This is especially practical if the aim of a study is to explore the impacts of a continuously changing emission source such as combustion processes. OFRs, similarly to aerosol chambers, aim to reduce wall losses and thus are made of similar materials as aerosol chambers and aim to reduce surface to volume (S/V) by adapting a cylindrical shape and optimizing internal flow. OFRs can generally be separated into two types, 185 nm and 254 nm OFRs. The key difference between the two types lies in the formation of ozone, while the type is simply a reference to the OFRs lowest wavelength UV light used. 254 nm OFRs use only 254 nm UV light and the continuous addition of water vapor and ozone to form ·OH through the reactions described in eq.1-2. 185 nm OFRs also use 254 nm light for ·OH formation, but do not need added ozone to the system as 185 nm light allows for photodissociation of O_2 into 2 Oxygen atoms(eq. 7) which can react with O_2 to form O_3 (eq. 5).

$$\lambda(185nm) + O_2 \rightarrow 2O(^3P) \qquad \text{Eq. (7)}$$

3. Impacts of atmospheric aerosols

Atmospheric aerosols impact both the environment and human health. The environmental impact is primarily a cooling effect due to enhanced cloud coverage associated with aerosols and particle light interactions resulting in backscattering of solar radiation. Health is impacted through inhalation of the aerosols leading to cardiovascular diseases and other respiratory issues. However, the impact on human health and environment is not even between all aerosols. Large hydroscopic aerosols contribute more to cloud formation, whilst smaller aerosols contribute more to direct scattering.[40, 54, 55] Further it has been shown that different SOA impact human health differently, meaning that the impact on health is dependent on aerosol source and atmospheric oxidation.[2]

3.1. Environmental impact of aerosols

The environmental impact from aerosols is still a source of major uncertainties in the understanding of climate and climate change.[4] The main impacts of aerosols on the environment are through aerosol radiation interaction, aerosol clod interaction and light absorbing particle deposition on snow and ice.

Aerosol radiation interaction can be subdivided into a direct scattering effect and light absorption. Both direct particle light interactions, and the combination of the two is referred to as the light extinction of the particle. All particles scatter light, resulting in a net cooling of the atmosphere and is the direct physical effect of small particles in the atmosphere. As interaction between light and particle causes light to scatter, the primary direction of the scattered light is dependent on the particle diameter to light wavelength. Particles of a diameter larger than the wavelength of the light primarily scatter light forwards, thus having a low cooling impact. And Particles with a diameter 10 times smaller than that of the wavelength of the light scatter equally in all directions, which is referred to as Rayleigh scattering. The wavelength of sunlight that reaches the earth's troposphere is primarily above 300 nm.[56] Thus, particles smaller than 30 nm do Rayleigh scattering, which results in significant backscattering of sunlight and thus a cooling effect. For particles of diameter size $\lambda > D > \frac{1}{10}\lambda$ the scattering is best described by Mie theory, but simplified as the particle size increases so does the percentage of light that scatters forwards.[57] However, a large particle, whilst it scatters a larger fraction of light forward,

still backscatters, and due to its volume the total backscattering effect is likely larger than that of a smaller particle. However, small particles with a total volume equal to that of a large particle would result in a larger backscattering effect. Light absorption in particles result in a heating of the particle, leading to an overall heating of the atmosphere. The primary attributes resulting in light absorption are related to the particle size and the particle composition. The largest contributor to particle light absorption is BC aerosols, typically emitted from combustion processes, both anthropogenic and biogenic. In terms of anthropogenic radiative forcing aerosol radiation interaction is estimated to be -0,22 [-0,47 to 0,04] W m^{-2}.

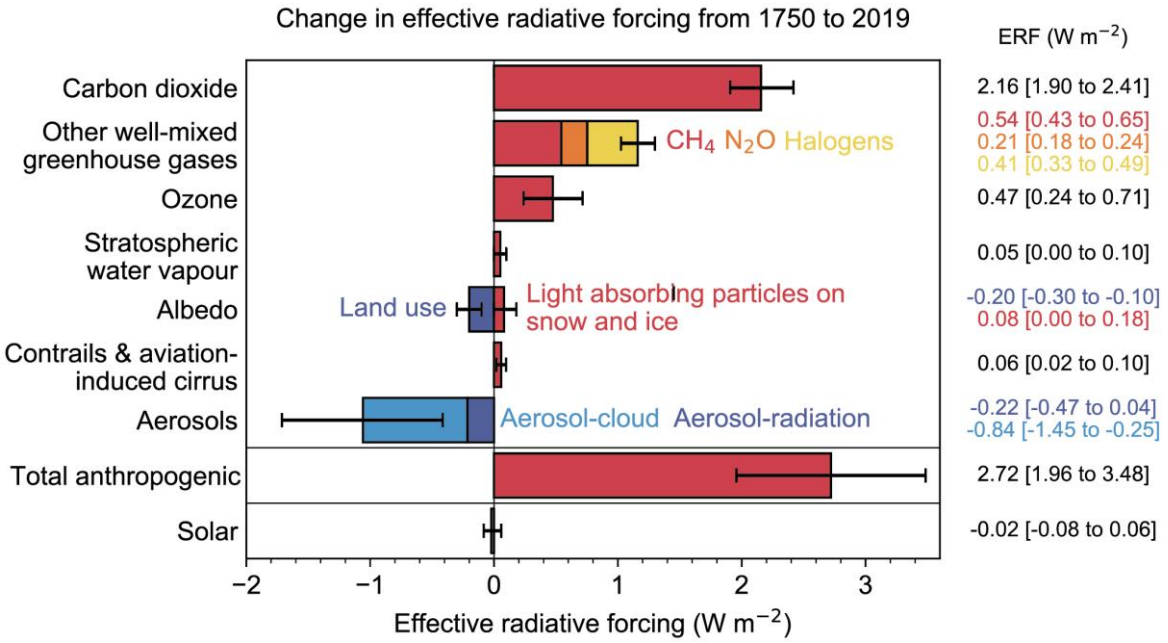

Figure 27. The effective radiative forcing in W m^{-2} for all major groupings of climate forcers. Adapted from figure 7.6 in chapter 7 of the IPCC Working Group I Sixth Assessment Report.

In addition to BCs light absorption ability in its airborne aerosol phase, it can also deposit on high albedo surfaces such as snow and ice in the arctic regions. Deposition of BC on such surfaces result in a net increase in effective radiative forcing by 0.08 [0.00 to 0.18] W m^{-2}, as the black carbon lowers the albedo through absorption and shading of reflective surface.

Cloud formation is an indirect effect of aerosols which results in a net cooling of the atmosphere, estimated to be -0,84 [-1,45 to -0,25] W m^{-2}. Aerosols contribute to cloud formation as they function as cloud condensation nuclei (CCN). The ability of aerosols to be effective CCN is described by the Köhler equation which shows that large particles or particles with a high water activity, thus hydrophilic compounds, require a lower supersaturation to initiate cloud condensation. Thus, the most effective CCN are large hydrophilic aerosols such as those emitted from sea spray, or sulphate containing aerosols such as those formed from SOx emissions from high sulfur fuel combustion.

3.2. Health

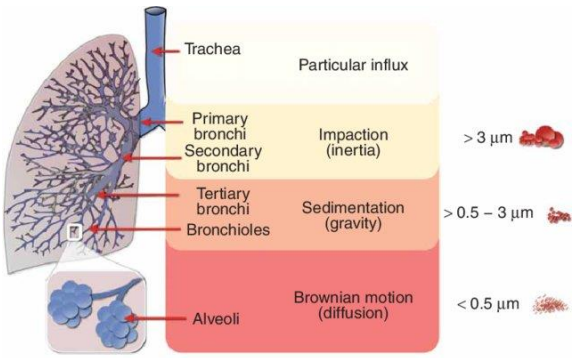

Figure 28 the penetration of lungs by aerosols dependent diameter. Adapted from Klinger-strobel M. Et al 2014

Aerosols are well known to pose a significant risk to human health, as they enter the body through the lungs, but can translocate to essentially all organs. The toxicity of aerosols is dependent on a multitude of factors, with toxicity increasing with smaller particle size, larger surface area, adsorbed surface material and the physical characteristics of the particle. Particles size impacts the depth of penetration into the lungs. Particles in the size range of PM2.5 (2.5 µm and below) penetrate the bronchi and ultrafine particles even penetrate the alveoli (figure 6).[58] Particles larger than 10 µm are generally considered significantly less toxic as these particles do not penetrate the lungs and get stopped at the nasal passages.[59] Further, the chemical composition of aerosols significantly impacts the toxicity, with aerosols formed from aromatic VOCs showing higher short- and long-term toxicity.[2] Ultrafine particles of diameters less than 0.1 µm (PM0.1) have the ability to penetrate the alveoli and thus compounds such as condensed VOCs are transported into the alveoli and with that into the bloodstream. Toxins on PM0.1 can thus greatly impact cardiovascular health, and in some instances impact the nervous system. The health concerns of high quantities of aerosol exposures can be divided into short-term and long-term consequences.[60] Short-term effects are those that can be felt directly due to raised aerosol concentrations in the environment and can range from lung and heart issues to headaches and nausea. Long-term contact with elevated levels of aerosol air pollution can lead to damage of nervous, reproductive and respiratory processes, potentially leading to cancer and cardiac arrest.[61] Recently, air pollution was found to be the 4th leading course of disability adjusted life years (DALYs) globally with more than 8% of all DALYs lost globally.[3] The majority of DALYs attributable to air pollution came from cardiovascular and respiratory diseases.

Children are generally more vulnerable to health effects of air pollution and can have both acute and lifelong consequences such as the development of asthma or other respiratory deasese.[62] It has been suggested that the influence of local sources of air pollution such as traffic emission are a more important factor than long distance sources on development of chronic respiratory diseases. In particular 5 groups have been found to especially impact the development of asthma in kids under 6 years of age: elemental carbon, NOx, PM2.5, PM10 and ammonium.[63, 64]

4. Combustion processes as aerosol source

Combustion processes are a major source of aerosol, comprising 30% of global organic aerosol mass.[49] Combustions processes include both biogenic sources such as forest fires, and anthropogenic sources such as combustion engines from the transport sector, biomass burning, waste burning, and fossil fuel burning for energy including both coal and oil. Aerosols from combustion processes range in size from millimeter-sized cinders and soot aggregates to ultrafine particles (PM0.1). The largest of these particles deposit rapidly as ash but smaller particles travel with the exhaust gas and contribute significantly to ambient air pollution. The composition of combustion aerosols is a mixture of

inorganics, soot and organics.[65] Inorganic combustion aerosols include metal particles, such as Si, Fe and Z. Additionally, secondary inorganic aerosol precursors are emitted like SO_x and NO_x which can form H_2SO_4 and ammonium sulfate amongst other inorganic salts and acids upon oxidation. Further, polyaromatic hydrocarbons (PAHs) are often found in combustion exhausts, and due to their low volatilities they rapidly enter the particle phase. PAHs are additionally of interest due to their carcinogenic nature.[66, 67] Additionally, organic aerosols can be emitted directly or be formed from the VOCs emitted as a result of incomplete combustion.

4.1. Light duty vehicle emissions

Light duty vehicles (LDV) represent a large fraction of the transport sector's aerosol emissions in highly populated areas, with 5% to 61% of aerosols in urban cities originating from on-road traffic.[68] To combat the health risks associated with LDVs, governing bodies around the world have introduced a range of regulations on the permitted emissions per kilometer driven. The first of such regulations in Europe were the Euro 1 regulations introduced in 1992 limiting CO, HC and NOx to, 2.72 g/km, 0.97 g/km and 0.97 g/km, respectively.[16] Further, PM was limited, but for diesel vehicles only. Regulations have been updated regularly, and car manufacturers have had to adapt and innovate to meet regulations. Initial adaptation came with optimization of the engine. However, with the introduction of the Euro 4 in 2005 came the diesel particle filter to meet the PM limit of 0.025g/km for diesel vehicles.[69] Further, to improve fuel economy for gasoline vehicles the common car changed from port fuel injection (PFI) engines to gasoline direct injection (GDI) engines. With the introduction of the Euro 5 regulations in 2009, PM was limited to 0.005 g/km for all vehicles and NOx was limited to 0.06 g/km for petrol and to 0.18 g/km for diesel vehicles. Additionally, it mandated the addition of a three-way catalyst (TWC) as exhaust after treatment to reduce NOx, hydrocarbon (HC) and CO emissions through the catalytic reactions eq.8-9.

TWCs use precious metals, typically palladium (Pd) or platinum (Pt) for oxidation, of CO and HC, and Rh for the reduction of NOx in most modern vehicles. The precious metals are dispersed on a mixed oxide support material, such as AL_2O_3, CeO_2 or ZrO_2.[70] The conversion efficiency of the TWC depends greatly on the Air to Fuel ratio and the operational temperature.[71] In general, all TWCs require temperatures above 200°C to operate, allowing for higher conversion efficiency. The heat required to operate is supplied by the engine exhaust. CO generally requires lower temperatures than HC and NOx for similar conversion efficiencies.

$$2CO + 2NO \rightarrow \ N_2 + 2CO_2 \qquad \text{Eq. (8)}$$

$$C_xH_y + O_2 \ \rightarrow \ H_2O + \ CO_2 \qquad \text{Eq. (9)}$$

The newest European regulations are the Euro 6d regulations that limit NOx further, but, importantly, the emissions of PA in terms of particle number (PN) emitted to $6x10^{11}$/km. It further mandated that this reduction come from the addition of a gasoline particle filter (GPF) as of 2020 for GDI vehicles.[72] Most commercial GPFs are ceramic cellular devices, where incoming gas is forced to flow across the porous ceramic walls capturing soot. GPF efficiencies have been reported to filter between 60 and 99% of PM dependent primarily on the size, diameter and length of the GPF. However, an important factor for optimization other than the size of the GPF is the pressure drop through the filter.[73]

4.1.1 LDV emission composition

Gasoline fuel is composed of low molecular weight HC compounds in the C4-C10 range, and commonly mixed with an ethanol share such as E10 fuel, containing 10% ethanol. The primary components of gasoline fuel are thus alkanes, cycloalkanes and aromatics as seen in figure 7, with alkanes C5-C8 branched and unbranched comprising above 40% of the total mass, and aromatics primarily in the C6-C10 range as the second biggest component of gasoline. These emissions however are expected to lead to SOA formation exclusively from the aromatic component, due to the low SOA formation potential of the short <C10 alkanes. Nordin et al 2013[74] and Liu et al 2015[75] both found that for GDI vehicles 60-90% of SOA formation could be assigned to C6-C10 aromatics. However, gasoline vehicular SOA is additionally formed from evaporative gasoline due to the low molar weight and thus high volatility of the fuel. The evaporative components are primarily the alkanes and ethanol, with a small aromatic component. However, SOA yield is expected only from the small aromatic component.[76]

Recent studies have highlighted that modern cars emit NH_3. NH_3 emissions from modern cars are almost completely due to the TWC as shown by Liu et al 2020,[27] where retrofitting TWCs to Euro 5 compliant LDVs showed a 72-fold increase in NH_3 emissions. The formation of NH_3 in the TWC is a result of the water vapor emissions causing the reaction between NO, CO and H_2 (eq.10) to occur in the TWC. The H_2 formed from this reaction then results in NH_3 formation (eq.11) instead of the intended TWC reaction (eq.8).

$$CO + H_2O \rightarrow \ H_2 + CO_2 \qquad \text{Eq. (10)}$$

$$2NO + 2CO + 3H_2 \rightarrow \ 2CO_2 + 2NH_3 \qquad \text{Eq. (11)}$$

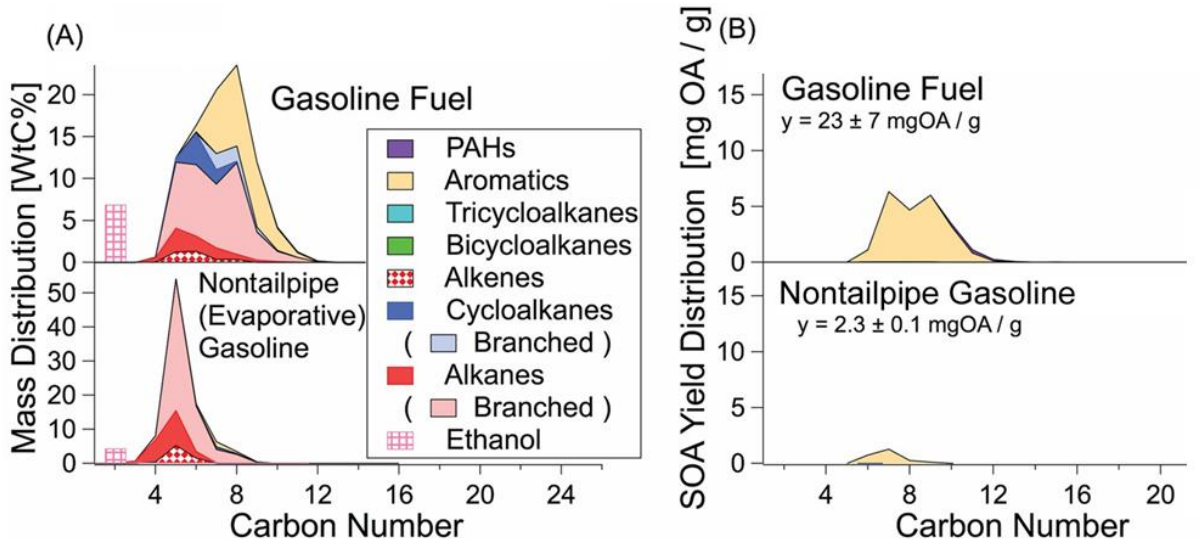

Figure 29 illustrates the mass distribution (A) and expected SOA yield(B) from gasoline fuel; adapted from Gentner et al. 2017.

A recent study have attempted to retrofit Euro 5 cars with GPFs, and found that 96.7% of gas phase emission aromatics were within the C6 to C10 spectrum with only 3.3% of the emissions being C11 or larger.[22] Whilst retrofitting GPFs to Euro 5 cars has shown that the primary PM is significantly reduced, SOA formation from VOCs remains largely unchanged.

4.2. Shipping emissions

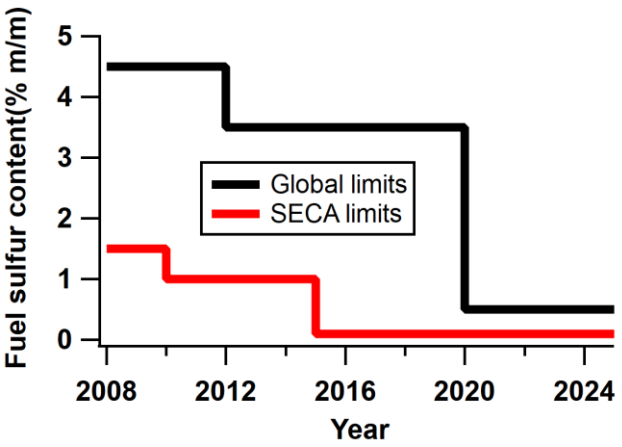

Figure 30 the FSC regulation changes from 2008 to 2025 for both Global FSC limits and SECA specific limitations.

Ship emissions come primarily from the goods transport sector as 90% of international trades is done through shipping, accounting for 80% by volume and 70% by value goods globally.[77] Further, trade by shipping is expected to triple from 2019 to 2050.[78] in 2018, shipping accounted for 17% NOx, 9% of SOx, 4% of PM 2.5 and 4% of non-methane volatile organic compounds (NMVOCs) of anthropogenic emissions,[8, 10-12] with 70% of shipping emissions being emitted within 400 km of the coast.[79] These emissions account for 11-19% of coastal particle number (PN) concentration, impacting health significantly with an estimate of 400.000 premature deaths per year prior to 2020.[18] As of 2020, the international marine organization (IMO) have implemented regulations on the allowed fuel sulfur content (FSC) reducing it from 3.5% to 0.5% (m/m) globally.[9] Prior to 2020, some sulfur emission controlled areas (SECAs) had been established lowering FSC to below 0.1% in select areas such as the Baltic and US coastline, and previous regulations on FSC had been made globally in 2012 as seen in figure 8. With the new regulations on global FSC in 2020, premature deaths from shipping emissions are expected to drop by about 30% as SOx emissions from shipping drop by 77%.[9, 18]

The two most commonly adapted methods of dealing with new regulations have been adding exhaust aftertreatment methods or changing fuel type from high sulfur heavy fuel oil (HFO) with an FSC of 3.5% to either low sulfur HFO (FSC<0.5%) or marine gas oil (MGO) with an FSC of less than 0.1%. The addition of a scrubber has been studied in previous literature and showed significant reduction in emissions both in terms of SA and PA.[21, 80] A few studied have examined the impact of changing fuel. Direct emissions of MGO was studied in comparison to HFO in terms of fresh emissions by Karjalainen et al 2023, but was not subjected to atmospheric aging.[21] The fresh emissions were found to be reduced for MGO in terms of both POA and black carbon. However, significant amounts of SOA (38%) in harbor cities have been reported originating from shipping after 2020 regulations suggesting that the SOA was not impacted by the change from HFO to MGO.[81]

The search for alternative fuel sources within the maritime shipping industry has led to a multitude of innovative ideas, with suggested alternative fuels for the future including NH_3, methanol, liquid natural gas and hydrogen.[77] However, whilst all these ideas are promising and could significantly change the magnitude and composition of ship emissions, they all currently lack the infrastructure for rapid implementation. Therefore, currently the transition from a heavy sulfur fuel to a lower sulfur diesel like fuel remains the most common adaptation.[10, 82] Nevertheless, in the future these alternative fuels will likely increase in importance.

4.2.1 Shipping fuel composition

The traditional fossil fuels used in ships are complex mixtures of hydrocarbons. The main differences between fuels are the processing level, sulfur content and the source of the fuel. In general, liquid fuels

can be divided into two main types: residual and distillate fuels. Residual fuels are made of the residue from distillation of refined crude oil. Residual fuels are viscous and aromatic. Distillate fuels are paraffinic and are thus much lighter and cleaner than residual fuels. Residual fuels are often mixed with distillate fuels in so called mixed fuels. The average demand for shipping fuels is 640000 tons per day, with a need for 250000 tons of distillate fuels per day.[82, 83] Traditionally the most common residual fuel is heavy fuel oil (HFO) with a sulfur content above 0.5%, as this sulfur content is no longer permitted, HFO can be mixed with lighter fuel resulting in low sulfur HFO (LS-HFO) with sulfur content below 0.5%. Marine gas oil (MGO) is the most commonly used distillate fuel with a sulfur content below 0.1%. MGO specifically is used in SECA areas to comply with the sulfur requirements of these regions. Further fuels are required to limit the amount of non-combustible inorganics by the 0.2% ash requirement to fuels. Residual fuels intrinsically contain more inorganics such as nickel, vanadium and zinc compared to distillate fuels.[17, 84]

5. Methods & instrumentation

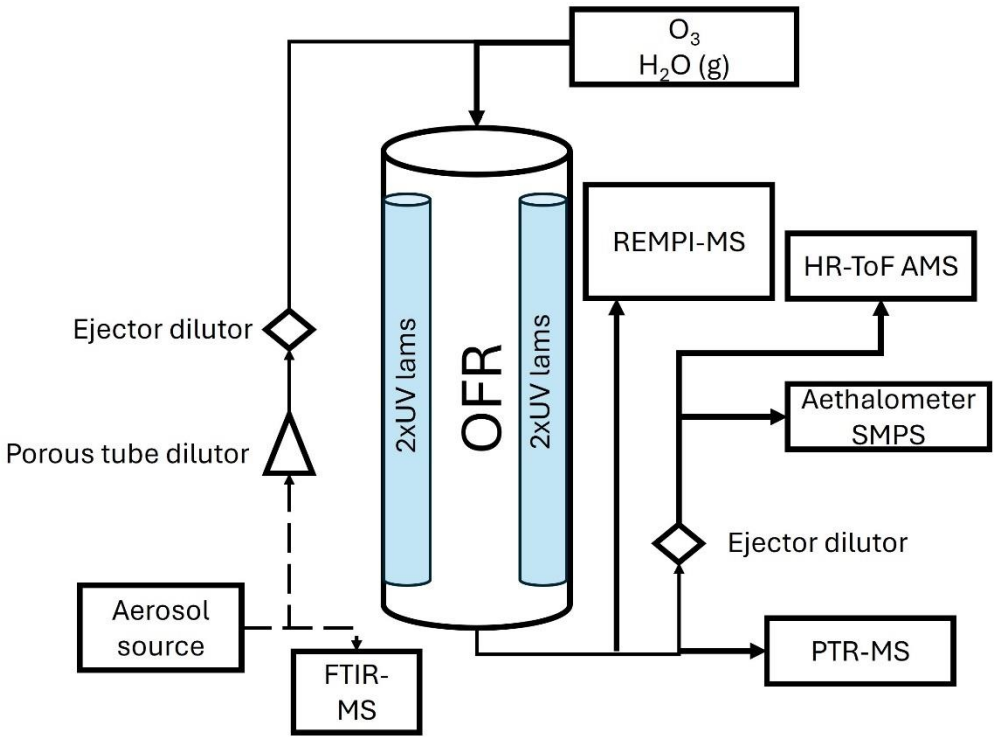

Figure 31 experimental setup overview, where dashed lines represent heated tubing and was used for the combustion engine experiments. The porous tube diluter and the ejector dilutor diluted the emissions prior to mixing with O_3 and H_2O before entrance to the OFR. Only the REMPI measured both before and after the OFR.

Figure 9 illustrates the general setup for the experiments with a focus on the analytical instruments used I this work. The dilution level reached with the porous tube diluter and ejector diluter prior to the OFR is dependent on the aerosol source. Further the ejector dilutor between the OFR and the aerosol measurement devices, Aethalometer, SMPS and HR-ToF AMS was 1:10 diluted with synthetic air.

5.1. Aerosol phase instrumentation

Aerosol phase instrumentation can be separated into two groups, the instruments focused on the physical properties of the aerosol such as SMPS and APM, and the instruments focused on the chemical composition of the aerosol such as the HR-ToF-AMS, DIP-HR-ToF-MS, and the TD-GCxGC-ToF-MS. The three mass spectrometry methods HR-ToF-AMS, DIP-HR-TOF-MS, and the TD-GCxGC-TOF-MS are compared in table 1. All Time of flight (TOF) mass spectrometers use the speed of ions to determine the mass of the ions. A longer time of flight thus longer pathway results in greater separation and higher mass resolution.

Table 5 shows an overview over the properties of three different electron ionisation method; HR-ToF-AMS, DIP-HR-ToF-MS and TD-GCxGC-ToF-MSs.

	HR–TOF–AMS	**DIP–HR-TOF-MS**	**TD–GC × GC–TOF-MS**
analyses time	online (4 min/cycle)	atline (10 min)	offline (3 h)
thermal sample introduction	flash vaporization/pyrolysis (isotherm at 600°C); vacuum condition (10^{-9} to 10^{-6} mbar)	vaporization and pyrolysis by ramped heating (gradient 2 K s^{-1}); vacuum condition (10^{-6} to 10^{-3} mbar)	gradual TD (gradient 2 K s^{-1}); >1 bar overpressure; inert helium atmosphere
vaporization temperature (accessible content)	600°C (non-refractory aerosols)	40–400°C (non-refractory aerosols)	40–300°C (volatile/semivolatile compounds)
mass resolution	2.1×10^3* (*m*/*z* 200)	2.5×10^4 (*m*/*z* 218.99)	1.3×10^3 (*m*/*z* 218.99)
mass accuracy	<28 ppm* (*m*/*z* 10–200)	<2 ppm (*m*/*z* 218.99)	45 ppm (*m*/*z* 218.99)
mass range	9–459 Da (analyzed range: 10–200 Da)	15–600 Da	20–700 Da
chemical/physical information	superimposed spectra; fragment ion peaks (thermal & EI fragments); size segregation of PM	superimposed spectra; fragment ion peaks (EI & thermal fragments); thermal pre-separation according to volatility	individual spectra for each compound; fragment ion peaks (mostly EI fragments); separation of individual compounds by chromatography

5.1.1. Scanning mobility particle sizer (SMPS)

The scanning mobility particle sizer (SMPS) is comprised of the combination of a condensation particle counter (CPC) and a differential mobility analyzer (DMA). The CPC functions by leading the aerosol stream through a super saturated chamber, typically with either butanol or water vapor. This super saturated chamber causes submicron particles to grow sufficiently large enough to be optically detectable, thereby an optical sensor can count the number of particles. The DMA functions by first charging the aerosols beam, establish a known equilibrium charge distribution, with either X-rays or radiation-based neutralizers using ^{85}Kr, ^{210}Po or ^{241}Am. After the aerosols have been charged, the aerosol stream is led into a long cylindrical chamber with an electrically charged core. At the bottom of the charge core is a slit through which the aerosol flow exists the instrument. By changing the flow rate and the charge of the core, the diameter of the aerosol that reaches the output flow can be inferred from the set of parameters assuming spherical single charge particles. The DMA therefore filters particles with a certain size and charge to pass through based on their electrical mobility diameter. Combining the DMA and CPC to form a SMPS allows for the DMA to scan through a size range of diameters, and the CPC to count the number of particles in each bin giving a size distribution of the aerosol. This size distribution can thus be used to determine the particle volume by assuming spherical particles. Further aerosol mass can be estimated by assuming particle density. For experiments presented in this work an SMPS was used scanning a size range of 10-700 nm or 10-300 nm depending on the experiment. Further, the SMPS system used ^{85}Kr for particle charge and a water-based CPC, to avoid potential flow back of butanol into the experiment chamber. Particle density is dependent on the composition of the aerosol, common density values include 1.7 g/cm^3 for ammonium sulphate and 1,4 g/cm^3 for purely organic compounds.[85] In one experiment presented here the availability of an aerosol particle mass analyzer (APM) allowed for the determination of particle density. However, when this was not available, a density of 1.5±0,2 g/cm^3 was assumed in order to cover both the upper and lower limit of common particle densities.

5.1.2. Aerosol particle mass analyzer (APM)

The APM analyzer was used along with the SMPS system to determine the density of the particles. The APM itself classifies particles according to their mass to charge ratio, where the SMPS uses charge neutralization to determine the volume of the aerosol. The effective particle density (P_{eff}) can thus be determined with the electrical mobility diameter (d_{em}) determined by the SMPS and the single particle mass (m_p) determined by the APM using Eq. 12.

$$p_{eff} = \frac{6m_p}{\pi d_{em}^3} \qquad \text{Eq. (12)}$$

5.1.3. High-resolution time of flight aerosol mass spectrometer(HR-ToF AMS)

The High-resolution time of flight aerosol mass spectrometer (HR-ToF AMS) is an instrument for quantitative determination of the aerosol composition, mass and size. The AMS is designed to measure the chemical composition of aerosols in a size range depending on the critical orifice located at the inlet of the instrument (figure 10). In these experiments the critical orifice allowed for particles in the size of 42 nm to 645 nm to be measured. The aerodynamic lens system then focuses the aerosol into a beam which passes through the low vacuum (10^{-9} to 10^{-6} mbar) directly to the ionization site adjacent to the heated tungsten (600°C), resulting in flash vaporization of the non-refractory aerosol and subsequent electron ionization of the resulting ions at 70 eV. The ions then travel through the HR-ToF segment operated in V-mode for all experiments, allowing for a high mass resolution of 2.1×10^3 (m/z 200). Further mass spectrum specific values can be found in table 1 and Hartner et al 2022. [86]

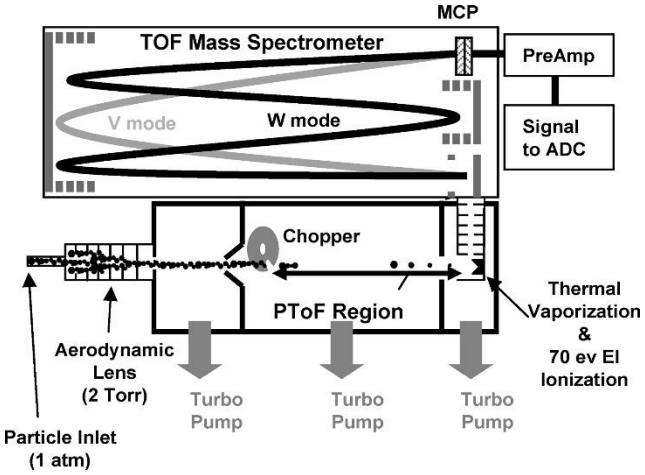

Figure 32 Schematic of HR-ToF-AMS showing both ion time of flight modes. adapted from P.F. Decarlo et al 2006

The HR-ToF AMS is further capable of determining aerosol diameter size based on the particle time of flight mode (PToF). This method uses the aerodynamic drag assuming spherical particles and a known distance from a chopper to the ionization site. The chopper rotates at a known speed either blocking the aerosol allowing only gas phase to reach the ionization site or not blocking the aerosol allowing both aerosol and gas phase to reach the ionization site. The distance from the chopper to the ionization site can thus be used to determine the particle size. Additionally, the gas phase only measurements are used as background measurement and are subtracted from the combined measurements to give the aerosol mass spectrum.

All data was treated in the ToF-AMS analysis toolkit 1.65(squirrel), and high-resolution analysis was performed with ToF-AMS HR analysis 1.25 (PIKA). CO_2 and air beam corrections were done during each experiment, by running the sample flow through a particle HEPA filter. Ionization efficiency calibrations were done weekly using ammonium nitrate according to the calibration protocol. Additionally, the relative ionization efficiency was determined by using ammonium sulphate.[87]

As the HR-ToF-AMS is expected to lose information outside its particle diameter range, the SMPS was used to determine total mass and the AMS to determine the ratios of organic, NO_3, NH_4, Chl and SO_4 aerosols. The total amount of aerosol containing x is then calculated as seen in eq. 13,

$$m_x = \left(m_{smps} - eBC\right) * \frac{x}{m_{org} + m_{SO4} + m_{NH4} + m_{chl} + m_{SO4}} \qquad \text{Eq. (13)}$$

where m_x is the total aerosol mass of x, m_{smps} is the total aerosol mass measured in the SMPS, and eBC the effective black carbon mass as determined by aethalometer (see equation X). x is the AMS measured mass of the aerosol type of interest. Where m_{org} is the mass of organic aerosol, m_{SO4} is the mass of SO_4 containing aerosols, M_{NH4} the mass of NH_4 containing aerosols, M_{chl} the mass of chloride containing aerosols and M_{NO3} the mass of NO_3 containing aerosols determined by AMS, respectively.

5.1.4. Direct insertion probe (DIP)

The Direct insertion probe high resolution time of flight mass spectrometer, DIP-HRTOFMS (referred to as DIP), was performed on a Pegasus GC-HRT 4D (leco,USA) equipped with a direct inlet probe (SIM GmbH, Germany).

A pushrod was used to transfer a 2 mm diameter filter sample into the ion source where a temperature gradient was applied from 40 to 400°C ramping with 2K S^{-1}. Background signals from PFTBA, O_2, N_2, H_2O and the internal standard were removed and accurate m/z values assigned to elemental composition within a mass window of 5 ppm. The mass resolution and further specification can be found in table 1 or in Uwe Käfers et al 2019.[88]

5.1.5. Gas chromatography (GC)

Gas chromatography (GC) is a method of separating compounds based on polarity and size. The GCxGC employed a Pegasus BT 4D GCxGC TOFMS, with an OPTIC-4 GC inlet and helium was applied as the carrier gas. Analyte compounds were initially cryogenically trapped at -100°C at the head of the collum through the CryoFocus-4 system. Analytes were then released from the cryotrap with a heating ramp of 2K s-1 from -100 to 300°C. Specifics on the MS can be found in table 1.

GCxGC has the benefit of having almost no fragmentation due to its controlled temperature ramping. and separation based on polarity and size, allowing for complete molecules to be resolved in the aerosol phase. Additionally, it has the ability to separate these molecules based on polarity even if the m/z is identical, allowing for isomeric separation. Though for all its benefits, GCxGC has a major disadvantage in terms of its time resolution, as it relies on filter measurements and off-line analysis. This means that whilst the GCxGC can find valuable information about which compounds have condensed into the particle phase, it does so for an average over a certain period depending on the filter loading time.

5.1.6. Aethalometer

An aethalometer (AE33-7, Aerosol Magee Scientific) was used to measure optically defined black carbon. The Aethalometer attenuates light through a filter tape with wavelengths between 370 nm and 950 nm. Absorption at 880 nm is generally assumed to be caused only by (BC), which allows for absorption to be converted to equivalent black carbon (eBC). eBC is than calculated based on equation 14,

$$eBC(880\ nm) = \frac{A \cdot \left(\frac{\Delta ATN(880\ nm)}{100}\right)}{F_{meas} \cdot (1-\zeta) \cdot (1 - k \cdot ATN(880\ nm)_t) \cdot \Delta t \cdot C \cdot MAC(880\ nm)} \quad \text{Eq. (14)}$$

where A is the surface area of the filter spot, ΔATN the change of attenuation during a time interval Δt, F_{meas} the measured flow rate, ζ the leakage factor (default value 0.01), k the real-time loading compensation parameter,[89] ATN_t the attenuation at time t, C the multiple-scattering coefficient (here C = 2.80 based on reference absorption measurement by PAX-870 during the campaign), and MAC the mass absorption coefficient (here $MAC(880\ nm)$ = 5.47 m^2/g, based on reference refractory black carbon (rBC) measurement by LII 300 and elemental carbon (EC) measurement by DRI 2015 during the campaign).

5.2. Gas phase instrumentation

5.2.1. Resonance enhanced multiphoton ionization (REMPI)

Resonance enhanced multiphoton ionization (REMPI) is a method used in this work to measure aromatic gas phase components, for which it was calibrated. Specifically compound quantity is determined based on the REMPI cross-section at 266 nm relative to toluene. (REF REMPI paper) However, due to this the sensitivity to benzene is low. Thus, benzene measurements from the REMPI have not been included in this work. Nevertheless, the information gained from the REMPI on all other aromatics is very beneficial. Additionally, measurements were conducted directly before and after the PEAR, allowing for online loss determination of gas phase aromatics. [90]

5.2.2. Fourier transformed infrared (FTIR)

Fourier transformed infrared (FTIR) was used to measure exhaust gases prior to any dilution. The FTIR operates by collecting high-resolution information of absorption and emission in the infrared spectrum between 4000-400 cm^{-1}. As all molecules have a unique "fingerprint", it is possible to rapidly monitor molecules, even small gas phase molecules such as CO and NOx that have significant impact on oxidation.[90, 91] The FTIR measured both organic and inorganic gas phase components directly at exhaust using continuous sampling. The FTIR was operated at time resolution of seconds allowing for the characterizing of rapid changes in exhaust.

5.2.3. Proton transfer reaction mass spectrometer (PTR-MS)

Proton transfer reaction mass spectrometer (PTR-MS) is used to measure online VOCs with high sensitivity and a fast responds rate. The PTR-MS method is a chemical ionization method using $H3O^+$ for proton-transfer onto VOCs, which results in a soft ionization causing little fragmentation. However, the PTR-MS method is limited to compounds with a higher proton affinity than H_2O (691.0 kJ mol^{-1}). This includes atmospherically relevant VOCs such as aromatics and most hydrocarbons with the exception of alkanes smaller than C5. Further, oxygenated compounds or compounds containing nitrogen or sulfur are all measurable by the PTR-MS instrument. Internal mass calibration was performed with 1,3-Diiodobenzene.

5.3. Laboratory aerosol sources

Laboratory aerosol sources vary greatly from experiment to experiment depending on the aim of the experiment. The simplest laboratory aerosol sources are aerosol generators, such as commercial ones used for producing aerosols for calibration of the HR-ToF AMS. These aerosol generators use spray impact of an aerosol compound of interest dissolved in water such as ammonium nitrate or other salts. These create a poly disperse aerosol in the size range of <10 nm-200 µm in diameter (TSI). These aerosol generators produce only primary aerosol which can be used for measurements on their own[54] or used as seed particles for VOCs to condense onto.[92] Combining a seed particle with a VOC is a common method of producing SOA when the mixture is exposed to oxidation. VOCs are typically diffused through evaporation into the chamber along with the seed particles. An alternative seed particle such as soot can be produced through controlled combustion such as propane burners (see section 5.3.1: propane burners and naphthalene). For more realistic emissions, engines or fireplaces can be used as source for both VOCs and primary aerosols.

5.3.1. Propane burner and naphthalene

The simplest combustion method used in these experiments was a combustion aerosol standard (CAST) propane burner used for soot generation. The soot particle was then used as a seed particle, an initial particle where secondary aerosol can condense onto. Gas phase naphthalene was mixed with the seed and exposed to atmospheric aging allowing for the formation of SOA which condensed on to the soot particles.

5.3.2. Light duty vehicle

The exhaust from a car, a Skoda scala model year 2021, driven on a Rototest VPA-RX3 2WD chassis dynamometer and fueled with standard European E10 gasoline was observed. Further model specifications can be found in the supplementary material published in Paul et al 2024.[90] The car was driven over a 4 hour driving cycle, which could be broken into four 1 hour driving cycles. Each one hour driving cycle started with 5 minutes of idling, followed by 15 min at 50 km/h, 100 km/h and 80 km/h. The 4 cycles have further been separated in two sections with the first cycle considered a cold start cycle and the later 3 cycles considered hot start. Driving conditions for cold and warm cycles differ on a few key parameters. A cold start has a starting exhaust temperature of room temperature which rises rapidly to around 400°C during initial idling, whereas the exhaust temperature during hot cycles does not have this rise as the exhaust temperature is already at 400°C as shown in figure 12. Further, the coolant and engine oil temperature both increase from below 40°C to 100°C during the first 35 min of the driving cycle, corresponding to the last minute of driving at 100 km/h. This is in contrast with the hot start where the increase from idling temperature to maximum temperature goes from 90 – 100°C. The driving conditions found after 35 min of driving is equivalent to those found during the hot start and thus the cold starting conditions primarily impact the start. This could be used to determine what is a hot start for future tests. Further, a potentially important factor is the ambient temperature in the lab as this could impact the aerosol formation in the PEAR. Operating the car in the laboratory increased the ambient temperature from 16°C to 24°C from cold start to peak temperature, during hot starts the ambient temperature never dropped below 20°C. However as indicated by the PEAR temperature there were no significant changes to the internal temperature of the oxidation flow reactor.

The driving cycle features long periods of driving at constant speeds in order to study the impact of consistent driving as most previous literature use shorter driving cycles featuring short accelerations and highly variable speed. In order to eliminate all impacts of acceleration or deceleration on the emissions and resulting aerosol formation, the steady state speed is defined as the last 10 minutes at a specific speed, thus removing the first 5 minutes.

5.3.3. Research Ship engine

In order to simulate an anthropogenic marine aerosol source, a single cylinder research engine capable of producing 80 kWh was operated for two set of experiments. The first experiment set featured a “driving” cycle spanning 4 hours and testing 4 sets of engine loads, 25%, 50%, 75% and 100%. The second set of experiments focused on the impact of atmospheric ageing of the emissions during docking and harbor maneuvers with engine load of 20 kWh or 25% of the total engine output, as these are expected to have a higher impact on populations due to their emission proximity. The experiments intended to map the impact of the SECA regulations compared to the global FSC regulations, and the impact of aging on the formation on aerosols in harbor areas. Two fuels were tested HFO with a FSC= 0.5% and the MGO with a FSC =0.01% as seen in table 2.

Table 6 Main fuel components from MGO and HFO: carbon, hydrogen, and sulfur mass percentages.

Fuel	C (w%)	H (w%)	S (w%)
MGO	87.80	13.10	0.01
HFO	86.30	11.10	0.5

Additionally, the HFO contained more metals as evident in table 2, where it is clear that the fraction of metals in MGO all are <1 mg/kg_{fuel}, with the HFO fuel containing 12 mg/kg of both V and Fe in addition to other metals.

5.3.4 Emissions factors

In order to have data intercomparable between different vehicles, fuel types and vehicles speeds, it is customary to convert emission results to emission factors (EF). An EF represents the emission in comparison to the amount of fuel consumed, typically in mg or gram per kg fuel consumed. This EF is useful to compare engine combustion efficiency. An alternative EF is emissions per km driven, which is more relevant for fuel efficiency. Due to the difference in functionality between these two emission factors, emissions per kg fuel are often used whereas most regulations for LDVs are based on emissions per km driven.

5.4. Oxidation Flow reactors

The two most common methods for in laboratory simulation of atmospheric aging are batch chamber simulations and oxidation flow reactors (OFRs). Both methods use ultraviolet light to start the photodissociation process, which can be predominantly achieved either by UV(254nm), H_2O and O_3 (eq.1-2), or H_2O and UV (185nm), or H_2O and UV(254nm) (eq.5 & 7). However, photodissociation of other compounds such as H_2O_2 and HONO can also be used.

Batch chamber experiments are operated in batches with well defined starting conditions. This allows for the study of aerosol formation with high time resolution with respect to the oxidation. Batch chamber experiments thus typically operate at concentrations comparable to the atmosphere allowing for a atmospheric simulations at the timescale of hours or days. OFRs are operated as steady state reactors this allows for a constant photochemical age with a changing input. As a result, OFRs are typically operated at high concentrations of OH to reach a photochemical age of multiple days in seconds or minutes. However, it is possible to operate a OFR at lower concentrations equally as it is possible to operate a batch chamber with an accelerated photochemical age. The high operation speed of the OFR thus allows for

the continuous aging of rapidly changing systems, such as vehicle exhausts or ship emissions.

5.4.1. Potential aerosol mass oxidation flow reactor (PAM)

The Potential aerosol mass (PAM) OFR[93, 94] was used to simulate the atmospheric aging for the soot naphthalene experiments. The atmospheric age in the PAM was controlled with VUV-lamps and H_2O maintaining Ozone and ·OH concentrations as described in eq.1-2. The PAM simulated an atmospheric age equivalent of 2-9 days determined by the PTR-MS method. The PAM operates at a flow rate of 5 to 20 L min^{-1}.

5.4.2. Photochemical emissions ageing flow tube reactor (PEAR)

The photochemical emissions ageing flow tube reactor (PEAR) was used in order to study combustion engines. The PEAR was operated with a flow rate of 120 lpm or 100 lpm depending on the experiment, giving an average residence time in the PEAR of 64 s or 70 s, respectively. The PEAR is operated with 4 UV lights and the UV intensity in terms of photon flux was determined with the formular of eq.15., where UV_{tot} is the total voltage of the UV light.

$$Photonflux = -1.34e13 + 2.95e14 * (UV_{tot}) \quad \text{Eq. (15)}$$

The aging was adjusted by the voltage and thus intensity of the four UV lamps from 4x0V through 2x3V to 4x10V, resulting in a photonflux from 0 through $1.8 \cdot 10^{15}$ to $9.4 \cdot 10^{15}$ With such a photon flux, the age determined by the PTR-MS is between 0 and 10 days. At the operating flow rate (above 100 lpm) the wall losses are expected to be below 30% for particles with a 20 nm diameter and below 10% for particles larger than 50nm. Further wall losses of low volatile organic carbon (LVOC) is estimated to below 2.1%.[95] At the input of the PEAR the unaged exhaust is mixed with ozone in concentrations of either 7 or 10 ppm depending on the experiment. Thus, any ozone quenching compounds will lower the potential age, such as NO reacting with ozone to form NO_2, this is especially an issue when working with combustion engines, which are a significant source of NO.[96-98]

5.4.3. Simulating oxidation flow reactor chemistry

When working with highly complex gas mixtures, it can be beneficial to simulate the oxidation occurring in the OFR. This can be done with models such as the KinSim model, a kinetic simulation model giving insight into the chemistry and concentrations in the OFR.[99] This gives valuable information in order to verify atmospheric relevance for the aging scheme.

Here, the KinSim version 3.73 was used in combination with the RO_2 fate estimator version 1.0 to determine the effects on RO_2 radical fate. Due to the complex nature of the exhaust emissions, some assumptions had to be made to simulate the reactions in the PEAR. For one, it was assumed that SO_2 could be used as a surrogate for non-methane hydrocarbons (NMHC), as described in Peng et al 2015-2018.[100-104] This reaction leads to a realistic ·OH – HO_2· ratio for exposure (eq. 16-17) and RO_2· fate without including the reaction scheme of every organic component to the model. This assumption is thus necessary for validating the atmospheric relevance of the oxidation. Further, it is assumed that once a compound leaves the gas phase and enters the liquid or particle phase, it does not react any further or otherwise impact the chemistry in the PEAR neither through repartitioning nor evaporation. The full reaction pathway of compounds simulated can be found in the supplement and is further described in Paul et al 2024. [90]

$$\cdot OH + SO_2 \rightarrow HOSO_2 \quad \text{Eq. (16)}$$

$$HOSO_2 + O_2 \rightarrow HO_2 \cdot + SO_3 \quad \text{Eq. (17)}$$

Additionally, as O_3 is mixed with the exhaust flow directly before the PEAR, we assume rapid reaction between O_3 and NO ($K=1.96 \cdot 10^{-14}$ cm^3 $molecule^{-1}$ s^{-1}) before competition with light for photodissociation, resulting in a complete consumption of NO and loss of O_3 (eq. 18).

$$NO + O_3 \rightarrow NO_2 + O_2 \quad \text{Eq. (18)}$$

This assumption is crucial as the decrease in initial O_3 impacts the formation of ·OH as shown in eq. 1-2. Without this assumption, the atmospheric age in the KinSim model would thus be overestimated.

However, with this assumption the atmospheric age could be underestimated as a 100% consumption of O_3 is unlikely, but it is nevertheless the best assumption possible.

5.4.4. Determination of atmospheric age

The atmospheric age in a given experiment is determined by adding isotope labelled N-buthanol (d9-BuOH 98%, Cambridge Isotope Laboratories) at a known concentration and measuring the decay of d9-BuOH with the PTR-MS (Barmet et al. 2012).[105] The ·OH concentration is then determined based on the buthanol decay and the known reaction rate ($k_{\text{butanol-d9}}$ = 3.4(±0.88) × 10^{-12} cm^3 $molecule^{-1}$ s^{-1}) between d9-BuOH and OH radical. The atmospheric age is typically given in days for OFRs, where it is assumed that the average ·OH exposure per days in the atmosphere is 1.5e+6 cm^3.

6. Results

6.1 Aim and vision

Studying the impacts of aging and operational conditions of aerosols from combustion engines requires instruments with high time resolution in order to track changes associated with operations such as accelerations. But it also requires instruments that can differentiate between aerosol types such as nitrate, sulfate and organic containing aerosols. Therefore, my PhD work revolves around the HR-ToF-AMS for determination of aerosol composition, in combination with the SMPS for total aerosol mass. Further, to gain good insight into the fresh emissions such as VOCs and inorganic gas phase emissions such as CO, SO_2 and NO, the HR-ToF AMS was supported by FTIR, PTR-MS and REMPI. All instruments capable of operating online with time resolutions below 5 minutes, which allowed for online determination of aged aerosol and determining the causes and effects of the aging of combustion engine emissions.

The initial hypothesis in regards to Euro 6d car emissions was that there should be a reduction in primary aerosols as a result of the GPF in comparison with literature about previous emission standards. Further, it was expected that accelerations would cause a short term rapid increase in emissions and thus in the aerosol formation. As single events of high emissions could cause unwanted damage on biological cell experiments that were conducted adjacent to the chemical and physical characterization experiments, the driving cycle was designed to feature few accelerations and instead maintain cruising speeds for 15 minutes at a time. This coupled with the 4-hour total driving time for the experiment allowed for testing of cold versus hot started runs as well as to study the impacts of the cruising speeds.

To represent ship engine exhaust, a four-stroke single cylinder diesel engine, commonly operated as an auxiliary engine, was used. The experimental design revolved around studying the impact of photochemical age on different fuels with the aim to access the potential impacts on human health predominantly in urban areas close to coastal aeras with high shipping traffic. testing the impacts of using cleaner fuels near human settlements as it was expected that distilled fuels with less FSC such as MGO would significantly reduce all aerosol formation compared to residual fuels such as LS-HFO.[9, 83] The experimental matrix was simple with two testing fuels and the ability to test various photochemical ages in order to understand not only the impact on fresh emission but also on the secondary aerosol formation. Further, for the first time to my knowledge ship emissions were

characterized with an AMS from fresh to 9 days of age with small enough photochemical changes between each measurement point that it has been possible to gain information about the oxidation pathway.

A significant amount of time was dedicated to the modelling of the chemistry within oxidation flow reactors such as the PEAR using the KinSim model. It became apparent that the fresh emissions, especially the NO emissions, from the combustion engines varied to such a degree that it would significantly impact the attainable photochemical age due to quenching of ozone. Further, the varying emissions impacted the RO_2 fate and thus the oxidation pathways leading to secondary aerosol formation.

6.2. Naphthalene SOA formation

To access the complex chemical reactions of emissions upon aging of real engine exhaust a simplified study was conducted focusing on the oxidation of naphtalene, typically asscociated with fuel combustion. Soot was added as a seed particle and would typically take the function of the PA and naphthalene that of the complex mixture of VOCs are emitted during combustions. With this approach it is possible to simplify the system and gain insight into the methodology. Furthermore, this system was used to test the impacts of SOA on lung cells through exposure[2, 106, 107] The methodology study was focused on aerosol analysis with HR-ToF AMS, DIP and GCxGC, an on-line (measuring continuously), at-line (rapid analysis of filter samples) and off-line (long term analysis of filters) instrument, respectively. HR-ToF AMS is used for quantitative analysis of the aerosol composition in high time resolution. However, aerosols with a diameter smaller than the transmission efficiency of the critical orifice of the AMS cannot be measured. With regard to chemical composition it features high thermal and ionization fragmentation. Therefore, the AMS is not well suited for determining the molecular composition in the aerosol phase as large compounds will fragment and be analyzed as its smaller fragment thus providing information on the chemical composition in terms of elemental ratios. Therefore, complementary data to the HR-ToF AMS can be gained, with the additional use of off-line GCxGC analysis generating quality data due to its low thermal fragmentation. Alternatively, one can use the direct insert probe. Both options require filters and thus these methods are subjected to potential filter artefacts such as losses of highly volatile compounds due to evaporating from the filters.

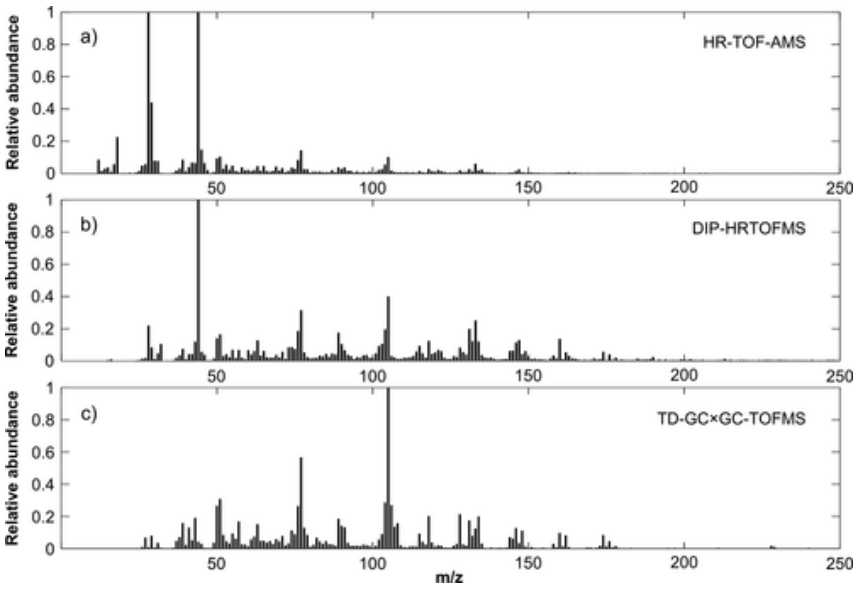

Figure 33 is adapted from Hartner et al 2022 and illustrates the mass spectrum of an aerosol formed through the combination of soot and naphthalene exposed to atmospheric OH aging equivalent to 4 days at 40% RH. Figure A illustrates the mass spectrum observed in the HR-ToF-AMS, figure B the DIP-HR-TOF-MS and figure C the TD-GCxGC-TOF-MS.

Figure 11 highlights the differences in a mass spectrum of the same aerosol measured with AMS (figure 11A), DIP (figure 11B) and GCxGC (figure 11C). Here it can be demonstrated that the majority of mass observed in the AMS is found below 100 m/z, whereas all the GCxGC find significant mass above 100 m/z. GCxGC additionally is able to resolve isomeric composition and thus allows for the determination of "fingerprints" and molecular details. However, a limit to the analysis by GCxGC is that it is unable to resolve highly oxidized compounds and thus was unable to observe significant changes as the aerosol was aged. DIP was found to be an excellent at-line instrument, with its lower thermal fragmentation compared to the AMS and its high resolution was able to derive structural information such as major structural building blocks in terms of functional groups of the analytes. Such information could benefit the AMS analysis significantly as it could reduce some of the ambiguity for compound identification in the AMS analysis. Overall, no single technique is capable of providing all the desired information of a complex aerosol and the impacts of aging on such a system. However, in combination the three methods capture a significant range of chemical properties such as elemental composition, functional groups, molecular aerosol composition of initial oxidation steps, product formation, and isomeric information. With these three methods determining aerosol sources, fate and chemical oxidation pathways could be greatly enhanced.

6.3. LDV-emissions

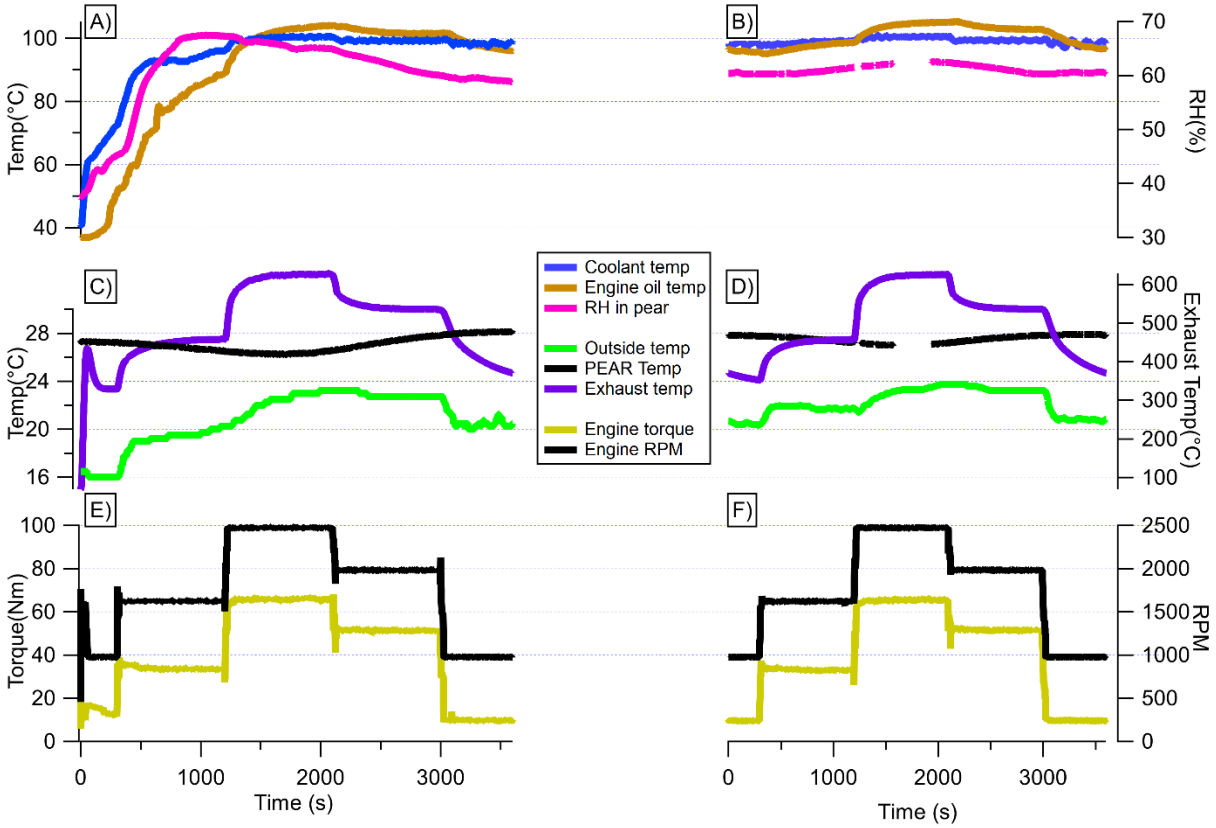

Figure 34 shows the time resolved average of varies factors related to the car performance and temperatures. A) coolant temperature, engine oil temperature and RH in the PEAR for cold starts and B) similar as in A) but for warm starts. C) outside temperature of the laboratory, the temperature of the PEAR and the exhaust temperature for cold start D) same parameters for warm starts. E) and F) illustrate the engine tourque and rounds per minute (RPM) for cold and warm starts respectively.

The emissions of Euro 6d compliant GDI engine light duty vehicles are subject to two key exhaust aftertreatment methods, the three-way catalyst intended to reduce NOx to N2 and oxidize HC and CO to CO_2 and H_2O, and the GPF intended to reduce fresh PM emissions. In order to understand the impact

of these aftertreatment methods, the chemical composition of the exhaust was characterized and compared to literature. Further, the impact of driving speed on emissions and SOA formation was studied during steady state driving in order to remove any impacts of acceleration on the emissions.

Due to the 4-hour driving cycle a clear difference in engine and ambient temperatures was observed during the first 1500s (25 min) of the experiment, see figure 12. During the first 1500s of the experiment laboratory temperature (outside temperature), engine oil temperature and coolant temperature all increased significantly from a cold start. The coolant temperature and engine oil temperature increased from 37°C to above 100°C and the ambient temperature from 16°C to 23°C, whereas relatively stable temperatures were observed for the warm start runs, where temperature varies depending on vehicle speed for ambient temperature between 21°C and 24°C, coolant temperature between 97°C and 101°C, and the engine oil temperature between 95°C and 105°C. After 1500s maximum temperatures were reached and there were no significant differences between cold and warm start after this point. It should be noted that due to the design of the experiment there were 3 times as many experiments with warm start (n=12) compared to cold starts (n=4).

6.3.1 Fresh emissions

Fresh PM emitted from Euro 5 cars with no GPF has been observed in multiple studies,[22, 108, 109] with one study finding fresh emissions during hot starts, comprised of POA between 1-10 mg/kg and eBC between 10 - 100 mg/kg.[22] Retrofitting GPF has proven successful with studies reporting between a 84-98% reduction in fresh aerosol.[22, 110] These papers highlighted that the addition of the GPF was more effective at lowering eBC than POA which was only reduced by 54-64%.[22] The factory installed GPF in an Euro 6d compliant car was not observed to emit any fresh PM.[90] This shows an improvement in comparison to previous studies where regardless of the type of car and retrofitted GPF fresh PM in the size range 10-700 nm was always observable. A paper from 2019 by Simonen et al. has however highlighted that ultra small particles between 3-23 nm could be significant especially for PN emissions, but due to their small size for the impact concerning their contribution to the overal particle mass is limited.[25]

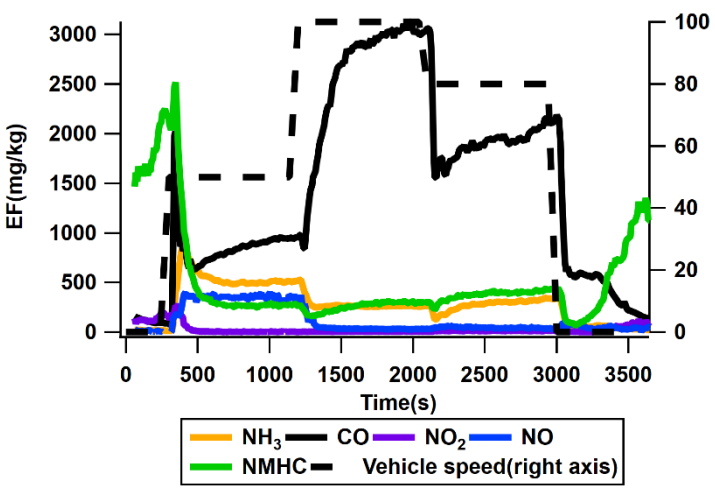

Figure 35 the fresh emision factors as mg per kg fuel consumed of all major emissions groups determined by FTIR-MS for warm start runs.

Figure 13 shows the emissions factors measured by FTIR data of NMHC, CO, NO_2 NO and NH_3, as mg fresh emissions per kg fuel consumed. The emission profile changes drastically depending on vehicle speed (illustrated with the black dashed line). The NMHC emissions are at a maximum at the end of idling and acceleration to 50 km/h from idling, and otherwise remain at a level between 150 and 400 mg/kg throughout the driving cycle. These results suggest that driving within the speed of 50-100 km/h does not significantly change the NHMC emission factor. However, it has been shown that THC for a

China VI compliant car only significantly increases when vehicle speed increases beyond 100 km/h.[111] Thus, there is likely a maximum efficiency for modern cars around 100 km/h where emissions are at a minimum. However, this maximum efficiency could be variable from vehicle to vehicle, thus requiring further research. CO emissions correlate with vehicle speed, reaching the highest emissions during 100 km/h and with no emissions during extended idling. However, the first 10 minutes of idling CO is still emitted at significant levels. NO_2 was observed at below 10 mg/kg during driving and is thus insignificant. However, during idling and acceleration to 50 km/h emissions vary between 110 and 283 mg/kg. Figure 13 further shows that NO emissions are only detected at significant levels (350+-26 mg/kg) during 50 km/h, coinciding with the highest concentrations of NH_3 emissions. NO should be

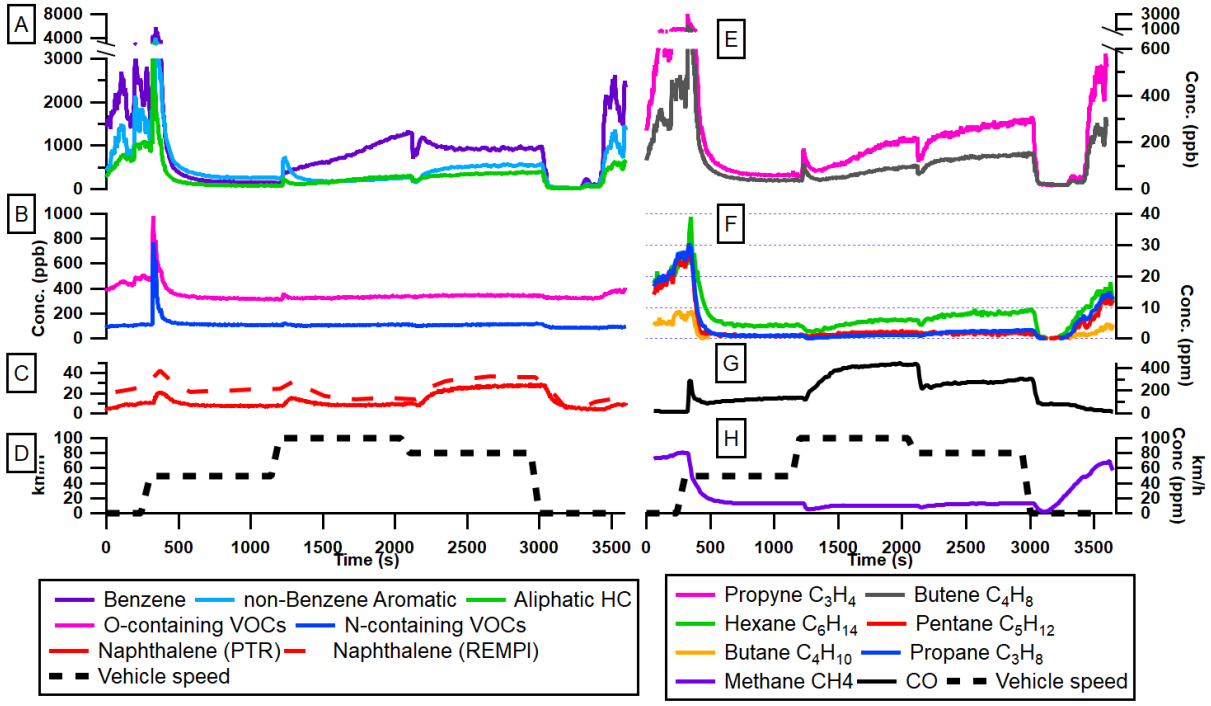

Figure 36 Figure A, B and E illustrate values measured by PTR-MS in terms of concentrations at tailpipe as ppb. Figure A and B highlight the main organic groupings of gas phase compounds. Figure E highlights the two main compounds of the aliphatic group shown in A. D shows naphthalene measured by REMPI (dotted line) and PTR-MS (solid line). Figure D and H both show the vehicle speed as reference for the other graphs. Figure F, G and H all show data measured by FTIR in ppm at the tailpipe. Figure F shows the main non-benzene NMHC. G shows the CO concentration and H the methane concentration both in ppm as measured by FTIR. A,B,C and D were presented in figure 3 in Paul et al 2024.

converted to N_2 in the TWC (eq.8), thus the high concentrations during 50 km/h could suggest suboptimal operational conditions for the TWC. However, the engine oil temperature and exhaust temperature do not drop below 95°C and 300°C, respectively. Further, all temperature measurements suggest that the 50km/h operational temperature is reached within 2 minutes. Thus, the TWC is not impacted purely by temperature. Additionally the high NH_3 emissions suggest that the TWC does convert significant NO.

Therefore, we can assume that the TWC was operational during this stage. However, emissions of NO during this stage (50 km/h) are simply too high for the TWC to completely convert NO, resulting in a breakthrough of NO and high NH_3 emissions. The significant difference in the NO emissions during 50 km/h and 80 km/h, suggests a nonlinear trend correlation between vehicular speed and the TWCs efficiency at removing NO. NH_3, as can be seen in figure 13, is constantly above 140mg/kg and reaches a minimum during 100 km/h, likely due to more efficient combustion. This additionally means the largest single gas phase emissions from a modern car disregarding CO and CO_2 are NH_3.

Figure 14A highlights the largest VOC groups measured by the PTR-MS. Benzene as the main component of the exhaust is found to reach its highest concentration at 8000 ppb, however, unlike the NMHC in figure 14B or the FTIR measured compounds in figure 14D, the benzene concentration is lowest during 50 km/h and highest during 100 km/h, excluding idling, suggesting that benzene emissions increase with vehicle speed. Non-Benzene aromatics and aliphatic HC follow the same trend as the NMHC, with a maximum during idling and acceleration from idle to 50 km/h. Both groups are between 30 ppb and 700 ppb throughout the driving speeds of 50-100 km/h. The non-benzene aromatics consist of Toluene, o-/m-/p- Xylene or ethylbenzene, C3-benzenes, C4-benzenes, naphthalene, styrene and methyl styrene primarily, this is similar to the composition found in previous papers that reported these compounds plus benzene as 96.7% of total aromatic hydrocarbon and 69.5% of total non-methane organic carbon.[22] Figure 14E shows the largest contributors to the aliphatic HC group measured by PTR-MS, showing contributions primarily from Butene and Propyne. The sharp rise of aliphatic HC and aromatic HC stands in sharp contrast to the NMHC's (figure 13) more gradual increase in concentration after idling is initiated. This could indicate that smaller non-polar compounds such as alkanes which are not detectable with the PTR-MS are emitted earlier during idling than larger compounds, potentially as a result of the cooling of the engine.

Figure 14B highlights O and N containing VOCs. These groupings both peak at acceleration to 50 km/h, but otherwise are at a consistent concentrations of 334±14 ppb and 105±10 ppb for O-Containing VOCs and N-Containing VOCs, respectively. Both PTR-MS and REMPI observed naphthalene and methyl-naphthalene (figure 14C), however no 3-ring PAHs were observed. The study by Roth et al 2019 identified 3 ring PAHs in the gas phase of Euro6 car emissions, however measured with offline instrumentation not available in this study.[110, 112]However, the impact on total SOA emission factors are likely low due to the concentrations of the PAHs compared to TXTMB.

Figure 14F-H highlight FTIR measurements of the raw exhaust in ppm. Figure 14F shows the 4 main contributors to NMHC, with Hexane, Propane, Pentane and Butane, with emission concentrations is from highest to lowest. Butane was only observed during idling and reached a maximum concentration of 9 ppm. Propane and pentane similarly were primarily observed during idling, both reaching 30±1 ppm as maximum concentration. Both propane and pentane concentrations consistently below 3.0±0.3 ppm during driving. Hexane, however, was observed throughout the driving cycle and followed the same trend as the general NMHC measurements. Figure 14G shows the emissions of CO which increase with vehicle speed. Figure 14H shows the driving cycle for reference and the methane emissions measured by FTIR. Methane was found to be significantly higher during idling reaching 82 ppm compared to the average emission of 12±3 ppm during driving. Further it was observed that whilst all emissions decrease rapidly when idling is initialized, methane only decreased to 2 ppm after 10 seconds after which methane emissions started to rise again.

6.3.2 Aged emissions

The emissions were oxidized in the PEAR with an addition of 7 ppm of ozone and a photon flux of $9.4 \cdot 10^{15} cm^{-2} s^{-1}$. However, as the emission profile changes, the atmospheric age of the aerosol after the PEAR is dependent on the operational condition of the vehicle. PTR-MS determined the age based on a single experiment where buthanol was added as described in Barmet et al 2012.[105] Further, the

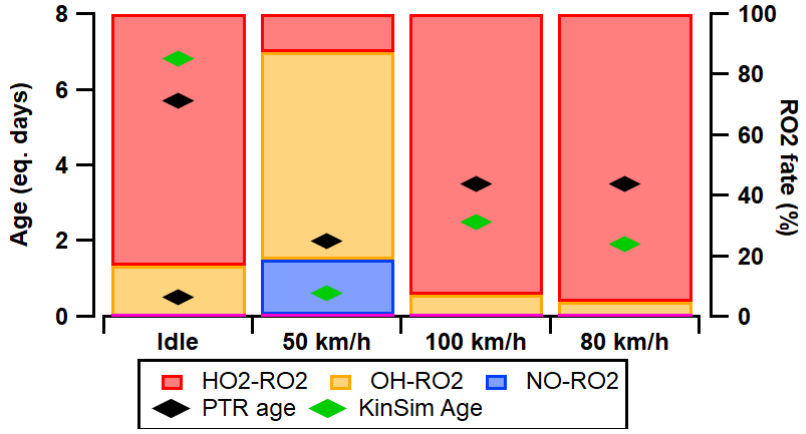

Figure 37 shows the age as measured by PTR-MS(PTR age) and the age calculated through the KinSim model (KinSIm Age) shown on the left axis. The RO_2 fate is shown with the bar plot indicating expected RO_2 fate in percentage on the right axis. Graphical illustration of data provided in Paul et al 2024 figure table S7 & S9

impacts of the changing emissions on both radical exposureand in PEAR chemistry with resulting RO_2 fate was estimated with the KinSim model. Additionally, the atmospheric equivalent age was determined by the KinSim in addition to the PTR-MS. The RO_2 fate and atmospheric age dependent on driving speed is shown in figure 15. The lowest atmospheric age was observed during 50 km/h as a result of the high NO emissions, reacting with O_3 as shown in eq. 18. The loss of O_3 prior to photolysis results in lower ·OH exposures, $7.46 \cdot 10^{10}$ molc.cm^{-3}s^{-1} (0.6 days) during 50 km/h compared to $3.27 \cdot 10^{11}$ molc.cm^{-3}s^{-1} (2.5days) and $2.44 \cdot 10^{11}$ molc.cm^{-3}s^{-1} (1.9 days) at 80 and 100 km/h. Figure 15 highlights that HO_2 exposure and RO_2-HO_2 fate is the predominant termination pathway of RO_2 radicals. The source of HO_2 changes throughout the driving phase. During idling, the primary source of HO_2 is the oxidation of Methane and other NMHCs. However, during driving as vehicle speed increases, CO emissions increase, and become an increasingly large source of HO_2. The change in photochemical age is thus best measured with the PTR-MS. However in combination with the KinSim model it is possible to explain the changes in age and the transferability with regards to the atmospheric relevance of the experiments.

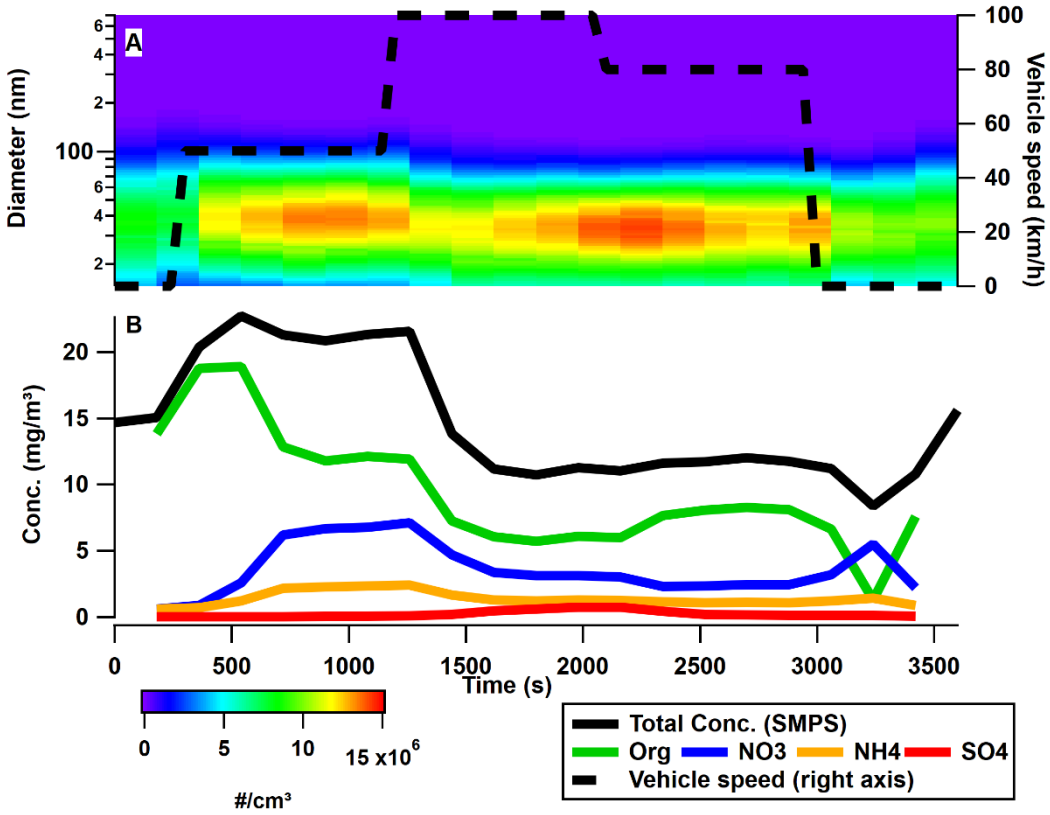

Figure 38 A shows the SMPS particle number distribution with the vehicle speed indicated on the left throughout the 1-hour driving cycle, with a warm engine start. B shows the same dirving cycle but in terms of mass concentration, observed with SMPS and the composition determined by HR-ToF AMS.

Substantial SA was formed throughout the driving cycle within all oxidation conditions ranging from 0.5 to 5.7 days of age. The SA had an electrical mobility diameter less than 100 nm, with a volumetric Geometric mean diameter (GMD) of 36 ± 3 nm and a Mass GMD of 88 ± 9 nm (figure 16a). The mass concentration of the aerosols was calculated with a density of 1.6 g/cm^3 as determined by the APM. The largest size mode of aerosols was observed at acceleration from idle to 50 and throughout 50km/h. This coincides with the peak SA mass formation. The age of the aerosol during 50 km/h is the lowest measured at 2 days (figure 15). However, the SA concentration at 21.5±0.7 mg/m^3 is in large due to the AN formation displayed by the NO_3 and NH_4 (figure 16b). NH_4 and NO_3 reach mass concentrations of 2.4 and 7.1 mg/m^3 respectively, with an average ratio of 2.5±0.3, similar to the expected AN ratio of 3.4 based on molecular mass. The formation of AN through oxidation of NO_2 is expected as described in eq. 19-20.

$$OH + NO_2 \rightarrow \ HNO_3 \qquad \text{Eq. (19)}$$

$$NH_3 + HNO_3 \rightarrow NH_4NO_3 \qquad \text{Eq. (20)}$$

AN or ammonium sulphate is commonly added in experiments as a seed particle to too increase surface area to enhance condensation of VOCs, increasing SOA yield.[93] It is likely that the formation of AN during the driving cycle functions in a similar way, thus elevating SOA formation compared to a scenario where SOA was forced to nucleate. During 100 and 80 km/h the SA concentration remained stable, however the composition changed as AN formation was 3.5±0.0 mg/m^3 at 80 km/h and 4.8±0.8 mg/m^3 at 100 km/h, meaning that there is a shift towards more organic formation during 80 km/h. This leads to an OM to NO_3 ratio of 1.85 ± 0.7 at 100 km/h to a ratio of 3.38 ± 0.06 at 80 km/h, signifying

a significant shift towards a more organic dominated SA (Fig 16B). During 50 km/h, the maximum NO_3 concentration is observed and an OM:NO_3 ratio of 1.8±0.2. The aerosol during idling however is almost completely organic with an OM:NO_3 of 22.0±1.4, except the short period at the onset of idling after 80 km/h where the composition changes from organic rich (OM:NO_3 3.38 ± 0.06) to a nitrate-rich aerosols (OM:NO_3 0.23 ± 0.03). This period coinces with the low NMHC emissions (<10 ppm) shown in figure 13, which lasts for approximatly 3 minutes. Thus, assuming that the observed emissions are typical for a Euro 6d vehicle, short term idling e.g., at red lights or during heavy traffic, will fall within this low organic aerosol formation period. However, if idling proceeds for more than 5 minutes, the aerosol composition returns to be organic-rich (OM:NO_3 > 10).

6.3.3 Steady state driving emission factors

The steady state emissions factors were determined with no influence of acceleration on the emission factors. This method allows for determining the impact of specific vehicular speeds. The maximum total aerosol mass formed per kg fuel was 131± 5 mg/kg at 50 km/h, as illustrated in figure 17. The emissions factors were lower at higher driving speeds with total aerosol mass formed of 68± 1 mg/kg and 72 ± 2 mg/kg for 100 and 80 km/h, respectively. The trend of decreasing total aerosol mass with vehicular speed in the range between 50-100 km/h is driven by the decrease in SOA mass formed. However, the fraction of SOA mass contributing to the total mass is not linear with vehicle speed, with a higher SOA contribution to total aerosol mass being 69% at a speed of 80 km/h and the lowest 54% at 100 km/h. The remaining contribution to total aerosol mass is found in AN formation from gas phase NH_3 and NO. These gas phase emissions were the highest during 50 km/h and lowest at 100 km/h, with a general trend of these inorganic gases to follow the emission pattern of organics during driving (excluding idling). The inorganic gases as well as the VOCs are intended to be removed through the TWC. This suggests that the TWC increases in efficiency with increasing temperature and vehicular speed. It is well known that idling results in high emissions of organics, which could lead to high SOA mass formed. However, in this study it was found that emission factors for SOA were higher during 50km/h than during idling. This, however, could be due to the increased formation of AN particles during 50 km/h driving which increased the SOA formation during this driving speed by functioning as seed particles for the VOCs to condense on to.

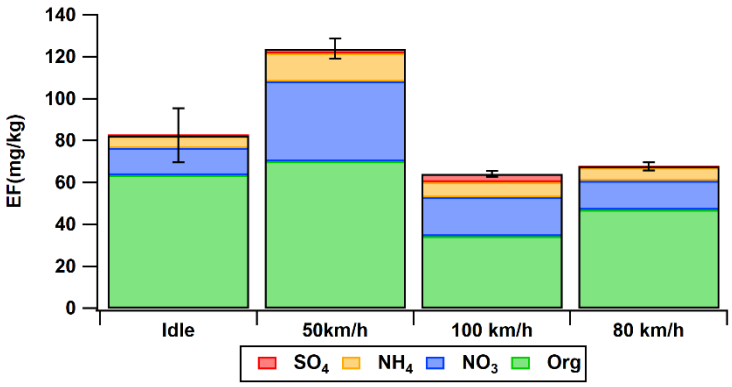

Figure 39 steady state driving emission factors in mg per kg fuel. Each point is the average value for the given speed measured for 10 min of each driving cycle (n=12) with standard deviation as error bars.

6.3.4 SOA precursors

A key indicator for predicting SOA sources is CO emissions. As CO is a product of incomplete combustion, SOA/CO can give an indication of whether a particular SOA is the result of incomplete combustion, which correlates with a low SOA/CO ratio as the CO emissions would be high, or alternatively a result of evaporated unburned fuel, which correlates with high SOA/CO as CO emissions are low. The formation of secondary organic carbon (SOC) aligns well with the SOA/CO, with a decreasing SOA/CO as vehicle speed increases (figure 18). Suggesting unburned fuels as the primary SOA source during idling and 50km/h with SOA/CO consistently above 100 µg/ppm and reaching a maximum of 729 µg/ppm. This aligns well with observation from other experiments published in recent years.[111]

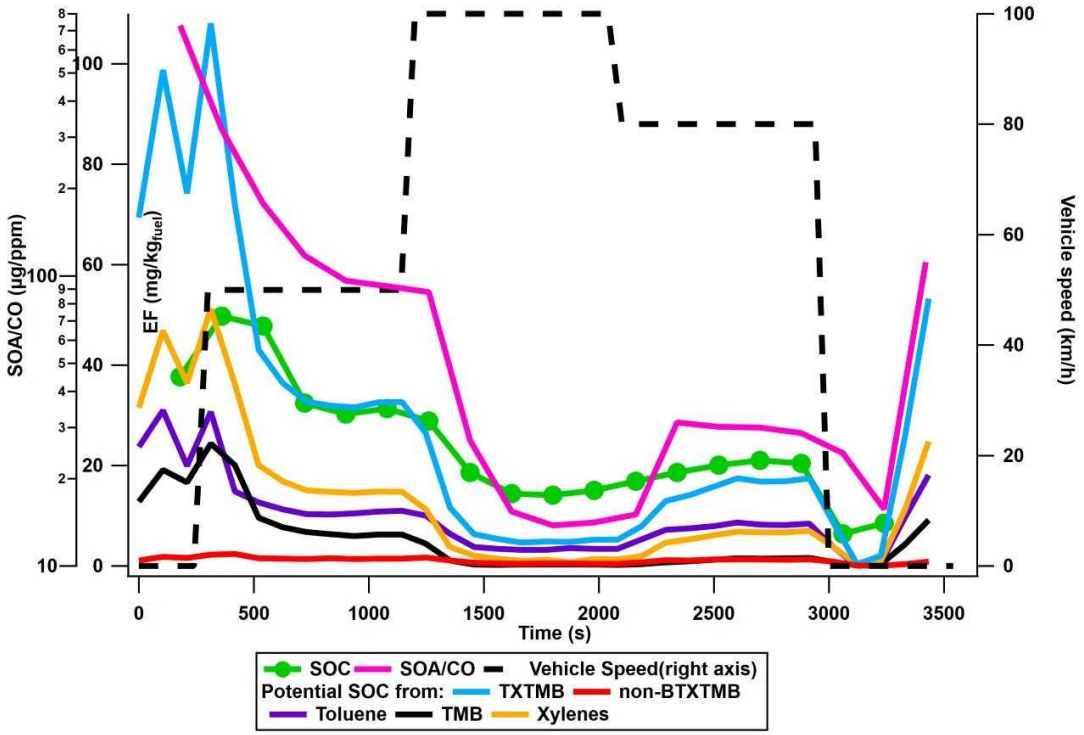

Figure 40 Secondary organic carbon (SOC) determined from AMS and SMPS data, compared to the lost carbon from aromatic determined by REMPI-MS. SOA/CO as determined by AMS+SMPS and FTIR-MS, note the log scale axis of SOA/CO. Vehicle speed is shown with a dashed line.

The REMPI-MS was used to measure aromatics entering and exiting the PEAR to get an online understanding of the losses of individual aromatic species in the gas phase. It had been hypothesized that SOA from driving primarily was attributable to a few aromatics such as toluene and trimethyl benzene, based on experiments with GPF retrofitted Euro 5 cars.[22] In order to compare directly between the concentrations of individual aromatic compounds of the exhaust in the gas phase and the emission factor of the SOA, the SOA was converted to secondary organic carbon emission factors and equally the loss of aromatics were converted to the loss of carbon related to the different aromatic species in terms of lost mg of carbon from the gas phase. Thereby, if the SOA yield would have been equal to 1 it would be expected that the total toluene, xylene and trimethyl benzene (TXTMB) should be equal to SOC. However, SOA yields are likely elevated compared to normal atmospheric conditions due to the presence of NH_3 and AN.[113] The potential SOC from aromatics thus represent the highest possible SOC that could have been formed based on the total conversion of carbon from the gas phase to the particle phase. It was found that 99% of aromatic VOCs that contributed to potential SOC was only from TXTMB. Comparing SOA/CO with the TXTMB shows clearly that the two correlate. This

implies that TXTMB is a result of unburned fuel and are the dominant SOA precursors during driving conditions below 80 km/h. However, at 100 km/h the SOC cannot be described by the loss of TXTMB in the gas phase, and with the low SOA/CO ratio the incomplete combustion must be the source of this SOA. This shows that whilst TXTMB is the primary source for SOA during driving below 80 km/h, it is not always the primary source of SOA. On highway driving with vehicle speeds consistently above 80 km/h incomplete combustion thus dominates as the SOA precursor. Further, the specific aromatic components do not attribute equally throughout the driving cycle. TMB and xylene account for a significant share of the potential SOC from TXTMB during idling and 50 km/h at for 19-30% and 45-50% for TMB and xylenes, respectively. However, this value drops to 4-10% for TMB and 15-40% for xylenes during vehicles speeds above 50 km/h. At vehicle speeds above 50 km/h, toluene thus accounts for up to 80% of the SOC that could potentially be derived from TXTMB. Whilst the primary aromatic compound of fuel is benzene and as it thus would be expected that benzene is be a significant source considering its high correlation in emissions with unburned fuel, benzene was not associated with any loss because of oxidation likely due to benzene's slow reaction rate with ·OH. Thus, the simulated atmospheric aging was too short to allow for benzene to undergo significant oxidation.

6.3.5 Cold vs Hot start

As discussed in segment 6.2 and figure 12, the key difference between hot and cold start can be attributed to the operational temperature of the vehicle. Whilst the impact of this was not discussed in Paul et al 2024, it is still relevant to discuss the results of the full data set collected. The impact of the operational temperature on the aerosol formation is illustrated in figure 19 and highlights the major differences in the two runs during the acceleration to 100 km/h from 50 km/h. The cold starts emit significant amounts of NO and thus form NO_3 containing aerosol with NH_4 aerosol increasing simultaneously, which likely happens as AN particle formation in the PEAR. This could be relevant for high NOx emissions on highway ramps as vehicles recently started to be able to accelerate more rapidly to 100 km/h. However, it should be kept in mind that this result is based on one vehicle with an N=4.

Literature shows repeatedly significant organic aerosol concentrations formed with cold start.[22, 25, 74, 114, 115] In this study however, cold start idling and long term (over 10 min) idling from warm start shows similar results despite significant differences in engine oil, ambient and coolant temperatures. Additionally, cold started gas phase concentrations during initial idling of xylenes at 18.2 ppm maximum and toluene at 22.9 ppm maximum are significantly higher than the comparable values during warm start where toluene is at 2.4 ppm and xylenes are at 1.2 ppm maximum concentration. However, the amount of SOA formed was similar in the two cases potentially due to the high NO emissions associated with cold startNO emissions during the first 300s of the cold start were measured to be 19±28 ppm with a maximum NO peak emission of 156 ppm within the first 9 s of ignition. Omitting the first 25s where NO emissions were consistently above 25 ppm, the average NO concentrations are at 12±9 ppm. During warm start runs, the NO emissions were 5±3 ppm, the primary impact of increased NO emissions during this period was the quenching of ozone prior to entering the PEAR. Any emissions above 78.66 ppm of NO resulting in a concentration of 4.37 ppm of NO after dilution would result in complete quenching of all ozone and thus no photochemistry would be possible. The increase in NO concentration emitted during cold start (12 ppm) from that of a warm start (5 ppm) would amount to a reduction of ozone available in the PEAR of 0.63 ppm of ozone about a 10% reduction from the 6.56 ppm available during initial idling to 5.94 ppm ozone available during cold starts. Along with higher CO and THC emissions, the resulting simulated age decreases

from 6.8 days of age to 1.5 days of age due to a significant reduction in available ·OH. Further, the resulting RO_2 fate changes from 83% HO_2 to 95% HO_2 as the primary RO_2 fate. As a result of the significant age differences between cold and warm idling runs, they cannot be compared even though they yield similar aerosol concentrations despite the higher concentrations of THC associated with cold start. In a non-laboratory setting thus the impact of a cold start would be greater as reported in literature .[22, 110, 111, 116]

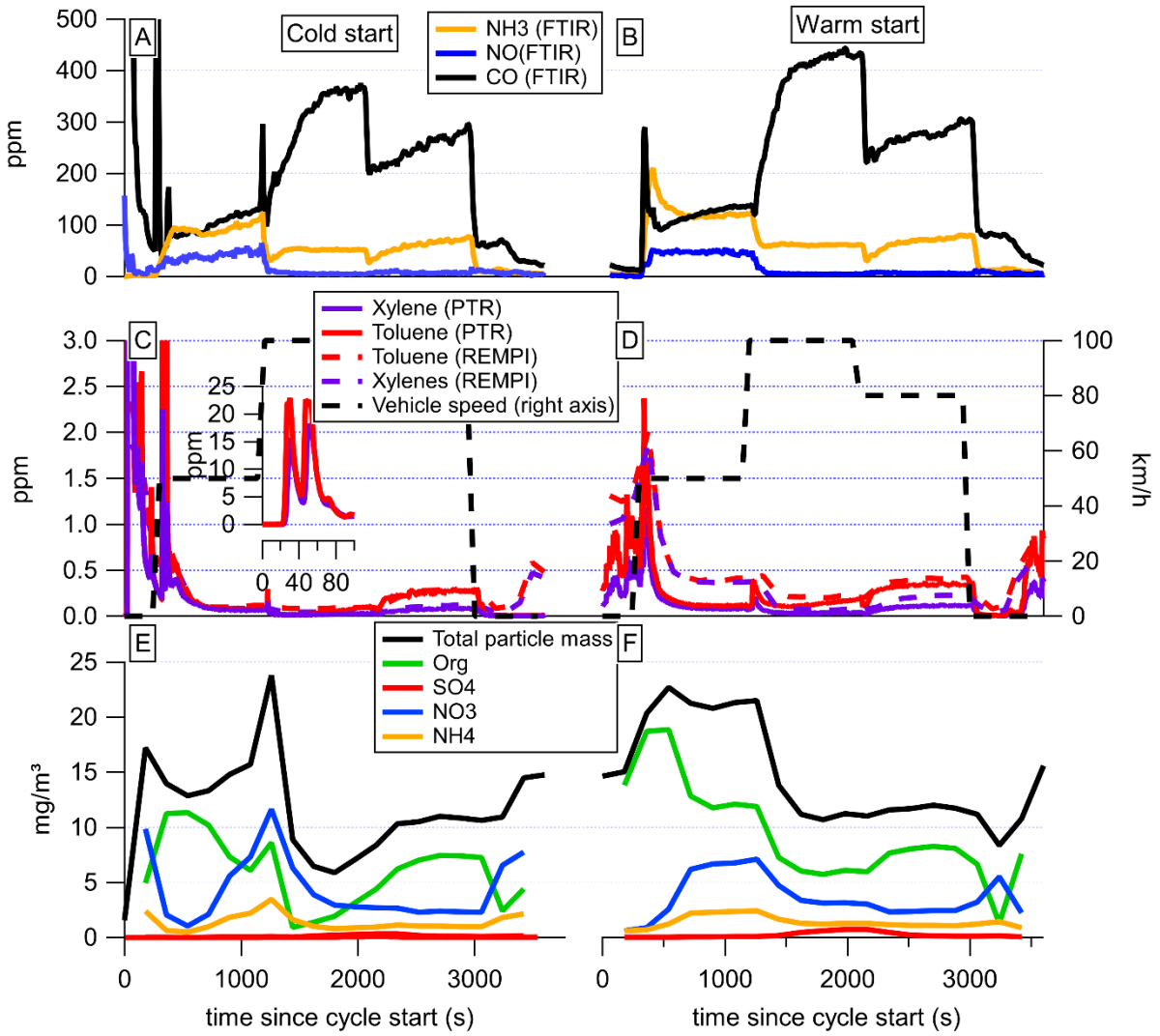

Figure 41 overview of cold and warm start emissions. The vehicle speed for both collumns A,C &E and B,D & F is shown in figure C and D for cold start and warm start respectivly. A,C and E show the cold start data for inorganic emissions, aromatic emissions and SOA formation respectivly. figure B,D and F show the equivalent data for warm start runs. All values are determined at tailpipe concentration.

6.4. Ship emissions

The air pollution associated with shipping aerosol has been estimated to have caused 266 thousand premature deaths globally prior to 2020 with up to 5.5 yearly premature deaths per 100.000 inhabitants in coastal cities.[14, 18, 117] Therefore, regulations in 2020 reduced the fuel sulfur content allowed in fuels to 0.5% such as in the LS-HFO which was used in these experiments to simulate the emissions of ships in non SECA. SECA further restrict the FSC below 0.1% such as the 0.01% FSC MGO fuel used to simulate SECA ship emissions.

With the single cylinder research engine capable of running at 80 kWh it was possible to operate at 4 different engine loads 25% (20kWh), 50% (40kWh), 75% (60kWh), and 100% (100kWh). However, as the atmospheric aging occurred in the PEAR with ozone addition and UV light, a key factor in the maximum possible aging achievable is the NOx emissions from the engine. NOx depletes the ozone at the entrance of the PEAR, thus reducing the OH radicals that can be formed from photolysis in the reaction chamber. Further, as the highest impact on human health is observed closest to the shore, the 25% engine load similar to that used in docking and near shore maneuvering was chosen as the operational engine load for aging experiments. Additional engine loads were tested but due to the increasing NOx emissions at higher engine loads with 20kWh at 25% and 60 kWh at 75% and above, the higher engine loads' emissions could not be aged and thus were only used for 4-hour measurements for cell exposures.

To increase aging, the options were to increase initial ozone concentration or increase UV light voltages as both ozonolysis and photodissociation of VOCs are possible and can alter the gas phase emissions. It was chosen to keep ozone concentrations at maximum (10 ppm) and alter the UV light intensity to obtain a photon flux up to 9.4E+15 (see section 5.4.2 for further information. Additionally, in order to determine the impact of ozonolysis, experiments were also performed with no UV light but with ozone addition, as well as fresh emissions where no ozone or UV light was added to the PEAR. Further, the conditions in the PEAR were stable at a relative humidity of 50% at 27°C with a residency time of 70 s. As the engine was in an isolated room there was no impact from the engine on the PEAR temperature.

Table 7. The photochemical age based on PTR-MS measurements and the KinSim age based on the UV voltage for both LS-HFO and MGO. All values are in ·OH equivalent days of age assuming ·OH concentration of $1.5*10^6$ molecules cm^{-3} in the atmosphere.

LS_HFO				MGO		
UV Voltage	PTR-MS	KinSim		UV Voltage	PTR-MS	KinSim
0V	0	0		0V	0	0
2x3V	1.5±0.1	0.8		2x3V	1.5±0.2	0.9
4x3V	3.3±0.1	2.16		4x3.8V	4.7±0.3	3.7
4x3.8V	6.0±0.2	2.9		4x5V	6.1±0.3	5.3
4x6V	7.4±0.3	5.1		4x6V	6.8±0.4	6.6
4x8.8V	8.7±0.3	7.9		4x7.5V	7.6±0.4	8.8
4x10V	8.5±0.3	9.0		4x8.8V	8.2±0.4	10.6
				4x10V	8.9±0.7	12.3

Finally, the main objective is to understand the difference in aerosol formed from the two different fuel types LS-HFO and MGO. Each fuel type was thus tested at 25% engine load with 10 ppm ozone and tested through the UV light intensities seen in table 3. The table further highlights the age determined by PTR-MS and the modelled age through the KinSim model.

6.4.1 Fresh emissions

The fresh emissions, thus not exposed to atmospheric aging, are the baseline for the aging experiments and thus determine the composition introduced into the PEAR. It is therefore important to have a good understanding of the composition of fresh emissions to further analyze the impact of aging.

The gas phase composition of key inorganic components such as NOx, COx, THC and SO_2 was observed with FTIR-MS for both LS-HFO and MGO. The fresh aerosol emissions for both MGO and HFO were composed of organics, POA and black carbon as seen in figure 21. The LS-HFO aerosol consisted of 47% organic matter and 53% black carbon with a total aerosol emission of 2.1±0.5 g/kg. In comparison, the fresh aerosol emitted using MGO was composed of 34% organics and 66% black carbon of a total aerosol emission of 0.8±0.1 g/kg. Therefore, the total POA emitted through the consumption of 1 kg LS-HFO is more than 5 times higher than the emissions associated with an equivalent consumption of MGO. The GMD shows that the fresh LS-HFO particles were about 20 nm larger than those emitted from MGO. Additionally, LS-HFO emitted 80% more particles in terms of number than MGO which combined with the larger GMD results in the larger particle mass emitted.

6.4.1.1 Ozonolysis

The ozonolysis of fresh emissions was performed by directing the exhaust through the PEAR with 10 ppm ozone added with no UV lights switched on. This resulted in no significant change in the aerosol composition, size or GMD for either MGO or LS-HFO. However, an increase in particle number concentrations was observed in the ozonolysis experiment with MGO increasing particle count by 67% (see table 4). This, along with a minor increase in organics of 1.2 enhancement factor is illustrated in figure 21. The results suggest that ozonolysis has a minor impact on the formation of the SOA.

Table 8 the impact of photochemical age on particle diamter shown as GMD and particle number for both LS-HFO and MGO.

LS-HFO				MGO		
age(days)	GMD(nm)	PN(cm^{-3})		age(days)	GMD(nm)	PN(cm^{-3})
0	94,4±2,8	3,30E+06		0	75,1±6,1	1,83E+06
ozone	91,4±5,5	3,62E+06		ozone	77,1±9,9	3,07E+06
1,5	32,4±2,2	4,00E+07		1,5	33,1±5,3	2,68E+07
3,3	37,1±0,7	8,10E+07		4,7	36,3±1,0	7,82E+07
6	44,3±0,9	1,02E+08		6,1	36,0±0,4	8,81E+07
7,4	42,8±2,1	1,35E+08		6,8	35,4±1,4	9,59E+07
8,5	46,5±0,5	1,24E+08		7,6	36,0±0,7	9,77E+07
8,7	46,6±0,8	1,22E+08		8,2	35,6±0,4	1,04E+08
				8,9	35,3±0,6	1,14E+08

6.4.3. Engine load dependent emissions

The fresh emissions can be compared between the different engine loads that were tested as part of a larger experimental setup. However, a comparison after photochemical aging is limited as the NO emissions observed during engine loads of at 75% (60kWh) and above effectively quenched radical production. Further, whilst the NO emissions during the 25% engine load (20kWh) were 398 ppm and 426 ppm, the increase to 50% engine load (40KWH) increased the NO emission to 506 ppm and 518 ppm for MGO and LS-HFO, respectively, which equates a roughly 25% increase. With a dilution prior to the PEAR of 1:100 this resulted in a decrease of ozone from 3.6 ppm to 1.9 ppm for MGO and from 3.1 ppm to 1.7 ppm for LS-HFO in the PEAR and thus the KinSim estimated age decreases from 12 hours to 3 hours of atmospheric equivalent days of photochemical aging for MGO and decreased the

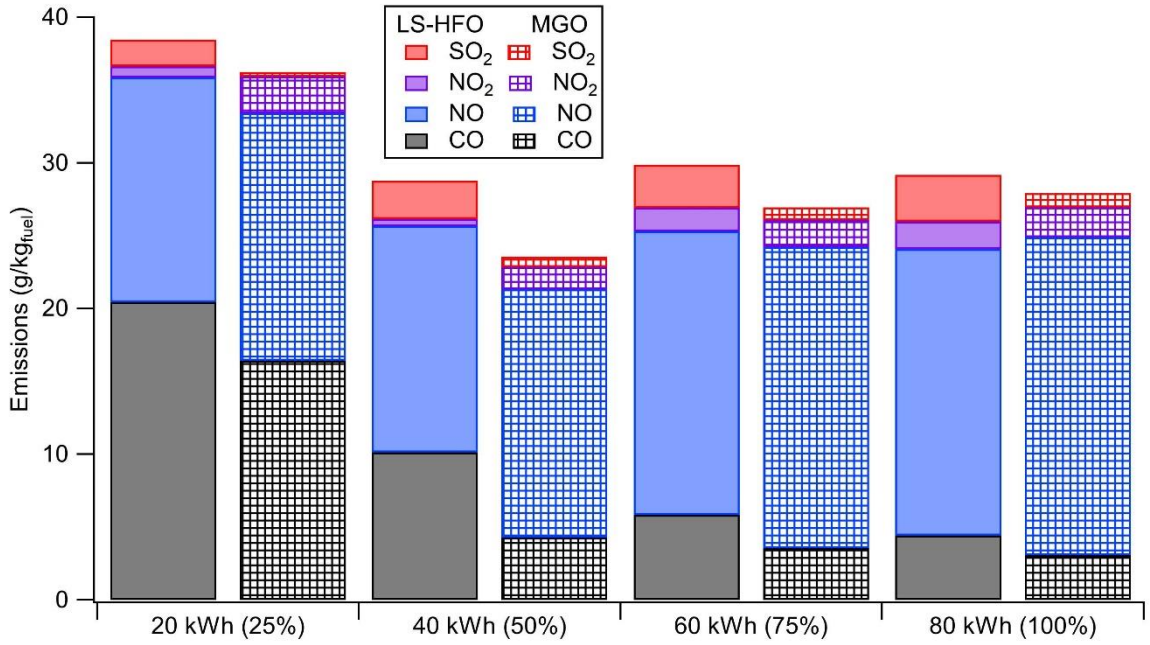

Figure 42 The inorganic gas phase emissions for both fuels, MGO in dashed bars and LS-HFO in solid bars for the engine loads 20, 40, 60 and 80kWh.

estimated atmospheric age from 9 hours to 3 hours for LS-HFO. Therefore, with the laboratory setup and restrictions associated therewith only the fresh emissions are compared.

As seen in figure 20, low engine loads are characterized by high CO (16 g/kg for MGO and 20 g/kg for LS-HFO) and relatively low NO (17 g/kg for MGO and 15 g/kg for LS-HFO) emissions. As engine load increases the emissions of CO decrease whilst the NO and SO_2 emissions increase. This suggests a high degree of incomplete combustion during low engine loads. Whilst SO_2 emissions are higher for LS-HFO at all engine loads, the relative increase in SO_2 emissions from 20 kWh to 80 kWh are only 1.75 times higher for LS-HFO whereas the same increase in engine load leads to 3 times increase in SO_2 emissions per kg fuel consumed for MGO. The relative difference between the two fuels in terms of SO_2 emissions is thus larger at lower engine loads.

6.4.2 Secondary aerosol formation

As ·OH exposure increases, the total aerosol mass increases for both fuels. BC as expected is only associated with fresh emissions and thus does not significantly change with age and remains at 1.1±0.2 g/kg for LS-HFO and 0.4±0.1 g/kg for MGO. The increase in total aerosol mass per kg fuel is thus a result of SOA formation from VOCs and SO_4 aerosol formation from SOx emissions. The total aerosol mass formed from the consumption of a kg LS-HFO was consistently more than twice that of the aerosol formed from the consumption of a kg MGO.

The chemical composition of the aerosol changes significantly as aging increases. At an atmospheric equivalent age of 1.5 days, LS-HFO is comprised of 60% OM with 0.94 g/kg POA and 0.97 g/kg SOA, an organic enhancement factor of 2.03. As the atmospheric equivalent age increases to 3.3 days, the organic mass fraction accounts for 59% with 1.5 ± 0.4 g/kg SOA formed. Thus, the highest organic fraction is observed at 1.5 days of age, whilst the highest SOA formation is observed at 3.3 days of age. This is a result of the SO_4 formation, at 1.5 days of age SO_4 aerosol comprised 0.38 g/kg for a 16% of the total aerosol and at 3.3 days of age this increases to 1.67g/kg SO_4 aerosol and 39%. As the atmospheric equivalent age increases, the fraction of SO_4 aerosol increases and at 8.7 days 73% of the aerosol is sulphate related mass for LS-HFO with 6.28g/kg. In comparison, the composition of the

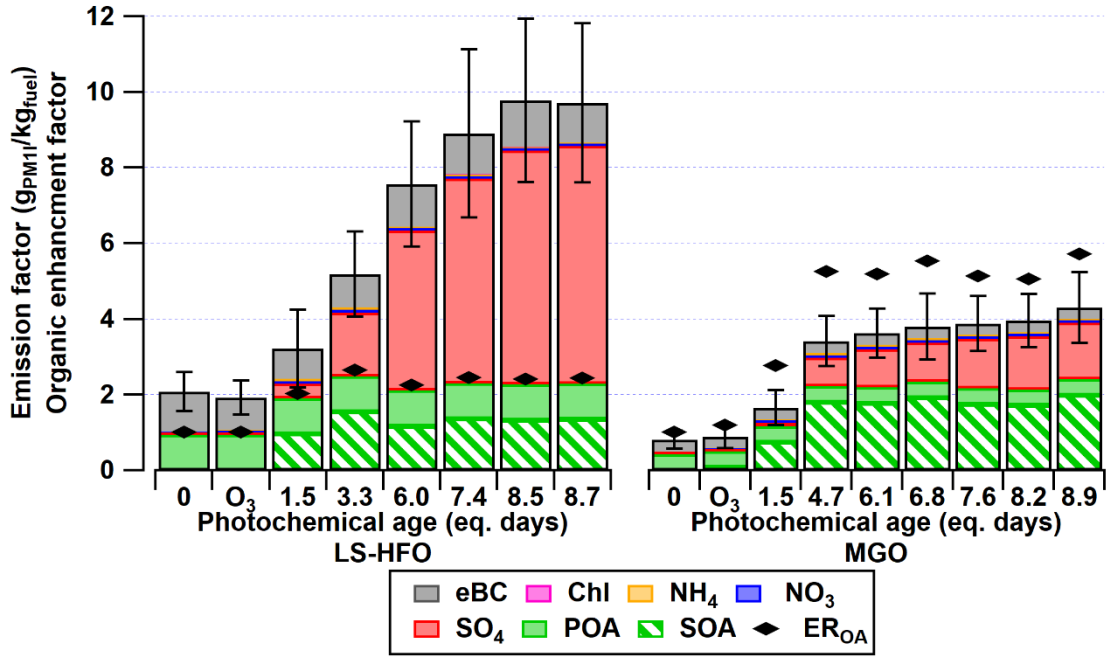

Figure 43 The left axis indicates the emission factor in grams of PM1 measured per kg fuel consumed and the organic enhancement factor (ER_{OA}). The left set of the graph represents the LS-HFO results and the right the MGO aerosol emissions, both with a photochemical age displayed in atmospheric equivalent days at the bottom. (adopted from Paul et al 2024b)

aerosol associated to MGO fuel was composed of 1.17 g/kg OM, 0.75g/kg SOA, with only 6% SO_4 at 1.5 days. Thus, for MGO the SOA comprised 74% of the total mass at 1.5 days and the total OM had increased 2.77 times as illustrated by the organic enhancement factor. At 4.7 days of atmospheric equivalent age, 1.8 ± 0.4 g/kg SOA was formed from emissions of 1 kg MGO consumed by the engine. This shows that whilst the total aerosol formed at a similar age from LS-HFO is higher than the total aerosol formed from MGO, the SOA mass formed associated with MGO is at least equivalent if not higher than the SOA mass formed from LS-HFO. Further, SO_4 aerosol comprised 25% of the aerosol at 0.76±0.01 g/kg at 4.7 days of age, increasing up to 39% and 1.49 g/kg at 8.9 days. The clear result associated with the change from LS-HFO would thus be a significant reduction in POA, BC and SO_4 aerosol, with the SO_4 aerosol reduction as a direct result of the lower FSC in MGO. However, SOA formation would likely remain similar regardless of the fuel type used.

6.4.2.1 Elemental composition

The elemental composition of the aerosol changes significantly from emission as VOCs oxidize and condense resulting in a more oxidized aerosol. Compositionally, the fresh organic aerosol of MGO and LS-HFO contained similar amounts of oxygen atoms per carbon atom with an O/C ratio of 0.05±0.01,

see figure 22 C and D. Additionally, the fraction of m/z=44 (f44) value was similar at 0.020±0.005 for both MGO and LS-HFO, see figure 22 A and B. Both compositional values are common for non-oxidized organic aerosols. However, the MGO contained more hydrogen per carbon atom with an H/C ratio of 1.79 ± 0.05 in comparison to the H/C of 1.67 ± 0.03 for the LS-HFO. Further, the fraction of m/z=43 (f43; (typically dominated by the C_2H_3O+ fragment and C_3H_7)) value for MGO was slightly higher than the f43 value of LS-HFO at 0.070±0.006 for MGO compared to 0.060±0.007 for LS-HFO. The lower f43 and H/C could suggest a higher degree of aromaticity in the LS-HFO aerosol. Aromatic compounds typically have H/C values nearing 1 and low f43 values when emitted. Naphthalene aerosol regardless of age is found to have an f43 of below 0.03. LS-HFO has been shown to contain larger aromatics, with low volatility, which potentially could condense into the particle phase during the transport time from exhaust to HR-ToF AMS.

The elemental composition at the highest photochemical age was similar for both fuel types, with both MGO and HFO reaching O/C ratios of 0.73±0.05, H/C ratios of 1.22±0.03, f43 of 0.06±0.01 and the fraction of 0.19±0.01 for m/z=44 (f44; (typically dominated by the CO_2+ fragment)). The elemental composition throughout all aging points was similar between the two fuels, suggesting that the only major differences for the elemental composition of the organic aerosol is found in the fresh emissions, which could be linked to low volatile aromatics.

6.4.2.2 Oxidation pathways

The oxidation pathway of an aerosol describes how the VOCs oxidize prior to entering the particle phase. Common Van Krevelen graphs such as illustrated in figure 22C and 22D are used to describe oxidation pathways as the slope of the graph gives information on how much oxygen is added for each lost hydrogen.[118] A slope of 0 would suggest the addition of alcohol or peroxides as a hydrogen is lost but replaced with an ·OH group, thus there would be 0 hydrogen net loss but the gain of one oxygen. A slope of -1 thus would be equivalent to carboxylic acid formation, as two hydrogens are lost but 1 regained along with two oxygen atoms resulting in a net gain of 2 oxygen and 1 hydrogen per carbon atom. Finally, a slope of -2 in the Van Krevelen plot would be equivalent to the addition of ketones or aldehydes where 2 hydrogens are lost and replaced with one oxygen atom. In figure 22C and 22D, a slope of -0.97±0.08 (r^2=0.97) for fresh aerosol to 4.7 days of equivalent photochemical aging and a slope of -0.89±0.04 (r^2=0.98) for fresh aerosol to 3.3 days of age of for MGO and LS-HFO are observed, respectively. However, the slope for both MGO and LS-HFO at ages above 4.7 days of equivalent photochemical age was -0.54±0.02 (r^2=0.99). The oxidation pathway thus changes after 4.7 days of photochemical age from being equivalent to carboxylic acid formation without fragmentation to that

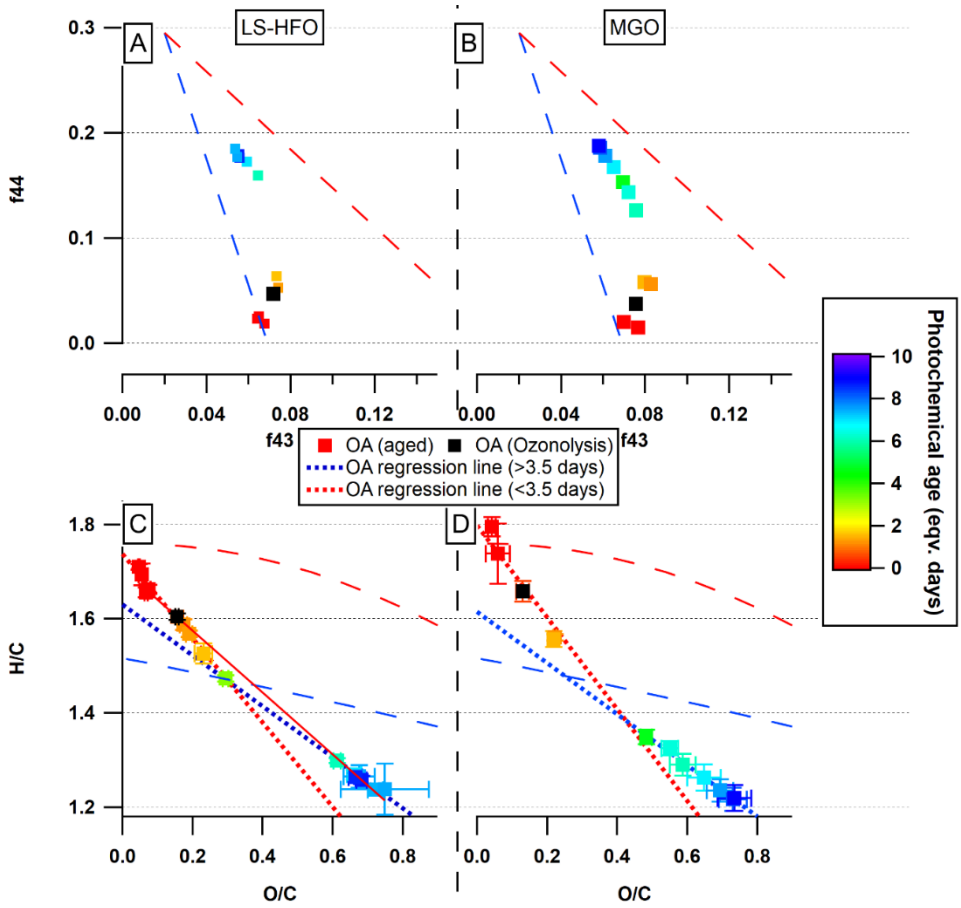

Figure 44 22A and 22B show a triangle plot as first published by Ng et al 2010, illustrating the f43 and f44 of the organic aerosol (OA). Figure 22A shows the impact of aging on these two fractions for LS-HFO and figure 22B shows the same for MGO. The photochemical age of the aerosol is illustrated by color as seen on the right. Figure 22C and 22D illustrate a Van Krevelen plot.[36,38] with hydrogen to carbon ratio on the y axis and oxygen to carbon ratio on the x axis, showing the chemical composition of the OA: the OA regression line is shown with dotted lines, and the dashed lines highlight the area where ambient aerosol typically fall within. Adapted from paul et al 2024

of carboxylic acid formation with fragmentation. This is further supported as there is no increase in SOA mass after the change in oxidation pathway as observed in figure 21. Additionally, figure 22A and 22B show that as photochemical age increases, initially both f43 and f44 increase. This suggests a general increase in oxidized organics, both with carbons with a single or no oxygen atoms associated with the f43 value and carbon with two oxygen atoms associated with f44.[119] This, along with the Van Krevelen slope of close to -1, suggests carboxylic acid formation with no or limited fragmentation until maximum SOA formation is reached. After the maximum SOA formation point when the photochemical age is further increased, f44 continues to rise, the f43 decreases however to values lower than the initial fresh f43 value. This shows a transition in the structure of the organic aerosol getting saturated with CO_2+ molecules, but likely including fragmentation as the Van Krevelen slope decreases to close to -0.5. The fragmentation additionally explains how oxygen can be added to the aerosol, but total SOA mass stagnates, as fragmented CO or CO_2+ would return to the gas phase and thus not contribute to SOA mass. Further, the oxidation pathway is not significantly impacted by a change in RO_2 fate as seen in figure 20. The primary RO_2 fate accounting for more than 50% of lost RO_2 are RO_2-HO_2 reactions, whilst the secondary RO_2 loss pathway are RO_2-HO reactions, accounting for more than 25% of lost RO_2. Thus, we find that once oxidized for more than 4.7 the oxidation of VOCs from a ship diesel generator engine follow a similar oxidation pathways regardless of fuel used.

7. Summary & Outlook

The dissertation presents an in-depth analysis of PM emitted from complex real world emission sources: a EURO 6d compliant combustion engine running on gasoline, and a ship combustion engine running on LS-HFO and MGO, with and FSC of 0.5% and 0.01%, respectively. A major focus here is the impact of atmospheric aging on those combustion emissions for which OFRs were used in combination with multiple high resolution mass spectrometry methods to map both particle and gas phase.

A comparison of multiple electron ionization-based mass spectrometry methods, HR-ToF AMS, DIP, and GCxGC showed while using the same ionization methods, the three instruments can be used complementary to each other. The HR-ToF AMS retains more complete information about the aerosol composition quantitatively and is thus significantly better suited in following changes related to increased oxidation of the aerosol. The DIPs high resolution and lower thermal fragmentation was found to be useful in determining the structure of larger molecules at-line. The GCxGC can resolve the molecular structure of aerosols and of determining the isomeric composition, which gives valuable qualitative information to combine with the quantitative data found by the HR-ToF AMS.

Further it was found that due to the extreme NO emissions by the combustion engines, it is necessary to consider the quenching effects these gases can have on the oxidation potential in laboratory oxidation flow reactors (eq. 18). Additionally, the modeling using KinSim highlighted the potential to determine RO_2 reaction pathways dependent on emissions, allowing for good indication on the atmospheric relevance of OFR measurement.

Through the observation of SOA formation from a modern Euro 6d compliant light duty vehicle, the initial hypothesis that modern vehicles with a GPF should have low primary emissions were confirmed for both cold and warm start. Further it could be determined that during warm start experiments, the main precursors of aerosols are aromatics, primarily toluene, xylene and trimethyl benzene. Additionally, the aromatics were found to be a result of unburned fuel which is the main source of SOA during vehicle driving speeds below 100 km/h. Additionally, it was shown that there are significant differences in the SOA formation depending on the operational conditions of the car. Cold starts compared to warm starts had significant impact on NO emissions as well as toluene and xylene. Furthermore, idling and driving at 50 km/h was shown to have higher SOA mass formation, likely as a result of unburned fuel, whereas the lower SOA mass formed during 80 -100 km/h is governed by incomplete combustion where aromatics play a less dominant role as SOA precursor.

In this dissertation it was shown as well that changing from LS-HFO, a low sulfur residual fuel, to a distilled fuel with a significantly lower FSC such as MGO not only impacts the sulfate aerosol formation occurring in the atmosphere as a result of atmospheric oxidation, but additionally. impacts the fresh emissions where LS-HFO emits 3 times the black carbon and 2 times the POA compared to MGO. However, there was no significant difference in the SOA mass formed between the two fuels. Further, the SOA composition was similar throughout the aging, showing that the SOA precursors were similar between the two fuels. This explains similar oxidation pathways, which until an atmospheric age of 4.7 days increase both SOA mass, f44 and f43 and show a -0.9 slope in the VK plot, indicating carboxylic acid formation or equivalent reactions. After 4.7 days however, SOA mass no longer increases with atmospheric aging and whilst f44 increases, the f43 decreases after this age. This, along with the change in slope to -0.5 suggests a change in oxidative pathway where carboxylic acid groups are formed but with fragmentation.

8. References

1. Allen, M.; Babiker, M.; Chen, Y.; de Coninck, H.; Connors, S.; van Diemen, R.; Dube, O. P.; Ebi, K. L.; Engelbrecht, F.; Ferrat, M.; Ford, J.; Forster, P.; Fuss, S.; Bolanos, T. G.; Harold, J.; Hoegh-Guldberg, O.; Hourcade, J.-C.; Huppmann, D.; Jacob, D.; Jiang, K.; Johansen, T. G.; Kainuma, M.; de Kleijne, K.; Kriegler, E.; Ley, D.; Liverman, D.; Mahowald, N.; Masson-Delmotte, V.; Matthews, J. B. R.; Millar, R.; Mintenbeck, K.; Morelli, A.; Moufouma-Okia, W.; Mundaca, L.; Nicolai, M.; Okereke, C.; Pathak, M.; Payne, A.; Pidcock, R.; Pirani, A.; Poloczanska, E.; Pörtner, H.-O.; Revi, A.; Riahi, K.; Roberts, D. C.; Rogelj, J.; Roy, J.; Seneviratne, S. I.; Shukla, P. R.; Skea, J.; Slade, R.; Schindell, D.; Singh, C.; Solecki, W.; Steg, L.; Taylor, M.; Tschakert, P.; Waisman, H.; Warren, R.; Zhai, P.; Zickfeld, K. *IPCC: Summary for Policymakers. In: Global Warming of 1.5°C. An IPCC Special Report on the impacts of global warming of 1.5°C above pre-industrial levels and related global greenhouse gas emission pathways, in the context of strengthening the global response to the threat of climate change, sustainable development, and efforts to eradicate poverty*; 2018, 2018.
2. Offer, S.; Hartner, E.; Di Bucchianico, S.; Bisig, C.; Bauer, S.; Pantzke, J.; Zimmermann Elias, J.; Cao, X.; Binder, S.; Kuhn, E.; Huber, A.; Jeong, S.; Käfer, U.; Martens, P.; Mesceriakovas, A.; Bendl, J.; Brejcha, R.; Buchholz, A.; Gat, D.; Hohaus, T.; Rastak, N.; Jakobi, G.; Kalberer, M.; Kanashova, T.; Hu, Y.; Ogris, C.; Marsico, A.; Theis, F.; Pardo, M.; Gröger, T.; Oeder, S.; Orasche, J.; Paul, A.; Ziehm, T.; Zhang, Z.-H.; Adam, T.; Sippula, O.; Sklorz, M.; Schnelle-Kreis, J.; Czech, H.; Kiendler-Scharr, A.; Rudich, Y.; Zimmermann, R., Effect of Atmospheric Aging on Soot Particle Toxicity in Lung Cell Models at the Air–Liquid Interface: Differential Toxicological Impacts of Biogenic and Anthropogenic Secondary Organic Aerosols (SOAs). *Environmental Health Perspectives* **2022,** *130* (2), 027003.
3. Murray, C. J. L., Global burden of 87 risk factors in 204 countries and territories, 1990–2019: a systematic analysis for the Global Burden of Disease Study 2019. *The Lancet* **2020,** *396* (10258), 1223-1249.
4. Masson-Delmotte, V.; P. Zhai; A. Pirani; S.L. Connors; C. Péan; S. Berger; N. Caud; Y. Chen; L. Goldfarb; M.I. Gomis; M. Huang; K. Leitzell; E. Lonnoy; J.B.R. Matthews; T.K. Maycock; T. Waterfield; O. Yelekçi; R. Yu; (eds.), B. Z., IPCC, 2021:Climate Change 2021: The Physical Science Basis. Contribution of Working Group I to the Sixth

Assessment Report of the Intergovernmental Panel on Climate Change. *Cambridge University Press. In Press* **2021**.
5. Pörtner, H.-O.; Roberts, D. C.; Masson-Delmotte, V.; Zhai, P.; Tignor, M.; Poloczanska, E.; Mintenbeck, K.; Nicolai, M.; Okem, A.; Petzold, J.; Rama, B.; Weyer, N. *IPCC: Summary for Policymakers. In: IPCC Special Report on the Ocean and Cryosphere in a Changing Climate*; 2019, 2019.
6. IPPC, Summary for Policymakers. In: Global Warming of 1.5°C. An IPCC Special Report on the impacts of global warming of 1.5°C above pre-industrial levels and related global greenhouse gas emission pathways, in the context of strengthening the global response to the threat of climate change, sustainable development, and efforts to eradicate poverty. **2018**.
7. Tollefson, J., Soot a major contributor to climate change. *Nature* **2013**.
8. IMO Fourth IMO greenhouse gas study. https://www.imo.org/en/ourwork/Environment/Pages/Fourth-IMO-Greenhouse-Gas-Study-2020.aspx (accessed 08/02).
9. IMO IMO 2020 – cutting sulphur oxide emissions https://www.imo.org/en/MediaCentre/HotTopics/Pages/Sulphur-2020.aspx (accessed 01/02).
10. Shi, Z.; Endres, S.; Rutgersson, A.; Al-Hajjaji, S.; Brynolf, S.; Booge, D.; Hassellöv, I.-M.; Kontovas, C.; Kumar, R.; Liu, H.; Marandino, C.; Matthias, V.; Moldanová, J.; Salo, K.; Sebe, M.; Yi, W.; Yang, M.; Zhang, C., Perspectives on shipping emissions and their impacts on the surface ocean and lower atmosphere: An environmental-social-economic dimension. *Elementa: Science of the Anthropocene* **2023,** *11* (1), 00052.
11. McDuffie, E. E.; Smith, S. J.; O'Rourke, P.; Tibrewal, K.; Venkataraman, C.; Marais, E. A.; Zheng, B.; Crippa, M.; Brauer, M.; Martin, R. V., A global anthropogenic emission inventory of atmospheric

pollutants from sector- and fuel-specific sources (1970–2017): an application of the Community Emissions Data System (CEDS). *Earth Syst. Sci. Data* **2020,** *12* (4), 3413-3442.
12. European, C.; Joint Research, C.; Olivier, J.; Guizzardi, D.; Schaaf, E.; Solazzo, E.; Crippa, M.; Vignati, E.; Banja, M.; Muntean, M.; Grassi, G.; Monforti-Ferrario, F.; Rossi, S., *GHG emissions of all world – 2021 report*. Publications Office of the European Union: 2021.
13. Corbett, J. J.; Winebrake, J. J.; Green, E. H.; Kasibhatla, P.; Eyring, V.; Lauer, A., Mortality from Ship Emissions: A Global Assessment. *Environmental Science & Technology* **2007,** *41* (24), 8512-8518.
14. Mueller, N.; Westerby, M.; Nieuwenhuijsen, M., Health impact assessments of shipping and port-sourced air pollution on a global scale: A scoping literature review. *Environmental Research* **2023,** *216*, 114460.
15. Organization, W. H. Burden of disesase from teh joint effects of household and ambient air pollution for 2016'. https://cdn.who.int/media/docs/default-source/air-quality-database/aqd-2018/ap_joint_effect_bod_results_may2018.pdf?sfvrsn=4dc44c26_3 (accessed 08/02).
16. Union, C. o. t. E., Council Directive 91/441/EEC of 26 June 1991 amending Directive 70/220/EEC on the approximation of the laws of the Member States relating to measures to be taken against air pollution by emissions from motor vehicles. DG III – Industry, D., Ed. https://eur-lex.europa.eu/legal-content/EN/ALL/?uri=CELEX%3A31991L0441, 1991.
17. Streibel, T.; Schnelle-Kreis, J.; Czech, H.; Harndorf, H.; Jakobi, G.; Jokiniemi, J.; Karg, E.; Lintelmann, J.; Matuschek, G.; Michalke, B.; Müller, L.; Orasche, J.; Passig, J.; Radischat, C.; Rabe, R.; Reda, A.; Rüger, C.; Schwemer, T.; Sippula, O.; Stengel, B.; Sklorz, M.; Torvela, T.; Weggler, B.; Zimmermann, R., Aerosol emissions of a ship diesel engine operated with diesel fuel or heavy fuel oil. *Environmental Science and Pollution Research* **2017,** *24* (12), 10976-10991.
18. Sofiev, M.; Winebrake, J. J.; Johansson, L.; Carr, E. W.; Prank, M.; Soares, J.; Vira, J.; Kouznetsov, R.; Jalkanen, J.-P.; Corbett, J. J., Cleaner fuels for ships provide public health benefits with climate tradeoffs. *Nature Communications* **2018,** *9* (1), 406.
19. Weber, C.; Sundvor, I.; Figenbaum, E., Comparison of regulated emission factors of Euro 6 LDV in Nordic temperatures and cold start conditions: Diesel- and gasoline direct-injection. *Atmospheric Environment* **2019,** *206*, 208-217.
20. Chu-Van, T.; Ristovski, Z.; Pourkhesalian, A. M.; Rainey, T.; Garaniya, V.; Abbassi, R.; Kimball, R.; Luong Cong, N.; Jahangiri, S.; Brown, R. J., A comparison of particulate matter and gaseous emission factors from two large cargo vessels during manoeuvring conditions. *Energy Reports* **2019,** *5*, 1390-1398.
21. Karjalainen, P.; Teinilä, K.; Kuittinen, N.; Aakko-Saksa, P.; Bloss, M.; Vesala, H.; Pettinen, R.; Saarikoski, S.; Jalkanen, J.-P.; Timonen, H., Real-world particle emissions and secondary aerosol formation from a diesel oxidation catalyst and scrubber equipped ship operating with two fuels in a SECA area. *Environmental Pollution* **2022,** *292*, 118278.
22. Pieber, S. M.; Kumar, N. K.; Klein, F.; Comte, P.; Bhattu, D.; Dommen, J.; Bruns, E. A.; Kılıç, D.; El Haddad, I.; Keller, A.; Czerwinski, J.; Heeb, N.; Baltensperger, U.; Slowik, J. G.; Prévôt, A. S. H., Gas-phase composition and secondary organic aerosol formation from standard and particle filter-retrofitted gasoline direct injection vehicles investigated in a batch and flow reactor. *Atmos. Chem. Phys.* **2018,** *18* (13), 9929-9954.
23. Hartikainen, A. H.; Ihalainen, M.; Yli-Pirilä, P.; Hao, L.; Kortelainen, M.; Pieber, S. M.; Sippula, O., Photochemical transformation and secondary aerosol formation potential of Euro6 gasoline and diesel passenger car exhaust emissions. *Journal of Aerosol Science* **2023,** *171*, 106159.
24. Chen, L.; Liang, Z.; Zhang, X.; Shuai, S., Characterizing particulate matter emissions from GDI and PFI vehicles under transient and cold start conditions. *Fuel* **2017,** *189*, 131-140.
25. Simonen, P.; Kalliokoski, J.; Karjalainen, P.; Rönkkö, T.; Timonen, H.; Saarikoski, S.; Aurela, M.; Bloss, M.; Triantafyllopoulos, G.; Kontses, A.; Amanatidis, S.; Dimaratos, A.; Samaras, Z.; Keskinen, J.; Dal Maso, M.; Ntziachristos, L., Characterization of laboratory and real driving emissions of individual Euro 6 light-duty vehicles – Fresh particles and secondary aerosol formation. *Environmental Pollution* **2019,** *255*, 113175.

26. Suarez-Bertoa, R.; Pechout, M.; Vojtíšek, M.; Astorga, C., Regulated and Non-Regulated Emissions from Euro 6 Diesel, Gasoline and CNG Vehicles under Real-World Driving Conditions. *Atmosphere* **2020,** *11* (2), 204.
27. Liu, Y.; Ge, Y.; Tan, J.; Wang, H.; Ding, Y., Research on ammonia emissions characteristics from light-duty gasoline vehicles. *Journal of Environmental Sciences* **2021,** *106*, 182-193.
28. Liu, T.; Hong, Y.; Li, M.; Xu, L.; Chen, J.; Bian, Y.; Yang, C.; Dan, Y.; Zhang, Y.; Xue, L.; Zhao, M.; Huang, Z.; Wang, H., Atmospheric oxidation capacity and ozone pollution mechanism in a coastal city of southeastern China: analysis of a typical photochemical episode by an observation-based model. *Atmos. Chem. Phys.* **2022,** *22* (3), 2173-2190.
29. Decker, Z. C. J.; Robinson, M. A.; Barsanti, K. C.; Bourgeois, I.; Coggon, M. M.; DiGangi, J. P.; Diskin, G. S.; Flocke, F. M.; Franchin, A.; Fredrickson, C. D.; Gkatzelis, G. I.; Hall, S. R.; Halliday, H.; Holmes, C. D.; Huey, L. G.; Lee, Y. R.; Lindaas, J.; Middlebrook, A. M.; Montzka, D. D.; Moore, R.; Neuman, J. A.; Nowak, J. B.; Palm, B. B.; Peischl, J.; Piel, F.; Rickly, P. S.; Rollins, A. W.; Ryerson, T. B.; Schwantes, R. H.; Sekimoto, K.; Thornhill, L.; Thornton, J. A.; Tyndall, G. S.; Ullmann, K.; Van Rooy, P.; Veres, P. R.; Warneke, C.; Washenfelder, R. A.; Weinheimer, A. J.; Wiggins, E.; Winstead, E.; Wisthaler, A.; Womack, C.; Brown, S. S., Nighttime and daytime dark oxidation chemistry in wildfire plumes: an observation and model analysis of FIREX-AQ aircraft data. *Atmos. Chem. Phys.* **2021,** *21* (21), 16293-16317.
30. Li, Z.; Xie, P.; Hu, R.; Wang, D.; Jin, H.; Chen, H.; Lin, C.; Liu, W., Observations of N2O5 and NO3 at a suburban environment in Yangtze river delta in China: Estimating heterogeneous N2O5 uptake coefficients. *Journal of Environmental Sciences* **2020,** *95*, 248-255.
31. Cobos, C.; Castellano, E.; Schumacher, H. J., The kinetics and the mechanism of ozone photolysis at 253.7 nm. *Journal of Photochemistry* **1983,** *21* (3), 291-312.
32. Matsumi, Y.; Kawasaki, M., Photolysis of Atmospheric Ozone in the Ultraviolet Region. *Chemical Reviews* **2003,** *103* (12), 4767-4782.
33. Hayes, P. L.; Ortega, A. M.; Cubison, M. J.; Froyd, K. D.; Zhao, Y.; Cliff, S. S.; Hu, W. W.; Toohey, D. W.; Flynn, J. H.; Lefer, B. L.; Grossberg, N.; Alvarez, S.; Rappenglück, B.; Taylor, J. W.; Allan, J. D.; Holloway, J. S.; Gilman, J. B.; Kuster, W. C.; de Gouw, J. A.; Massoli, P.; Zhang, X.; Liu, J.; Weber, R. J.; Corrigan, A. L.; Russell, L. M.; Isaacman, G.; Worton, D. R.; Kreisberg, N. M.; Goldstein, A. H.; Thalman, R.; Waxman, E. M.; Volkamer, R.; Lin, Y. H.; Surratt, J. D.; Kleindienst, T. E.; Offenberg, J. H.; Dusanter, S.; Griffith, S.; Stevens, P. S.; Brioude, J.; Angevine, W. M.; Jimenez, J. L., Organic aerosol composition and sources in Pasadena, California, during the 2010 CalNex campaign. *Journal of Geophysical Research: Atmospheres* **2013,** *118* (16), 9233-9257.
34. Lu, Y.; Khalil, M. A. K., Tropospheric OH: model calculations of spatial, temporal, and secular variations. *Chemosphere* **1991,** *23* (3), 397-444.
35. Heyder, J., Definition of an Aerosol. *Journal of Aerosol Medicine* **1991,** *4* (3), 217-221.
36. Curtius, J., Nucleation of atmospheric aerosol particles. *Comptes Rendus Physique* **2006,** *7* (9), 1027-1045.
37. Textor, C.; Schulz, M.; Guibert, S.; Kinne, S.; Balkanski, Y.; Bauer, S.; Berntsen, T.; Berglen, T.; Boucher, O.; Chin, M.; Dentener, F.; Diehl, T.; Easter, R.; Feichter, H.; Fillmore, D.; Ghan, S.; Ginoux, P.; Gong, S.; Grini, A.; Hendricks, J.; Horowitz, L.; Huang, P.; Isaksen, I.; Iversen, I.; Kloster, S.; Koch, D.; Kirkevåg, A.; Kristjansson, J. E.; Krol, M.; Lauer, A.; Lamarque, J. F.; Liu, X.; Montanaro, V.; Myhre, G.; Penner, J.; Pitari, G.; Reddy, S.; Seland, Ø.; Stier, P.; Takemura, T.; Tie, X., Analysis and quantification of the diversities of aerosol life cycles within AeroCom. *Atmos. Chem. Phys.* **2006,** *6* (7), 1777-1813.
38. Anguelova, M.; Barber, R. P.; Wu, J., Spume Drops Produced by the Wind Tearing of Wave Crests. *Journal of Physical Oceanography* **1999,** *29* (6), 1156-1165.
39. Samaké, A.; Bonin, A.; Jaffrezo, J. L.; Taberlet, P.; Weber, S.; Uzu, G.; Jacob, V.; Conil, S.; Martins, J. M. F., High levels of primary biogenic organic aerosols are driven by only a few plant-associated microbial taxa. *Atmos. Chem. Phys.* **2020,** *20* (9), 5609-5628.
40. Stocker, T. F., D. Qin, G.-K. Plattner, M. Tignor, S.K. Allen, J. Boschung, A. Nauels, Y. Xia, V. Bex and P.M. Midgley (eds.), IPCC, 2013: Climate Change 2013: The Physical Science Basis. Contribution of

Working Group I to the Fifth Assessment Report of the Intergovernmental Panel on Climate Change. *Cambridge University Press* **2013**, 1535 pp.
41. Weng, H.; Lin, J.; Martin, R.; Millet, D. B.; Jaeglé, L.; Ridley, D.; Keller, C.; Li, C.; Du, M.; Meng, J., Global high-resolution emissions of soil NOx, sea salt aerosols, and biogenic volatile organic compounds. *Scientific Data* **2020,** *7* (1), 148.
42. Mahilang, M.; Deb, M. K.; Pervez, S., Biogenic secondary organic aerosols: A review on formation mechanism, analytical challenges and environmental impacts. *Chemosphere* **2021,** *262*, 127771.
43. Behera, S. N.; Sharma, M.; Aneja, V. P.; Balasubramanian, R., Ammonia in the atmosphere: a review on emission sources, atmospheric chemistry and deposition on terrestrial bodies. *Environmental Science and Pollution Research* **2013,** *20* (11), 8092-8131.
44. Luo, Z.; Zhang, Y.; Chen, W.; Van Damme, M.; Coheur, P. F.; Clarisse, L., Estimating global ammonia (NH3) emissions based on IASI observations from 2008 to 2018. *Atmos. Chem. Phys.* **2022,** *22* (15), 10375-10388.
45. Ozgen, S.; Cernuschi, S.; Caserini, S., An overview of nitrogen oxides emissions from biomass combustion for domestic heat production. *Renewable and Sustainable Energy Reviews* **2021,** *135*, 110113.
46. Short-lived Climate Forcers. In *Climate Change 2021 – The Physical Science Basis: Working Group I Contribution to the Sixth Assessment Report of the Intergovernmental Panel on Climate Change*, Intergovernmental Panel on Climate, C., Ed. Cambridge University Press: Cambridge, 2023; pp 817-922.
47. Farmer, D. K.; Boedicker, E. K.; DeBolt, H. M., Dry Deposition of Atmospheric Aerosols: Approaches, Observations, and Mechanisms. *Annu Rev Phys Chem* **2021,** *72*, 375-397.
48. Ryu, Y.-H.; Min, S.-K., Improving Wet and Dry Deposition of Aerosols in WRF-Chem: Updates to Below-Cloud Scavenging and Coarse-Particle Dry Deposition. *Journal of Advances in Modeling Earth Systems* **2022,** *14* (4), e2021MS002792.
49. Tsimpidi, A. P.; Karydis, V. A.; Pandis, S. N.; Lelieveld, J., Global combustion sources of organic aerosols: model comparison with 84 AMS factor-analysis data sets. *Atmos. Chem. Phys.* **2016,** *16* (14), 8939-8962.
50. Kristiansen, N. I.; Stohl, A.; Olivié, D. J. L.; Croft, B.; Søvde, O. A.; Klein, H.; Christoudias, T.; Kunkel, D.; Leadbetter, S. J.; Lee, Y. H.; Zhang, K.; Tsigaridis, K.; Bergman, T.; Evangeliou, N.; Wang, H.; Ma, P. L.; Easter, R. C.; Rasch, P. J.; Liu, X.; Pitari, G.; Di Genova, G.; Zhao, S. Y.; Balkanski, Y.; Bauer, S. E.; Faluvegi, G. S.; Kokkola, H.; Martin, R. V.; Pierce, J. R.; Schulz, M.; Shindell, D.; Tost, H.; Zhang, H., Evaluation of observed and modelled aerosol lifetimes using radioactive tracers of opportunity and an ensemble of 19 global models. *Atmos. Chem. Phys.* **2016,** *16* (5), 3525-3561.
51. Goldman, M. J.; Green, W. H.; Kroll, J. H., Chemistry of Simple Organic Peroxy Radicals under Atmospheric through Combustion Conditions: Role of Temperature, Pressure, and NOx Level. *The Journal of Physical Chemistry A* **2021,** *125* (48), 10303-10314.
52. Peng, Z.; Lee-Taylor, J.; Orlando, J. J.; Tyndall, G. S.; Jimenez, J. L., Organic peroxy radical chemistry in oxidation flow reactors and environmental chambers and their atmospheric relevance. *Atmos. Chem. Phys.* **2019,** *19* (2), 813-834.
53. Kim, H.; Kang, D.; Jung, H. Y.; Jeon, J.; Lee, J. Y. Review of Smog Chamber Experiments for Secondary Organic Aerosol Formation *Atmosphere* [Online], 2024.
54. Rosati, B.; Paul, A.; Iversen, E. M.; Massling, A.; Bilde, M., Reconciling atmospheric water uptake by hydrate forming salts. *Environmental Science: Processes & Impacts* **2020,** *22* (8), 1759-1767.
55. Ma, Q.; Ma, J.; Liu, C.; Lai, C.; He, H., Laboratory study on the hygroscopic behavior of external and internal C2-C4 dicarboxylic acid-NaCl mixtures. *Environ Sci Technol* **2013,** *47* (18), 10381-8.
56. Seinfeld, J. H.; Pandis, S. N., *Atmospheric Chemistry and Physics: From Air Pollution to Climate Change*. Wiley: 2016.
57. Wriedt, T., A Review of Elastic Light Scattering Theories. *Particle & Particle Systems Characterization* **1998,** *15* (2), 67-74.
58. Klinger-Strobel, M.; Lautenschläger, C.; Fischer, D.; Mainz, J. G.; Bruns, T.; Tuchscherr, L.; Pletz, M. W.; Makarewicz, O., Aspects of pulmonary drug delivery strategies for infections in cystic fibrosis--where do we stand? *Expert Opin Drug Deliv* **2015,** *12* (8), 1351-74.

59. Kim, K.-H.; Kabir, E.; Kabir, S., A review on the human health impact of airborne particulate matter. *Environment International* **2015,** *74*, 136-143.
60. Pope Iii, C. A.; Burnett, R. T.; Thun, M. J.; Calle, E. E.; Krewski, D.; Ito, K.; Thurston, G. D., Lung Cancer, Cardiopulmonary Mortality, and Long-term Exposure to Fine Particulate Air Pollution. *JAMA* **2002,** *287* (9), 1132-1141.
61. Mohanraj, R.; Azeez, P. A., Health effects of airborne particulate matter and the Indian scenario. *Current Science* **2004,** *87* (6), 741-748.
62. Akinbami, L. J.; Simon, A. E.; Rossen, L. M., Changing Trends in Asthma Prevalence Among Children. *Pediatrics* **2016,** *137* (1), e20152354.
63. Holst, G. J.; Pedersen, C. B.; Thygesen, M.; Brandt, J.; Geels, C.; Bønløkke, J. H.; Sigsgaard, T., Air pollution and family related determinants of asthma onset and persistent wheezing in children: nationwide case-control study. *BMJ* **2020,** *370*, m2791.
64. Khreis, H.; Kelly, C.; Tate, J.; Parslow, R.; Lucas, K.; Nieuwenhuijsen, M., Exposure to traffic-related air pollution and risk of development of childhood asthma: A systematic review and meta-analysis. *Environment International* **2017,** *100*, 1-31.
65. Lighty, J. S.; Veranth, J. M.; Sarofim, A. F., Combustion Aerosols: Factors Governing Their Size and Composition and Implications to Human Health. *Journal of the Air & Waste Management Association* **2000,** *50* (9), 1565-1618.
66. Aretaki, M. A.; Desmet, J.; Viana, M.; van Drooge, B. L., Comprehensive methodology for semi-volatile organic compound determination in ambient air with emphasis on polycyclic aromatic hydrocarbons analysis by GC–MS/MS. *Journal of Chromatography A* **2024,** *1730*, 465086.
67. Atkinson, R.; Arey, J., Atmospheric chemistry of gas-phase polycyclic aromatic hydrocarbons: formation of atmospheric mutagens. *Environmental Health Perspectives* **1994,** *102* (suppl 4), 117-126.
68. Heydari, S.; Tainio, M.; Woodcock, J.; de Nazelle, A., Estimating traffic contribution to particulate matter concentration in urban areas using a multilevel Bayesian meta-regression approach. *Environ Int* **2020,** *141*, 105800.
69. European, C., REPORT FROM THE COMMISSION TO THE EUROPEAN PARLIAMENT AND

THE COUNCIL

on the effects of the Euro 5 Environmental Step for L-category vehicles. Brussels: 2018; Vol. COM(2018).
70. Chen, K.; Wan, J.; Lin, J.; Zhou, R., Comparative study of three-way catalytic performance over Pd/CeO2-ZrO2-Al2O3 and Pd/La-Al2O3 catalysts: New insights into microstructure and thermal stability. *Molecular Catalysis* **2022,** *526*, 112361.
71. Rood, S.; Eslava, S.; Manigrasso, A.; Bannister, C., Recent advances in gasoline three-way catalyst formulation: A review. *Proceedings of the Institution of Mechanical Engineers, Part D: Journal of Automobile Engineering* **2019,** *234* (4), 936-949.
72. EU, COM(2022) 586 Final REGULATION OF THE EUROPEAN PARLIAMENT AND OF THE COUNCIL on type-approval of motor vehicles and engines and of systems, components and separate technical units intended for such vehicles, with respect to their emissions and battery durability (Euro 7) and repealing Regulations (EC) No 715/2007 and (EC) No 595/2009.

: 2022.
73. Joshi, A.; Johnson, T. V., Gasoline Particulate Filters—a Review. *Emission Control Science and Technology* **2018,** *4* (4), 219-239.
74. Nordin, E. Z.; Eriksson, A. C.; Roldin, P.; Nilsson, P. T.; Carlsson, J. E.; Kajos, M. K.; Hellén, H.; Wittbom, C.; Rissler, J.; Löndahl, J.; Swietlicki, E.; Svenningsson, B.; Bohgard, M.; Kulmala, M.; Hallquist, M.; Pagels, J. H., Secondary organic aerosol formation from idling gasoline passenger vehicle emissions investigated in a smog chamber. *Atmos. Chem. Phys.* **2013,** *13* (12), 6101-6116.
75. Liu, T.; Wang, X.; Deng, W.; Hu, Q.; Ding, X.; Zhang, Y.; He, Q.; Zhang, Z.; Lü, S.; Bi, X.; Chen, J.; Yu, J., Secondary organic aerosol formation from photochemical aging of light-duty gasoline vehicle exhausts in a smog chamber. *Atmos. Chem. Phys.* **2015,** *15* (15), 9049-9062.

76. Gentner, D. R.; Jathar, S. H.; Gordon, T. D.; Bahreini, R.; Day, D. A.; El Haddad, I.; Hayes, P. L.; Pieber, S. M.; Platt, S. M.; de Gouw, J.; Goldstein, A. H.; Harley, R. A.; Jimenez, J. L.; Prévôt, A. S. H.; Robinson, A. L., Review of Urban Secondary Organic Aerosol Formation from Gasoline and Diesel Motor Vehicle Emissions. *Environmental Science & Technology* **2017,** *51* (3), 1074-1093.
77. Gray, N.; McDonagh, S.; O'Shea, R.; Smyth, B.; Murphy, J. D., Decarbonising ships, planes and trucks: An analysis of suitable low-carbon fuels for the maritime, aviation and haulage sectors. *Advances in Applied Energy* **2021,** *1*, 100008.
78. OECD Ocean shipping and shipbuilding. https://www.oecd.org/ocean/topics/ocean-shipping/ (accessed 01/02).
79. Contini, D.; Merico, E. Recent Advances in Studying Air Quality and Health Effects of Shipping Emissions *Atmosphere* [Online], 2021.
80. Jeong, S.; Bendl, J.; Saraji-Bozorgzad, M.; Käfer, U.; Etzien, U.; Schade, J.; Bauer, M.; Jakobi, G.; Orasche, J.; Fisch, K.; Cwierz, P. P.; Rüger, C. P.; Czech, H.; Karg, E.; Heyen, G.; Krausnick, M.; Geissler, A.; Geipel, C.; Streibel, T.; Schnelle-Kreis, J.; Sklorz, M.; Schulz-Bull, D. E.; Buchholz, B.; Adam, T.; Zimmermann, R., Aerosol emissions from a marine diesel engine running on different fuels and effects of exhaust gas cleaning measures. *Environmental Pollution* **2023,** *316*, 120526.
81. Jang, E.; Choi, S.; Yoo, E.; Hyun, S.; An, J., Impact of shipping emissions regulation on urban aerosol composition changes revealed by receptor and numerical modelling. *npj Climate and Atmospheric Science* **2023,** *6* (1), 52.
82. Vedachalam, S.; Baquerizo, N.; Dalai, A. K., Review on impacts of low sulfur regulations on marine fuels and compliance options. *Fuel* **2022,** *310*, 122243.
83. Andrew Slaughter, S. R., Thomas Shattuck., international maritime organiyation(IMO) 2020 strategies in a non-compliant world. **2019**.
84. Czech, H.; Stengel, B.; Adam, T.; Sklorz, M.; Streibel, T.; Zimmermann, R., A chemometric investigation of aromatic emission profiles from a marine engine in comparison with residential wood combustion and road traffic: Implications for source apportionment inside and outside sulphur emission control areas. *Atmospheric Environment* **2017,** *167*, 212-222.
85. Kostenidou, E.; Pathak, R. K.; Pandis, S. N., An Algorithm for the Calculation of Secondary Organic Aerosol Density Combining AMS and SMPS Data. *Aerosol Science and Technology* **2007,** *41* (11), 1002-1010.
86. Hartner, E.; Paul, A.; Käfer, U.; Czech, H.; Hohaus, T.; Gröger, T.; Sklorz, M.; Jakobi, G.; Orasche, J.; Jeong, S.; Brejcha, R.; Ziehm, T.; Zhang, Z.-H.; Schnelle-Kreis, J.; Adam, T.; Rudich, Y.; Kiendler-Scharr, A.; Zimmermann, R., On the Complementarity and Informative Value of Different Electron Ionization Mass Spectrometric Techniques for the Chemical Analysis of Secondary Organic Aerosols. *ACS Earth and Space Chemistry* **2022,** *6* (5), 1358-1374.
87. Drewnick, F.; Hings, S. S.; DeCarlo, P.; Jayne, J. T.; Gonin, M.; Fuhrer, K.; Weimer, S.; Jimenez, J. L.; Demerjian, K. L.; Borrmann, S.; Worsnop, D. R., A New Time-of-Flight Aerosol Mass Spectrometer (TOF-AMS)—Instrument Description and First Field Deployment. *Aerosol Science and Technology* **2005,** *39* (7), 637-658.
88. Käfer, U.; Gröger, T.; Rüger, C. P.; Czech, H.; Saraji-Bozorgzad, M.; Wilharm, T.; Zimmermann, R., Direct inlet probe – High-resolution time-of-flight mass spectrometry as fast technique for the chemical description of complex high-boiling samples. *Talanta* **2019,** *202*, 308-316.
89. Drinovec, L.; Močnik, G.; Zotter, P.; Prévôt, A. S. H.; Ruckstuhl, C.; Coz, E.; Rupakheti, M.; Sciare, J.; Müller, T.; Wiedensohler, A.; Hansen, A. D. A., The "dual-spot" Aethalometer: an improved measurement of aerosol black carbon with real-time loading compensation. *Atmos. Meas. Tech.* **2015,** *8* (5), 1965-1979.
90. Paul, A.; Fang, Z.; Martens, P.; Mukherjee, A.; Jakobi, G.; Ihalainen, M.; Kortelainen, M.; Somero, M.; Yli-Pirilä, P.; Hohaus, T.; Czech, H.; Kalberer, M.; Sippula, O.; Rudich, Y.; Zimmermann, R.; Kiendler-Scharr, A., Formation of secondary aerosol from emissions of a Euro 6d-compliant gasoline vehicle with particle filter. *Environmental Science: Atmospheres* **2024**.
91. Bacsik, Z.; Mink, J.; Keresztury, G., FTIR Spectroscopy of the Atmosphere. I. Principles and Methods. *Applied Spectroscopy Reviews* **2004,** *39* (3), 295-363.

92. Lambe, A. T.; Chhabra, P. S.; Onasch, T. B.; Brune, W. H.; Hunter, J. F.; Kroll, J. H.; Cummings, M. J.; Brogan, J. F.; Parmar, Y.; Worsnop, D. R.; Kolb, C. E.; Davidovits, P., Effect of oxidant concentration, exposure time, and seed particles on secondary organic aerosol chemical composition and yield. *Atmos. Chem. Phys.* **2015,** *15* (6), 3063-3075.
93. Kang, E.; Root, M. J.; Toohey, D. W.; Brune, W. H., Introducing the concept of Potential Aerosol Mass (PAM). *Atmos. Chem. Phys.* **2007,** *7* (22), 5727-5744.
94. Bruns, E. A.; El Haddad, I.; Keller, A.; Klein, F.; Kumar, N. K.; Pieber, S. M.; Corbin, J. C.; Slowik, J. G.; Brune, W. H.; Baltensperger, U.; Prévôt, A. S. H., Inter-comparison of laboratory smog chamber and flow reactor systems on organic aerosol yield and composition. *Atmos. Meas. Tech.* **2015,** *8* (6), 2315-2332.
95. Ihalainen, M.; Tiitta, P.; Czech, H.; Yli-Pirilä, P.; Hartikainen, A.; Kortelainen, M.; Tissari, J.; Stengel, B.; Sklorz, M.; Suhonen, H.; Lamberg, H.; Leskinen, A.; Kiendler-Scharr, A.; Harndorf, H.; Zimmermann, R.; Jokiniemi, J.; Sippula, O., A novel high-volume Photochemical Emission Aging flow tube Reactor (PEAR). *AEROSOL SCIENCE AND TECHNOLOGY* **2019,** *53* (3), 276-294.
96. Abd-Alla, G. H., Using exhaust gas recirculation in internal combustion engines: a review. *Energy Conversion and Management* **2002,** *43* (8), 1027-1042.
97. Eyzat, P.; Guibet, J. C., A New Look at Nitrogen Oxides Formation in Internal Combustion Engines. *SAE Transactions* **1968,** *77*, 481-500.
98. Agarwal, A. K.; Singh, A. P.; Maurya, R. K., Evolution, challenges and path forward for low temperature combustion engines. *Progress in Energy and Combustion Science* **2017,** *61*, 1-56.
99. Peng, Z.; Jimenez, J. L., KinSim: A Research-Grade, User-Friendly, Visual Kinetics Simulator for Chemical-Kinetics and Environmental-Chemistry Teaching. *Journal of Chemical Education* **2019,** *96* (4), 806-811.
100. Peng, Z.; Palm, B. B.; Day, D. A.; Talukdar, R.; Hu, W.; Lambe, A. T.; Brune, W. H.; Jimenez, J. L., Model Evaluation of New Techniques for Maintaining High-NO Conditions in Oxidation Flow Reactors for the Study of OH-Initiated Atmospheric Chemistry. *ACS Earth Space Chem* **2018,** *2* (2), 72-86.
101. Peng, Z.; Jimenez, J. L., Modeling of the chemistry in oxidation flow reactors with high initial NO. *Atmos. Chem. Phys.,* **2017,** *17* (17), 11991-12010.
102. Peng, Z.; Day, D. A.; Ortega, A. M.; Palm, B. B.; Hu, W.; Stark, H.; Li, R.; Tsigaridis, K.; Brune, W. H.; Jimenez, J. L., Non-OH chemistry in oxidation flow reactors for the study of atmospheric chemistry systematically examined by modeling. *Atmos. Chem. Phys.,* **2016,** *16* (16), 4283-4305.
103. Peng, J.; Hu, M.; Guo, S.; Du, Z.; Zheng, J.; Shang, D.; Levy Zamora, M.; Zeng, L.; Shao, M.; Wu, Y.-S.; Zheng, J.; Wang, Y.; Glen, C. R.; Collins, D. R.; Molina, M. J.; Zhang, R., Markedly enhanced absorption and direct radiative forcing of black carbon under polluted urban environments. *Proceedings of the National Academy of Sciences* **2016,** *113* (16), 4266.
104. Peng, Z.; Day, D. A.; Stark, H.; Li, R.; Lee-Taylor, J.; Palm, B. B.; Brune, W. H.; Jimenez, J. L., HO_x radical chemistry in oxidation flow reactors with low-pressure mercury lamps systematically examined by modeling. *Atmos. Meas. Tech.* **2015,** *8* (11), 4863-4890.
105. Barmet, P.; Dommen, J.; DeCarlo, P. F.; Tritscher, T.; Praplan, A. P.; Platt, S. M.; Prévôt, A. S. H.; Donahue, N. M.; Baltensperger, U., OH clock determination by proton transfer reaction mass spectrometry at an environmental chamber. *Atmos. Meas. Tech.* **2012,** *5* (3), 647-656.
106. Pardo, M.; Offer, S.; Hartner, E.; Di Bucchianico, S.; Bisig, C.; Bauer, S.; Pantzke, J.; Zimmermann, E. J.; Cao, X.; Binder, S.; Kuhn, E.; Huber, A.; Jeong, S.; Käfer, U.; Schneider, E.; Mesceriakovas, A.; Bendl, J.; Brejcha, R.; Buchholz, A.; Gat, D.; Hohaus, T.; Rastak, N.; Karg, E.; Jakobi, G.; Kalberer, M.; Kanashova, T.; Hu, Y.; Ogris, C.; Marsico, A.; Theis, F.; Shalit, T.; Gröger, T.; Rüger, C. P.; Oeder, S.; Orasche, J.; Paul, A.; Ziehm, T.; Zhang, Z.-H.; Adam, T.; Sippula, O.; Sklorz, M.; Schnelle-Kreis, J.; Czech, H.; Kiendler-Scharr, A.; Zimmermann, R.; Rudich, Y., Exposure to naphthalene and β-pinene-derived secondary organic aerosol induced divergent changes in transcript levels of BEAS-2B cells. *Environment International* **2022,** *166*, 107366.
107. Pardo, M.; Czech, H.; Offer, S.; Sklorz, M.; Di Bucchianico, S.; Hartner, E.; Pantzke, J.; Kuhn, E.; Paul, A.; Ziehm, T.; Zhang, Z.-H.; Jakobi, G.; Bauer, S.; Huber, A.; Zimmermann, E. J.; Rastak, N.; Binder, S.; Brejcha, R.; Schneider, E.; Orasche, J.; Rüger, C. P.; Gröger, T.; Oeder, S.; Schnelle-Kreis, J.; Hohaus, T.; Kalberer, M.; Sippula, O.; Kiendler-Scharr, A.; Zimmermann, R.; Rudich, Y., Atmospheric

aging increases the cytotoxicity of bare soot particles in BEAS-2B lung cells. *Aerosol Science and Technology* **2023,** *57* (5), 367-383.
108. Wang, H.; Guo, S.; Yu, Y.; Shen, R.; Zhu, W.; Tang, R.; Tan, R.; Liu, K.; Song, K.; Zhang, W.; Zhang, Z.; Shuai, S.; Xu, H.; Zheng, J.; Chen, S.; Li, S.; Zeng, L.; Wu, Z., Secondary aerosol formation from a Chinese gasoline vehicle: Impacts of fuel (E10, gasoline) and driving conditions (idling, cruising). *Science of The Total Environment* **2021,** *795*, 148809.
109. Zhang, Y.; Deng, W.; Hu, Q.; Wu, Z.; Yang, W.; Zhang, H.; Wang, Z.; Fang, Z.; Zhu, M.; Li, S.; Song, W.; Ding, X.; Wang, X., Comparison between idling and cruising gasoline vehicles in primary emissions and secondary organic aerosol formation during photochemical ageing. *Science of The Total Environment* **2020,** *722*, 137934.
110. Roth, P.; Yang, J.; Fofie, E.; Cocker, D. R., III; Durbin, T. D.; Brezny, R.; Geller, M.; Asa-Awuku, A.; Karavalakis, G., Catalyzed Gasoline Particulate Filters Reduce Secondary Organic Aerosol Production from Gasoline Direct Injection Vehicles. *Environmental Science & Technology* **2019,** *53* (6), 3037-3047.
111. Zhang, J.; Peng, J.; Song, A.; Lv, Z.; Tong, H.; Du, Z.; Guo, J.; Wu, L.; Wang, T.; Hallquist, M.; Mao, H., Marked impacts of transient conditions on potential secondary organic aerosol production during rapid oxidation of gasoline exhausts. *npj Climate and Atmospheric Science* **2023,** *6* (1), 59.
112. Yang, J.; Roth, P.; Durbin, T. D.; Johnson, K. C.; Cocker, D. R., III; Asa-Awuku, A.; Brezny, R.; Geller, M.; Karavalakis, G., Gasoline Particulate Filters as an Effective Tool to Reduce Particulate and Polycyclic Aromatic Hydrocarbon Emissions from Gasoline Direct Injection (GDI) Vehicles: A Case Study with Two GDI Vehicles. *Environmental Science & Technology* **2018,** *52* (5), 3275-3284.
113. Ahlberg, E.; Eriksson, A.; Brune, W. H.; Roldin, P.; Svenningsson, B., Effect of salt seed particle surface area, composition and phase on secondary organic aerosol mass yields in oxidation flow reactors. *Atmos. Chem. Phys.* **2019,** *19* (4), 2701-2712.
114. Karjalainen, P.; Timonen, H.; Saukko, E.; Kuuluvainen, H.; Saarikoski, S.; Aakko-Saksa, P.; Murtonen, T.; Bloss, M.; Dal Maso, M.; Simonen, P.; Ahlberg, E.; Svenningsson, B.; Brune, W. H.; Hillamo, R.; Keskinen, J.; Rönkkö, T., Time-resolved characterization of primary particle emissions and secondary particle formation from a modern gasoline passenger car. *Atmos. Chem. Phys.* **2016,** *16* (13), 8559-8570.
115. Kuittinen, N.; McCaffery, C.; Peng, W.; Zimmerman, S.; Roth, P.; Simonen, P.; Karjalainen, P.; Keskinen, J.; Cocker, D. R.; Durbin, T. D.; Rönkkö, T.; Bahreini, R.; Karavalakis, G., Effects of driving conditions on secondary aerosol formation from a GDI vehicle using an oxidation flow reactor. *Environmental Pollution* **2021,** *282*, 117069.
116. Zhao, Y.; Lambe, A. T.; Saleh, R.; Saliba, G.; Robinson, A. L., Secondary Organic Aerosol Production from Gasoline Vehicle Exhaust: Effects of Engine Technology, Cold Start, and Emission Certification Standard. *Environmental Science & Technology* **2018,** *52* (3), 1253-1261.
117. Viana, M.; Rizza, V.; Tobías, A.; Carr, E.; Corbett, J.; Sofiev, M.; Karanasiou, A.; Buonanno, G.; Fann, N., Estimated health impacts from maritime transport in the Mediterranean region and benefits from the use of cleaner fuels. *Environment International* **2020,** *138*, 105670.
118. Krevelen, D. W. V., Graphical-statistical Method for the Study of Structure and Reaction Processes of Coal. *Fuel* **1950,** *29*, 269-284.
119. Ng, N. L.; Canagaratna, M. R.; Zhang, Q.; Jimenez, J. L.; Tian, J.; Ulbrich, I. M.; Kroll, J. H.; Docherty, K. S.; Chhabra, P. S.; Bahreini, R.; Murphy, S. M.; Seinfeld, J. H.; Hildebrandt, L.; Donahue, N. M.; DeCarlo, P. F.; Lanz, V. A.; Prévôt, A. S. H.; Dinar, E.; Rudich, Y.; Worsnop, D. R., Organic aerosol components observed in Northern Hemispheric datasets from Aerosol Mass Spectrometry. *Atmos. Chem. Phys.* **2010,** *10* (10), 4625-4641.

9. Complete manuscripts

Environmental Science: Atmospheres

ROYAL SOCIETY OF CHEMISTRY

PAPER

View Article Online
View Journal | View Issue

Cite this: *Environ. Sci.: Atmos.*, 2024, **4**, 802

Formation of secondary aerosol from emissions of a Euro 6d-compliant gasoline vehicle with a particle filter†

Andreas Paul, *[ad] Zheng Fang,[b] Patrick Martens,[d] Arya Mukherjee,[e] Gert Jakobi,[c] Mika Ihalainen,[e] Miika Kortelainen,[e] Markus Somero,[e] Pasi Yli-Pirilä,[e] Thorsten Hohaus, *[a] Hendryk Czech,[cd] Markus Kalberer,[f] Olli Sippula,[eg] Yinon Rudich,[b] Ralf Zimmermann[cd] and Astrid Kiendler-Scharr ‡[a]

The most recent European regulation, the Euro 6d emission standard, requires all gasoline direct injection (GDI) vehicles to use both a three-way catalyst (TWC) and a gasoline particle filter (GPF) as exhaust aftertreatment. These aftertreatment methods are aimed at reducing NO_x and primary particle emissions. However, the formation of secondary organic aerosols (SOAs) from the volatile organic compound (VOC) emissions of a Euro 6d compliant GDI vehicle, factory equipped with a GPF is not yet investigated. Therefore, to explore the SOA formation and effects of the GPF, the exhaust of a Euro 6d compliant GDI vehicle was characterized at 4 different steady state speeds, idling (0 km h^{-1}), 50, 80 and 100 km h^{-1}. The exhaust was oxidised in a photochemical emission aging flow tube reactor (PEAR) by reactions with OH radicals equivalent of 2.2 days of atmospheric day time oxidation. It was found that the GPF completely removes primary particles larger than 10 nm, at all investigated vehicle speeds. However, significant SOA was formed after oxidation, with the highest SOA formation potential per kg fuel consumed at 50 km h^{-1}. The main SOA precursors were determined to be toluene, xylene and trimethyl-benzene which were found to account for at least 50% of SOA formed at all driving speeds. Furthermore, high emissions of ammonia (NH_3) could be observed in the exhaust under all driving conditions which resulted in the subsequent formation of ammonium nitrate (NH_4NO_3) after aging. The formation of NH_4NO_3 additionally facilitated the co-condensation of organic gas phase products after OH oxidation enhancing SOA mass even further.

Received 24th November 2023
Accepted 3rd June 2024

DOI: 10.1039/d3ea00165b

rsc.li/esatmospheres

Environmental significance

Particulate matter (PM) from gasoline vehicles' exhaust impacts health and urban air quality. Recent studies of PM formation from Euro 6 compliant cars did not include a Gasoline Particle Filter (GPF). As the GPF has become mandatory to remove PM it is critical to understand the fate of the remaining gas phase emissions after atmospheric oxidation. In this study, emissions of a GPF equipped Euro 6 car were aged in an oxidation flow reactor simulating atmospheric photochemistry processing. While primary PM emissions are below the detection limit, emission factors of secondary aerosols formed from organics, NH_3 and NO_x can reach 124 ± 5 mg kg^{-1} fuel. Furthermore, analysis of major organic precursors highlights the importance of the remaining vehicular emissions regarding their aerosol formation potential.

[a]*IEK-8 Troposhere, Forschungszentrum Jülich GmbH, Jülich, 52428, Germany. E-mail: an.paul@fz-juelich.de; t.hohaus@fz-juelich.de*

[b]*Department of Earth and Planetary Science, Weizmann Institute of Science, Rehovot, 7610001, Israel*

[c]*Group of Comprehensive Molecular Analytics, Helmholtz Zentrum München, Neuherberg, 85764, Germany*

[d]*Department of Technical and Analytical Chemistry, University of Rostock, Rostock, 18051, Germany*

[e]*Department of Environmental and Biological Science, University of Eastern Finland, Kuopio, 70210, Finland*

[f]*Department of Environmental Science, University of Basel, Basel, 4056, Switzerland*

[g]*Department of Chemistry, University of Eastern Finland, Joensuu, 80101, Finland*

† Electronic supplementary information (ESI) available. See DOI: https://doi.org/10.1039/d3ea00165b

‡ Astrid Kiendler-Scharr passed away on February 6th, 2023.

Introduction

Atmospheric aerosol has been ranked as the top global environmental health risk[1] having an estimated impact on life expectancy of up to 2.9 years lost on a global scale.[2,3] A clear link between secondary organic aerosol (SOA) and cardiovascular and respiratory diseases has shown that secondary aerosols may be more impactful on human health than primary aerosols.[4] Furthermore, it has been shown that typical anthropogenic SOAs formed from aromatic precursors have a more adverse impact on lung cells.[5] Among others, combustion processes and traffic-related aerosol emissions have been identified as

particularly health-relevant sources of atmospheric aerosol.[6,7] Regulations for vehicle emissions are regularly updated based on new evidence for human health effects and climate impact. With the introduction of the Euro 6 emission standards by the European Union, the total particle number (PN) emitted per km (# km^{-1}) driven from a gasoline direct injection (GDI) vehicle has been limited to 6×10^{11} # km^{-1}. In contrast, the older Euro 5 regulations did not limit the PN per km but placed only an overall limit on the particle mass emitted (up to 4.5 mg km^{-1}), a regulation which still applies to the Euro 6d emission standard. To comply with new regulations, the gasoline particle filter (GPF) has been implemented as a standard exhaust aftertreatment technology for GDI vehicles. The GPF has proven to be efficient at reducing primary aerosol (PA), often achieving a filter efficiency of >90%.[8] Regulations on CO (1000 mg km^{-1}) and NO_x (60 mg km^{-1}) emissions resulted in the introduction of the three-way catalyst (TWC), intended to convert NO_x to N_2, and CO and non-methane hydrocarbons (NMHCs) to CO_2. Furthermore, current standards limit the emission of the total concentration of NMHCs to 68 mg km^{-1} and the total hydrocarbon (THC) emissions to 100 mg km^{-1}.

However, it has been shown that volatile organic compounds (VOCs), particularly single ring aromatics, emitted during driving or idling with a GDI vehicle form significant SOA when oxidized in the atmosphere.[9–12] Nordin *et al.* 2013 and Liu *et al.* 2015 found that 60–90% of SOA formation could be assigned to C6–C10 aromatics for Euro 1–Euro 4 compliant gasoline cars.[13,14] Whilst these are likely Port Fuel Injection (PFI) engines the composition of the gasoline is still comparable. Measurements of the exhaust from Euro 5 cars retrofitted with GPF showed similar results that 96.7% of the gas phase aromatics were composed of C6–C10 aromatics.[11] Roth *et al.* 2019 showed that retrofitting a GPF to a Euro 5 compliant car resulted in significantly reduced primary aerosol, however significant SOA formation was still an important contribution to the total particle mass measured. The GPF has additionally been found to reduce some SOA precursors and thus also SOA formation.[15–17] Furthermore, most studies have focused on dynamic driving cycles such as the L92 or the worldwide harmonized light vehicle test cycle (WLTC) and batch experiments to assess average emissions of a full cycle or cold start emissions. Additionally, emission of NH_3 is particularly important as it is known to enhance new particle formation and increase SOA yields, promoting further nucleation and growth of aerosol from vehicle exhaust.[18–23] Both SOA and NH_3 are currently unregulated although the proposed Euro 7 emission standards[24] aim to limit NH_3 emissions from gasoline vehicles to 20 mg km^{-1}.

Therefore, dedicated experiments are necessary to evaluate the fate of vehicle emissions of modern cars after release into the atmosphere and upon timescale of typical atmospheric aging processes. Various simulation chamber and oxidation flow reactor studies have investigated SOA formation by the oxidation of vehicle emission from older car models *via* reactions with hydroxyl radicals (OH) being the major chemical reaction in the troposphere.[11–16,23,25–29] However, the primary emissions and secondary aerosol formation potential from a Euro 6d personal GDI vehicle with both TWC and GPF as part of the original factory setup are not well known. Additionally, there are only a few experiments conducted on steady state driving from a warm engine start.[25] Therefore, it remains relevant to understand the emissions at different vehicle speeds and the impacts of atmospheric aging on these emissions.

Materials and methods

Emissions of a Euro 6d emission standard compliant Skoda Scala passenger vehicle (model year 2021, factory equipped with a GDI engine, a GPF, and a TWC) were measured. All detailed vehicle specifications are shown in Table S1.† The vehicle was fuelled with 95 E10 gasoline, consisting of 10% ethanol as the biofuel component and connected to a Rototest VPA-RX3 2WD chassis dynamometer, which enabled its operation under steady-state conditions. The duration of the test cycle was set to be in total 60 minutes, comprising of four 15 min long segments evenly distributed to idling, 50 km h^{-1}, 100 km h^{-1} and 80 km h^{-1}. The test cycle was repeated 16 times in 4 experiments, each experiment consisting of 4 uninterrupted consecutive test cycles. The initial test cycle in each experiment is not considered in the analysis of this paper as it represents a cold start of the engine. The remaining 12 warm test cycles have thus been analysed and subsequently averaged ($n = 12$). A detailed overview of the driving cycle is summarized in the supplement (Fig. S1, 2 and Table S2†). All vehicle speeds are equivalent to flat surface driving (Table S3†). For analysis of steady state driving conditions, the initial 5 minutes of driving time for each test cycle segment is excluded to ensure that there are no effects of (de-) accelerations on the steady state measurements.

The experimental setup is illustrated in Fig. 1. The vehicle exhaust pipe was connected to the diluters *via* a heated tubing, consistently heated to 120 °C. A portion of the exhaust flow was sampled and subsequently diluted using a combination of a porous tube diluter and an ejector diluter (DAS; Venacontra, Finland). The dilution process was carefully regulated by

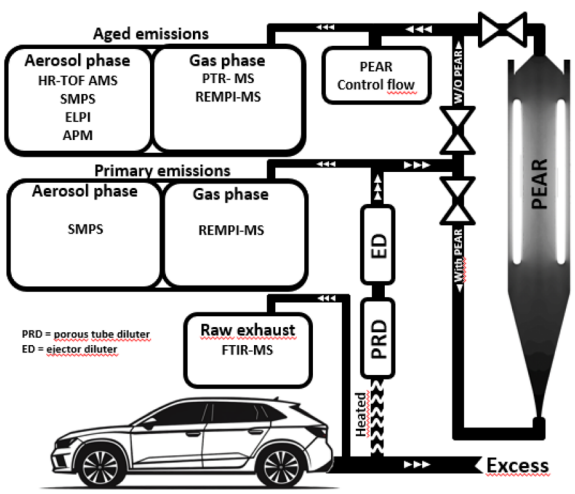

Fig. 1 The setup includes all instruments on the primary emission run without the PEAR, and aged emissions run with the PEAR.

adjusting the flow rate of the porous tube diluter, while maintaining a constant flow rate in the ejector diluter, to achieve a controlled dilution factor of 17. The dilution factor was defined based on the measured CO_2 concentrations before and after the dilution process. Primary gas phase emissions were measured directly at the exhaust with Fourier transform Infrared (FTIR) spectroscopy. The diluted exhaust was drawn into the Photochemical Emission Aging flow tube Reactor (PEAR), operated at a constant flow of 120 l min^{-1}. Based on this flow rate the transmission efficiency of aerosols is estimated to be above 70% for 20 nm aerosols and above 90% above 40 nm.[30] Furthermore, the total dilution in the PEAR was 1 : 18 in relation to the exhaust. Aerosols were measured before (primary emissions) and after the PEAR (aged emissions). Background measurements were preformed prior to each experiment ensuring that no significant aerosol formation (<0.5 μg m^{-3}) occurred in the PEAR. At the entrance of the PEAR, water vapor was added to reach a minimum relative humidity of 40%, which varied between 40% and approximately 65% depending on the driving conditions. OH-radicals were generated inside the PEAR by ozone (7 ppm) and photolysis at 254 nm. The formed singlet oxygen ($O(^1D)$) reacts with water vapor, producing OH radicals which initiates oxidation in the PEAR. Furthermore, some ozonolysis occurs in the PEAR due to the ozone concentration. A proton-transfer-reaction mass spectrometer (PTR-MS-8000; Ionicon, Austria) was used to measure VOCs from the outlet of the PEAR with time resolution of 10 s. The PTR-MS operated in H_3O^+ mode, and an E/N ratio of 137 was reached. 1,3-Diiodobenzene was used as an internal standard for mass calibration, and the mass resolution was ~5000 at m/z 59. The equivalent photochemical age was determined to be on average 3.3 days based on the principle of the "photochemical clock".[31] About 65 ppb of isotope-labelled *N*-butanol (d9-BuOH, 98%, Cambridge Isotope Laboratories) was added to the primary emissions. The decay of d9-BuOH measured by PTR-MS was used to calculate the photochemical age. This calculation is based on a known rate constant of d9-BuOH with OH ($k_{\text{butanol-d9}}$ = 3.4(±0.88) × 10^{-12} cm^3 per molecule per s),[32] assuming an ambient concentration of OH radicals of 1.5 × 10^6 cm^{-3}.[33] To evaluate the relevance of the aging process in the PEAR compared to typical ambient conditions, the oxidation conditions in the OFR were modelled following the approach by Peng *et al.* 2019.[34–38] Due to high concentrations of VOCs, NO and other trace gases in the exhaust, the total external OH reactivity ($OHR_{ext} = \sum k_x c_x$ where c_x is the concentration of an OH-consuming species, x, and k_x the rate constant between x and OH) is high compared to the photolysis rate. This results in conditions in the PEAR that are still reasonably close to ambient oxidation processes but might have contributions from photolysis at 254 nm that are significant (>15%) during idling and 50 km h^{-1} (Table S8†). These conditions are classified as "risky" for typical OFR oxidation processes (details, ESI Tables S4–7†). SO_2 was used as a surrogate for NMHC.[38] Additionally during driving CO emissions cause additional formation of HO_2. Thus, the RO_2 fate pathway during idling, 80 km h^{-1} and 100 km h^{-1} was primarily the HO_2–RO_2 reaction (>80%). Only during the 50 km h^{-1} segment due to high NO emissions did the RO_2 fate pathway change as a significant fraction of the RO_2 reacted with NO (18.1%) with RO_2–OH (68.5%) and RO_2–HO_2 (12.6%) (Table S7†).

Furthermore, the age of the experiment was modelled assuming an OH exposure of 1.5 × 10^6 cm^{-3},[33] the harmonic mean age of the experiment is found to be 1.5 days in comparison to the measured age of 2.2 days, thus the model is a reasonable comparison to the measured age. The idling phase is overestimated in terms of OH exposure, however, calculating an average age of the idling segment is not ideal due to the large dynamic changes that occur during this period, and the measured age varies from 0.5 days (last 5 min) to 5.7 days (first 10 min). Additionally, the model consistently underestimates the exposure at all other driving speeds. Notably, the modelled age is calculated on an $n = 12$ basis and the measured age from an $n = 1$ experiment thus some deviation should be expected (Table S9†).

A resonance-enhanced multi-photon ionization mass spectrometer (REMPI-MS)[39] was alternatingly measuring before and after the PEAR using an 8-port-2-way-valve (VICI; Switzerland) to monitor the changes in aromatic concentrations after aging with 1 minute time resolution. Isotopically labelled toluene (d3-toluene, isotopic purity of 98%; Cambridge Isotope Inc.) was added as an internal standard for quantification.[40] Quantification of aromatic VOC was based on photoionization cross-sections determined by Gehm *et al.* 2018.[41] The aerosol size distributions were measured with a scanning mobility particle sizer (SMPS). Aerosol effective densities were determined using an Aerosol Particle Mass analyser (APM) combined with an SMPS as described by Leskinen *et al.* (2014).[42] The aerosol composition was determined using a High-Resolution Time of Flight Aerosol Mass Spectrometer (HR-ToF AMS). The AMS was operated on an additional 1 : 10 dilution using a similar dilution method to that described above. The AMS gas phase CO_2 was corrected according to CO_2 measurements using a Vaisala CO_2 sensor, measuring directly at the AMS inlet. The PM1 aerosol mass concentrations were separated into organics (org), NH_4, NO_3 and SO_4 using the AMS. Additionally, the AMS was used to determine the elemental composition in terms of the ratio of oxygen to carbon (O : C) and hydrogen to carbon (H : C). The HR-TOF-AMS is limited in aerosol size range, ~50–~600 nm as a result of the aerodynamic lens,[43] the composition of the aerosols is assumed to remain the same regardless of size and the total compositional mass is thus determined using eqn (1)

$$m_x = m \times \frac{x}{\text{org} + \text{NO}_3 + \text{NH}_4 + \text{SO}_4} \quad (1)$$

where m_x is the total aerosol mass of species x. Org, NO_3, NH_4, and SO_4 are the mass of the respective species determined by the AMS, x is equal to one of four species. m is the total aerosol mass determined by the SMPS, assuming a density of 1.6 g cm^{-3} determined by APM.

Secondary Organic Carbon (SOC) was calculated based on m_x and the organic matter to organic carbon ratio (OM/OC).

$$\text{SOC} = \frac{m_{\text{org}}}{\text{OM/OC}} \quad (2)$$

The potential SOC mass of compound x ($SOCP_x$) is calculated based on the losses of aromatic gas phase compounds measured by REMPI-MS.

$$SOCP_x = \Delta X \times \frac{C_x}{M_x} \quad (3)$$

where ΔX is the difference in concentration in mg m^{-3} of compound X before and after aging in the PEAR and C_x is the ratio of carbon weight to the molecular weight M_x of compound X.

Emission factor calculation

The emission factor (EF) is calculated to represent the PM emitted and SOA formed as mg per distance driven (mg km^{-1}) or mg per kg fuel consumed (mg kg^{-1}). The fuel consumption and distance driven were tracked online by the vehicle on-board diagnostics and the dynamometer, respectively. Emission factors were then calculated as in eqn (4).

$$EF = \frac{C \times Q_{dry}}{F} \quad (4)$$

where EF is the emission factor, C is the concentration in milligrams per cubic meter, Q_{dry} is the volume of the dry exhaust from the car in cubic meters per second and F is either the fuel consumption in kg per second or the distance driven in kilometres per second (S1.1†).

Results and discussion

In the primary emissions, aerosol number concentrations (electrical mobility diameter >10 nm) appeared close to the limit of detection throughout the driving cycle, an expected effect from the GPF (Fig. 2A). Therefore, there is a distinct improvement in primary aerosol emission reduction compared to previous studies on Euro 6 cars[44] and especially an improvement compared to Euro 5 primary emissions[11,25,45] without GPF. One other study has reported comparable reductions by retrofitting a modern GPF to a Euro 5 compliant GDI vehicle.[16]

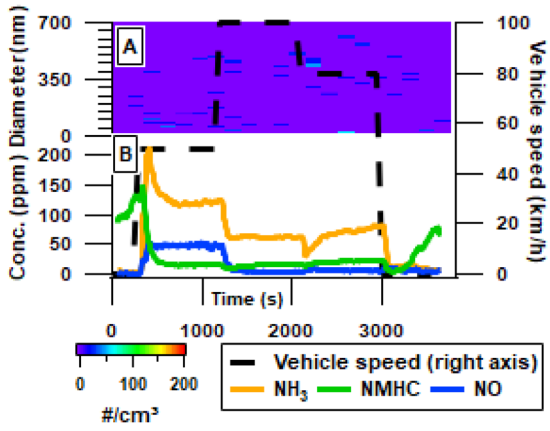

Fig. 2 Time resolved fresh emissions of number concentration measured by SMPS (A), and gas phase emissions measured by FTIR in ppm (B). Concentrations are provided at tailpipe levels.

However, it has been shown that GDI vehicles with no GPF emit primary aerosols in the 3–10 nm diameter range,[44] such nanoparticles are however outside the accessible measurement range of the used SMPS. In contrast to the reduction of aerosols, inorganic and organic gases were detected with dynamic concentrations throughout the driving cycle (Fig. 2B). During warm idling, emissions are dominated by NMHC, and these emissions reach maximum at the initial acceleration from idling to 50 km h^{-1}. This coincides with a sharp rise of NH_3, which had a concentration of 4.1 ± 0.6 ppm during idling. Emissions of NMHC remained relatively stable during the driving phase and varied only between 10 and 25 ppm upon acceleration or deceleration. Throughout the driving phase NH_3 remains the largest emission, disregarding CO and CO_2. High NH_3 emissions are a direct result of the TWC, and forms due to the H_2 produced in the CO to CO_2 reaction. The higher H_2 concentration thus interferes in the catalytic reaction intended to convert NO_x to N_2 and instead forms NH_3. This increase in NH_3 was reported to be up to 72 times the NH_3 emissions without the TWC.[19] At speeds of 100 km h^{-1} and 80 km h^{-1} only low amounts of NO (5.3 ± 1.2 ppm) were detected indicating efficient removal of NO during these speeds. However, at a speed of 50 km h^{-1}, a significant amount of NO (47.1 ± 3.1 ppm) is not converted to N_2 or NH_3. Particularly at speed 50 km h^{-1} the NO concentrations exceed the level of NMHC, changing the oxidation pathways and composition of the aerosol significantly.

Fig. 3A illustrates the 3 largest VOC groups as measured by PTR-MS, with benzene emitted at comparable levels to all other

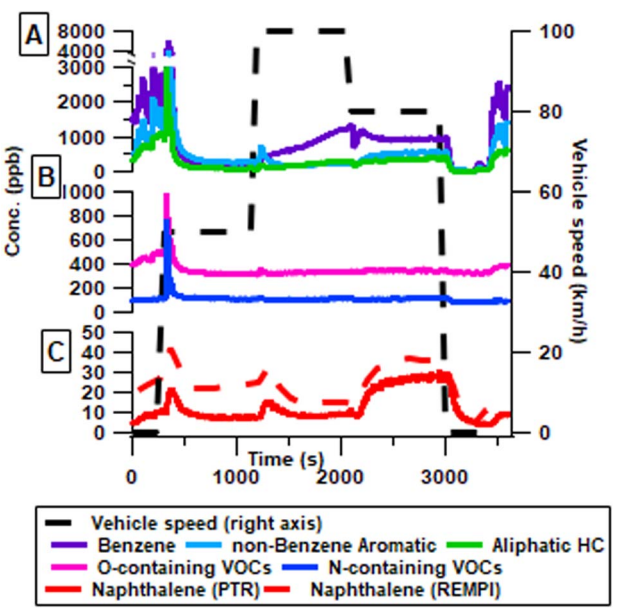

Fig. 3 VOC concentrations measured with PTR (solid lines) over the average driving cycle (N = 9) for primary emissions at tail pipe concentrations. (A) shows benzene, non-benzene aromatic and the combined aliphatic hydrocarbon. (B) shows both oxygen containing VOCs and nitrogen containing VOCs. (C) shows the time series of the aromatic compound naphthalene as measured with both, PTR and REMPI (n = 12).

aromatics combined. However, during 100 and 80 km h^{-1} the benzene emissions are the highest contribution to the total VOC. Aliphatic hydrocarbon (HC) is at a similar level to the non-benzene aromatic, throughout the driving cycle. The non-benzene aromatics consist of toluene, o-/m-/p-xylene or ethylbenzene, C3-benzenes, C4-benzenes, naphthalene, styrene and methyl styrene primarily, this is similar to the composition found in previous papers that reported these compounds plus benzene as 96.7% of total aromatic hydrocarbon and 69.5% of total non-methane organic carbon.[11] Previous papers have reported significant gas phase poly aromatic hydrocarbons (PAHs) with offline instrumentation, however no 3+ ringed PAHs were observed in this study with online instrumentation.[15,29] The main peak for all major groups is found during acceleration to 50 km h^{-1} after 15 min of idling. As idling starts after driving a drop in all VOCs occurs for 5 minutes after which there is a rapid increase in all major components. The same trends are significant for oxygen containing and nitrogen containing VOCs (Fig. 3B). The sudden and sharp rise in aromatic and aliphatic HC stands in contrast to the more gradual increase of NMHCs starting after only 2 minutes. This could indicate that some smaller non-polar compounds which are not detectable by the PTR-MS are emitted from the car earlier than the larger compounds potentially because of the cooling of the engine. Independent measurements of VOCs with aromatic functionalities by REMPI-ToF-MS and PTR-ToF-MS showed similar trends (exemplarily shown for naphthalene in Fig. 3C); REMPI-TOFMS consistently measured higher concentration than the PTR-MS, which may be related to the uncertainty of the photoionization cross-section.[41] Furthermore, analysis of aromatics was performed with the REMPI-MS as it alternated between measuring fresh emissions and aged emissions.

Formation of secondary aerosol

Substantial aerosol formation was observed after oxidation by OH of the exhaust emission equivalent to 2.2 days, assuming an ambient OH concentration of 10^6 cm^{-3} (Fig. 4A). The secondary aerosol had an electrical mobility diameter below 100 nm, with a geometric mean diameter of 36 ± 3 nm, a mass geometric mean of 88 ± 9 nm, and a driving condition-dependent size distribution, which showed the largest size mode during acceleration from idling to 50 km h^{-1}. The mass concentration for aerosols below 100 nm was determined by incorporating the aerosol density of 1.6 ± 0.1 g cm^{-3} derived from APM measurements (Fig. 4B). The highest short-term concentrations occur during accelerations and the highest stable concentrations are observed at 50 km h^{-1}. The total concentrations of secondary aerosol formed during 80 and 100 km h^{-1} remain stable. In order to predict if SOA is formed from unburned fuel or incomplete combustion the SOA/CO ratio can be used, as CO is only formed in incomplete combustion. Thus a high SOA/CO ratio would indicate that SOA formation occurs as a result of unburned fuel, whereas a low SOA/CO indicates that the SOA formed is associated with incomplete combustion. The SOA/CO ratio (Fig. 4B) shows a significant change throughout all driving speeds, with idling SOA/CO reaching 729 μg ppm^{-1}, indicating that the SOA is formed primarily from unburned fuel. At increasing speed the SOA/CO ratio decreases suggesting a transition to incomplete combustion away from unburned fuel. This aligns well with the observations made in the literature.[17]

Throughout the driving phase the O : C and H : C remained stable between 0.93–1.03 ± 0.02 and 0.99–1.08 ± 0.01 respectively. The highest O : C ratio was found during 100 km h^{-1} and the lowest during 50 km h^{-1}, inverse for H : C (Table S10†). These changes suggest a stable oxidation process during the steady state driving. However, the composition of the aerosol changes between 100 km h^{-1} and 80 km h^{-1} as the OM to NO_3 ratio changes from 1.85 ± 0.7 to 3.38 ± 0.06 (Fig. 4B). Maximum concentrations of organic aerosol and nitrate can be measured during accelerations, particularly going from idling to 50 km h^{-1}, resulting in a primarily large increase in the organic aerosol concentration, fitting to gas phase analysis previously discussed regarding the primary emissions. At the onset of warm idling after driving 80 km h^{-1}, the aerosol concentration decreases, and the composition changes from organic-rich (Org : NO_3 3.38 ± 0.06) to nitrate-rich aerosol (Org : NO_3 0.23 ± 0.03). This period of low SOA formation coincided with low NHMC emissions of less than 10 ppm for approximately 3 minutes (Fig. 2B). Thus, idling at, *e.g.*, red lights or short idling in general traffic are typical periods with low organic aerosol formation. However, inorganic SA formation is increased during warm idling. For idling times longer than 3 minutes, however, NMHC emissions significantly increased resulting in enhanced SOA formation which may be a consequence of the enhanced release of alkanes from lubrication oil.[46,47] After 5 to 6 minutes of idling, the aerosol composition turns organic-rich (org : NO_3 > 10), which agrees with higher HC emissions than NO emissions in a previous study on idling emissions from gasoline cars.[48] The nitrate concentration throughout the driving cycle follows the trend of NH_4 with an average ratio of 2.5 ± 0.3, suggesting that nucleation of ammonium nitrate (AN) is limited by the concentration of NO_3, and therefore that most aerosol phase NO_3 is AN bound. The relatively high concentrations of NH_3 remain unaffected after exposure to OH and O_3, while the concentration of aerosol phase nitrate increased by the oxidation of NO and NO_2. This follows the expected reaction pathway of $NO_2 + OH \rightarrow HNO_3$ which reacts rapidly with NH_3 to form NH_4NO_3(s). As NH_3 is available in large quantities the conversion of NO_x to HNO_3 is the limiting factor in this experiment. The secondary production of AN during driving enhances aerosol formation, observed in this experiment as it provides a condensation sink and overcomes the nucleation boundary for oxidized organic vapours, allowing for condensable gas phase oxidation products to partition to the aerosol phase.

Secondary aerosol precursors

SOC was calculated using eqn (2) and compared with potential SOC formed from aromatics measured by REMPI according to eqn (3) (Fig. 5). Determination of SOC was used alternatively to SOA as calculating SOA formation from the initial VOCs requires accurate knowledge of the individual SOA yields, for

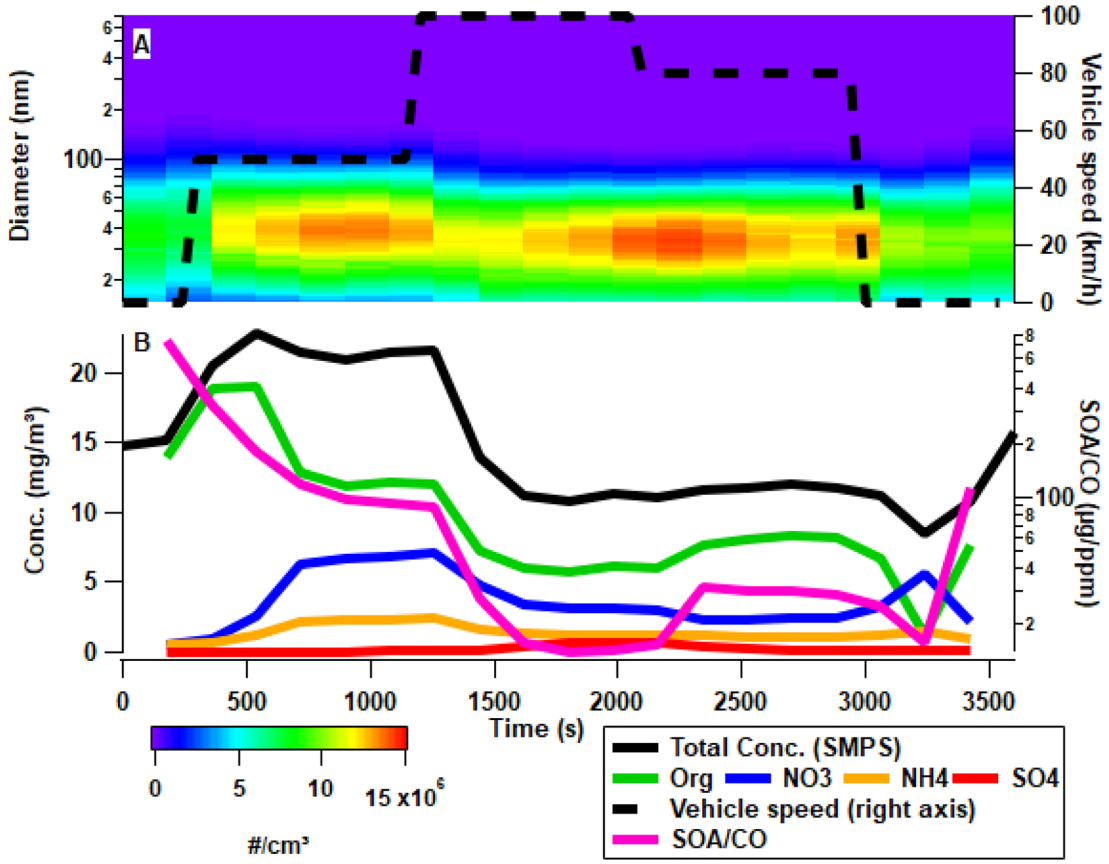

Fig. 4 The vehicle speed is shown on the right axis and illustrates the driving conditions. (A) Average ($n = 12$) aerosol number concentration at the tailpipe. (B) Average ($n = 12$) aerosol mass concentration at the tailpipe derived from SMPS assuming a density of 1.6 g cm^{-3} and the secondary organic aerosol measured by AMS.

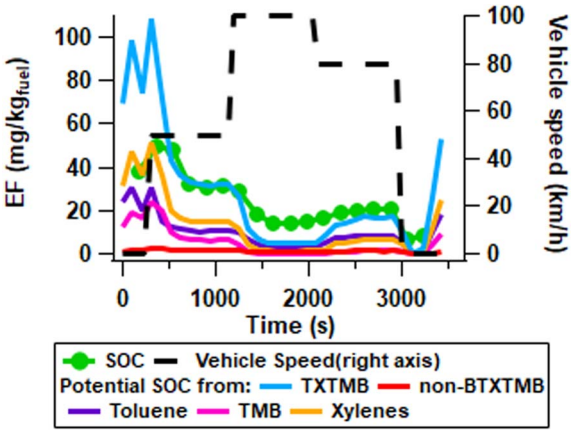

Fig. 5 Secondary organic carbon (SOC) as calculated in eqn (2) and converted to mg aerosol per kg fuel, compared with potential SOC mass derived from measured aromatics by REMPI and eqn (3). Toluene, xylene and trimethyl-benzene (TXTMB) are the most important sources of SOC covering 99% of the total aromatic SOC potential ($n = 12$).

each precursor and mixtures thereof. Due to the high VOC concentrations in the PEAR and high NH_3 conditions, which potentially increases the SOA yield, literature SOA yields would likely underestimate the SOA mass formed.[11,20,49,50] The SOC potential indicates the highest possible SOC that could be formed based on the total conversion of lost aromatic carbon mass from the gas phase to the aerosol phase. Among all aromatic VOCs 99% of the total aromatic SOC potential results only from toluene, xylene and trimethyl-benzene (TXTMB). TXTMB follows the SOA/CO ratio displayed in Fig. 4B. This implies that unburned fuel dominates SOA formation at lower vehicle speeds, however at 100 km h^{-1} the SOA formation is driven by incomplete combustion. It should be noted that during incomplete combustion aromatic formation can occur in the engine as a result of pyrosynthesis.[51] PTR-MS was analysed, and the main components were found to be propyne and butene (Table S12†). However, with emissions <9 mg kg^{-1}, and low SOA yields, these compounds' expected SOA formation contribution are considered low. FTIR measured emissions of hexane and pentane above 490 mg kg^{-1} during idling (Table S13†). The highest emission of a single aliphatic NMHC was hexane, regardless of vehicular speed. Due to the concentrations in the PEAR, hexane could be a significant SOA precursor. Previous papers have reported similarly that TXTMB account for the majority of reacted aromatics.[11] During idling the SOC potential from TXTMB was found to be much higher than the SOC formed. This loss of carbon is expected as the potential

assumes a conversion of unity from the gas phase to the aerosol, whilst the SOA yield likely is higher in the PEAR than would be expected in the atmosphere due to higher concentrations of organics and AN particle formation during driving. Additionally, there are losses by photolysis at 254 nm (Table S8†), further there is no AN formation during idling which likely decreases the amount of VOCs that partition to the particle phase through oxidation. During 50 and 80 km h^{-1}, the levels of potential SOC from TXTMB and the measured SOC are comparable. However, there are likely other sources that contribute to the SOC formation. This is evident in the 100 km h^{-1} driving phase where the TXTMB SOC potential is only sufficient to explain 50% of the formed SOC. Other notable aromatics that may affect SOC formation can be naphthalene and benzene. Whilst naphthalene concentration was reduced after aging as would be expected from its high SOA yield[52] the concentrations are too low to have significant impact on the potential SOC formation. In contrast, benzene was the most abundant aromatic compound in the exhaust. However, there is no observed reduction in benzene concentration as a result of aging in the PEAR, due to its slow reaction rate with OH ($k(298\ \mathrm{K}) = 1.22 \times 10^{-12}$ cm^3 per molecule per s).[53] Similarly very low reduction in benzene at a low atmospheric age was observed by Pieber *et al.* 2018.[11] TMB was observed to impact the potential SOC primarily during idling and 50 km h^{-1} where it accounts for 19–30%, whereas during the 80 and 100 km h^{-1} driving conditions the contribution was between 4 and 10% of the potential TXTMB SOC. This trend is comparable to that of xylene which is the main source of potential aromatic SOC during idling and 50 km h^{-1} accounting for 45–50% of the potential SOC from TXTMB. This decreased to 15–40% during 80 and 100 km h^{-1}, at these driving speeds toluene accounts for up to 80% of the total aromatic potential SOC. These results indicate that as driving speeds increase the share of aromatic SOC from toluene increases, as well. However, the importance of aromatics on SOC decreases as driving speed increases, suggesting that SOC formed from other sources such as long chained alkanes or polyaromatic hydrocarbons is more important at higher driving speeds. Yang *et al.* 2018 suggested that there should still be significant PAHs in the gas-phase though it was found that the GPF reduced the PAH emissions.[15]

However, with the online instrumentation used in this experiment, it was not possible to observe any significant concentration of long chained alkanes or PAHs.

Emission factors

To compare the emissions observed with previous studies and emission standard limits, emission factors (EFs) are calculated based on eqn (4). The average aerosol EFs (Fig. 6) refer to steady state driving defined as the condition reached after cruising at a speed for more than 5 minutes, which was chosen to avoid the influence of accelerations (Fig. 4B). Secondary organic aerosol mass per kilogram fuel decreased with increasing vehicle speed (Fig. 6), which suggests an increased engine combustion or TWC conversion efficiency at higher driving speeds within the range of 50 to 100 km h^{-1}. Under faster steady state driving

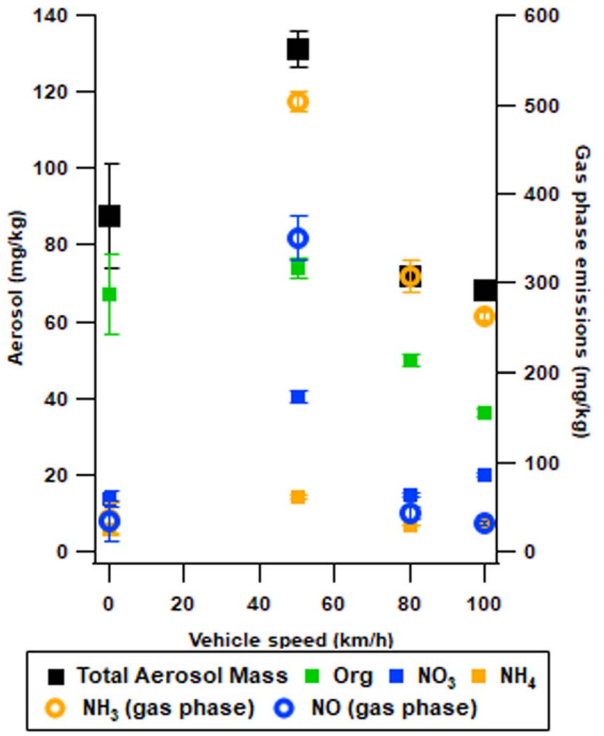

Fig. 6 Emission factors in mg per kg fuel. Squares illustrate the particle phase, circles the gas phase constituents. Each point is the average value for each speed measured for 10 min of each driving cycle ($n = 12$) and error bars are the standard deviation.

conditions, which are more relevant for highway cruising emissions, the observed trend between speed and EFs may change. Furthermore, slower driving conditions such as residential zone driving should not be directly compared with steady state driving. The total aerosol mass formed is highest at 50 km h^{-1} reaching 131 ± 5 mg kg^{-1}, compared to 68 ± 1 mg kg^{-1} and 72 ± 2 mg kg^{-1} for speeds of 100 and 80 km h^{-1}, respectively. However, at a speed of 100 km h^{-1}, SOA formation accounted for 36 ± 1 mg kg^{-1}, that is, 54% of the total aerosol mass, in comparison to 50 ± 1 mg kg^{-1}, that is, 69% of the total aerosol mass, at a speed of 80 km h^{-1}. Moreover, gas phase NH_3 and NO emissions are the highest at 50 km h^{-1}, but lowest when driving 100 km h^{-1}. For EFs of secondary nitrate, the trend with speed differs from SOA as it slightly increases at 100 km h^{-1}. It is worth noting that the formation of AN aerosol might function as an effective seed particle for the organics to condense on increasing the SOA yield when AN is high.

Roth *et al.* 2019 found a similar composition of the aerosol with a Euro 5 retrofitted with a GPF, with SOA forming roughly 50% of the secondary aerosol mass and ammonium nitrate forming the remaining 50% of the total secondary aerosol.[16] Pieber *et al.* 2018 (ref. 11) with retrofitted GPF on Euro 5 found that in SOA and nitrate SA was similar in concentrations and thus that SOA accounted for less than 50% of total SOA when operating in a smog chamber. However, in an OFR similar levels were observed at low atmospheric ages with SOA accounting for roughly 50% of total SA, with the share of SOA increasing with

increasing atmospheric age.[11] Zhang *et al.* 2023 reported lower SOA formation from China VI cars at cruising speeds between 30 and 60 km h^{-1}, however they saw a significant increase in SOA as speeds increased beyond 60 km h^{-1}. Additionally, the idling SOA formation is comparable between China VI and Euro 6d.[17]

These results are comparable despite the clear differences in driving cycle with cold started LA92 and WLTC used by Roth *et al.* 2019 [16] and Pieber *et al.* 2018 [11] respectively compared to the hot start steady state driving presented in this study and Zhang *et al.* 2023.[17]

Emission standards for cars, such as the Euro 6, are given in mg per km driven. The Euro 6 limits particulate matter to 4.5 mg km^{-1}. With the introduction of the GPF emission of primary aerosols is well below this limit. However, there is still significant aerosol formation after aging, during 50 km h^{-1} secondary aerosols reach 5.1 mg km^{-1} during the steady state (Table S4†).

Generally, more dynamic driving in the real world and more dynamic driving cycles, such as WLTP, may lead to higher emissions of SOA precursors,[44] hence the results denote a lower limit. Furthermore, NH_3 enhances SOA yields and new particle formation under high concentrations,[20,25] and thus introducing cars with increased NH_3 emissions to urban centres would enhance particle nucleation and thus the formation of secondary ultrafine particles, although the high surface area of condensation sinks in an urban environment.[54] Moreover, NH_3 can further react with additional species nucleating into the aerosol for SOA from other sources as well.[55] It is well known that idling conditions have large emissions of organics,[25] which may form large amounts of SOA. In this study, the mass of SOA formed was lower during idling than at a speed of 50 km h^{-1}. This is likely linked to the NO emissions, during 50 km h^{-1} forming AN particles. The AN particles function as seed particles for organic compounds allowing condensation of organic matter. Thus, the SOA from idling might be underestimated due to low AN formation during this phase.

Conclusions

The results demonstrate the efficiency of the GPF, reducing primary aerosol mass to close to zero. However, the removal of primary aerosol does not limit the formation of secondary aerosol from the remaining VOCs in the exhaust of gasoline cars. Particularly, aromatic VOCs, TXTMB, originating either from unburned fuel or pyro synthesis *via* radical reactions, and NO_x are potent precursors of secondary aerosols. Once released to the atmosphere, oxidative gas-to-particle photochemical conversion leads to SOA and secondary nitrate formation. The observed SOA formation cannot be completely explained by the TXTMB and thus an additional VOC precursor must exist. However, PTR-MS and FTIR-MS were unable to identify species that would give closure to the SOA formation. Only during idling could the TXTMB account for the total observed SOA, this further suggests that these compounds are linked to unburned fuel. Moreover, gasoline cars equipped with a TWC may be a significant source of NH_3. Furthermore, with the incomplete conversion of NO_x emissions in the TWC along with the high NH_3 emissions, the TWC equipped cars also become a source of secondary inorganic aerosol due to the production of ammonium nitrates in the atmosphere. Therefore, attempts to reduce aromatic VOC, NO_x and NH_3 are most promising to further reduce tailpipe emissions from gasoline cars which lead to significant secondary aerosol formation.

Current regulation standards in the European union, Euro 6d, have no restrictions for aromatic VOCs or NH_3. Even though the aromatic VOCs are indirectly restricted through total NMHCs, it could be possible to reduce NMHC without affecting the SOA formation as the composition of the NMHC has a significant impact on SOA formation. The proposed Euro 7 would restrict NH_3 emissions, and thus the implementation of such legislation would likely improve air quality.

Author contributions

Andreas Paul: conceptualization, investigation, formal analysis, methodology, visualization, and writing – original draft. Zheng Fang: investigation, and writing – review & editing. Patrick Martens: investigation, and writing – review & editing. Arya Mukherjee: investigation, and writing – review & editing. Gert Jakobi: investigation and methodology. Mika Ihalainen: investigation, methodology and writing – original draft. Miika Kortelainen: investigation. Markus Somero: investigation. Pasi Yli-Pirilä: investigation. Thorsten Hohaus: conceptualization, supervision, and writing – review & editing. Hendryk Czech: conceptualization, investigation, project administration, supervision, and writing – review & editing. Markus Kalberer: resources, supervision, and writing – review & editing. Olli Sippula: funding acquisition, project administration, resources, supervision, and writing – review & editing. Yinon Rudich: funding acquisition, resources, supervision, and writing – review & editing. Ralf Zimmermann: funding acquisition, resources, supervision, and writing – review & editing. Astrid Kiendler-Scharr: funding acquisition, and supervision.

Conflicts of interest

There are no conflicts to declare.

Acknowledgements

We thank the Helmholtz International Laboratory AeroHEALTH (InterLabs-0005; **https://aerohealth.eu**) and the ULTRHAS Horizon Europe project (agreement 955390) for supporting this work.

References

1 O. World Health, *Ambient Air Pollution: A Global Assessment of Exposure and Burden of Disease*, World Health Organization, Geneva, 2016.
2 J. Lelieveld, A. Pozzer, U. Pöschl, M. Fnais, A. Haines and T. Münzel, Loss of life expectancy from air pollution

compared to other risk factors: a worldwide perspective, *Cardiovasc. Res.*, 2020, **116**(11), 1910–1917.

3 C. J. L. Murray, Global burden of 87 risk factors in 204 countries and territories, 1990–2019: a systematic analysis for the Global Burden of Disease Study 2019, *Lancet*, 2020, **396**(10258), 1223–1249.

4 H. O. T. Pye, C. K. Ward-Caviness, B. N. Murphy, K. W. Appel and K. M. Seltzer, Secondary organic aerosol association with cardiorespiratory disease mortality in the United States, *Nat. Commun.*, 2021, **12**(1), 7215.

5 S. Offer, E. Hartner, S. Di Bucchianico, C. Bisig, S. Bauer, J. Pantzke, J. Zimmermann Elias, X. Cao, S. Binder, E. Kuhn, A. Huber, S. Jeong, U. Käfer, P. Martens, A. Mesceriakovas, J. Bendl, R. Brejcha, A. Buchholz, D. Gat, T. Hohaus, N. Rastak, G. Jakobi, M. Kalberer, T. Kanashova, Y. Hu, C. Ogris, A. Marsico, F. Theis, M. Pardo, T. Gröger, S. Oeder, J. Orasche, A. Paul, T. Ziehm, Z.-H. Zhang, T. Adam, O. Sippula, M. Sklorz, J. Schnelle-Kreis, H. Czech, A. Kiendler-Scharr, Y. Rudich and R. Zimmermann, Effect of Atmospheric Aging on Soot Particle Toxicity in Lung Cell Models at the Air–Liquid Interface: Differential Toxicological Impacts of Biogenic and Anthropogenic Secondary Organic Aerosols (SOAs), *Environ. Health Perspect.*, 2022, **130**(2), 027003.

6 S. Edwards, G. Zhao, J. Tran, K. T. Patten, A. Valenzuela, C. Wallis, K. J. Bein, A. S. Wexler, P. J. Lein and X. Rao, Pathological Cardiopulmonary Evaluation of Rats Chronically Exposed to Traffic-Related Air Pollution, *Environ. Health Perspect.*, 2020, **128**(12), 127003.

7 J. A. Holme, B. C. Brinchmann, M. Refsnes, M. Låg and J. Øvrevik, Potential role of polycyclic aromatic hydrocarbons as mediators of cardiovascular effects from combustion particles, *Environ. Health*, 2019, **18**(1), 74.

8 A. Joshi and T. V. Johnson, Gasoline Particulate Filters—a Review, *Emiss. Control Sci. Technol.*, 2018, **4**(4), 219–239.

9 D. R. Gentner, S. H. Jathar, T. D. Gordon, R. Bahreini, D. A. Day, I. El Haddad, P. L. Hayes, S. M. Pieber, S. M. Platt, J. de Gouw, A. H. Goldstein, R. A. Harley, J. L. Jimenez, A. S. H. Prévôt and A. L. Robinson, Review of Urban Secondary Organic Aerosol Formation from Gasoline and Diesel Motor Vehicle Emissions, *Environ. Sci. Technol.*, 2017, **51**(3), 1074–1093.

10 Y. Morino, Y. Li, Y. Fujitani, K. Sato, S. Inomata, K. Tanabe, S. H. Jathar, Y. Kondo, T. Nakayama, A. Fushimi, A. Takami and S. Kobayashi, Secondary organic aerosol formation from gasoline and diesel vehicle exhaust under light and dark conditions, *Environ. Sci.: Atmos.*, 2022, **2**(1), 46–64.

11 S. M. Pieber, N. K. Kumar, F. Klein, P. Comte, D. Bhattu, J. Dommen, E. A. Bruns, D. Kılıç, I. El Haddad, A. Keller, J. Czerwinski, N. Heeb, U. Baltensperger, J. G. Slowik and A. S. H. Prévôt, Gas-phase composition and secondary organic aerosol formation from standard and particle filter-retrofitted gasoline direct injection vehicles investigated in a batch and flow reactor, *Atmos. Chem. Phys.*, 2018, **18**(13), 9929–9954.

12 Y. Zhao, A. T. Lambe, R. Saleh, G. Saliba and A. L. Robinson, Secondary Organic Aerosol Production from Gasoline Vehicle Exhaust: Effects of Engine Technology, Cold Start, and Emission Certification Standard, *Environ. Sci. Technol.*, 2018, **52**(3), 1253–1261.

13 E. Z. Nordin, A. C. Eriksson, P. Roldin, P. T. Nilsson, J. E. Carlsson, M. K. Kajos, H. Hellén, C. Wittbom, J. Rissler, J. Löndahl, E. Swietlicki, B. Svenningsson, M. Bohgard, M. Kulmala, M. Hallquist and J. H. Pagels, Secondary organic aerosol formation from idling gasoline passenger vehicle emissions investigated in a smog chamber, *Atmos. Chem. Phys.*, 2013, **13**(12), 6101–6116.

14 T. Liu, X. Wang, W. Deng, Q. Hu, X. Ding, Y. Zhang, Q. He, Z. Zhang, S. Lü, X. Bi, J. Chen and J. Yu, Secondary organic aerosol formation from photochemical aging of light-duty gasoline vehicle exhausts in a smog chamber, *Atmos. Chem. Phys.*, 2015, **15**(15), 9049–9062.

15 J. Yang, P. Roth, T. D. Durbin, K. C. Johnson, D. R. Cocker III, A. Asa-Awuku, R. Brezny, M. Geller and G. Karavalakis, Gasoline Particulate Filters as an Effective Tool to Reduce Particulate and Polycyclic Aromatic Hydrocarbon Emissions from Gasoline Direct Injection (GDI) Vehicles: A Case Study with Two GDI Vehicles, *Environ. Sci. Technol.*, 2018, **52**(5), 3275–3284.

16 P. Roth, J. Yang, E. Fofie, D. R. Cocker III, T. D. Durbin, R. Brezny, M. Geller, A. Asa-Awuku and G. Karavalakis, Catalyzed Gasoline Particulate Filters Reduce Secondary Organic Aerosol Production from Gasoline Direct Injection Vehicles, *Environ. Sci. Technol.*, 2019, **53**(6), 3037–3047.

17 J. Zhang, J. Peng, A. Song, Z. Lv, H. Tong, Z. Du, J. Guo, L. Wu, T. Wang, M. Hallquist and H. Mao, Marked impacts of transient conditions on potential secondary organic aerosol production during rapid oxidation of gasoline exhausts, *npj Clim. Atmos. Sci.*, 2023, **6**(1), 59.

18 P. K. Hopke and X. Querol, Is Improved Vehicular NOx Control Leading to Increased Urban NH3 Emissions?, *Environ. Sci. Technol.*, 2022, **56**(17), 11926–11927.

19 Y. Liu, Y. Ge, J. Tan, H. Wang and Y. Ding, Research on ammonia emissions characteristics from light-duty gasoline vehicles, *J. Environ. Sci.*, 2021, **106**, 182–193.

20 S. Liu, D. Huang, Y. Wang, S. Zhang, X. Liu, C. Wu, W. Du and G. Wang, Synergetic effects of NH3 and NOx on the production and optical absorption of secondary organic aerosol formation from toluene photooxidation, *Atmos. Chem. Phys.*, 2021, **21**(23), 17759–17773.

21 K. Li, L. Chen, S. J. White, H. Yu, X. Wu, X. Gao, M. Azzi and K. Cen, Smog chamber study of the role of NH3 in new particle formation from photo-oxidation of aromatic hydrocarbons, *Sci. Total Environ.*, 2018, **619–620**, 927–937.

22 M. Wang, W. Kong, R. Marten, X.-C. He, D. Chen, J. Pfeifer, A. Heitto, J. Kontkanen, L. Dada, A. Kürten, T. Yli-Juuti, H. E. Manninen, S. Amanatidis, A. Amorim, R. Baalbaki, A. Baccarini, D. M. Bell, B. Bertozzi, S. Bräkling, S. Brilke, L. C. Murillo, R. Chiu, B. Chu, L.-P. De Menezes, J. Duplissy, H. Finkenzeller, L. G. Carracedo, M. Granzin, R. Guida, A. Hansel, V. Hofbauer, J. Krechmer, K. Lehtipalo, H. Lamkaddam, M. Lampimäki, C. P. Lee, V. Makhmutov, G. Marie, S. Mathot, R. L. Mauldin, B. Mentler, T. Müller, A. Onnela, E. Partoll, T. Petäjä,

M. Philippov, V. Pospisilova, A. Ranjithkumar, M. Rissanen, B. Rörup, W. Scholz, J. Shen, M. Simon, M. Sipilä, G. Steiner, D. Stolzenburg, Y. J. Tham, A. Tomé, A. C. Wagner, D. S. Wang, Y. Wang, S. K. Weber, P. M. Winkler, P. J. Wlasits, Y. Wu, M. Xiao, Q. Ye, M. Zauner-Wieczorek, X. Zhou, R. Volkamer, I. Riipinen, J. Dommen, J. Curtius, U. Baltensperger, M. Kulmala, D. R. Worsnop, J. Kirkby, J. H. Seinfeld, I. El-Haddad, R. C. a. Flagan and N. M. Donahue, Rapid growth of new atmospheric particles by nitric acid and ammonia condensation, *Nature*, 2020, **581**(7807), 184–189.

23 R. Suarez-Bertoa, M. Pechout, M. Vojtíšek and C. Astorga, Regulated and Non-Regulated Emissions from Euro 6 Diesel, Gasoline and CNG Vehicles under Real-World Driving Conditions, *Atmosphere*, 2020, **11**(2), 204.

24 EU, COM(2022) 586 Final Regulation Of The European Parliament and of The Council on type-approval of motor vehicles and engines and of systems, components and separate technical units intended for such vehicles, with respect to their emissions and battery durability (Euro 7) and repealing regulations (EC) No. 715/2007 and (EC) No. 595/2009: 2022.

25 H. Wang, S. Guo, Y. Yu, R. Shen, W. Zhu, R. Tang, R. Tan, K. Liu, K. Song, W. Zhang, Z. Zhang, S. Shuai, H. Xu, J. Zheng, S. Chen, S. Li, L. Zeng and Z. Wu, Secondary aerosol formation from a Chinese gasoline vehicle: Impacts of fuel (E10, gasoline) and driving conditions (idling, cruising), *Sci. Total Environ.*, 2021, **795**, 148809.

26 E. Kostenidou, A. Martinez-Valiente, B. R'Mili, B. Marques, B. Temime-Roussel, A. Durand, M. André, Y. Liu, C. Louis, B. Vansevenant, D. Ferry, C. Laffon, P. Parent and B. D'Anna, Technical note: Emission factors, chemical composition, and morphology of particles emitted from Euro 5 diesel and gasoline light-duty vehicles during transient cycles, *Atmos. Chem. Phys.*, 2021, **21**(6), 4779–4796.

27 L. Chen, Z. Liang, X. Zhang and S. Shuai, Characterizing particulate matter emissions from GDI and PFI vehicles under transient and cold start conditions, *Fuel*, 2017, **189**, 131–140.

28 A. H. Hartikainen, M. Ihalainen, P. Yli-Pirilä, L. Hao, M. Kortelainen, S. M. Pieber and O. Sippula, Photochemical transformation and secondary aerosol formation potential of Euro6 gasoline and diesel passenger car exhaust emissions, *J. Aerosol Sci.*, 2023, **171**, 106159.

29 Y. Zhao, R. Saleh, G. Saliba, A. A. Presto, T. D. Gordon, G. T. Drozd, A. H. Goldstein, N. M. Donahue and A. L. Robinson, Reducing secondary organic aerosol formation from gasoline vehicle exhaust, *Proc. Natl. Acad. Sci. U. S. A.*, 2017, **114**(27), 6984–6989.

30 M. Ihalainen, P. Tiitta, H. Czech, P. Yli-Pirilä, A. Hartikainen, M. Kortelainen, J. Tissari, B. Stengel, M. Sklorz, H. Suhonen, H. Lamberg, A. Leskinen, A. Kiendler-Scharr, H. Harndorf, R. Zimmermann, J. Jokiniemi and O. Sippula, A novel high-volume Photochemical Emission Aging flow tube Reactor (PEAR), *Aerosol Sci. Technol.*, 2019, **53**(3), 276–294.

31 P. Barmet, J. Dommen, P. F. DeCarlo, T. Tritscher, A. P. Praplan, S. M. Platt, A. S. H. Prévôt, N. M. Donahue and U. Baltensperger, OH clock determination by proton transfer reaction mass spectrometry at an environmental chamber, *Atmos. Meas. Tech.*, 2012, **5**(3), 647–656.

32 A. Allani, Y. Bedjanian, D. K. Papanastasiou and M. N. Romanias, Reaction Rate Coefficient of OH Radicals with d9-Butanol as a Function of Temperature, *ACS Omega*, 2021, **6**(28), 18123–18134.

33 P. L. Hayes, A. M. Ortega, M. J. Cubison, K. D. Froyd, Y. Zhao, S. S. Cliff, W. W. Hu, D. W. Toohey, J. H. Flynn, B. L. Lefer, N. Grossberg, S. Alvarez, B. Rappenglück, J. W. Taylor, J. D. Allan, J. S. Holloway, J. B. Gilman, W. C. Kuster, J. A. de Gouw, P. Massoli, X. Zhang, J. Liu, R. J. Weber, A. L. Corrigan, L. M. Russell, G. Isaacman, D. R. Worton, N. M. Kreisberg, A. H. Goldstein, R. Thalman, E. M. Waxman, R. Volkamer, Y. H. Lin, J. D. Surratt, T. E. Kleindienst, J. H. Offenberg, S. Dusanter, S. Griffith, P. S. Stevens, J. Brioude, W. M. Angevine and J. L. Jimenez, Organic aerosol composition and sources in Pasadena, California, during the 2010 CalNex campaign, *J. Geophys. Res.: Atmos.*, 2013, **118**(16), 9233–9257.

34 Z. Peng, D. A. Day, A. M. Ortega, B. B. Palm, W. Hu, H. Stark, R. Li, K. Tsigaridis, W. H. Brune and J. L. Jimenez, Non-OH chemistry in oxidation flow reactors for the study of atmospheric chemistry systematically examined by modeling, *Atmos. Chem. Phys.*, 2016, **16**(16), 4283–4305.

35 Z. Peng and J. L. Jimenez, Modeling of the chemistry in oxidation flow reactors with high initial NO, *Atmos. Chem. Phys.*, 2017, **17**(17), 11991–12010.

36 Z. Peng, B. B. Palm, D. A. Day, R. Talukdar, W. Hu, A. T. Lambe, W. H. Brune and J. L. Jimenez, Model Evaluation of New Techniques for Maintaining High-NO Conditions in Oxidation Flow Reactors for the Study of OH-Initiated Atmospheric Chemistry, *ACS Earth Space Chem.*, 2018, **2**(2), 72–86.

37 Z. Peng and J. L. Jimenez, KinSim: A Research-Grade, User-Friendly, Visual Kinetics Simulator for Chemical-Kinetics and Environmental-Chemistry Teaching, *J. Chem. Educ.*, 2019, **96**(4), 806–811.

38 Z. Peng, D. A. Day, H. Stark, R. Li, J. Lee-Taylor, B. B. Palm, W. H. Brune and J. L. Jimenez, HO_x radical chemistry in oxidation flow reactors with low-pressure mercury lamps systematically examined by modeling, *Atmos. Meas. Tech.*, 2015, **8**(11), 4863–4890.

39 T. Streibel, F. Mühlberger, R. Geißler, M. Saraji-Bozorgzad, T. Adam and R. Zimmermann, Influence of sulphur addition on emissions of polycyclic aromatic hydrocarbons during biomass combustion, *Proc. Combust. Inst.*, 2015, **35**(2), 1771–1777.

40 H. Czech, O. Sippula, M. Kortelainen, J. Tissari, C. Radischat, J. Passig, T. Streibel, J. Jokiniemi and R. Zimmermann, On-line analysis of organic emissions from residential wood combustion with single-photon ionisation time-of-flight mass spectrometry (SPI-TOFMS), *Fuel*, 2016, **177**, 334–342.

41 C. Gehm, T. Streibel, J. Passig and R. Zimmermann, Determination of Relative Ionization Cross Sections for Resonance Enhanced Multiphoton Ionization of Polycyclic Aromatic Hydrocarbons, *Appl. Sci.*, 2018, **8**(9), 1617.

42 J. Leskinen, M. Ihalainen, T. Torvela, M. Kortelainen, H. Lamberg, P. Tiitta, G. Jakobi, J. Grigonyte, J. Joutsensaari, O. Sippula, J. Tissari, A. Virtanen, R. Zimmermann and J. Jokiniemi, Effective Density and Morphology of Particles Emitted from Small-Scale Combustion of Various Wood Fuels, *Environ. Sci. Technol.*, 2014, **48**(22), 13298–13306.

43 F. Drewnick, S. S. Hings, P. F. Decarlo, J. T. Jayne, M. Gonin, K. Fuhrer, J. L. Jimenez, K. L. Demerjian, S. Borrmann and D. R. Worsnop, A New Time-of-Flight Aerosol Mass Spectrometer (TOF-AMS)—Instrument Description and First Field Deployment, *Aerosol Sci. Technol.*, 2015, **39**(39), 637–658.

44 P. Simonen, J. Kalliokoski, P. Karjalainen, T. Rönkkö, H. Timonen, S. Saarikoski, M. Aurela, M. Bloss, G. Triantafyllopoulos, A. Kontses, S. Amanatidis, A. Dimaratos, Z. Samaras, J. Keskinen, M. Dal Maso and L. Ntziachristos, Characterization of laboratory and real driving emissions of individual Euro 6 light-duty vehicles – Fresh particles and secondary aerosol formation, *Environ. Pollut.*, 2019, **255**, 113175.

45 Y. Zhang, W. Deng, Q. Hu, Z. Wu, W. Yang, H. Zhang, Z. Wang, Z. Fang, M. Zhu, S. Li, W. Song, X. Ding and X. Wang, Comparison between idling and cruising gasoline vehicles in primary emissions and secondary organic aerosol formation during photochemical ageing, *Sci. Total Environ.*, 2020, **722**, 137934.

46 D. R. Worton, G. Isaacman, D. R. Gentner, T. R. Dallmann, A. W. H. Chan, C. Ruehl, T. W. Kirchstetter, K. R. Wilson, R. A. Harley and A. H. Goldstein, Lubricating Oil Dominates Primary Organic Aerosol Emissions from Motor Vehicles, *Environ. Sci. Technol.*, 2014, **48**(7), 3698–3706.

47 G. Caravaggio, J.-P. Charland, P. Macdonald and L. Graham, n-Alkane Profiles of Engine Lubricating Oil and Particulate Matter by Molecular Sieve Extraction, *Environ. Sci. Technol.*, 2007, **41**, 3697–3701.

48 M. R. Aosaf, Y. Wang and K. Du, Comparison of the emission factors of air pollutants from gasoline, CNG, LPG and diesel fueled vehicles at idle speed, *Environ. Pollut.*, 2022, **305**, 119296.

49 N. L. Ng, J. H. Kroll, A. W. H. Chan, P. S. Chhabra, R. C. Flagan and J. H. Seinfeld, Secondary organic aerosol formation from m-xylene, toluene, and benzene, *Atmos. Chem. Phys.*, 2007, **7**(14), 3909–3922.

50 K. Sato, A. Takami, Y. Kato, T. Seta, Y. Fujitani, T. Hikida, A. Shimono and T. Imamura, AMS and LC/MS analyses of SOA from the photooxidation of benzene and 1,3,5-trimethylbenzene in the presence of NOx: effects of chemical structure on SOA aging, *Atmos. Chem. Phys.*, 2012, **12**(10), 4667–4682.

51 V. Kumar, N. C. Kothiyal, Saruchi, P. Vikas and R. Sharma, Sources, distribution, and health effect of carcinogenic polycyclic aromatic hydrocarbons (PAHs) – current knowledge and future directions, *J. Chin. Adv. Mater. Soc.*, 2016, **4**(4), 302–321.

52 A. W. H. Chan, K. E. Kautzman, P. S. Chhabra, J. D. Surratt, M. N. Chan, J. D. Crounse, A. Kürten, P. O. Wennberg, R. C. Flagan and J. H. Seinfeld, Secondary organic aerosol formation from photooxidation of naphthalene and alkylnaphthalenes: implications for oxidation of intermediate volatility organic compounds (IVOCs), *Atmos. Chem. Phys.*, 2009, **9**(9), 3049–3060.

53 Z. Yang, L. Du, Y. Li and X. Ge, Secondary organic aerosol formation from monocyclic aromatic hydrocarbons: insights from laboratory studies, *Environ. Sci.: Processes Impacts*, 2022, **24**(3), 351–379.

54 S. Tuovinen, J. Kontkanen, J. Jiang and M. Kulmala, Investigating the effectiveness of condensation sink based on heterogeneous nucleation theory, *J. Aerosol Sci.*, 2020, **149**, 105613.

55 M. Shrivastava, O. A. Meinrat, P. Artaxo, H. M. J. Barbosa, L. K. Berg, J. Brito, J. Ching, R. C. Easter, J. Fan, J. D. Fast, Z. Feng, J. D. Fuentes, M. Glasius, A. H. Goldstein, E. G. Alves, H. Gomes, D. Gu, A. Guenther, S. H. Jathar, S. Kim, Y. Liu, S. Lou, S. T. Martin, V. F. McNeil, A. Medeiros, S. S. De Sá, J. E. Shiling, S. R. Springston, R. A. F. Souza, J. A. Thornton, G. Isaacman-VanWertz, L. D. Yee, R. Ynoue, R. A. Zaveri, A. Zelenyuk and C. Zhao, Urban pollution greatly enhances formation of natural aerosols over the Amazon rainforest, *Nat. Commun.*, 2019, **10**(10), 1046.

The impact of photochemical aging on secondary aerosol formation from a marine engine

Andreas Paul

an.paul@fz-juelich.de

ICE-3 Forchungzentrum Jülich

Tuukka Kokkola

Department of Environmental and Biological Science, University of Eastern Finland

Zheng Fang

Department of Earth and Planetary Science, Weizmann Institute of Science

Mika Ihalainen

Department of Environmental and Biological Science, University of Eastern Finland

Hendryk Czech

Department of Analytical and Technical Chemistry, University of Rostock

Uwe Etzien

Department of Piston Machinery and Internal Combustion Engines University of Rostock

Thorsten Hohaus

ICE-3 Forchungzentrum Jülich

Olli Sippula

Department of Environmental and Biological Science, University of Eastern Finland

Yinon Rudich

Department of Earth and Planetary Science, Weizmann Institute of Science

Bert Buchholz

Department of Piston Machinery and Internal Combustion Engines University of Rostock

Ralf Zimmerman

Department of Analytical and Technical Chemistry, University of Rostock

---

Article

Keywords: Ship emissions, maneuvering conditions MGO, HFO, emission factors, SOA, Secondary aerosol, OFR, Sulfur content

Posted Date: September 27th, 2024

DOI: https://doi.org/10.21203/rs.3.rs-4983538/v1

Additional Declarations: No competing interests reported.

Abstract

Ship traffic is known as one important contributor to air pollution. Recent regulations aimed at reducing sulfur oxide (SOx) pollution by limiting the fuel sulfur content (FSC) may also decrease fresh particulate matter (PM) emitted from ships. However, there is a knowledge gap regarding how the FSC affects secondary aerosol formation. Aerosol particle emissions from a research ship engine operated with either low sulfur heavy fuel oil (LS-HFO) (FSC=0.5%) or marine gas oil (MGO) (FSC=0.01%), were studied. The emissions were photochemically processed in the oxidation flow reactor “PEAR” to equivalent photochemical aging between 0-9 days in the atmosphere. It was found that FSC had no significant impact on secondary organic aerosol (SOA) formation after 3 days of aging, at 1.8±0.4g/kg and 1.5±0.4g/kg for MGO and LS-HFO, respectively. Furthermore, the composition and oxidative pathways remained similar regardless of FSC. However, as a result of the higher secondary SO4 formation and fresh aerosol emissions, LS-HFO had significantly higher total PM1 than MGO. Black carbon (BC) specifically was found to be 3 times higher for HFO than MGO. While the fuel with the lower sulfur content produces significantly less PM, the SOA formation remains similar regardless of FSC.

Synopsis

Atmospheric oxidation of ship engine exhaust, reveals significant impact of new regulations but highlights secondary organic aerosols as key pollutant.

Introduction

International trade is dominated by the shipping industry, accounting for approximately 80% by volume[1] and is expected to triple from 2019 to 2050[2]. Currently, international shipping is responsible for about 3% of global anthropogenic greenhouse gas emissions[2, 3] approximately 9% SO_x, 17% NO_x, 4% PM2.5 and 4% non-methane volatile organic compounds (NMVOCs) of global anthropogenic emissions.[4–6]

Up to 7% of global premature mortalities are attributable to air pollution.[7–10] As 70% of marine traffic occurs within 400 km from the coastline, ship emissions are relevant for public health.[11] Air pollution from shipping prior 2020 was estimated to attribute above 400 thousand premature deaths per year globally.[12] In 2020 the International maritime organisation (IMO) introduced global regulations limiting the maximum fuel sulfur content (FSC) from 3.5 to 0.5w%. These regulations aimed to directly reduce SO_x emissions from shipping by 77%,[13] but indirectly also lower emissions of PM by the implied ban of most heavy fuel oils (HFO).[14] These new regulations are expected to reduce premature deaths due to air pollution from ships by about 30%.[12] Furthermore, in 2015 sulfur emission control areas (SECA) were defined, including the North Sea, Baltic Sea, and North American coastal waters, with a maximum allowed FSC of 0.1%. From July 2024, HFO defined as fuels with a kinematic viscosity greater than 180 mm s^{-1} at 50°C and a density larger than 900 kg m^{-3} at 15°C are banned in Arctic waters.[15]

Introducing lower global FSC limit led to an increase in the use of marine gas oil (MGO), low-sulfur HFO (LS-HFO) and hybrid fuels with boiling ranges and impurities between MGO and LS-HFO. The boiling fraction of MGO, being a diesel-like fuel, has an intrinsically lower FSC than LS-HFO and is available with FSC ≤ 0.1%. Nevertheless, MGO has a significantly higher FSC than diesel used for road traffic, which has FSC < 0.001%.[16]

Beyond SO_x, substantial amounts of PM, BC, NO_x and NMVOCs are emitted at high levels from marine diesel engines, which are not equipped with exhaust aftertreatment technology, such as diesel oxidation catalysts (DOC) which reduces NMHC emissions. NMVOCs participate in oxidative gas-to-particle conversion, forming secondary organic aerosol (SOA). Observational studies have found that the highest contributor to SOA formation in coastal urban areas is shipping emissions with about 38%.[17] The highest emission factors for hydrocarbons, black carbon (BC) and particulate mass (PM) were found during the lowest engine loads, such as near shore maneuvering conditions.[16, 18, 19] Potential SOA precursors such as light poly aromatic hydrocarbons (PAHs) and other IVOCs have been reported from different fuel types with heavier fuels containing more PAHs than lighter diesel fuels[20]. Furthermore, a significant increase in PAH and oxy-PAH was observed during low engine load.[21]

SOA from IVOCs, such as naphthalene representative for combustion-derived IVOC, have been shown to have adverse effect on human health.[22] Even with a change from HFO to LS-HFO or MGO it has been predicted that shipping will remain a significant source of anthropogenic aerosol.[23] A recent study explored the impact of aging on HFO emissions at 65% engine load. The ship was equipped with a sulphur scrubber and a DOC as exhaust aftertreatment, and showed no significant SOA formation.[24] Therefore, in order to explore the SOA formation potential for other engine conditions and better understand the impacts of new IMO regulations on SOA formation, our study investigates the impacts of aging on low sulphur fuels such as LS-HFO and MGO fuel at low engine load.

Results and discussion

SOA formation from LS-HFO and MGO photooxidation

Figure 1 illustrates the chemical composition of aerosols for both LS-HFO and MGO. At 0 days of equivalent photochemical aging the fresh aerosol has an OM/PM of 0.47 for LS-HFO and 0.34 for MGO, respectively. The MGO thus contains relatively less organic and more soot, however the total aerosol emitted is much lower for MGO than for LS-HFO. The LS-HFO emissions of POA were more than 5 times higher than those of the MGO, while BC emissions were approximately 3 times higher in LS-HFO than in MGO. Other non-refractory PM components including SO4 and NO3 were negligible for the total PM.

The fresh particles have a geometric mean diameter of 75 ± 6 nm for MGO and 94 ± 3 nm for LS-HFO (supplementary table S12), which is comparable to fresh particles emitted from HFO published by Karjalainen et al. 2022.[24] The most notable change from previous studies is that there is no SO4

contribution to the fresh aerosol emissions due to the fuel used in this study LS-HFO(FSC = 0.5%) in comparison to Karjalainen et al 2022 with an FSC of 1.9%. HFO with a FSC of 0.12% has previously been found to emit 2.57 ± 0.41g/kg total PM at 25% engine load,[19] this is a lower FSC content than in the LS-HFO of this study, but the emissions factors are nevertheless similar.

Ozonolysis had the lowest impact on the aerosol in the PEAR in terms of chemical composition, particle size and PM. The total aerosol mass per kg fuel consumed for LS-HFO is consistently from fresh to 9 days of equivalent photochemical age more than twice that of MGO. As the emissions were photochemically processed in the PEAR, also the aerosol composition changed. At 1.5 days the aerosol composition is dominated by organics with an OM/PM of 0.60 for LS-HFO and 0.69 for MGO. BC is comparatively not affected by photochemical aging and the total BC mass remains constant at 1.1 ± 0.2g/kg for LS-HFO and 0.4 ± 0.1g/kg for MGO for all oxidation experiments. The increase in total mass can be attributed to SO4 and particularly SOA formation (Fig. 1). The SOA emission factor for both MGO and LS-HFO is similar and reaches a maximum of 1.5 ± 0.4 g/kg LS-HFO and 1.8 ± 0.4 g/kg MGO after 3.3 and 4.7 days of equivalent photochemical aging respectively, though smaller aging steps would be required to determine the specific maximum. However, the majority of SOA is formed within the first 1.5 days of equivalent photochemical aging. Some results from recent studies have suggested the majority of secondary aerosol (SA) from shipping is even formed within the first 3 hours after emission.[34] While photochemical aging increases SOA formation equally for the two fuels, SO4 aerosol formation is greatly enhanced in the LS-HFO emissions due to the higher FSC and thus emission of SO_2 compared to MGO.

Figure 1 shows that photochemical aging beyond 4.7 days does not yield additional SOA formation, and a further increase in total aerosol results from SO4 formation. After 9 days of equivalent photochemical aging, the LS-HFO aerosol is in a SO4 dominated state where OM/PM decreased to 0.23. For MGO, however, the aerosol remains organic-dominated with OM/PM > 0.5. This is further highlighted by the organic aerosol enhancement ratio, which indicates the 5-fold increase in organics for the MGO, whereas LS-HFO only increases 2-fold compared to POA. Therefore, the low FSC in the MGO significantly decreases the total aerosol mass concentration as secondary SO4 aerosol mass is reduced. But a change from LS-HFO to MGO does not significantly reduce SOA formation, resulting in an organic dominated aerosol.

Elemental composition and oxidation pathway

While more than 4.7 days of equivalent photochemical aging does not increase OA mass for either MGO or LS-HFO, the composition of the OA changes significantly. Initial photochemical aging from 0 to 4.7 days increases both f43 (the fraction of 43 m/z of total mass spectrum, mostly $C_2H_3O^+$) and f44 (the fraction of 44 m/z mostly CO_2^+) fraction, consistent with the increase in OA mass (Fig. 2A-B).[35, 36] However, an equivalent age higher than 4.7 days results in a decrease of f43 and an increase of f44, similar to observations from EURO2 diesel vehicles .[37] This coincides with the plateau in SOA formation that was observed, suggesting a change in the oxidative pathway. This observation is valid for both MGO

and LS-HFO. All aged aerosols fall within the triangular space, representing the occurrence of ambient aerosol .[35]

The similarity between MGO and LS-HFO is further supported by the elemental ratios depicted as a Van Krevelen diagram (Fig. 2C-D).[36, 38] The main difference in the elemental composition was found in the fresh aerosol, with the H/C ratio of (1.79 ± 0.05) for MGO and (1.67 ± 0.03) for LS-HFO aerosol, resulting in a slope from fresh aerosol to 3 days of equivalent photochemical aging of -0.97±0.08 (r^2=0.97) and − 0.89±0.04 (r^2 = 0.98) for MGO and LS-HFO, respectively. This result suggests that the initial photochemical aging from fresh to maximum SOA formation is equivalent to carboxylic acid formation with no fragmentation or carbonyl and hydroxyl addition on different carbons.[36] Further after just 3–4 days of photochemical aging there is no significant difference in the elemental ratios between two fuels. The slope of both MGO and LS-HFO after 3 days of age is -0.54±0.02 (r^2 = 0.99). Photochemical aging beyond the maximum SOA formation point thus suggests carboxylic acid formation with fragmentation. This is fitting with decrease in f43 but continued increase in f44 suggesting acid formation.[36] The fragmentation effectively results in a lower SOA yield which leads to a net zero mass change in SOA at higher photochemical age. Based on KinSim simulation the difference in oxidation is not a result of the difference in RO2 fate as HO2-RO2 reactions accounted for the > 50% of lost RO2 and HO accounting for > 25% at all ages for both fuels (supplementary table S8-9).

Discussion

Implementing a global FSC limit to the current SECA level could incentivize the use of cleaner shipping fuels instead of residual fuel oils, potentially lowering emissions of total PM, BC, POA and sulphate. However, this may not impact the SOA mass formed after atmospheric aging. As both POA and BC are reduced, the fresh PM at emission point is significantly reduced by changing from current global FSC regulations to SECA compliant FSC fuels. The use of MGO over LS-HFO in harbor areas would thus decrease PM.

The majority of SOA was formed after only 1.5 days of equivalent photochemical aging while maximum SOA formation was reached at 3.3 days of equivalent photochemical age. Thus, SOA will presumably form close to the emission point, i.e. harbors and nearby populated areas, considering the emission scenario of low engine load. Since most of the population is located along coastlines, shipping emissions could have large public health effects. Notably the SOA levels would not be expected to decrease in these areas with a change from LS-HFO to MGO. Secondary sulfate formation proceeded much slower but continued to increase in mass during photochemical aging to the maximum of almost 9 days of equivalent photochemical age. The reduction in sulfate aerosol associated with changing from LS-HFO to MGO would thus have an environmental and air quality impact further from the emission point than the OA.

Regarding the composition of SOA, a high similarity was found for H/C, O/C, f43 and f44 for the LS-HFO and MGO. This suggests that the precursor for the SOA is similar between the two fuels, which are likely

alkylated aromatic mono- to tricyclic structures.[39] Reducing aromatic VOC emissions would improve air quality and lessen the health burden associated with ship emissions during harbour maneuvers .

Methods

A four-stroke single-cylinder research diesel engine (80kW nominal power) was operated on either MGO (FSC = 0.01 S w%) or LS-HFO (FSC = 0.5 S w%) at low engine load (20kW, 25% of nominal power), representing docking maneuvers. Raw exhaust emissions were connected to diluters via heated tubing (constant at 350°C), see Fig. 3. A series configuration of a porous tube diluter and an ejector diluter was employed to achieve a dilution ratio of 1:250. The dilution ratio was determined by measuring the CO₂ concentrations in the raw exhaust, the diluted exhaust, and the dilution air. The dilution ratio was regulated by automatically adjusting the flow rate of the porous tube diluter, while maintaining a constant flow rate for the ejector diluter.

The diluted (1:250) exhaust sample passed through the oxidation flow reactor “Photochemical Emission Aging flow tube Reactor” (PEAR), which was operated at a flow rate of 100 lpm. [25] At these flow conditions, the mean residence time in the PEAR is 70 s. At the entrance to the PEAR 10ppm of ozone was added in addition to water vapor keeping the relative humidity (RH) at approximately 50%. The photochemical aging was controlled through UV-lamp(254nm) intensity, water vapour supply for 50% relative humidity and constant ozone (10ppm) addition in order to obtain atmospheric aging equivalent to 0 to 9 days (supplementary table S7). The photochemical age was determined with d9-butanol decay measured by a Proton-transfer-reaction mass spectrometry (PTR-MS) based on the principle of the “photochemical clock”.[26] The Kinsim[27–31] model was used to verify the atmospheric relevancy by simulating the chemistry within the PEAR, by determining the RO2 fate to remove speculations on non-tropospheric chemistry occurring in the OFR. (supplementary table S7-9)

An additional ejector diluter was added after the PEAR for a further 10-fold dilution before online instruments, resulting in a total dilution ratio of 1:2500 for aerosol instruments presented here. Aerosol phase measurement were done with High-Resolution Time of Flight Aerosol Mass Spectrometer (HR-ToF-AMS)[32] for obtaining the chemical composition of the non-refractory aerosol, aethalometer for BC and a scanning mobility particle sizer (SMPS) for particle number concentration and size distribution. SMPS data was treated with the AIM V. 10.3.1.0 software.

Optically defined black carbon (BC), “equivalent black carbon" (eBC), was quantified by the Aethalometer (AE33-7, Aerosol Magee Scientific), which measures light attenuation through a filter tape at 7 wavelengths (UV–IR, 370–950 nm). Using different corrections, such as multiple-scattering correction and loading compensation, attenuation coefficients were converted to absorption coefficients, and further to black carbon concentrations. A mass absorption coefficient (MAC) was used to quantify light absorption as a mass concentration. Absorption at 880 nm is generally assumed to be only caused by BC. Thus, the equivalent black carbon mass concentrations (eBC) was calculated (Eq. 1)

$$eBC = \frac{A \bullet \left(\frac{\Delta\ ATN}{100}\right)}{F_{meas} \bullet\ (1-\zeta) \bullet\ (1-k \bullet\ ATN_t) * \Delta\, t \bullet\ C \bullet\ MAC}\ ,\ (eq.1)$$

where A is the surface area of the filter spot, $\Delta\ ATN$ the change of attenuation at 880nm during a time interval $\Delta\, t$, F_{meas} the measured flow rate, ζ the leakage factor (default value 0.01), k the real-time loading compensation parameter[3] ATN_t the attenuation at time t for 880nm, C the multiple-scattering coefficient (here C = 2.80 based on reference absorption measurement by PAX-870 during the campaign), and MAC the mass absorption coefficient (here $MAC\,(880\ nm)$ = 5.47 m^2/g, based on reference refractory black carbon (rBC) measurement by LII 300 and elemental carbon (EC) measurement by DRI 2015 during the campaign).

AMS data was treated in Tof-AMS Analysis Toolkit 1.65 (squirrel), and HR analysis was performed with ToF-AMS HR Analysis 1.25 (PIKA). Elemental analysis was performed by the Aiken method (aiken et al. 2007) The AMS was equipped to handle particles with an aerodynamic diameter between 42nm and 645nm. With small aerosol diameters, (supplementary table S12), falling outside the size range of the AMS.

Moreover, to the best of our knowledge no information is available on the density of aged aerosol emissions from ships but aging of aerosol emissions from solid fuel combustion demonstrate a particle size dependent increases in effective density with differences between fuels.[33] Therefor the mass of the aerosol is determined by the SMPS, with an assumed density of 1,5+-0,2 g/cm3. Composition of the aerosol is then calculated based on AMS and aethalometer as in Eq. 2.

$$EF_x = (EF_{SMPS} - EF_{eBC}) * \frac{Conc_x}{Conc_{ams}},\quad (eq.2)$$

Where EF_X is the emission factor of an aerosol group, $Conc_x$ is the concentration of the aerosol group measured by the AMS, $Conc_{AMS}$ is the total concentration of aerosols measured by the AMS. EF_{SMPS} is the emission factor determined by the SMPS and EF_{eBC} is the emission factor of eBC determined by aethalometer. Primary organic aerosol (POA) was determined as the organic fraction with no photochemical aging. The SOA fraction was calculated by subtracting the POA from the total OA mass at a given simulated ageeq.3. Organic enhancement factor was calculated as the fractional increase of organics, see supplement equation Eq. 4.

$$SOA_x = OM_x - POA,\quad (eq.3)$$

$$Org_{enh,x} = \frac{OM_x}{POA},\quad (eq.4)$$

Where POA is the total organic mass at 0 days of atmospheric aging and OMx is the total organic mass at X days of atmospheric aging.

Declarations

Supporting Information

Additional experimental details, methods, fuel composition, model input & output and supporting tables (Supplement.docx)

Conflicts of interest

There are no conflicts to declare.

Author Contribution

A.P. wrote the main manuscript and prepared all figures.T.K., Z.F. and M.I. wrote parts of the methods segments in the main manuscript.U.E. prepared supplementary table 1-2.Data acquisition was conducted by A.P., T.K., Z.F., M.I., U.E. and H.C.All authors contributed to data analysis and interpretation.Supervision and funding by T.H.,H.C., O.S., Y.R., B.B. and R.Z.All authors revised the manuscript.Critical revision by T.H., H.C. T.K., Z.F., Y.R. and O.S.

Acknowledgement

We Thank the Helmholtz international Laboratory aeroHEALTH (InterLabs-0005; https://aerohealth.eu) and the ULTRHAS Horizon Europe project (agreement 955390) for supporting this work.

Data Availability

The datasets associated with the current study are available from the corresponding authors [an.paul@fz-juelich.de or T.Hohaus@fz-juelich.de] on reasonable request.

References

1. Gray, N.; McDonagh, S.; O'Shea, R.; Smyth, B.; Murphy, J. D., Decarbonising ships, planes and trucks: An analysis of suitable low-carbon fuels for the maritime, aviation and haulage sectors. Advances in Applied Energy 2021, *1*, 100008.
2. OECD Ocean shipping and shipbuilding. https://www.oecd.org/ocean/topics/ocean-shipping/ (accessed 01/02).
3. IMO Fourth IMO greenhouse gas study. https://www.imo.org/en/ourwork/Environment/Pages/Fourth-IMO-Greenhouse-Gas-Study-

2020.aspx (accessed 08/02).

4. Shi, Z.; Endres, S.; Rutgersson, A.; Al-Hajjaji, S.; Brynolf, S.; Booge, D.; Hassellöv, I.-M.; Kontovas, C.; Kumar, R.; Liu, H.; Marandino, C.; Matthias, V.; Moldanová, J.; Salo, K.; Sebe, M.; Yi, W.; Yang, M.; Zhang, C., Perspectives on shipping emissions and their impacts on the surface ocean and lower atmosphere: An environmental-social-economic dimension. Elementa: Science of the Anthropocene 2023, *11* (1), 00052.
5. McDuffie, E. E.; Smith, S. J.; O'Rourke, P.; Tibrewal, K.; Venkataraman, C.; Marais, E. A.; Zheng, B.; Crippa, M.; Brauer, M.; Martin, R. V., A global anthropogenic emission inventory of atmospheric pollutants from sector- and fuel-specific sources (1970–2017): an application of the Community Emissions Data System (CEDS). Earth Syst. Sci. Data 2020, *12* (4), 3413–3442.
6. European, C.; Joint Research, C.; Olivier, J.; Guizzardi, D.; Schaaf, E.; Solazzo, E.; Crippa, M.; Vignati, E.; Banja, M.; Muntean, M.; Grassi, G.; Monforti-Ferrario, F.; Rossi, S., *GHG emissions of all world – 2021 report*. Publications Office of the European Union: 2021.
7. Murray, C. J. L., Global burden of 87 risk factors in 204 countries and territories, 1990–2019: a systematic analysis for the Global Burden of Disease Study 2019. The Lancet 2020, *396* (10258), 1223–1249.
8. Corbett, J. J.; Winebrake, J. J.; Green, E. H.; Kasibhatla, P.; Eyring, V.; Lauer, A., Mortality from Ship Emissions: A Global Assessment. Environmental Science & Technology 2007, *41* (24), 8512–8518.
9. Mueller, N.; Westerby, M.; Nieuwenhuijsen, M., Health impact assessments of shipping and port-sourced air pollution on a global scale: A scoping literature review. Environmental Research 2023, *216*, 114460.
10. Organization, W. H. Burden of disesase from teh joint effects of household and ambient air pollution for 2016'. https://cdn.who.int/media/docs/default-source/air-quality-database/aqd-2018/ap_joint_effect_bod_results_may2018.pdf?sfvrsn=4dc44c26_3 (accessed 08/02).
11. Contini, D.; Merico, E. Recent Advances in Studying Air Quality and Health Effects of Shipping Emissions *Atmosphere* [Online], 2021.
12. Sofiev, M.; Winebrake, J. J.; Johansson, L.; Carr, E. W.; Prank, M.; Soares, J.; Vira, J.; Kouznetsov, R.; Jalkanen, J.-P.; Corbett, J. J., Cleaner fuels for ships provide public health benefits with climate tradeoffs. Nature Communications 2018, *9* (1), 406.
13. IMO IMO 2020 – cutting sulphur oxide emissions https://www.imo.org/en/MediaCentre/HotTopics/Pages/Sulphur-2020.aspx (accessed 01/02).
14. Yuan, T.; Song, H.; Oreopoulos, L.; Wood, R.; Bian, H.; Breen, K.; Chin, M.; Yu, H.; Barahona, D.; Meyer, K.; Platnick, S., Abrupt reduction in shipping emission as an inadvertent geoengineering termination shock produces substantial radiative warming. Communications Earth & Environment 2024, *5* (1), 281.
15. IMO Marine Environment Protection Committee (MEPC) 75, 16–20 November (virtual session). https://www.imo.org/en/MediaCentre/MeetingSummaries/Pages/MEPC-75th-session.aspx.

16. Aakko-Saksa, P. T.; Lehtoranta, K.; Kuittinen, N.; Järvinen, A.; Jalkanen, J.-P.; Johnson, K.; Jung, H.; Ntziachristos, L.; Gagné, S.; Takahashi, C.; Karjalainen, P.; Rönkkö, T.; Timonen, H., Reduction in greenhouse gas and other emissions from ship engines: Current trends and future options. Progress in Energy and Combustion Science 2023, *94*, 101055.
17. Jang, E.; Choi, S.; Yoo, E.; Hyun, S.; An, J., Impact of shipping emissions regulation on urban aerosol composition changes revealed by receptor and numerical modelling. npj Climate and Atmospheric Science 2023, *6* (1), 52.
18. Chu-Van, T.; Ristovski, Z.; Pourkhesalian, A. M.; Rainey, T.; Garaniya, V.; Abbassi, R.; Kimball, R.; Luong Cong, N.; Jahangiri, S.; Brown, R. J., A comparison of particulate matter and gaseous emission factors from two large cargo vessels during manoeuvring conditions. Energy Reports 2019, *5*, 1390–1398.
19. Anderson, M.; Salo, K.; Hallquist, Å. M.; Fridell, E., Characterization of particles from a marine engine operating at low loads. Atmospheric Environment 2015, *101*, 65–71.
20. *International Journal of Environmental Research and Public Health* [Online], 2023.
21. Sippula, O.; Stengel, B.; Sklorz, M.; Streibel, T.; Rabe, R.; Orasche, J.; Lintelmann, J.; Michalke, B.; Abbaszade, G.; Radischat, C.; Gröger, T.; Schnelle-Kreis, J.; Harndorf, H.; Zimmermann, R., Particle Emissions from a Marine Engine: Chemical Composition and Aromatic Emission Profiles under Various Operating Conditions. Environmental Science & Technology 2014, *48* (19), 11721–11729.
22. Offer, S.; Hartner, E.; Di Bucchianico, S.; Bisig, C.; Bauer, S.; Pantzke, J.; Zimmermann Elias, J.; Cao, X.; Binder, S.; Kuhn, E.; Huber, A.; Jeong, S.; Käfer, U.; Martens, P.; Mesceriakovas, A.; Bendl, J.; Brejcha, R.; Buchholz, A.; Gat, D.; Hohaus, T.; Rastak, N.; Jakobi, G.; Kalberer, M.; Kanashova, T.; Hu, Y.; Ogris, C.; Marsico, A.; Theis, F.; Pardo, M.; Gröger, T.; Oeder, S.; Orasche, J.; Paul, A.; Ziehm, T.; Zhang, Z.-H.; Adam, T.; Sippula, O.; Sklorz, M.; Schnelle-Kreis, J.; Czech, H.; Kiendler-Scharr, A.; Rudich, Y.; Zimmermann, R., Effect of Atmospheric Aging on Soot Particle Toxicity in Lung Cell Models at the Air–Liquid Interface: Differential Toxicological Impacts of Biogenic and Anthropogenic Secondary Organic Aerosols (SOAs). *Environmental Health Perspectives* 2022, *130* (2), 027003.
23. Kuittinen, N.; Jalkanen, J.-P.; Alanen, J.; Ntziachristos, L.; Hannuniemi, H.; Johansson, L.; Karjalainen, P.; Saukko, E.; Isotalo, M.; Aakko-Saksa, P.; Lehtoranta, K.; Keskinen, J.; Simonen, P.; Saarikoski, S.; Asmi, E.; Laurila, T.; Hillamo, R.; Mylläri, F.; Lihavainen, H.; Timonen, H.; Rönkkö, T., Shipping Remains a Globally Significant Source of Anthropogenic PN Emissions Even after 2020 Sulfur Regulation. Environmental Science & Technology 2021, *55* (1), 129–138.
24. Karjalainen, P.; Teinilä, K.; Kuittinen, N.; Aakko-Saksa, P.; Bloss, M.; Vesala, H.; Pettinen, R.; Saarikoski, S.; Jalkanen, J.-P.; Timonen, H., Real-world particle emissions and secondary aerosol formation from a diesel oxidation catalyst and scrubber equipped ship operating with two fuels in a SECA area. Environmental Pollution 2022, *292*, 118278.
25. Ihalainen, M.; Tiitta, P.; Czech, H.; Yli-Pirilä, P.; Hartikainen, A.; Kortelainen, M.; Tissari, J.; Stengel, B.; Sklorz, M.; Suhonen, H.; Lamberg, H.; Leskinen, A.; Kiendler-Scharr, A.; Harndorf, H.; Zimmermann, R.;

Jokiniemi, J.; Sippula, O., A novel high-volume Photochemical Emission Aging flow tube Reactor (PEAR). AEROSOL SCIENCE AND TECHNOLOGY 2019, *53* (3), 276–294.

26. Barmet, P.; Dommen, J.; DeCarlo, P. F.; Tritscher, T.; Praplan, A. P.; Platt, S. M.; Prévôt, A. S. H.; Donahue, N. M.; Baltensperger, U., OH clock determination by proton transfer reaction mass spectrometry at an environmental chamber. Atmos. Meas. Tech. 2012, *5* (3), 647–656.
27. Peng, Z.; Jimenez, J. L., KinSim: A Research-Grade, User-Friendly, Visual Kinetics Simulator for Chemical-Kinetics and Environmental-Chemistry Teaching. Journal of Chemical Education 2019, *96* (4), 806–811.
28. Peng, Z.; Palm, B. B.; Day, D. A.; Talukdar, R.; Hu, W.; Lambe, A. T.; Brune, W. H.; Jimenez, J. L., Model Evaluation of New Techniques for Maintaining High-NO Conditions in Oxidation Flow Reactors for the Study of OH-Initiated Atmospheric Chemistry. ACS Earth Space Chem 2018, *2* (2), 72–86.
29. Peng, Z.; Jimenez, J. L., Modeling of the chemistry in oxidation flow reactors with high initial NO. Atmos. Chem. Phys., 2017, *17* (17), 11991–12010.
30. Peng, Z.; Day, D. A.; Ortega, A. M.; Palm, B. B.; Hu, W.; Stark, H.; Li, R.; Tsigaridis, K.; Brune, W. H.; Jimenez, J. L., Non-OH chemistry in oxidation flow reactors for the study of atmospheric chemistry systematically examined by modeling. Atmos. Chem. Phys., 2016, *16* (16), 4283–4305.
31. Peng, Z.; Day, D. A.; Stark, H.; Li, R.; Lee-Taylor, J.; Palm, B. B.; Brune, W. H.; Jimenez, J. L., HO < sub > x</sub > radical chemistry in oxidation flow reactors with low-pressure mercury lamps systematically examined by modeling. Atmos. Meas. Tech. 2015, *8* (11), 4863–4890.
32. Decarlo, P. F.; Kimmel, J. R.; Trimborn, A.; Northway, M.; Jayne, J. T.; Aiken, A. C.; Gonin, M.; Fuhrer, K.; Horvath, T.; Docherty, K. S.; Worsnop, D. R.; Jimenez, J. L., Field-Deployable, High-Resolution, Time-of-Flight Aerosol Mass Spectrometer. Anal. Chem. 2006, *78* (28), 8281–8289.
33. Leskinen, J.; Hartikainen, A.; Väätäinen, S.; Ihalainen, M.; Virkkula, A.; Mesceriakovas, A.; Tiitta, P.; Miettinen, M.; Lamberg, H.; Czech, H.; Yli-Pirilä, P.; Tissari, J.; Jakobi, G.; Zimmermann, R.; Sippula, O., Photochemical Aging Induces Changes in the Effective Densities, Morphologies, and Optical Properties of Combustion Aerosol Particles. Environmental Science & Technology 2023, *57* (13), 5137–5148.
34. Gryspeerdt, E.; Goren, T.; Smith, T. W. P., Observing the timescales of aerosol–cloud interactions in snapshot satellite images. Atmos. Chem. Phys. 2021, *21* (8), 6093–6109.
35. Ng, N. L.; Canagaratna, M. R.; Zhang, Q.; Jimenez, J. L.; Tian, J.; Ulbrich, I. M.; Kroll, J. H.; Docherty, K. S.; Chhabra, P. S.; Bahreini, R.; Murphy, S. M.; Seinfeld, J. H.; Hildebrandt, L.; Donahue, N. M.; DeCarlo, P. F.; Lanz, V. A.; Prévôt, A. S. H.; Dinar, E.; Rudich, Y.; Worsnop, D. R., Organic aerosol components observed in Northern Hemispheric datasets from Aerosol Mass Spectrometry. Atmos. Chem. Phys. 2010, *10* (10), 4625–4641.
36. Ng, N. L.; Canagaratna, M. R.; Jimenez, J. L.; Chhabra, P. S.; Seinfeld, J. H.; Worsnop, D. R., Changes in organic aerosol composition with aging inferred fromaerosol mass spectra. Atmos. Chem. Phys. 2011, *11* (11), 6465–6474.

37. Heringa, M. F.; DeCarlo, P. F.; Chirico, R.; Tritscher, T.; Clairotte, M.; Mohr, C.; Crippa, M.; Slowik, J. G.; Pfaffenberger, L.; Dommen, J.; Weingartner, E.; Prévôt, A. S. H.; Baltensperger, U., A new method to discriminate secondary organic aerosols from different sources using high-resolution aerosol mass spectra. Atmos. Chem. Phys. 2012, *12* (4), 2189–2203.
38. Krevelen, D. W. V., Graphical-statistical Method for the Study of Structure and Reaction Processes of Coal. Fuel 1950, *29*, 269–284.
39. Czech, H.; Stengel, B.; Adam, T.; Sklorz, M.; Streibel, T.; Zimmermann, R., A chemometric investigation of aromatic emission profiles from a marine engine in comparison with residential wood combustion and road traffic: Implications for source apportionment inside and outside sulphur emission control areas. Atmospheric Environment 2017, *167*, 212–222.

Figures

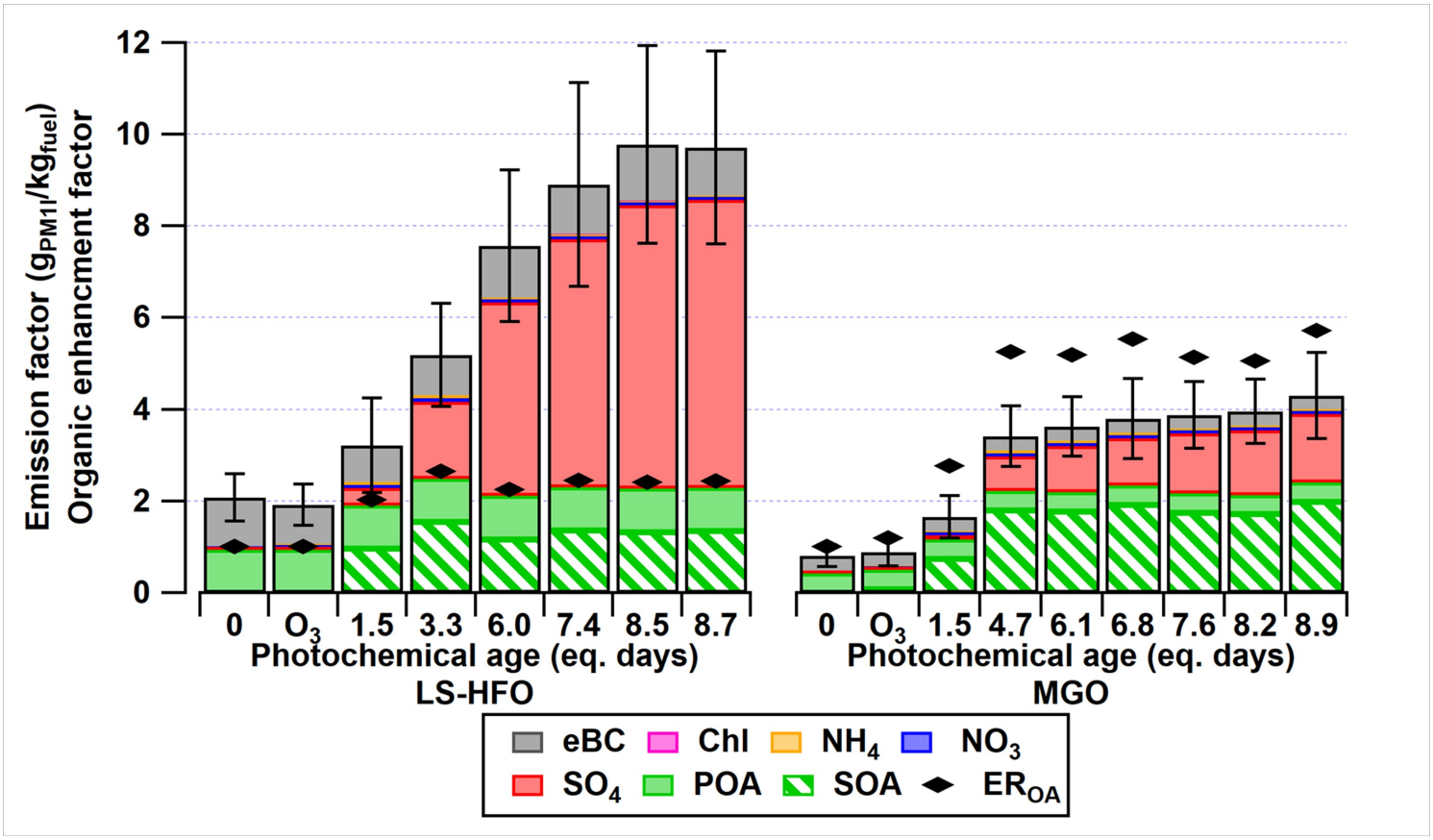

Figure 1

Chemical composition emission factors for both LS-HFO and MGO.

The left axis indicates the emission factor in grams of PM1 measured per kg fuel consumed and the organic enhancement factor (ER_{OA}) The left set of the graph represents the LS-HFO results and the right the MGO aerosol emissions, both with a photochemical age displayed in atmospheric equivalent days at the bottom.

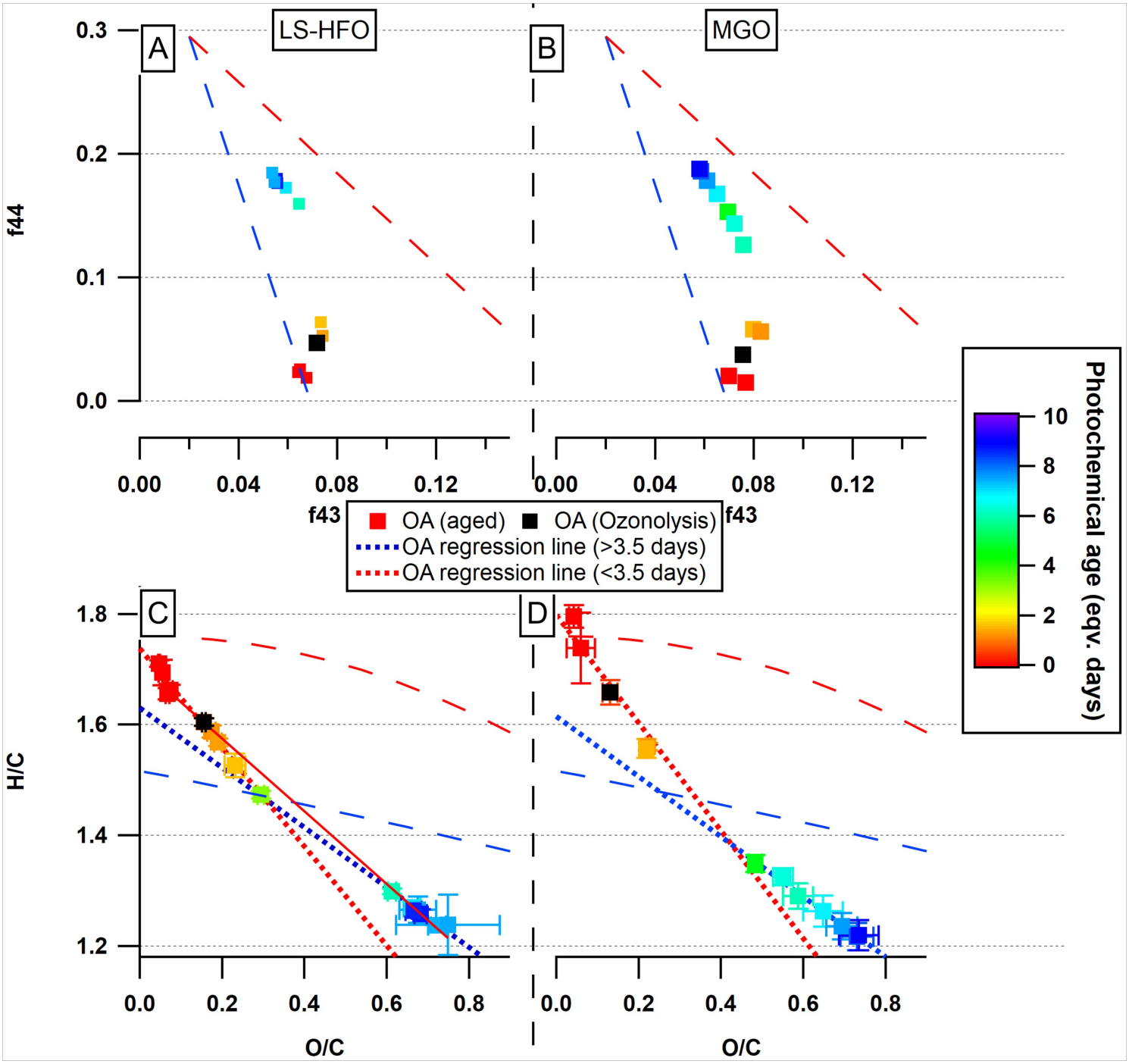

Figure 2

Elemental composition of LS-HFO and MGO and its dependency of photochemical age.

2A and 2B show a triangle plot as first published by Ng et al 2010[35] illustrating the f43 and f44 of the organic aerosol (OA). Figure 2A shows the impact of aging on these two fractions for LS-HFO and figure 2B shows the same for MGO. The photochemical age of the aerosol is illustrated by colour as seen on the right. Figure 2C and 2D illustrate a Van Krevelen plot.[36,38] with hydrogen to carbon ratio on the y axis and oxygen to carbon ratio on the x axis, showing the chemical composition of the OA: the OA regression

line is shown with dotted lines, and the dashed lines highlight the area where ambient aerosol typically fall within.

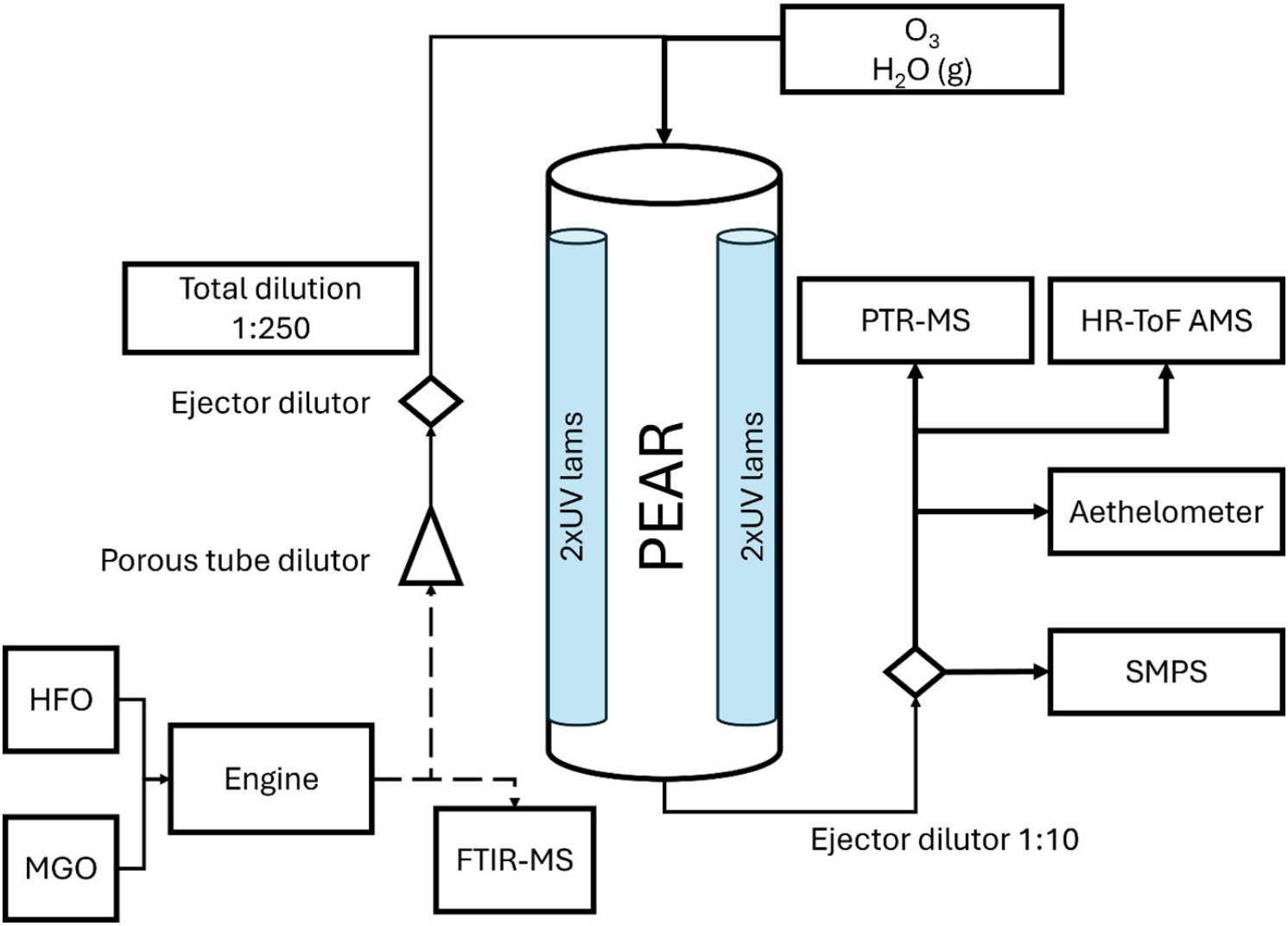

Figure 3

experimental setup.

The dotted line signifies heated tubing(350°C). Only Either HFO or MGO was added to the engine.

Supplementary Files

This is a list of supplementary files associated with this preprint. Click to download.

- supplement.docx

ACS EARTH AND SPACE CHEMISTRY

http://pubs.acs.org/journal/aesccq

Article

On the Complementarity and Informative Value of Different Electron Ionization Mass Spectrometric Techniques for the Chemical Analysis of Secondary Organic Aerosols

Elena Hartner, Andreas Paul, Uwe Käfer, Hendryk Czech, Thorsten Hohaus, Thomas Gröger,* Martin Sklorz, Gert Jakobi, Jürgen Orasche, Seongho Jeong, Ramona Brejcha, Till Ziehm, Zhi-Hui Zhang, Jürgen Schnelle-Kreis, Thomas Adam, Yinon Rudich, Astrid Kiendler-Scharr, and Ralf Zimmermann

Cite This: *ACS Earth Space Chem.* 2022, 6, 1358−1374

Read Online

ACCESS | Metrics & More | Article Recommendations | Supporting Information

ABSTRACT: The atmospheric aging of volatile organic compounds leads to the formation of complex mixtures of highly oxidized secondary organic aerosols (SOAs). State-of-the-art mass spectrometry (MS) has become a pivotal tool for their chemical characterization. In this study, we characterized the chemical complexity of naphthalene-derived SOA by three different time-of-flight (TOF) mass spectrometric techniques applying electron ionization: high-resolution−TOF−aerosol MS (AMS), direct inlet probe (DIP)−high-resolution TOFMS, and thermal desorption—comprehensive two-dimensional gas chromatography—TOFMS (GC × GC). We discuss AMS as an online, DIP as an atline, and GC × GC as an offline technique to compare their informative value for studying the oxidation state, volatility, and molecular composition of laboratory-generated SOA. For GC × GC, the accessible organic content was limited to (semi-)volatile compounds and supported a reliable assignment of the molecular composition. DIP and AMS were used to derive secondary parameters such as O/C and H/C ratios, the general functionality of the compound classes and their abundance upon photochemical aging. Thereby, while the induced pyrolysis in the AMS extended the accessibility range to polar, high-molecular-weight compounds, thermal fragmentation also led to limited molecular information. For DIP, low-volatility compounds could be volatilized and the high mass resolution was useful to resolve isobaric mass fragments and assign reliable sum formulas of fragments and molecular ions. Although no single technique can provide information to describe the full chemical complexity of the SOA, AMS, DIP, and GC × GC in their complementarity are well suited to investigate the impact of SOA on health and environment.

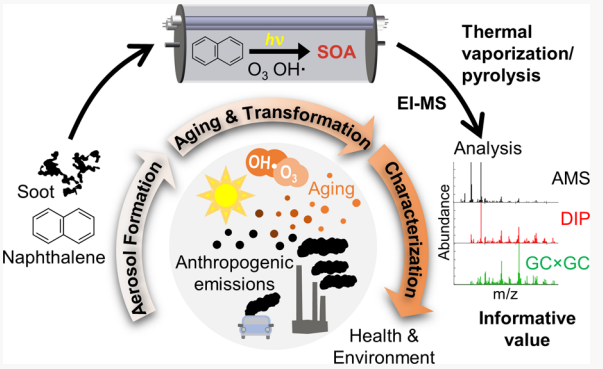

KEYWORDS: *secondary organic aerosols, comprehensive two-dimensional gas chromatography, aerosol mass spectrometry, direct inlet probe, high-resolution mass spectrometry, thermal fragmentation, particulate matter, electron ionization*

1. INTRODUCTION

Atmospheric aerosol is a suspension of liquid or solid particles in air. These mixtures of solid, liquid, and volatile gaseous organic and inorganic components can undergo chemical reactions and physical alteration. A major source of organic aerosol is the atmospheric oxidation of volatile organic compounds (VOCs) by atmospheric oxidants, such as hydroxyl ($OH^{\bullet}$) and nitrate ($NO_3^{\bullet}$) radicals as well as ozone (O_3), generating secondary organic aerosols (SOAs).[1,2] Throughout the atmospheric lifetime of aerosols (up to ∼2 weeks), continuous chemical aging leads to the generation of highly complex organic mixtures and the introduction of hetero atoms, such as oxygen and nitrogen.[3] As a result, atmospheric aging can rapidly alter the physicochemical composition of aerosols, thus affecting their impact on human health, climate, and environment.[4]

To understand the impact of this transformation process on health and environment, a comprehensive characterization of SOA in terms of its chemical and physical properties is required. In practice, this can be done by both online and offline techniques. Mass spectrometry (MS) has established

Received: February 4, 2022
Revised: April 14, 2022
Accepted: April 15, 2022
Published: May 6, 2022

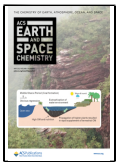

itself as a key technique for the investigation of such complex mixtures of organic compounds.[5] Although all mass spectrometric techniques in general are based on the ionization of molecules and their characterization as ions by mass and charge, they differ in their informative value and fields of application. Electron ionization (EI), also known as "electron impact ionization", is a very commonly used ionization method in MS due to its high sensitivity and molecular specificity toward complex organic mixtures. During EI, the energy of accelerated electrons is transferred to molecules in the gas phase, which leads to ionization and fragmentation of the parent molecule. The standardized application of 70 eV for EI has a high ionization efficiency and is almost universal for organic compounds and results in reproducible fragmentation, which is beneficial for the identification of organic compounds due to the availability of large spectral libraries for EI−MS spectra. This is typically done with gas chromatography MS (GC−MS) approaches. However, compared to "soft" ionization techniques (e.g., chemical ionization, photo ionization, and electrospray ionization), which result in a limited degree of analyte fragmentation, EI is a "hard" ionization technique; thus, as a result of the induced fragmentation, the molecular ion is often not detected. This makes data interpretation more challenging for superimposed spectra or compound spectra not found in spectral libraries.[6] Nonetheless, interpretation rules for mass spectral fragmentation are well-developed for EI−MS and fragmentation pathways are well described due to the consistent and fragment-rich mass spectra.[7]

At present, the most common MS system for online in-situ aerosol analyses in real time is the aerosol MS (AMS).[8] The working principle of the AMS is based on an aerodynamic lens system to sample sub-micron aerosols into vacuum. Particulate matter (PM) is aerodynamically sized by determining the terminal velocity measured in a particle-sizing chamber. After rapid thermal vaporization/pyrolysis on a heated surface of 600 °C, the detection occurs by 70 eV EI−MS. Herein, the high resolution time-of-flight AMS (HR−TOF−AMS) has some advantages over the quadrupole configuration of the MS such as improved sensitivity, time resolution, and mass resolution.[9,10] This enables the determination of the elemental composition and oxidation states of organic aerosol,[9,11,12] whereas molecular information is limited due to the fragmentation induced by pyrolysis and ionization processes.[13]

Thermal desorption (TD)−GC−MS is the state-of-the-art technique for the offline analysis of collected aerosol and allows the separation and identification of VOC and semivolatile organic compounds. However, especially for the analysis of highly complex environmental samples, the separation of the multitude of compounds by one-dimensional GC is limited due to its peak capacity. Therefore, for the chemical characterization of complex matrices on a molecular level, comprehensive two-dimensional gas chromatography (GC × GC) has gained attention as a powerful separation technique since the early 2000s.[5] Since then, GC × GC has been used in numerous studies[14−18] to resolve a large number of compounds present in atmospheric aerosols. In GC × GC, two capillary columns with different physicochemical characteristics are coupled by a modulator. The mixture of evaporated analytes is successively chromatographically separated by two independent orthogonal separation mechanisms, resulting in a two-dimensional separation. The increased peak resolution is a significant advantage for EI−MS library searching, leading to more confident peak identification. Also, for the great number of compounds commonly present in environmental samples, covering a wide range of concentrations, the increased separation power has been shown to be most useful, especially when GC × GC is coupled to a TOFMS, which acquires complete mass spectra in fractions of a second.[5] Offline chromatographic separation prolongs analysis time and requires previously collected sample material, which comes along with a low temporal resolution.

A further experimental approach for the chemical characterization of aerosol particles is direct inlet probe (DIP)−MS. DIP is one of the oldest introduction techniques for MS[19] and has been applied for high-boiling petroleum samples,[20,21] polymers,[22] or biomass.[23,24] Despite this, DIP has only rarely been used for aerosol characterization.[25] In DIP, the sample is thermally ramped and vaporized under vacuum conditions directly in the MS ion source. Moreover, the application of direct inlet probe—HR and accurate mass TOF MS (DIP−HRTOFMS) through usage of a multireflection MS with resulting high mass resolution is particularly useful to assign the elemental composition of superimposing mass fragments sharing the same unit masses. Nevertheless, as a direct mass spectrometric technique, the separation of compounds is limited to their volatility profile. Furthermore, DIP measurements require high amounts of sample material.

This study was designed to investigate the complementarity of these three different EI mass spectrometric techniques for the determination of SOA components. Hereby, both HR−TOF−AMS as an online technique and TD−GC × GC−TOFMS as an offline technique account for two established methods in the field of atmospheric aerosol chemical characterization. As a new emerging technique for the chemical characterization of complex environmental matrices, we further applied DIP−HRTOFMS measurements. From here on, the techniques will be abbreviated as AMS, GC × GC, and DIP. Although AMS, DIP, and GC × GC share certain similarities regarding sample introduction by thermal vaporization and detection by EI−TOFMS, they greatly differ in their general working principle. Thus, by applying these three techniques, we target different fractions of the organic aerosol. For GC × GC, the application range is limited to volatile and semivolatile compounds, which are thermally desorbed from filters and evaporated in a protective helium atmosphere. Thermal fragmentation during the sample introduction of organic aerosols can be expected for AMS and DIP, but is not as pronounced for GC × GC, which preserves the chemical structure of the molecules. Conversely, the AMS can vaporize and detect polar compounds of high molecular weight as thermal fragments due to the applied flash-vaporization process under vacuum conditions. During this process in the vaporizer, particles are either flash-vaporized very rapidly within a few tens of microseconds, slowly vaporized or thermally decomposed.[26] DIP enables the vaporization of thermally labile compounds under controlled heating due to the reduced pressure, increasing the range of high-molecular weight compounds which are volatilized before thermal decomposition.

These three techniques were applied for the chemical characterization of SOA generated by the OH-dominated photochemical aging of naphthalene (NAP) mixed with flame-generated propane soot particles (SPs) as condensation nuclei from a combustion aerosol standard (CAST) burner. Photochemical aging was performed by means of a potential aerosol mass (PAM) oxidation flow reactor (OFR). The PAM

https://doi.org/10.1021/acsearthspacechem.2c00039
ACS Earth Space Chem. 2022, 6, 1358−1374

OFR[27,28] was used to experimentally simulate different aging conditions by maintaining defined concentrations of $OH^{\bullet}$ and O_3 by regulating the intensity of the VUV-lamps and the relative humidity. In this simulation, the generated SP represented air pollution by primary combustion emissions.[29] NAP, which is mainly formed during combustion processes (e.g., fossil fuel combustion, biomass burning, chemical, and metal industries)[30] with potential for SOA formation,[31] served as a typical anthropogenic precursor model compound for generating anthropogenic SOA proxy (SOA_{NAP}-SP) by atmospheric processing.

This study was designed to evaluate both state-of-the-art and emerging techniques in the field of aerosol science, covering on-, at-, and off-line approaches, in the context of their informative value for studying the complex chemistry of SOA (oxidation state, volatility, and molecular composition). The objective of this study is to evaluate the analytical tool set for investigations on the chemical complexity of atmospheric processes. Furthermore, we aim to demonstrate the complementarity, but also the differences of HR−TOF−AMS, DIP−HRTOFMS, and TD−GC × GC−TOFMS on the basis of a matrix, which is of high relevance for atmospheric chemistry. These findings could help understand the possible limitations of the applied techniques and contribute to a better interpretation and assessment of the results with possible implications for human health, climate, and environment.

2. MATERIALS AND METHODS

2.1. Experimental Setup for Aerosol Generation, Online Characterization, and Filter Sampling. The experimental setup has been previously described in detail by Offer et al.[32] and Zhang et al.[33] and is only briefly presented here. Elemental carbon (EC)-rich SPs with a geometric mean diameter of about 100 nm were produced by means of a miniature CAST soot generator (model 5201C, Jing Ltd., Switzerland). The SPs, serving as a condensation sink for SOA, were mixed with the vapor from pure NAP (Sigma-Aldrich, 147141-25G, 99%), serving as an anthropogenic precursor model compound for the subsequent OFR experiments.

This mixture of SPs and NAP was then diluted with humidified air (moistened by a PermaPure humidifier FC125-240, Perma Pure, USA) in an ejector diluter (model VKL 10, Palas GmbH, Germany) before entering the OFR (PAM reactor[27,28]) for the experimental simulation of atmospheric photooxidation (SOA formation and aging) by OH radicals. During aging, the low volatile SOA condensed onto the SP, resulting in predominantly internally mixed particles with organic coatings and SP cores (SOA_{NAP}-SP) as was shown by transmission electron microscopy images in Offer et al.[32] As we investigated 4 times lower concentrations in this study, some smaller particles (<50 nm) were produced, indicating the simultaneous occurrence of externally mixed particles. Differences in aged aerosol composition were experimentally assessed by varying the aging conditions in the PAM reactor, such as variations in relative humidity of either 40% or 70% and varying OH equivalent aging times (2−9 days). The OH-radical and ozone concentrations were adjusted and regulated by setting the light intensity of two VUV lamps with emission lines at 185 and 254 nm (BHK Inc., CA, USA) in the PAM reactor. The atmospheric OH aging equivalent time was estimated by monitoring the decay of added deuterated butanol (D_9-butanol, 98% isotopic purity; Sigma-Aldrich, Germany) with a proton-transfer reaction MS (Ionicon, Austria),[34] under the assumption of an average ambient OH concentration of 10^6 molecules cm^{-3} and a rate constant of 3.4×10^{-12} cm^3 s^{-1} for D_9-butanol.[34,35] For each 1 h experiment of constant conditions, 0.25 mg m^{-3} SP and 1 mg m^{-3} NAP, as well as 80 ppbV D_9-butanol were introduced into the PAM. The aging of NAP under the described conditions was strongly dominated by $OH^{\bullet}$ photooxidation.[36] Calculations accounting for the different rate constants of NAP toward OH radicals [$k_{NAP}(OH) = 23 \times 10^{-12}$ cm^3 molecules s^{-1}] and O_3 [$k_{NAP}(O_3) < 0.02 \times 10^{-17}$ cm^3 molecules s^{-1}][37,38] as well as the concentration of the respective oxidant in the PAM show that NAP has a much higher reactivity toward $OH^{\bullet}$ compared to O_3 by a factor of 1000 or greater (Table S1). The table also contains the respective aging conditions (OH atmospheric aging equivalent and relative humidity) for the 11 conducted OFR experiments (Exp1−Exp11).

The produced aged SOA was characterized in terms of its physicochemical properties, which comprised both online and offline analyses. For the characterization of the organic constituents in the particulate phase, HR−TOF−AMS (Aerodyne Inc., Billerica, MA, USA) was applied and will be described in more detail in the following section.

PM was sampled on pre-baked (5 h at 500 °C) quartz fiber (QF) filters (T293, Ahlstrom-Munksjö, Finland) over 1 h using a pre-impactor to remove particles larger than 2.5 μm ($PM_{2.5}$). For analyses by TD−GC × GC−TOFMS, 10-fold diluted PM was sampled on 47 mm QF filters with a total sampling volume of 600 L at a flow rate of 10 L min^{-1}. Furthermore, EC and organic carbon (OC) were determined from the same QF filters (0.503 cm^3 punch) using a thermal−optical carbon analyzer (Desert Research Institute model 2001A, Atmoslytic Inc., Calabasas, CA, USA) following the IMPROVE_A protocol.[39] For analyses by DIP−HRTOFMS, QF filters with an effective diameter of 18 mm were collected directly from a non-diluted auxiliary flow at the outlet of the PAM. This flow was used to maintain a constant total PAM flow of 8 L min^{-1}, independently of other instrumentation connected to the PAM outlet. This resulted in a total sampling volume between 100 and 200 L at flow rates between 1.7 and 3.3 L min^{-1} (60 min collection time). The collected filters were individually stored at −20 °C before offline analysis by TD−GC × GC−TOFMS and DIP−HRTOFMS, respectively. No unexpected or unusually high safety hazards were encountered during this study.

2.2. Instrumental Descriptions of the AMS, DIP, and GC × GC. For a general overview, the key parameters and features of HR−TOF−AMS, DIP−HRTOFMS, and TD−GC × GC−TOFMS are given in Table 1. Further operating conditions of the MS are given in Table S2 for all three techniques. Schematic diagrams of each technique are shown in Figure S1.

AMS. A detailed description of the HR−TOF−AMS (Aerodyne Research, Inc.) can be found elsewhere.[9] In brief, the AMS was developed to measure non-refractory aerosols in the size range between 50 and 1000 nm in diameter in real time.[13] This was technically realized by an aerodynamic lens system and a vaporizer directly at the ionization site made of tungsten and heated to 600 °C.[40] The AMS has a few distinct modes of operation. First, the AMS can operate in the particle-TOF (PTOF)-mode and the MS-mode. The MS-mode is used to measure the mass spectrum of the aerosol stream, whereas the PTOF-mode is used to calculate the particles' aerodynamic diameter.[9,41] The MS-mode works by repeatedly measuring the

https://doi.org/10.1021/acsearthspacechem.2c00039
ACS Earth Space Chem. 2022, 6, 1358−1374

Table 1. Comparison of the Applied Key Parameters and Features of HR−TOF−AMS, DIP−HRTOFMS, and TD−GC × GC−TOFMS Measurements[a]

	HR−TOF−AMS	DIP−HRTOFMS	TD−GC × GC−TOFMS
analyses time	online (4 min/cycle)	atline (10 min)	offline (3 h)
thermal sample introduction	flash vaporization/pyrolysis (isotherm at 600 °C); vacuum condition (10^{-9} to 10^{-6} mbar)	vaporization and pyrolysis by ramped heating (gradient 2 K s^{-1}); vacuum condition (10^{-6} to 10^{-3} mbar)	gradual TD (gradient 2 K s^{-1}); >1 bar overpressure; inert helium atmosphere
vaporization temperature (accessible content)	600 °C (non-refractory aerosols)	40−400 °C (non-refractory aerosols)	40−300 °C (volatile/semivolatile compounds)
mass resolution	2.1 × 10^3* (m/z 200)	2.5 × 10^4 (m/z 218.99)	1.3 × 10^3 (m/z 218.99)
mass accuracy	<28 ppm* (m/z 10−200)	<2 ppm (m/z 218.99)	45 ppm (m/z 218.99)
mass range	9−459 Da (analyzed range: 10−200 Da)	15−600 Da	20−700 Da
chemical/physical information	superimposed spectra; fragment ion peaks (thermal & EI fragments); size segregation of PM	superimposed spectra; fragment ion peaks (EI & thermal fragments); thermal pre-separation according to volatility	individual spectra for each compound; fragment ion peaks (mostly EI fragments); separation of individual compounds by chromatography

[a]The specified mass resolution for a single peak corresponding to singly charged ions at a mass m are depicted as $m/\Delta m$, where Δm is the width of the peak defined as full width at half height (FWHH); parameters from the AMS marked with * are taken from literature[9] and were not experimentally determined for our study.

mass spectrum of the aerosol stream and air beam together, which is defined as MS-O (mass spectrum open). Then, the air beam alone is measured by blocking the aerosol stream with the chopper, which is defined as MS-C (mass spectrum closed). By doing this, the air beam can be subtracted from the combined aerosol and air beam and the aerosol composition itself can be determined. We applied the AMS with a mass resolution of 2.1 × 10^3 (specification for m/z 200).[9] The PTOF-mode uses the chopper to interrupt the aerosol stream repeatedly, thereby determining the aerosol TOF to specify the particle size. Throughout all the experiments, the AMS was operated in V-mode and PTOF-mode alternating with 15 s MS-C, 15 s MS-O, and 30 s PTOF, which was repeated four times for each measurement cycle. This results in a time resolution of 4 min, which was chosen due to the stable nature of the aerosol generation and aging, with little to no changes in aerosol composition within each experiment. An ionization efficiency calibration was regularly performed before and after a set of experiments using a set of ammonium nitrate particles.[13,41,42] Furthermore, after each set of three or four experiments, a filter measurement was taken as a blank run, which was used for flow and background correction of the AMS.

All analysis of the AMS data was done in the PIKA software[9] and assuming that for SOA_{NAP}-SP there was only significant contribution of carbon, oxygen, and hydrogen, for elemental analysis, the values were calculated based on Aiken et al.[43] The output from the AMS is a sum mass spectrum, which displays the linear superposition of the mass spectra of individual organic species based on their concentrations.

DIP. The general setup for the DIP−HRTOFMS measurements, which were performed on a Pegasus GC-HRT 4D (LECO, USA) equipped with direct inlet probe (SIM GmbH, Germany), was previously described.[21] For the measurements of SOA_{NAP}-SP, 1 μL toluene containing 15 ng fully deuterated benzo[ghi]perylene (D12, 98%) (Cambridge Isotope Laboratories, Inc.) as internal standard was applied on filter punches with a diameter of 2 mm, which were transferred to single-use sample containers placed in the vessel-holder of the push rod. After an equilibration time of 2 min, the push rod transferred the sample into the ion source, where a temperature gradient was applied from 40 to 400 °C (ramping with 2 K s^{-1}). Instrumental parameters for the MS are presented in the Supporting Information (Table S2). Filter samples were measured in a randomized sequence for a total of four replicates per filter. Every fifth measurement was a blank QF filter with internal standard to determine the background signal. Perfluorotributylamine (PFTBA) was continuously introduced to the ion source for internal mass calibration.

Data processing was performed by home-built MATLAB (The MathWorks Inc., MA, USA) scripts. The raw data were normalized to the total ion count of m/z 288.1687 (internal deuterated benzo[ghi]perylene standard, $C_{22}D_{12}$), background signals from PFTBA, O_2, N_2, H_2O, and the internal standard were removed and found accurate m/z values were assigned to elemental compositions within a mass window of 5 ppm according to the smallest error. Finally, obtained data were corrected by considering the average of at least two background measurements before and after the position within the sequence. Alternatively to the summed spectrum, each DIP measurement can output temperature resolved mass spectra, which are aligned by the exact masses of assigned sum formula. This results in an m by n matrix with m corresponding to the

https://doi.org/10.1021/acsearthspacechem.2c00039
ACS Earth Space Chem. 2022, 6, 1358−1374

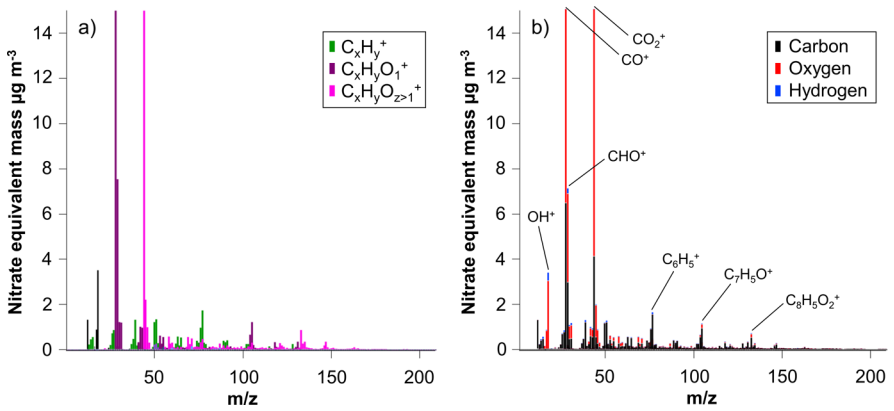

Figure 1. HR−TOF−AMS mass spectra for SOA_{NAP}-SP (Exp1, atmospheric OH aging equivalent ≈ 4 d; 40% rH) with the signal divided into (a) organic categories of $C_xH_y^+$, $C_xH_yO_1^+$, and $C_xH_yO_{z>1}^+$ and (b) elemental signals (C, H, O). The mass spectra are given in $\mu g\ m^{-3}$ based on the nitrate equivalent mass. Ammonium nitrate is used for the calibration of the AMS which allows the determination of the ion mass as nitrate equivalent mass.

number of elemental composition assignments and n corresponding to the DIP desorption temperature.

GC × GC. For analyses by TD−GC × GC−TOFMS we employed a Pegasus BT 4D GC × GC TOF mass spectrometer (LECO, USA) in combination with an OPTIC-4 GC inlet system (GL Sciences, Netherlands). Helium was applied as the carrier gas. A circular filter punch (diameter d = 6 mm) was introduced to the OPTIC-4 inlet system. For the removal of oxygen, the inlet purge time was set to 100 s at a column flow of 1 mL min^{-1} and a split flow of 100 mL min^{-1}. In order to thermally desorb the analytes from the filter, we applied a gradual TD gradient of 2 K s^{-1} from 40 to 300 °C at a desorption flow rate of 2.6 mL min^{-1} in the splitless mode. The compounds were cryogenically focused at −100 °C at the head of the column via the cryogenic trapping system CryoFocus-4 (GL Sciences, Eindhoven Netherlands). After TD, the column flow and the split flow were reduced to 1 and 100 mL min^{-1}, respectively, and the analytes were released from the cryotrap using a heating rate of 2 K s^{-1} from −100 to 300 °C to introduce them onto the GC column.

A 60 m long SGE BPX5 capillary column (5% phenyl polysilphenylene-siloxane, 60 m, 0.25 mm i.d., 0.25 μm df, SGE, Australia) was used to separate analytes based on volatility in the first dimension and combined with a 1.5 m long SGE BPX50 capillary column (50% phenyl polysilphenylene-siloxane, 1.5 m, 0.1 mm i.d., 0.1 μm df, SGE, Australia), allowing separation based on polarity in the second dimension. The initial primary oven temperature of 40 °C was held for 10 min and then ramped at 2 K min^{-1} to 250 °C, followed by a faster gradient of 5 °C min^{-1} to 350 °C which was held for 10 min. The secondary oven temperature offset was +20 °C to the primary oven and the modulator temperature offset was +15 °C to the secondary oven temperature. The modulation period was 5 s with a hot pulse time of 1.5 s. The MS transfer line temperature was 300 °C. Mass acquisition was from 20 to 700 Da at 100 spectra s^{-1}. The electron energy was 70 eV and the ion source temperature was 250 °C. Data acquisition and processing was carried out using the ChromaTOF software version 5.5 (LECO, USA). A first tentative identification of the compounds was done by comparing the deconvoluted (peak true) mass spectra with the US National Institute of Standards and Technology (NIST) library (NIST MS Search 2.3, 2017).

For GC × GC, the output matrix consists of multiple mass spectra that are a series of m/z and intensity pairs for each chromatographic data point. Compounds are separated along the chromatographic dimensions and are assigned to peaks. The data are typically displayed in a peak list and contour plot.

3. RESULTS AND DISCUSSION

In the first section, we will describe the information derived from the three different EI−MS techniques in order to evaluate their individual analytical performances for the characterization of SOA_{NAP}-SP (Sections 3.1−3.3). For this, we show results from one exemplary experiment/sample (Exp1) with an atmospheric OH aging equivalent of ≈4 d at 40% relative humidity. In the second part (see Section 3.4), we will evaluate and compare the spectral data from AMS, DIP, and GC × GC, as well as the obtained information on atmospheric aging/oxidation state and molecular composition of the SOA across different aging steps for the complete data set (see Table S1).

3.1. Characterization of SOA_{NAP}-SP by HR−TOF−AMS.

HR−TOF−AMS was utilized for the online characterization of SOA_{NAP}-SP and to determine the total organic aerosol along with its bulk composition and integral properties. The AMS determines the signals of specific ions by fitting a Gaussian-like function, which contains mathematical expressions for the average peak shape, to the background-subtracted mass spectral data and integrating the fitted peaks.[9,44] The distinction of ions from the peak at a specific unit mass is done through single area integration, where a list of possible ions is selected by the user to give the best possible peak shape fit to each unit mass. The mass resolution of the AMS is about 2.1 × 10^3 and determines the accuracy of the attributed composition of the measured ions. Based on the determined ion list, the mass spectrum is subsequently separated into organic families. An example for a stacked bar graph for different organic families based on an AMS spectrum is shown in Figure 1a. The most common organic families in the case of SOA_{NAP}-SP were organic molecules with z number of oxygen atoms, as well as hydrocarbons.

Most commonly, the AMS is used for quantitative measurements of the bulk chemical composition of organic aerosols and to determine the elemental ratios as an indicator of aerosol age and volatility, such as the oxygen to carbon ratio (O/C) and the hydrogen to carbon ratio (H/C).[11,45] The elemental analysis can be calculated as the weighted average of the organic ion signals throughout the mass spectrum[11,43] and

https://doi.org/10.1021/acsearthspacechem.2c00039
ACS Earth Space Chem. 2022, 6, 1358−1374

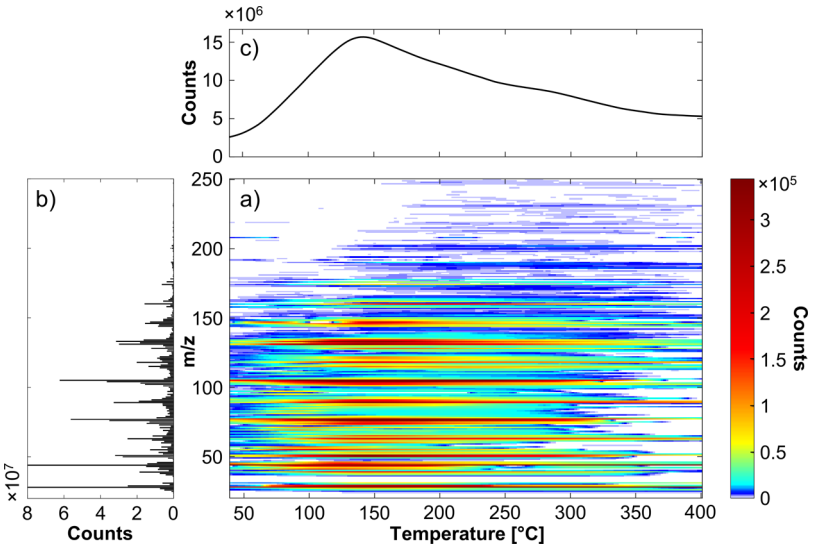

Figure 2. DIP−HRTOFMS thermogram of SOA_{NAP}-SP (Exp1, atmospheric OH aging equivalent ≈ 4 d; 40% rH): (a) m/z signals of detected ions are represented as a function of the temperature of the DIP. The color code depicts the abundance of found ions. The summed mass spectrum (b) and the total ion chromatogram (TIC) for the whole temperature range (c) are shown next to the respective axes. Figure 2b will be used in Section 3.4 to compare the spectra of the applied techniques.

is plotted as an elemental mass spectrum (Figure 1b). The resulting elemental compositions by mass for SOA_{NAP}-SP at an atmospheric OH aging equivalent time of ≈4 d and 40% rH were 51 ± 1% C, 4 ± 1% H, and 45 ± 1% O for m/z 10−200 (errors associated with average values are the standard deviations from all data points from the 1 h experiment). The largest contribution to the oxygen signal is represented by the CO_2^+ ion, which makes up approximately 22% of the total oxygen signal.

Another method to assess the composition of the organic aerosol is based on the sum of the total signal at m/z 43 and m/z 44, which is normalized to the total organic aerosol and referred to as f43 and f44, respectively. Specifically, f43 is mainly attributed to $C_2H_3O^+$ in oxidized organic aerosols and to $C_3H_7^+$ in hydrocarbon such as organic aerosols, whereas f44 is dominated by the CO_2^+ contribution. A major difference between these two compounds is their origin. CO_2^+ (f44) as a thermal fragment usually stems from acids and other highly oxidized functional groups. This means, that as the equivalent photochemical age of the aerosol increases and more highly oxidized compounds are formed, the f44 fraction will increase. In comparison, f43 ($C_2H_3O^+$ and $C_3H_7^+$) indicates a lower degree of oxidized functional groups and thus decreases with the increase in aerosol age.

3.2. Characterization of SOA_{NAP}-SP by DIP−HRTOFMS. As a second technique for the characterization of SOA_{NAP}-SP, we used DIP−HRTOFMS. In contrast to the AMS, SOA is not analyzed in real-time; instead, the particles have to be collected on filters, which could be analyzed atline at a later time point. In order to ensure the necessary high filter loading for DIP measurements, the filter samples for analyses were collected from the nondiluted flow directly after the PAM reactor. A small piece of a loaded filter is placed in an aluminum crucible, which is directly introduced in the ion source. By heating the sample to 400 °C at 2 K s^{-1}, semivolatile organic constituents are volatilized and conducted to gas phase EI and mass spectrometric analysis. Additional information about the volatility of the analytes can be obtained by applying a defined thermal gradient, which leads to progressive volatilization of the sample constituents. Moreover, in the ion source vacuum, molecules are vaporized at much lower temperatures compared to their atmospheric boiling points according to the Clausius−Clapeyron relationship. Therefore, DIP was used as thermal analysis technique in previous studies for the characterization of high boiling point complex matrices such as petroleum samples.[20,21] After EI, the generated ions are separated and detected in a multi-reflectron TOF mass spectrometer, which combines fast data acquisition and complete mass spectra information over a wide mass range with high mass resolution. In contrast to other high-resolution mass spectrometric techniques, such as Fourier-transform ion cyclotron MS instruments, this makes HRTOFMS attractive for coupling to fast analytical approaches[46,47] such as chromatographic or other highly time-dynamic processes. Compared to the AMS with one reflection in V-mode and three reflections in W-mode, the high-resolution TOFMS platform used for the DIP measurements allows up to 64 reflections. For this study, we operated the system in the most commonly used 32 reflection mode, achieving a mass resolution of >2.5 × 10^4 and a mass accuracy of <2 ppm (instrumental specification for m/z 219).

In the context of aerosol chemistry and in particular for the study of SOAs, especially the oxidation and nitration of SVOCs, aromatization and the reaction pathways are of major interest. Therefore, the CH_4/O (0.0364 Da) and CH_2/N (0.0126 Da) mass splits[46] are critical for the differentiation of isobaric species in this research field. The multi-reflectron TOFMS platform enables reliable elemental composition assignments in these complex mixtures at m/z up to 300. However, for this study on photooxidation of NAP mixed with SPs, no nitrogen can be expected. Thus, we limited the potential elemental compositions to $C_{0-50}H_{0-100}O_{0-5}$. The DIP−HRTOFMS mass spectrum with the signal divided into different organic categories is shown in Figure S2 and shows similar elemental composition assignments as the AMS (Figure 1).

A drawback from the direct insertion of the push rod from ambient conditions is the introduction of background signals.

https://doi.org/10.1021/acsearthspacechem.2c00039
ACS Earth Space Chem. 2022, 6, 1358−1374

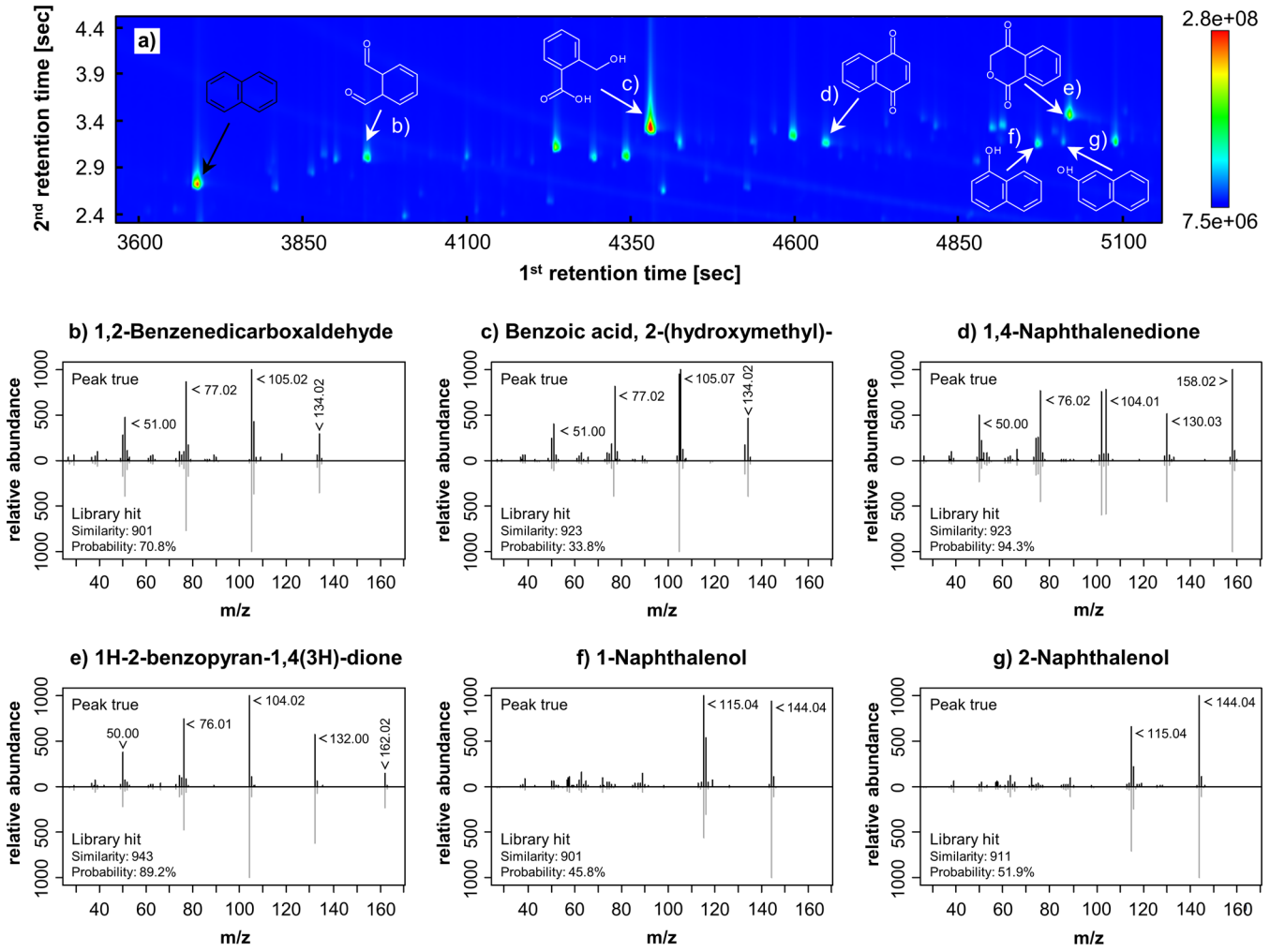

Figure 3. TD−GC × GC−TOFMS contour plot of SOA_{NAP}-SP (Exp1, atmospheric OH aging equivalent ≈ 4 d; 40% rH) (a). Tentative assignment of representative peaks to their molecular structure based on comparison with NIST mass spectral library (match quality ≥ 70%) and retention indices. Deconvoluted spectra (peak true) and NIST library hit spectra are shown for 1,2-benzenedicarboxaldehyde (b), benzoic acid, 2-(hydroxymethyl)- (c), 1,4-naphthalenedione (d), 1*H*-2-benzopyran-1,4(3*H*)-dione (e), 1-napthalenol (f), and 2-naphthalenol (g). Assignment of the two isomers, 1-naphthalenol (f) and 2-naphthalenol (g), could additionally be confirmed via retention times.

Therefore, samples from the non-diluted auxiliary flow had to be used to improve spectral quality by maximizing the relative abundance of the analytes compared to the background signal. Moreover, each filter sample was measured four times and the spectra were corrected by measurements of blank QF filters.

Figure 2a depicts detected ions as a function of the temperature and *m*/*z*. Typically for mixtures of organic compounds, larger molecules are detected with the increase in temperatures, which is reflected by an increase of *m*/*z* during the thermal ramping of the DIP. Although there is a clear trend to increasing masses, also smaller ions from EI fragmentation reactions are observed in high abundances during the whole run (Figure 2b). In the lower temperature range, between 50 and 200 °C, the major contribution of SVOC from SOA_{NAP}-SP (at an atmospheric OH aging equivalent time of ≈4 d and 40% rH) is detected (Figure 2c).

For an estimation of boiling points under normal conditions, the reduced pressure in the ion source has to be considered. In a previous study,[21] it was determined that the atmospheric equivalent boiling point is approximately 300−350 °C higher compared to the detection temperature with DIP−HRTOFMS. This was also confirmed within this study by comparing the atmospheric boiling point of the internal standard (deuterated benzo[ghi]perylene) to its DIP-detection temperature (Figure S3). Because of this boiling point reduction, most of the organic matrix detected at around 140 °C (Figure 2c) would transfer to boiling point temperatures of approximately 450−500 °C under atmospheric conditions. Nevertheless, this direct comparison between ambient and reduced pressure thermal analysis techniques is limited because decomposition and pyrolysis are not reflected in the same manner.

A DIP analysis could be considered similar to an evolved gas analysis (e.g., thermogravimetric analysis−MS), for which two distinct phases are generally distinguished; a TD phase (roughly <300 °C) and a thermal degradation or pyrolysis phase (roughly >320 °C) for organic matter.[48] Although for DIP these phases are not distinct, the transition desorption (mainly EI fragments) and thermal degradation (thermal fragments are further ionized) become evident when having a look at the spectra obtained at certain temperatures (40, 200, 400 °C) throughout the DIP run (Figure S4). With the increase in temperature, a shift toward the thermal fragment ions CO^+ (*m*/*z* 28) and CO_2^+ (*m*/*z* 44) is observed in the

https://doi.org/10.1021/acsearthspacechem.2c00039
ACS Earth Space Chem. 2022, 6, 1358−1374

mass spectra. However, although thermal decomposition of highly oxidized species can be observed already at temperatures below 100 °C, a certain part of the non-volatile sample matrix, such as extremely low volatility organic compounds (ELVOCs), can only be targeted by thermal decomposition at temperatures higher than 400 °C.[49] Because the maximum temperature of DIP−HRTOFMS is capped at 400 °C, complete pyrolysis cannot be guaranteed.

3.3. Characterization of SOA_{NAP}-SP by TD−GC × GC−TOFMS. The application of TD−GC × GC−TOFMS enables the interpretation of the results on a molecular level due to the separation and identification of individual compounds. Thus, it allows a selective analysis of the vaporizable aerosol compounds. In GC × GC, two capillary columns with different physicochemical characteristics are coupled by a modulator. The analytes are chromatographically separated by two independent orthogonal separations in the first and second dimension. This leads to greatly enhanced resolution capabilities and a high peak capacity compared to one-dimensional GC[50] or thermal separation techniques (e.g., DIP) and has been shown to be most useful (especially when GC × GC is coupled to a TOFMS) for the analyses of environmental samples for which a great number of compounds commonly are present at low concentrations.[14−18]

Figure 3a shows a GC × GC−TOFMS contour plot for SOA_{NAP}-SP with the assignment of exemplary peaks to their molecular structure (Figure 3b−g). The measurement was done with a nonpolar column in the first dimension and a mid-polar column in the second dimension, from which follows that compounds were first separated according to their vapor pressures, corresponding to the respective carbon number of a homologues row and boiling point on the *x*-axis, and by polarity on the *y*-axis. The separation capabilities of GC × GC with 200,000 and 9000 theoretical plates for the 60 m first- and 1.5 m second-dimension column, respectively, far exceed the separation capabilities of thermal analysis techniques for pre-separation (e.g., DIP) with one theoretical plate.[51] The more polar secondary dimension column incorporates a higher content of phenyl functional groups bound to the siloxane backbone which leads to $\pi-\pi$ interactions between the stationary phase and π-active compounds such as polycyclic aromatic hydrocarbons.[52] Thus, the second dimension separation of aging products from NAP oxidation which are characterized by their aromatic nature proved very effective. This special selectivity allows additional classification/evaluation of the eluting compounds based on their location in the 2D plot.

Due to the application of a standardized ionization energy of 70 eV, the identification of unknown peaks is possible by performing a mass spectral library search, for example, with the NIST library. Thereby, peaks are assigned to chemical compounds based on the similarity of the respective deconvoluted (peak true) mass spectrum with the reference library mass spectrum by comparison of the relative intensities of the matching m/z values. The increased peak capacity and well-resolved peaks in GC × GC, generally help to obtain high-quality library matches with high similarity and probability scores. Both are numbers defined by the NIST search algorithm. The similarity score expresses how closely two spectra match with a number between 0 and 1000, whereas the probability score expresses the relative likelihood that a matching compound has been assigned correctly, which also takes compounds with similar spectral fragmentation patterns into account. The representative peaks highlighted in Figure 3 all have been assigned library hits with similarity values above 900. Additional validation of the assigned library hits is possible via retention indices, which is especially useful for the identification of (stereo)isomers, for which the mass spectrum alone may not be a sufficient criteria. Due to the applied chromatography, compounds such as 1-naphthalenol (Figure 3f) and 2-naphthalenol (Figure 3g) could be chromatographically separated up to its isomeric composition, which supports a reliable assignment of the elemental composition of NAP SOA and therefore allows an investigation of the (dominating) reaction pathway.

Because GC × GC can identify single compounds, it enables the tracing of possible reaction pathways of the photochemical degradation of NAP or allows a first estimate of the toxicological relevance of an aerosol based on its individual constituents. In the exemplary case of the formation of naphthalenol, the first step is the addition of an OH radical at the C_1 or C_2 position of NAP, forming a pre-reactive molecular complex (hydroxyhexadienyl-type radical), from which the first-generation product naphthalenol is formed.[53] 1-Naphthalenol and 2-naphthalenol, were both generated in significant yields, although the GC × GC analyses revealed that the abundance of 1-naphthalenol exceed that of 2-naphthalenol by a factor of 2.5. This is in line with results from Bernstein and co-workers who found the production of 1-naphthalenol to be favored over 2-naphthalenol by a ratio of 2:1 (personal communication to Ricca and Bauschlicher).[53,71] Naphthalenol may be further oxidized by other oxidants, such as hydroperoxides, and O_2 to naphthalenediones[54] for which cytotoxic effects are well known. 1,4-Naphthalenedione (Figure 3d) may cause oxidative stress in cells and affect redox signaling.[55] Similar products as we present in this study from the gas-phase reaction of NAP with the OH radical were identified by Lee and Lane[56] by GC × GC−TOFMS. In summary, GC × GC allows the analyses of individual compounds, which is of great relevance for an assessment of the effects of aerosols on health and environment.

Because the application range of GC is limited to volatile and semivolatile compounds due to the maximum applied TD temperature of 300 °C to avoid excessive thermal stress for the analytes in the inlet, higher-molecular-weight compounds preferably need to be investigated by DIP or AMS. Nevertheless, it further should be noted that pyrolysis (Py) could also be applied in combination with GC × GC. First investigations of a two-step TD/pyrolysis (TD/Py−GC × GC−TOFMS) approach for aerosol filter samples showed promising results for ambient aerosol characterization.[57] In the first TD step, (semi-)volatile compounds were detected without the formation of thermal degradation products, whereas in the second pyrolysis step, which was applied to the same filter, thermal fragmentation products of higher molecular weight compounds were detected. In this context, not only the maximum applied temperature for sample introduction could play an important role but also the applied heating gradient could influence the extent of thermal degradation products.

Apart from TOFMS also various other detectors such as quadrupole MS,[58] flame ionization detection,[58,59] and nitrogen chemiluminescence detection[60] have been coupled to GC × GC for analyses of atmospheric organic aerosols. It also has to be noted that GC × GC could also be used in combination

https://doi.org/10.1021/acsearthspacechem.2c00039
ACS Earth Space Chem. 2022, 6, 1358−1374

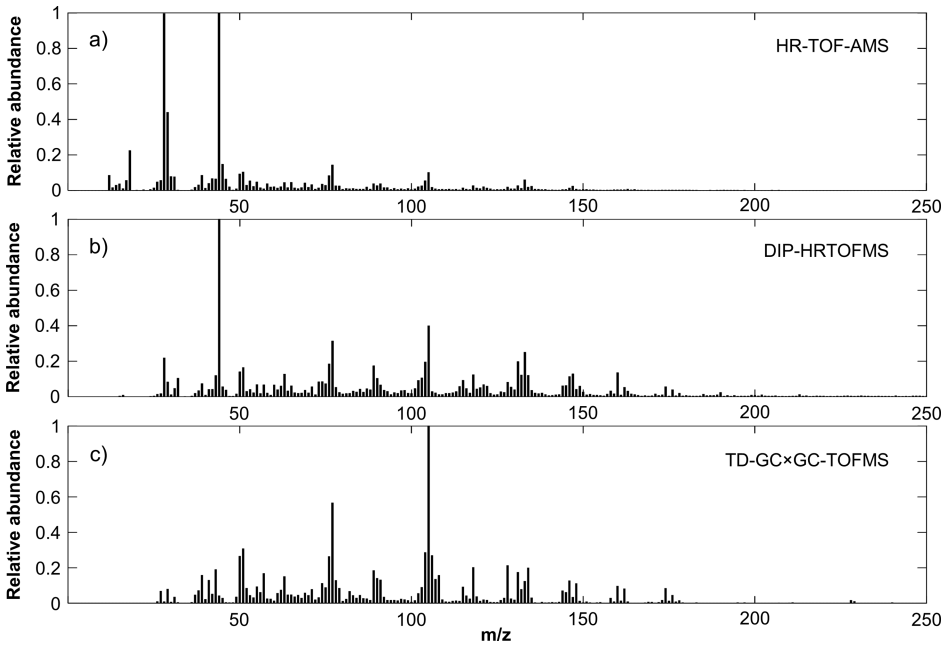

Figure 4. HR−TOF−AMS (a), DIP−HRTOFMS, (b) and TD−GC × GC−TOFMS (c) sum mass spectra of SOA_{NAP}-SP (Exp1, atmospheric OH aging equivalent ≈4 d; 40% rH).

with a high-resolution platform or even integrated into a DIP/GC × GC−HR−TOF hybrid system.[21]

3.4. Comparison. Although the three techniques are based on the thermal vaporization of aerosol particle constituents and detection by EI−MS (ionization energy of 70 eV), they differ in their application ranges. Furthermore, the applied techniques cover online to offline approaches and therefore, vary essentially in time resolution, which may be particularly important for specific analytes. In the case of, for example, highly reactive oxygen species (ROS), which are produced during the photochemical aging of NAP, their concentration may greatly be underestimated by offline methods due to their fast degradation.[33] In addition, sampling artifacts, as well as the storage and handling of QF filters, could affect the partitioning of the gas and particle phases compared to online methods.

On the other hand, also the different sample introduction systems play an important role for the accessibility of the different techniques. Because one of the major differences between analyses by AMS, DIP, and GC × GC is the maximum temperature, which is applied for the vaporization of the analytes, a closer look at the different OC fractions from thermal−optical carbon analyzer measurements could give a rough approximation of the accessible organic content. Following the Improve_A Protocol for EC/OC analysis,[39] the different temperature ranges for the OC fractions measured in 100% helium (OC1: 140 °C; OC2: 280 °C; OC3: 480 °C; OC4: 580 °C) can roughly be assigned to the temperature ranges of the three techniques, corresponding to OC1−OC2 for GC × GC (300 °C, inert helium atmosphere) and OC1−OC4 (with some restrictions described below) for DIP (400 °C, vacuum). While the AMS (600 °C, vacuum) also includes all four OC fractions, it cannot resolve them due to the flash vaporization process. Instead, the AMS determines the total organics along with their integral properties. Some restrictions to this comparison with the OC fractions also have to be noted for DIP. Due to the time delay of approximately 2 s needed to acquire one mass spectrum after sample introduction directly in the ion source under vacuum conditions, VOCs in the OC1 range cannot be completely gathered by DIP. On the other side, for OC4, despite the low pressure in the ion source, the DIP cannot reach temperatures for complete volatilization or pyrolysis of ELVOCs. Complete pyrolysis and capture of total organics can thus not be entirely assured.

In the case of SOA_{NAP}-SP, we observed decreasing concentrations of OC at aging times >4 days, whereas EC remains very stable across the different aging steps. Details on the EC/OC measurements across the different aging stages are shown in the Supporting Information (Figure S5). Upon photooxidation, fresh SOA is produced from gas-to-particle conversion. For such oxidized organic species, it has been shown that with photochemical aging, fragmentation reactions become increasingly important compared to functionalization, which leads to the production of small, volatile compounds which transition into the gas phase.[12,61,62] Hence, the OC content of the particle is decreased, which could explain the observed decrease of OC with aging. Simultaneously, functionalization reactions lead to the addition of oxygen-containing functional groups which subsequently leads to an increase of the absolute oxygen content in the particle.[61]

3.4.1. Summed Mass Spectra. The comparison of the summed mass spectra of the exemplary experiment/sample Exp1 (Figure 4) reveals major differences regarding sample introduction and working principle before detection by EI−MS (ionization energy of 70 eV) and gives an indication of whether the spectrum of the respective method is determined more by thermal or EI fragments.

The AMS mass spectrum is shifted to smaller m/z compared to both DIP and GC × GC and shows extensive thermal fragmentation due to the flash vaporization and pyrolysis process at 600 °C. This has the effect that the majority of the signal intensity can be attributed to lower m/z values, specifically to f44 (CO_2^+) and f28 (CO^+). CO_2^+ increases due to thermal decarboxylation, leading to limited chemical information. CO^+ is a likely thermal decomposition fragment

https://doi.org/10.1021/acsearthspacechem.2c00039
ACS Earth Space Chem. 2022, 6, 1358−1374

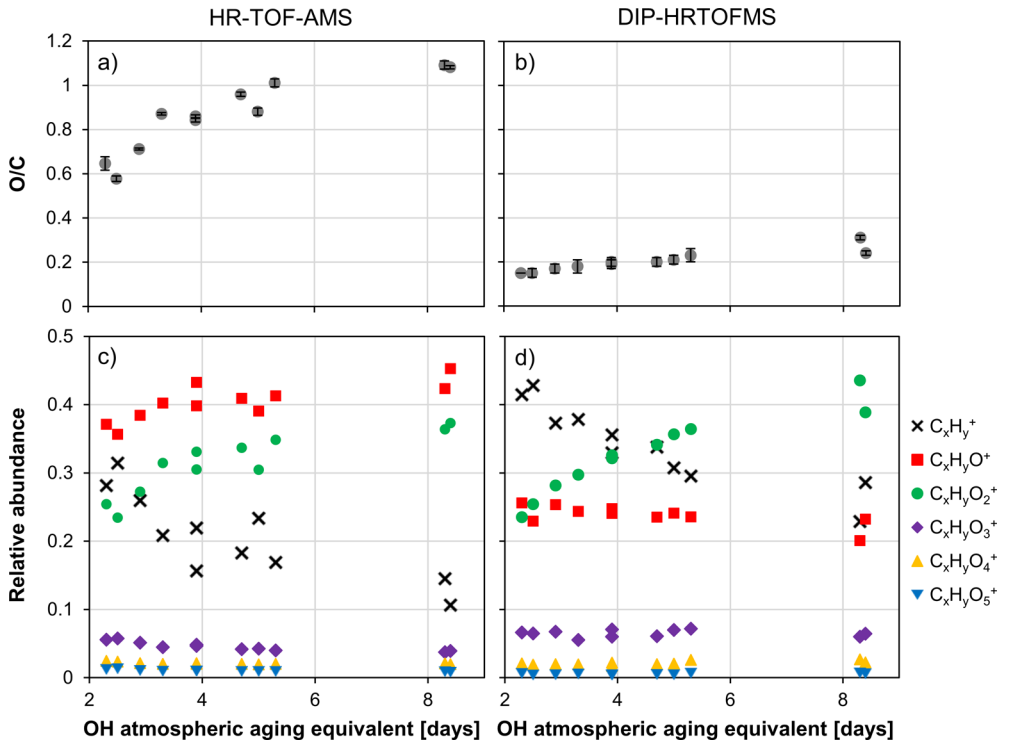

Figure 5. Influence of OH atmospheric aging equivalent on O/C for HR−TOF−AMS (a) and DIP−HRTOFMS (b) with standard deviation values from triplicate measurements (DIP) and all data points from the 1 h experiments (AMS). Relative abundance (ion counts) of organic families in % of total OC in respect to different OH atmospheric aging equivalent values for HR−TOF−AMS (c) and DIP−HRTOFMS (d).

of oxygenated organic species (e.g., carbonyls). In this regard, it has to be noted that for the AMS, it is difficult to accurately determine the CO^+ signal due to the significant interference from the gas phase N_2^+ background signal, which can overwhelm the spectrum at m/z 28.[11] Consequently, in the standard analysis the CO^+ signal is estimated from the CO_2^+ signal (Org_{28} = Org_{44} × 1) and may be overestimated when using this fragmentation assumption.[63]

In the DIP spectra, despite the high peak intensity from background air and probe carryover (which was corrected for with blank measurements) and the associated uncertainty of the result (Figure S6), there is a high CO_2^+ peak, which can be attributed to thermal fragmentation, although the CO^+ signal is much lower than for the AMS. Compared to the AMS spectra which shows mainly small fragments due to the extensive thermal decomposition of the compounds at 600 °C, the DIP spectra showed a higher abundance of larger masses. This is due to the direct introduction of the sample into the ionization region of the mass spectrometer without any discrimination of certain compounds. Additionally, high boiling compounds are evaporated at lower temperatures, as previously discussed, which leads to less thermal decomposition processes. On the other hand, the vaporization under reduced pressure leads to the discrimination of small and volatile compounds due to losses during the introduction phase of the analysis. When the sample is transferred from the gate valve to the ion source in the first few seconds of the analyses, some (semi-)volatile substances could evaporate outside of the ionization region and may thus not be detected.

As demonstrated in Figure 3, the strength of GC × GC with a mass spectrometric detector is its ability to generate highly selective mass spectral information due to peak deconvolution and reviewing of individual peak spectra. Nonetheless, it is possible to plot the GC × GC sum spectra for comparison to AMS and DIP (Figure 4c). For GC × GC, TD occurred with a gradual temperature gradient of 2 K s^{-1} (just as for DIP). However, instead of under vacuum conditions, in GC × GC, the sample vaporization takes place in a helium atmosphere under overpressure. Due to this moderately gentle thermal treatment, EI fragments dominate the spectrum, although thermal fragmentation can also be expected for GC × GC to some extent.[64] Thus, signals at m/z 28 (CO^+) and m/z 44 (CO_2^+) could also be expected for GC × GC and could provide information about the degree of thermal decomposition in the GC injector. However, CO^+ and CO_2^+ were not detected due to the applied acquisition delay. Furthermore, while cyrotrapping of CO_2 at −100 °C would be possible, its modulation with liquid nitrogen is difficult.

3.4.2. Oxidative State. Functionalization associated with the atmospheric aging of organic aerosols generally goes along with changes of O/C. Figure 5 shows increasing O/C value as an indication for increasing oxidation along with the increase in age for both AMS (Figure 5a) and DIP (Figure 5b). However, there is a major difference in the O/C ratio measured by the two instruments, the AMS measures a much higher O/C ratio between 0.5 and 1.1 compared to DIP with an O/C ratio in the range of 0.15−0.3. Furthermore, the relative abundance of different classes of hydrocarbons ($C_xH_y^+$) and oxygen-containing compounds ($C_xH_yO_z^+$) is shown. Thereby, the classes of $C_xH_yO^+$ and $C_xH_yO_2^+$ include the fragment ions CO^+ and CO_2^+. For AMS (Figure 5c), a clear reduction in the pure hydrocarbon fragments ($C_xH_y^+$) from above 30% to less than 20% could be seen with the increase in atmospheric aging. Reversely, the abundance of single oxygen ($C_xH_yO^+$) and double oxygen ($C_xH_yO_2^+$) compounds increased with atmospheric aging. Notably, there was no major change

https://doi.org/10.1021/acsearthspacechem.2c00039
ACS Earth Space Chem. 2022, 6, 1358−1374

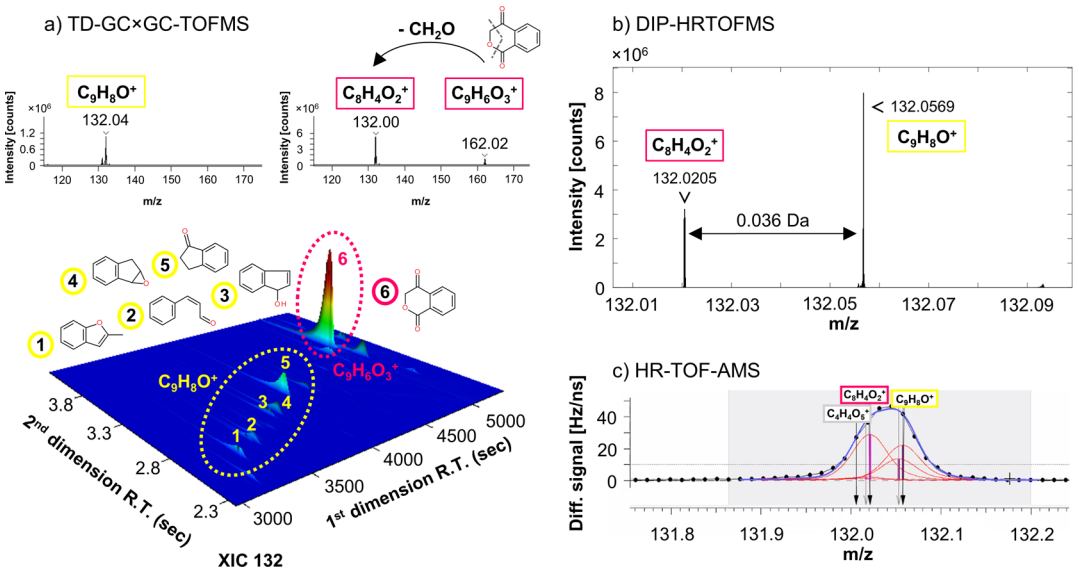

Figure 6. Example m/z 132 of SOA_{NAP}-SP (Exp1, atmospheric OH aging equivalent ≈ 4 d; 40% rH): GC × GC XIC with assignment of peaks to molecular formula and peak true spectrum (a); DIP high-resolution mass spectrum (b) and AMS "difference" spectra with sub-fitting of peaks (c). The AMS "difference" spectrum is calculated as the difference between the average aerosol (open chopper position) and average gas-phase (closed chopper position) mass spectrum by subtracting the gas phase from the aerosol phase. Thereby, the measured signal (black dotted line), fitted signal (blue line), as well as the fitted signals from the different compounds making up the total signal at m/z 132 (red lines) are depicted. The vertical, colored lines indicate the different fitted compounds.

found in compounds containing three to five oxygen molecules. For DIP (Figure 5d), not much change was observable except for the abundance of the $C_xH_y^+$ and $C_xH_yO_2^+$ compound classes, which were decreasing and increasing with atmospheric aging, respectively.

Accordingly, the difference between the O/C values of the two instruments can be primarily attributed to the higher abundance of $C_xH_yO^+$ in the AMS compared to DIP. This is largely due to the higher CO^+ signal for the AMS (Figure 4) which, as already mentioned above, is estimated from the CO_2^+ signal. It has to be noted, that in contrast to the AMS, no such fragmentation assumption or other factor corrections were applied to the DIP data. Especially in the case of more artificial aerosols generated from laboratory studies, the use of empirical correction factors for AMS data, such as the method applied here by Aiken et al.,[11] can affect the accuracy of the calculated elemental ratios.[45] In the case of the AMS, calibration factors are commonly applied to take differences between the elemental ratios of the detected fragment ions and their parent molecule into consideration. For instance, during the fragmentation process of polar oxygenated compounds such as, for example, alcohols or carboxylic acids, the loss of neutral fragments (e.g., CO_2, CO, and H_2O) could lead to the formation of ions, which add up to different elemental compositions than their parent molecules.[45] Furthermore, molecules containing a charge-stabilizing heteroatom typically yield relatively abundant molecular ions in EI−MS because the electron can be supplied from one of the free electron pairs of the heteroatom. This could potentially favor the abundance of heteroaromatic moieties. In principle, the DIP−HRTOFMS could be used in a similar fashion as the AMS and would offer additional benefits from its exact sum formula estimation due to its high mass resolution. For future studies, we will therefore measure several standard and reference aerosols for comparison. Furthermore, the lower abundance of $C_xH_yO^+$ for DIP could be due to the loss of volatile compounds during the sample introduction directly into the ion source or from QF filter handling and storage. Another reason for the higher O/C values in the AMS compared to DIP could be that neutral losses of CO or CO_2 during EI may be reduced in the AMS because the compounds are pyrolyzed to CO and CO_2 before ionization and detection as positive ions.

The increase in fragments pertaining to the double and or single oxygen classes in the AMS could potentially be attributed to the larger size of ELVOCs (e.g., highly oxidized oligomers), which in turn causes them to be more susceptible to thermal fragmentation. In contrast to the AMS, the DIP cannot target the whole range of volatility of compounds because the complete pyrolysis and thermal fragmentation of extremely low volatile compounds to CO and CO_2 cannot be guaranteed at a maximum temperature of 400 °C. Still, the relative abundance of the $C_xH_yO_3^+$ class for DIP is approximately twice that for AMS, which is due to the more gentle thermal treatment that results in fewer thermal fragments in DIP. Another commonly applied method to characterize aerosol aging is with a van-Krevelen diagram, which cross plots the H/C and O/C ratio and is depicted in the supplement for AMS and DIP data (Figure S7).

While first-generation products, which are continuously generated in the PAM reactor, are easily detected by GC × GC, (extremely) low-volatile and highly oxidized species, which are produced with increased photochemical age, cannot be detected as they exceed the accessibility of GC or are thermally degenerated during injection. The presence of such compounds in SOA_{NAP}-SP could be confirmed by Pardo et al.[65] by ultra-HR MS with electrospray ionization (ESI) in both positive (+ESI) and negative modes (−ESI) to investigate the molecular composition of the high-molecular-weight fraction. The +ESI mass spectra revealed oligomers around multiples of 10 carbon atoms up to tetramers with 40 carbon atoms and an average carbon oxidation state of −0.18.[65] Hence, observing aging trends up to an atmospheric age of 9

https://doi.org/10.1021/acsearthspacechem.2c00039
ACS Earth Space Chem. 2022, 6, 1358−1374

days is limited by GC × GC. Generally, only few differences in peak intensity were observed for samples of different aging conditions. The species with the highest peak intensities found by GC × GC showed a decreasing trend with photochemical age (Figure S8), as these early-generation products degrade and form highly oxidized species not detectable by GC × GC. In order to detect these polar constituents of organic PM, the in situ derivatization and TD of these compounds directly from the filter in the GC injector has been shown to be useful for aerosol aging studies.[66] Although it would be the standard practice for the analytes at hand, we did not apply derivatization in this study for reasons of comparability to AMS and DIP.

3.4.3. Structural Information. Structural information, which is of great importance for, for example, a toxicological assessment of aerosols or to elucidate reaction pathways, can be obtained by the three techniques in different analytical depths. In this regard, GC × GC is very well suited to separate individual compounds for further investigation of the molecular characterization up to their isomeric profiles. Primarily, this can be attributed to the high chromatographic resolution and peak capacity of two-dimensional chromatography, which, coupled with EI−MS, enables the spectral comparison of individual compounds with mass spectral libraries. Nonetheless, the identity of individual compounds should be further confirmed by retention indices and authentic standards, which often proves challenging because these are not always available for SOA constituents. In such cases, analytes can be identified using adequate surrogate standards with similar chemical moieties, for example, similar chromatographic properties and EI−MS fragmentation characteristics.[66]

The mass accuracy of the TD−GC × GC−TOFMS platform used here enabled the discrimination of compounds due to their exact masses despite the lower mass resolution compared to the other two techniques. However, also without a HR mass analyzer as detector valuable information on aerosol particle composition may be obtained. How GC × GC is able to resolve different peaks is illustrated in Figure 6a by the extracted ion chromatogram (XIC) of m/z 132. At this mass, multiple single analytes with the molecular formula of either $C_9H_8O^+$ or $C_8H_4O_3^+$ could be separated. A look to the mass spectra of these compounds illustrates the importance of differentiating fragment ions from molecular ions. For compounds with the sum formula $C_9H_8O^+$, the peak at m/z 132.04 is the molecular ion peak, whereas for $C_8H_4O_3^+$, the peak at m/z 132.00 is the $C_8H_4O_2^+$ fragment from 1*H*-2-benzopyran-1,4(3*H*)-dione ($C_9H_6O_3^+$) with the molecular ion at m/z 162.02. This differentiation and thus the assignment of the chemical structure is only possible due to chromatography. Besides the chromatographic separation in two dimensions, also the measured accurate masses of the peaks for $C_9H_8O^+$ (132.04) and $C_8H_4O_2^+$ (132.00), resulting in a mass difference of 40 mDa was sufficient to resolve the O versus CH_4 mass split (36.4 mDa). In order to resolve this mass split of 36.4 mDa at m/z 132 by MS only (without chromatographic separation) a mass resolution >3.0 × 10^3 would be necessary. Hence, in contrast to techniques that integrate the mass spectral raw data, such as the AMS or DIP, the masses could be resolved due to the separation in the chromatographic domain because the mass spectra are summed over a chromatographic peak. Consequently, in GC × GC the differentiation of certain isobaric masses is possible despite the theoretical limit of the MS.[46]

Neither AMS nor DIP allows molecular information to be acquired at the same level of detail, which in addition to the associated thermal degradation of the analytes, primarily is due to the accumulation of ions from different compounds in the same spectra. Therefore, only the elemental compositions in the sample can be determined. For both AMS and DIP, the various isomeric compounds separated by GC × GC such as 2-methylbenzofuran (1), 3-phenylacrylaldehyde (2), 1*H*-indenol (3), indan epoxide (4), and 2,3-dihydro-1*H*-inden-1-one (5) are summarized in one peak at m/z 132.06 ($C_9H_8O^+$) (Figure 6b,c). Thereby, a sharp, clear signal can be seen at the exact mass 132.0569 for DIP. For the AMS, a broad peak is seen at m/z 132.04, which is sub-fitted into peaks at several m/z. Hence, compared to GC × GC, neither the differentiation of structural nor stereo isomers is possible. Although for DIP with its high mass resolution, in some cases with specific fragmentation patterns, it may be possible to distinguish between structural or functional isomeric core structures, for example, if a heteroatom is located within versus if it is located outside the ring structure. In contrast to the AMS, the DIP spectra show less thermal fragments and mostly comprise well-characterized EI fragments. The aromatic backbone of NAP ring-retaining early oxidation products is relatively stable and show strong molecular ions in EI. With the high mass resolution of the DIP platform of >2.5 × 10^4, exact masses can be used to resolve isobaric mass fragments and assign reliable sum formulas up to high mass ranges. The obtained elemental compositions of ions enable calculations of the hydrogen deficiency or double bond equivalents, which gives additional information about structural features of organic molecules, such as the degree of aromaticity. In addition, the degree of oxidation can be directly derived from the number of oxygen atoms.

Although the AMS assigns elemental compositions based on the mass signals, this information is most commonly used to determine the elemental ratio. In order to extract information about the organic composition, the most plausible sub-peaks are fitted based on a peak list, which is selected by the user. For each peak, a number of compounds are fitted in order to get the best possible Gaussian fit to the measured exact mass in the spectrum. However, due to the limited mass resolution of the AMS, this approach becomes more and more difficult in the higher mass range because the number of possible formulas increases dramatically. In that regard, also the concentration ratio between two mass fragments to be resolved plays an important role for techniques without pre-separation because the necessary mass resolving power of peaks of unequal height with, for example, a peak height ratio of 100:1 is about 10 times higher than for peaks whose peak height is equal.[67] Thus, the AMS does not, by default, fit and assign elemental formulas in the mass range above m/z 100. As a result, the default peak list for ambient aerosols is prone to errors regarding the correct assignment of the molecular formulas, but the user may optimize the peak list in order to get more accurate fits. However, due to the strong fragmentation, typically the small ions account by far for the largest portion of the signal, which allows the determination of the elemental ratio without assigning larger ions. For structural assessment, this naturally requires the AMS user to have some general chemical understanding or pre-knowledge on the sample or underlying chemical processes. In this regard, DIP, which can use its higher mass resolution to determine each compound accurately, could assist as input for chemical information of

https://doi.org/10.1021/acsearthspacechem.2c00039
ACS Earth Space Chem. 2022, 6, 1358−1374

occurring ions. In the case of SOA_{NAP}-SP, with an improved peak list, the AMS assigned peaks quite accurately (Figure 6c) and the assigned formulas could often be confirmed with DIP. Thus, for well understood systems, such as the photooxidation of NAP in a PAM-OFR, the AMS achieves reasonable good fits even at higher m/z. However, with the increase in complexity, such as the addition of further oxidants (e.g., NO_x) or multiple VOCs, the accuracy of the AMS fit would likely decrease.

The example in (Figure 6) shows the separation of structural isomers (peaks 1−5) by GC × GC, which all share the same mass fragment (m/z = 132). AMS as well as DIP were unable to access the individual chemical species, even when applying accurate HR MS. For some of these components, specific toxicological studies are available in the literature. For example, cinnamaldehyde (2) was found to be a specific activator of the TRPA-1 receptor and elicited respiratory tenderness and cough.[68] On the other hand, 1-indanone (5) has been shown to exhibit antiangiogenic activity and may act as a moderately active anticancer agent.[69] Besides the specific effects, also the general functionality might exhibit different toxicological responses. Liu et al.[70] showed that organic compounds with different functionalities on the surface of SPs may have a decisive impact on the toxicological effect, which makes it important to be able to differentiate between furans (1), aldehydes (2), alcohols (3), epoxides (4), and ketones (5). Especially epoxide-containing compounds are associated with health risks in regards to oxidation potential. Additionally, both hydroxy and epoxide functional groups can be linked to an increased metabolic activity.[70]

4. CONCLUSIONS

In this study, we presented data from the analyses of NAP-derived SOA to assess how and to which extent the three different EI−MS instruments can determine organic chemical components in SOAs. The generation of SOA_{NAP}-SP was directly investigated by HR−TOF−AMS and in parallel PM was collected on QF filters for the analyses on a DIP−HRTOFMS platform and on a TD−GC × GC−TOFMS system with unit mass resolution. In each case, we consider the up-to-date design of the technique, preferring a TOF configuration of the mass spectrometric detector to a quadrupole in the case of the AMS, using a high-resolution mass spectrometer in the case of DIP and applying two-dimensional GC instead of one-dimensional GC. Detailed information on the chemical composition, as well as bulk parameters, such as the O/C and H/C ratio obtained from the different methods, were evaluated and compared.

The AMS, as an online instrument, was the only instrument that enabled the real-time quantitative analyses of the total organic aerosol. The rising O/C ratios with atmospheric OH aging equivalent indicated an increase in the average carbon oxidation state with the increase in photochemical age. Moreover, the AMS is a well-established and well-approved technique, but the resulting mass spectra are dominated by thermal fragments and the derived integral properties are often based on preliminary assumptions and correction factors that depend on the matrix in question. DIP could be applied atline and vaporizes the collected PM on QF filters under reduced pressure conditions, which also enables the volatilization of low-volatile compounds. The mild evaporation, compared to standard AMS operation, reduces thermal decomposition and, in combination with the applied EI, allows the derivation of some structural information such as major structural building blocks (functionalities) of the analytes. Additionally, the high mass resolution allows the discrimination of isobaric species and supports a reliable assignment to elemental compositions. These could be used as input data for the AMS data evaluation and could be confirmed by GC×GC. However, DIP is a direct infusion mass spectrometric technique such as the AMS, resulting in limited information on individual compounds with the separation of isomers restricted to their volatility profiles. For GC × GC, changes in composition of SOA_{NAP}-SP were difficult to determine at higher aging conditions due to its limited accessibility toward polar and higher-molecular-weight compounds without derivatization or pyrolyzing injection. However, the application of GC × GC allowed the fingerprinting and comprehensive analysis of the molecular composition of SOA_{NAP}-SP. As a major advantage, semivolatile organic constituents of PM can be chromatographically resolved up to their isomeric composition, which possibly allows the assignment of distinct health effects to individual constituents of the SOA.

We showed an assessment of the current strengths and limitations associated with both state-of-the-art and emerging instrumentation in the field of chemical aerosol characterization. Although no single technique is capable of providing all the desired information, in their complementarity, HR−TOF−AMS, DIP−HRTOFMS, and TD−GC × GC−TOFMS capture a great range of chemical properties. Due to the complexity of organic atmospheric aerosol, for future investigations on health effects, sources, fate, or pathways of atmospheric pollutants, the combination of mass spectrometric techniques could greatly enhance our chemical picture of the underlying processes.

■ ASSOCIATED CONTENT

Supporting Information

The Supporting Information is available free of charge at https://pubs.acs.org/doi/10.1021/acsearthspacechem.2c00039.

Dominance of OH radicals over ozone for atmospheric processing in the PAM OFR and an overview of the exact conditions of the 11 conducted experiments (Exp1 to Exp11); applied instrumental mass spectrometric parameters for HR−TOF−AMS, DIP−HRTOFMS, and TD−GC × GC−TOFMS; schematic diagrams for HR−TOF−AMS, DIP−HRTOFMS, and TD−GC × GC−TOFMS; DIP−HRTOFMS mass spectrum of SOA_{NAP}-SP with elemental composition assignments; DIP−HRTOFMS TIC and the XIC of the internal standard (benzo[ghi]perylene D12); DIP−HRTOFMS mass spectra at different temperatures in the ion source; OC and EC content of SOA_{NAP}-SP; abundance of CO^+ and CO_2^+ from DIP−HRTOFMS measurements and the associated uncertainty; van-Krevelen diagram for HR−TOF−AMS and DIP−HRTOFMS data and the influence of the OH atmospheric aging equivalent on H/C and O/C; and influence of atmospheric aging on the abundance of the selected aging species of SOA_{NAP}-SP by TD−GC × GC−TOFMS (PDF)

■ AUTHOR INFORMATION

Corresponding Author

Thomas Gröger − *Joint Mass Spectrometry Center (JMSC), Cooperation Group "Comprehensive Molecular Analytics"*

https://doi.org/10.1021/acsearthspacechem.2c00039
ACS Earth Space Chem. 2022, 6, 1358−1374

(CMA), Helmholtz Zentrum München, 85764 Neuherberg, Germany; Email: thomas.groeger@helmholtz-muenchen.de

Authors

Elena Hartner − *Joint Mass Spectrometry Center (JMSC), Cooperation Group "Comprehensive Molecular Analytics" (CMA), Helmholtz Zentrum München, 85764 Neuherberg, Germany; Joint Mass Spectrometry Center (JMSC), Chair of Analytical Chemistry, University of Rostock, 18059 Rostock, Germany;* orcid.org/0000-0002-6798-2403

Andreas Paul − *Joint Mass Spectrometry Center (JMSC), Chair of Analytical Chemistry, University of Rostock, 18059 Rostock, Germany; Institute of Energy and Climate Research, Troposphere (IEK-8), Forschungszentrum Jülich GmbH, 52425 Jülich, Germany*

Uwe Käfer − *Joint Mass Spectrometry Center (JMSC), Cooperation Group "Comprehensive Molecular Analytics" (CMA), Helmholtz Zentrum München, 85764 Neuherberg, Germany; Joint Mass Spectrometry Center (JMSC), Chair of Analytical Chemistry, University of Rostock, 18059 Rostock, Germany;* orcid.org/0000-0002-4016-0661

Hendryk Czech − *Joint Mass Spectrometry Center (JMSC), Cooperation Group "Comprehensive Molecular Analytics" (CMA), Helmholtz Zentrum München, 85764 Neuherberg, Germany; Joint Mass Spectrometry Center (JMSC), Chair of Analytical Chemistry, University of Rostock, 18059 Rostock, Germany;* orcid.org/0000-0001-8377-4252

Thorsten Hohaus − *Institute of Energy and Climate Research, Troposphere (IEK-8), Forschungszentrum Jülich GmbH, 52425 Jülich, Germany;* orcid.org/0000-0001-5722-6244

Martin Sklorz − *Joint Mass Spectrometry Center (JMSC), Cooperation Group "Comprehensive Molecular Analytics" (CMA), Helmholtz Zentrum München, 85764 Neuherberg, Germany*

Gert Jakobi − *Joint Mass Spectrometry Center (JMSC), Cooperation Group "Comprehensive Molecular Analytics" (CMA), Helmholtz Zentrum München, 85764 Neuherberg, Germany*

Jürgen Orasche − *Joint Mass Spectrometry Center (JMSC), Cooperation Group "Comprehensive Molecular Analytics" (CMA), Helmholtz Zentrum München, 85764 Neuherberg, Germany*

Seongho Jeong − *Joint Mass Spectrometry Center (JMSC), Cooperation Group "Comprehensive Molecular Analytics" (CMA), Helmholtz Zentrum München, 85764 Neuherberg, Germany; Joint Mass Spectrometry Center (JMSC), Chair of Analytical Chemistry, University of Rostock, 18059 Rostock, Germany*

Ramona Brejcha − *Joint Mass Spectrometry Center (JMSC), Cooperation Group "Comprehensive Molecular Analytics" (CMA), Helmholtz Zentrum München, 85764 Neuherberg, Germany*

Till Ziehm − *Institute of Energy and Climate Research, Troposphere (IEK-8), Forschungszentrum Jülich GmbH, 52425 Jülich, Germany*

Zhi-Hui Zhang − *Department of Environmental Sciences, University of Basel, 4056 Basel, Switzerland*

Jürgen Schnelle-Kreis − *Joint Mass Spectrometry Center (JMSC), Cooperation Group "Comprehensive Molecular Analytics" (CMA), Helmholtz Zentrum München, 85764 Neuherberg, Germany*

Thomas Adam − *Umwelttechnik und Chemie (WE 6), Universität der Bundeswehr München, 85577 Neubiberg, Germany*

Yinon Rudich − *Department of Earth and Planetary Sciences, Faculty of Chemistry, Weizmann Institute of Science, 76100 Rehovot, Israel;* orcid.org/0000-0003-3149-0201

Astrid Kiendler-Scharr − *Institute of Energy and Climate Research, Troposphere (IEK-8), Forschungszentrum Jülich GmbH, 52425 Jülich, Germany*

Ralf Zimmermann − *Joint Mass Spectrometry Center (JMSC), Cooperation Group "Comprehensive Molecular Analytics" (CMA), Helmholtz Zentrum München, 85764 Neuherberg, Germany; Joint Mass Spectrometry Center (JMSC), Chair of Analytical Chemistry, University of Rostock, 18059 Rostock, Germany*

Complete contact information is available at: https://pubs.acs.org/10.1021/acsearthspacechem.2c00039

Author Contributions

All authors contributed to the study conception and design. H.C., M.S., T.H., T.A., J.S.-K., T.G., A.K.-S., Y.R., and R.Z. conceived and supervised the study. Material preparation, data collection, analysis, and evaluation were performed by E.H., A.P., U.K., M.S., G.J., J.O., S.J., R.B., T.Z., and Z.-H.Z. The manuscript was written by E.H., A.P., and U.K. through contributions of all authors. All authors have given approval to the final version of the manuscript.

Notes

The authors declare no competing financial interest.

■ ACKNOWLEDGMENTS

This work was supported by the Helmholtz International Laboratory aeroHEALTH (InterLabs-0005; www.aerohealth.eu), the Helmholtz Association of German Research Centers (HGF), and the Helmholtz Virtual Institute of Complex Systems in Environmental Health (www.hice-vi.eu, Inhale-HICE). We thank William H. Brune (Pennsylvania State University) for providing the PAM OFR. Y.R. acknowledges support by a research grant from the Anita James Rosen Foundation. E.H. acknowledges support from her thesis committee with external supervisor Andreas Held (Technische Universität Berlin).

■ REFERENCES

(1) Goldstein, A. H.; Galbally, I. E. Known and Unexplored Organic Constituents in the Earth's Atmosphere. *Environ. Sci. Technol.* **2007**, *41*, 1514−1521.

(2) Shakya, K. M.; Griffin, R. J. Secondary Organic Aerosol from Photooxidation of Polycyclic Aromatic Hydrocarbons. *Environ. Sci. Technol.* **2010**, *44*, 8134−8139.

(3) Hallquist, M.; Wenger, J. C.; Baltensperger, U.; Rudich, Y.; Simpson, D.; Claeys, M.; Dommen, J.; Donahue, N. M.; George, C.; Goldstein, A. H.; Hamilton, J. F.; Herrmann, H.; Hoffmann, T.; Iinuma, Y.; Jang, M.; Jenkin, M. E.; Jimenez, J. L.; Kiendler-Scharr, A.; Maenhaut, W.; McFiggans, G.; Mentel, T. F.; Monod, A.; Prévôt, A. S. H.; Seinfeld, J. H.; Surratt, J. D.; Szmigielski, R.; Wildt, J. The formation, properties and impact of secondary organic aerosol: current and emerging issues. *Atmos. Chem. Phys.* **2009**, *9*, 5155−5236.

(4) Rudich, Y.; Donahue, N. M.; Mentel, T. F. Aging of Organic Aerosol: Bridging the Gap Between Laboratory and Field Studies. *Annu. Rev. Phys. Chem.* **2007**, *58*, 321−352.

(5) Johnston, M. V.; Kerecman, D. E. Molecular Characterization of Atmospheric Organic Aerosol by Mass Spectrometry. *Annu. Rev. Anal. Chem.* **2019**, *12*, 247−274.

(6) Parshintsev, J.; Hyötyläinen, T. Methods for characterization of organic compounds in atmospheric aerosol particles. *Anal. Bioanal. Chem.* **2015**, *407*, 5877−5897.
(7) Kind, T.; Fiehn, O. Advances in structure elucidation of small molecules using mass spectrometry. *Bioanal. Rev.* **2010**, *2*, 23−60.
(8) Zhang, Q.; Jimenez, J. L.; Canagaratna, M. R.; Ulbrich, I. M.; Ng, N. L.; Worsnop, D. R.; Sun, Y. Understanding atmospheric organic aerosols via factor analysis of aerosol mass spectrometry: a review. *Anal. Bioanal. Chem.* **2011**, *401*, 3045−3067.
(9) DeCarlo, P. F.; Kimmel, J. R.; Trimborn, A.; Northway, M. J.; Jayne, J. T.; Aiken, A. C.; Gonin, M.; Fuhrer, K.; Horvath, T.; Docherty, K. S.; Worsnop, D. R.; Jimenez, J. L. Field-Deployable, High-Resolution, Time-of-Flight Aerosol Mass Spectrometer. *Anal. Chem.* **2006**, *78*, 8281−8289.
(10) Drewnick, F.; Hings, S. S.; DeCarlo, P.; Jayne, J. T.; Gonin, M.; Fuhrer, K.; Weimer, S.; Jimenez, J. L.; Demerjian, K. L.; Borrmann, S.; Worsnop, D. R. A New Time-of-Flight Aerosol Mass Spectrometer (TOF-AMS)—Instrument Description and First Field Deployment. *Aerosol Sci. Technol.* **2005**, *39*, 637−658.
(11) Aiken, A. C.; DeCarlo, P. F.; Kroll, J. H.; Worsnop, D. R.; Huffman, J. A.; Docherty, K. S.; Ulbrich, I. M.; Mohr, C.; Kimmel, J. R.; Sueper, D.; Sun, Y.; Zhang, Q.; Trimborn, A.; Northway, M.; Ziemann, P. J.; Canagaratna, M. R.; Onasch, T. B.; Alfarra, M. R.; Prevot, A. S. H.; Dommen, J.; Duplissy, J.; Metzger, A.; Baltensperger, U.; Jimenez, J. L. O/C and OM/OC Ratios of Primary, Secondary, and Ambient Organic Aerosols with High-Resolution Time-of-Flight Aerosol Mass Spectrometry. *Environ. Sci. Technol.* **2008**, *42*, 4478−4485.
(12) Kroll, J. H.; Donahue, N. M.; Jimenez, J. L.; Kessler, S. H.; Canagaratna, M. R.; Wilson, K. R.; Altieri, K. E.; Mazzoleni, L. R.; Wozniak, A. S.; Bluhm, H.; Mysak, E. R.; Smith, J. D.; Kolb, C. E.; Worsnop, D. R. Carbon oxidation state as a metric for describing the chemistry of atmospheric organic aerosol. *Nat. Chem.* **2011**, *3*, 133−139.
(13) Canagaratna, M. R.; Jayne, J. T.; Jimenez, J. L.; Allan, J. D.; Alfarra, M. R.; Zhang, Q.; Onasch, T. B.; Drewnick, F.; Coe, H.; Middlebrook, A.; Delia, A.; Williams, L. R.; Trimborn, A. M.; Northway, M. J.; DeCarlo, P. F.; Kolb, C. E.; Davidovits, P.; Worsnop, D. R. Chemical and microphysical characterization of ambient aerosols with the aerodyne aerosol mass spectrometer. *Mass Spectrom. Rev.* **2007**, *26*, 185−222.
(14) An, Z.; Li, X.; Shi, Z.; Williams, B. J.; Harrison, R. M.; Jiang, J. Frontier review on comprehensive two-dimensional gas chromatography for measuring organic aerosol. *J. Hazard. Mater. Lett.* **2021**, *2*, 100013.
(15) Geldenhuys, G.; Rohwer, E. R.; Naudé, Y.; Forbes, P. B. C. Monitoring of atmospheric gaseous and particulate polycyclic aromatic hydrocarbons in South African platinum mines utilising portable denuder sampling with analysis by thermal desorption−comprehensive gas chromatography−mass spectrometry. *J. Chromatogr. A* **2015**, *1380*, 17−28.
(16) Liang, Y.; Jen, C. N.; Weber, R. J.; Misztal, P. K.; Goldstein, A. H. Chemical composition of PM2.5 in October 2017 Northern California wildfire plumes. *Atmos. Chem. Phys.* **2021**, *21*, 5719−5737.
(17) Weggler, B. A.; Ly-Verdu, S.; Jennerwein, M.; Sippula, O.; Reda, A. A.; Orasche, J.; Gröger, T.; Jokiniemi, J.; Zimmermann, R. Untargeted Identification of Wood Type-Specific Markers in Particulate Matter from Wood Combustion. *Environ. Sci. Technol.* **2016**, *50*, 10073−10081.
(18) Welthagen, W.; Schnelle-Kreis, J.; Zimmermann, R. Search criteria and rules for comprehensive two-dimensional gas chromatography−time-of-flight mass spectrometry analysis of airborne particulate matter. *J. Chromatogr. A* **2003**, *1019*, 233−249.
(19) Cronn, D. R.; Charlson, R. J.; Knights, R. L.; Crittenden, A. L.; Appel, B. R. A survey of the molecular nature of primary and secondary components of particles in urban air by high-resolution mass spectrometry. *Atmos. Environ.* **1967**, *11*, 929−937.
(20) Flego, C.; Carati, C.; Gaudio, L. D.; Zannoni, C. Direct Mass Spectrometry of tar sands: A new approach to bitumen identification. *Fuel* **2013**, *111*, 357−366.
(21) Käfer, U.; Gröger, T.; Rüger, C. P.; Czech, H.; Saraji-Bozorgzad, M.; Wilharm, T.; Zimmermann, R. Direct inlet probe − High-resolution time-of-flight mass spectrometry as fast technique for the chemical description of complex high-boiling samples. *Talanta* **2019**, *202*, 308−316.
(22) Guzzonato, A.; Mehlmann, H.; Krumwiede, D.; Harrad, S. A novel method for quantification of decabromodiphenyl ether in plastics without sample preparation using direct insertion probe − magnetic sector high resolution mass spectrometry. *Anal. Methods* **2016**, *8*, 5487−5494.
(23) Castilla, C.; Rüger, C. P.; Marcotte, S.; Lavanant, H.; Afonso, C. Direct Inlet Probe Atmospheric Pressure Photo and Chemical Ionization Coupled to Ultrahigh Resolution Mass Spectrometry for the Description of Lignocellulosic Biomass. *J. Am. Soc. Mass Spectrom.* **2020**, *31*, 822−831.
(24) Christensen, E.; Evans, R. J.; Carpenter, D. High-resolution mass spectrometric analysis of biomass pyrolysis vapors. *J. Anal. Appl. Pyrolysis* **2017**, *124*, 327−334.
(25) Schuetzle, D.; Crittenden, A. L.; Charlson, R. J. Application of Computer Controlled High Resolution Mass Spectrometry to the Analysis of Air Pollutants. *J. Air Pollut. Control Assoc.* **1973**, *23*, 704−709.
(26) Drewnick, F.; Diesch, J.-M.; Faber, P.; Borrmann, S. Aerosol mass spectrometry: particle−vaporizer interactions and their consequences for the measurements. *Atmos. Meas. Tech.* **2015**, *8*, 3811−3830.
(27) Bruns, E. A.; El Haddad, I.; Keller, A.; Klein, F.; Kumar, N. K.; Pieber, S. M.; Corbin, J. C.; Slowik, J. G.; Brune, W. H.; Baltensperger, U.; Prévôt, A. S. H. Inter-comparison of laboratory smog chamber and flow reactor systems on organic aerosol yield and composition. *Atmos. Meas. Tech.* **2015**, *8*, 2315−2332.
(28) Kang, E.; Root, M. J.; Toohey, D. W.; Brune, W. H. Introducing the concept of Potential Aerosol Mass (PAM). *Atmos. Chem. Phys.* **2007**, *7*, 5727.
(29) Andreae, M. O.; Gelencsér, A. Black carbon or brown carbon? The nature of light-absorbing carbonaceous aerosols. *Atmos. Chem. Phys.* **2006**, *6*, 3131−3148.
(30) Jia, C.; Batterman, S. A Critical Review of Naphthalene Sources and Exposures Relevant to Indoor and Outdoor Air. *Int. Res. J. Publ. Environ. Health* **2010**, *7*, 2903−2939.
(31) Chen, C.-L.; Kacarab, M.; Tang, P.; Cocker, D. R. SOA formation from naphthalene, 1-methylnaphthalene, and 2-methylnaphthalene photooxidation. *Atmos. Environ.* **2016**, *131*, 424−433.
(32) Offer, S.; Hartner, E.; Di Bucchianico, S.; Bisig, C.; Bauer, S.; Pantzke, J.; Zimmermann, E. J.; Cao, X.; Binder, S.; Kuhn, E.; Huber, A.; Jeong, S.; Käfer, U.; Martens, P.; Mesceriakovas, A.; Bendl, J.; Brejcha, R.; Buchholz, A.; Gat, D.; Hohaus, T.; Rastak, N.; Jakobi, G.; Kalberer, M.; Kanashova, T.; Hu, Y.; Ogris, C.; Marsico, A.; Theis, F.; Pardo, M.; Gröger, T.; Oeder, S.; Orasche, J.; Paul, A.; Ziehm, T.; Zhang, Z.-H.; Adam, T.; Sippula, O.; Sklorz, M.; Schnelle-Kreis, J.; Czech, H.; Kiendler-Scharr, A.; Rudich, Y.; Zimmermann, R. Effect of Atmospheric Aging on Soot Particle Toxicity in Lung Cell Models at the Air-Liquid Interface: Differential Toxicological Impacts of Biogenic and Anthropogenic Secondary Organic Aerosols (SOAs). *Environ. Health Perspect.* **2022**, *130*, 027003.
(33) Zhang, Z.-H.; Hartner, E.; Utinger, B.; Gfeller, B.; Paul, A.; Sklorz, M.; Czech, H.; Yang, B. X.; Su, X. Y.; Jakobi, G.; Orasche, J.; Schnelle-Kreis, J.; Jeong, S.; Gröger, T.; Pardo, M.; Hohaus, T.; Adam, T.; Kiendler-Scharr, A.; Rudich, Y.; Zimmermann, R.; Kalberer, M. Are reactive oxygen species (ROS) a suitable metric to predict toxicity of carbonaceous aerosol particles? *Atmos. Chem. Phys. Discuss.* **2021**, *2021*, 1−29.
(34) Barmet, P.; Dommen, J.; DeCarlo, P. F.; Tritscher, T.; Praplan, A. P.; Platt, S. M.; Prévôt, A. S. H.; Donahue, N. M.; Baltensperger, U. OH clock determination by proton transfer reaction mass

spectrometry at an environmental chamber. *Atmos. Meas. Tech.* **2012**, *5*, 647−656.
(35) Prinn, R. G.; Huang, J.; Weiss, R. F.; Cunnold, D. M.; Fraser, P. J.; Simmonds, P. G.; McCulloch, A.; Harth, C.; Salameh, P.; O'Doherty, S.; Wang, R. H. J.; Porter, L.; Miller, B. R. Evidence for Substantial Variations of Atmospheric Hydroxyl Radicals in the Past Two Decades. *Science* **2001**, *292*, 1882−1888.
(36) Atkinson, R. Atmospheric chemistry of VOCs and NOx. *Atmos. Environ.* **2000**, *34*, 2063−2101.
(37) Atkinson, R.; Arey, J. Atmospheric Degradation of Volatile Organic Compounds. *Chem. Rev.* **2003**, *103*, 4605−4638.
(38) Atkinson, R.; Carter, W. P. L. Kinetics and mechanisms of the gas-phase reactions of ozone with organic compounds under atmospheric conditions. *Chem. Rev.* **1984**, *84*, 437−470.
(39) Chow, J. C.; Watson, J. G.; Chen, L.-W. A.; Chang, M. C. O.; Robinson, N. F.; Trimble, D.; Kohl, S. The IMPROVE_A Temperature Protocol for Thermal/Optical Carbon Analysis: Maintaining Consistency with a Long-Term Database. *J. Air Waste Manage. Assoc.* **2007**, *57*, 1014−1023.
(40) Liu, P. S. K.; Deng, R.; Smith, K. A.; Williams, L. R.; Jayne, J. T.; Canagaratna, M. R.; Moore, K.; Onasch, T. B.; Worsnop, D. R.; Deshler, T. Transmission Efficiency of an Aerodynamic Focusing Lens System: Comparison of Model Calculations and Laboratory Measurements for the Aerodyne Aerosol Mass Spectrometer. *Aerosol Sci. Technol.* **2007**, *41*, 721−733.
(41) Jayne, J. T.; Leard, D. C.; Zhang, X.; Davidovits, P.; Smith, K. A.; Kolb, C. E.; Worsnop, D. R. Development of an Aerosol Mass Spectrometer for Size and Composition Analysis of Submicron Particles. *Aerosol Sci. Technol.* **2000**, *33*, 49−70.
(42) Allan, J. D.; Jimenez, J. L.; Williams, P. I.; Alfarra, M. R.; Bower, K. N.; Jayne, J. T.; Coe, H.; Worsnop, D. R. Quantitative sampling using an Aerodyne aerosol mass spectrometer 1. Techniques of data interpretation and error analysis. *J. Geophys. Res. Atmos.* **2003**, *108*, 4090.
(43) Aiken, A. C.; DeCarlo, P. F.; Jimenez, J. L. Elemental Analysis of Organic Species with Electron Ionization High-Resolution Mass Spectrometry. *Anal. Chem.* **2007**, *79*, 8350−8358.
(44) Corbin, J. C.; Othman, A.; Allan, J. D.; Worsnop, D. R.; Haskins, J. D.; Sierau, B.; Lohmann, U.; Mensah, A. Peak-fitting and integration imprecision in the Aerodyne aerosol mass spectrometer: effects of mass accuracy on location-constrained fits. *Atmos. Meas. Tech.* **2015**, *8*, 4615−4636.
(45) Canagaratna, M. R.; Jimenez, J. L.; Kroll, J. H.; Chen, Q.; Kessler, S. H.; Massoli, P.; Hildebrandt Ruiz, L.; Fortner, E.; Williams, L. R.; Wilson, K. R.; Surratt, J. D.; Donahue, N. M.; Jayne, J. T.; Worsnop, D. R. Elemental ratio measurements of organic compounds using aerosol mass spectrometry: characterization, improved calibration, and implications. *Atmos. Chem. Phys.* **2015**, *15*, 253−272.
(46) Byer, J. D.; Siek, K.; Jobst, K. Distinguishing the C3 vs SH4 Mass Split by Comprehensive Two-Dimensional Gas Chromatography−High Resolution Time-of-Flight Mass Spectrometry. *Anal. Chem.* **2016**, *88*, 6101−6104.
(47) Gröger, T. M.; Käfer, U.; Zimmermann, R. Gas chromatography in combination with fast high-resolution time-of-flight mass spectrometry: Technical overview and perspectives for data visualization. *Trac. Trends Anal. Chem.* **2020**, *122*, 115677.
(48) Rüger, C. P.; Grimmer, C.; Sklorz, M.; Neumann, A.; Streibel, T.; Zimmermann, R. Combination of Different Thermal Analysis Methods Coupled to Mass Spectrometry for the Analysis of Asphaltenes and Their Parent Crude Oils: Comprehensive Characterization of the Molecular Pyrolysis Pattern. *Energy Fuels* **2018**, *32*, 2699−2711.
(49) Nespor, B.; Cochran, R.; Jeong, H.; Bowman, F.; Delene, D.; Kozliak, E.; Kubátová, A. Occurrence of both nonvolatile and semivolatile carbonaceous air particulate markers using thermal desorption-pyrolysis-gas chromatography-mass spectrometry. *Atmos. Environ.* **2021**, *246*, 118058.
(50) Ahn, Y. G.; Jeon, S. H.; Lim, H. B.; Choi, N. R.; Hwang, G.-S.; Kim, Y. P.; Lee, J. Y. Analysis of Polycyclic Aromatic Hydrocarbons in Ambient Aerosols by Using One-Dimensional and Comprehensive Two-Dimensional Gas Chromatography Combined with Mass Spectrometric Method: A Comparative Study. *J. Anal. Methods Chem.* **2018**, *2018*, 8341630.
(51) Käfer, U.; Gröger, T.; Rohbogner, C. J.; Struckmeier, D.; Saraji-Bozorgzad, M. R.; Wilharm, T.; Zimmermann, R. Detailed Chemical Characterization of Bunker Fuels by High-Resolution Time-of-Flight Mass Spectrometry Hyphenated to GC × GC and Thermal Analysis. *Energy Fuels* **2019**, *33*, 10745−10755.
(52) Croes, K.; Steffens, A.; Marchand, D. H.; Snyder, L. R. Relevance of $\pi-\pi$ and dipole−dipole interactions for retention on cyano and phenyl columns in reversed-phase liquid chromatography. *J. Chromatogr. A* **2005**, *1098*, 123−130.
(53) Shiroudi, A.; Deleuze, M. S.; Canneaux, S. Theoretical Study of the Oxidation Mechanisms of Naphthalene Initiated by Hydroxyl Radicals: The OH-Addition Pathway. *J. Phys. Chem. A* **2014**, *118*, 4593−4610.
(54) Keyte, I. J.; Harrison, R. M.; Lammel, G. Chemical reactivity and long-range transport potential of polycyclic aromatic hydrocarbons − a review. *Chem. Soc. Rev.* **2013**, *42*, 9333−9391.
(55) Klotz, L.-O.; Hou, X.; Jacob, C. 1,4-Naphthoquinones: From Oxidative Damage to Cellular and Inter-Cellular Signaling. *Molecules* **2014**, *19*, 14902−14918.
(56) Lee, J. Y.; Lane, D. A. Unique products from the reaction of naphthalene with the hydroxyl radical. *Atmos. Environ.* **2009**, *43*, 4886−4893.
(57) Jones, N.; Wendt, J.; Wright, S.; Hartner, E.; Gröger, T. Analysis of Microplastics in Environmental Samples by Pyrolysis/Thermal Desorption-(GC)xGC-TOFMS. *Chromatography Today* **2021**, *14* (2), 36−40.
(58) Kallio, M.; Hyötyläinen, T.; Lehtonen, M.; Jussila, M.; Hartonen, K.; Shimmo, M.; Riekkola, M. L. Comprehensive two-dimensional gas chromatography in the analysis of urban aerosols. *J. Chromatogr. A* **2003**, *1019*, 251−260.
(59) Lyu, Y.; Xu, T.; Yang, X.; Chen, J.; Cheng, T.; Li, X. Seasonal contributions to size-resolved n-alkanes (C8-C40) in the Shanghai atmosphere from regional anthropogenic activities and terrestrial plant waxes. *Sci. Total Environ.* **2017**, *579*, 1918−1928.
(60) Özel, M. Z.; Hamilton, J. F.; Lewis, A. C. New Sensitive and Quantitative Analysis Method for Organic Nitrogen Compounds in Urban Aerosol Samples. *Environ. Sci. Technol.* **2011**, *45*, 1497−1505.
(61) Kroll, J. H.; Smith, J. D.; Che, D. L.; Kessler, S. H.; Worsnop, D. R.; Wilson, K. R. Measurement of fragmentation and functionalization pathways in the heterogeneous oxidation of oxidized organic aerosol. *Phys. Chem. Chem. Phys.* **2009**, *11*, 8005−8014.
(62) Ng, N. L.; Canagaratna, M. R.; Jimenez, J. L.; Chhabra, P. S.; Seinfeld, J. H.; Worsnop, D. R. Changes in organic aerosol composition with aging inferred from aerosol mass spectra. *Atmos. Chem. Phys.* **2011**, *11*, 6465−6474.
(63) Pieber, S. M.; El Haddad, I.; Slowik, J. G.; Canagaratna, M. R.; Jayne, J. T.; Platt, S. M.; Bozzetti, C.; Daellenbach, K. R.; Fröhlich, R.; Vlachou, A.; Klein, F.; Dommen, J.; Miljevic, B.; Jiménez, J. L.; Worsnop, D. R.; Baltensperger, U.; Prévôt, A. S. H. Inorganic Salt Interference on CO2+ in Aerodyne AMS and ACSM Organic Aerosol Composition Studies. *Environ. Sci. Technol.* **2016**, *50*, 10494−10503.
(64) Zhao, Z.; Yang, X.; Lee, J.; Tolentino, R.; Mayorga, R.; Zhang, W.; Zhang, H. Diverse Reactions in Highly Functionalized Organic Aerosols during Thermal Desorption. *ACS Earth Space Chem.* **2020**, *4*, 283−296.
(65) Pardo, M.; Offer, S.; Hartner, E.; Di Bucchianico, S.; Bisig, C.; Bauer, S.; Pantzke, J.; Zimmermann, E. J.; Cao, X.; Binder, S.; Kuhn, E.; Huber, A.; Jeong, S.; Käfer, U.; Schneider, E.; Mesceriakovas, A.; Bendl, J.; Brejcha, R.; Buchholz, A.; Gat, D.; Hohaus, T.; Rastak, N.; Karg, E.; Jakobi, G.; Kalberer, M.; Kanashova, T.; Hu, Y.; Ogris, C.; Marsico, A.; Theis, F.; Shalit, T.; Gröger, T.; Rüger, C. P.; Oeder, S.; Orasche, J.; Paul, A.; Ziehm, T.; Zhang, Z. H.; Adam, T.; Sippula, O.; Sklor, M.; Schnelle-Kreis, J.; Czech, H.; Kiendler-Scharr, A.; Zimmermann, R.; Rudich, Y. *Exposure to Naphthalene and β-Pinene-derived Secondary Organic Aerosol Induced Divergent Changes in*

https://doi.org/10.1021/acsearthspacechem.2c00039
ACS Earth Space Chem. 2022, 6, 1358−1374

Transcript Levels of BEAS-2B Cells; Environment International, 2022. (under review).
(66) Orasche, J.; Schnelle-Kreis, J.; Abbaszade, G.; Zimmermann, R. Technical Note: In-situ derivatization thermal desorption GC-TOFMS for direct analysis of particle-bound non-polar and polar organic species. *Atmos. Chem. Phys.* **2011**, *11*, 8977−8993.
(67) Marshall, A. G.; Blakney, G. T.; Chen, T.; Kaiser, N.; McKenna, A.; Rodgers, R.; Ruddy, B.; Xian, F. Mass resolution and mass accuracy: how much is enough? *Mass Spectrom.* **2013**, *2*, S0009 Spec Iss.
(68) Birrell, M. A.; Belvisi, M. G.; Grace, M.; Sadofsky, L.; Faruqi, S.; Hele, D. J.; Maher, S. A.; Freund-Michel, V.; Morice, A. H. TRPA1 agonists evoke coughing in guinea pig and human volunteers. *Am. J. Respir. Crit. Care Med.* **2009**, *180*, 1042−1047.
(69) Chanda, D.; Bhushan, S.; Guru, S. K.; Shanker, K.; Wani, Z. A.; Rah, B. A.; Luqman, S.; Mondhe, D. M.; Pal, A.; Negi, A. S. Anticancer activity, toxicity and pharmacokinetic profile of an indanone derivative. *Eur. J. Pharm. Sci.* **2012**, *47*, 988−995.
(70) Liu, Y.; Jiang, H.; Liu, C.; Ge, Y.; Wang, L.; Zhang, B.; He, H.; Liu, S. Influence of functional groups on toxicity of carbon nanomaterials. *Atmos. Chem. Phys.* **2019**, *19*, 8175−8187.
(71) Ricca, A.; Bauschlicher Jr, C. W The reactions of polycyclic aromatic hydrocarbons with OH. *Chem. Phys. Lett.* **2000**, *328*, 396−402.

https://doi.org/10.1021/acsearthspacechem.2c00039
ACS Earth Space Chem. 2022, 6, 1358−1374